ISSN 1348-5822

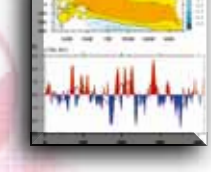
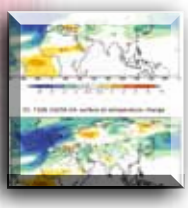

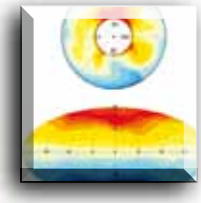
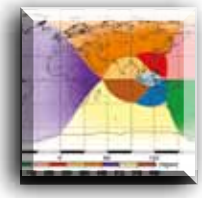
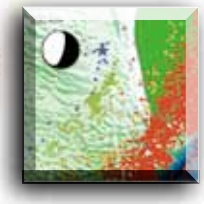
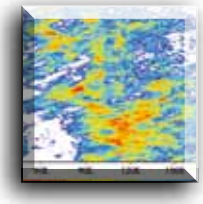

Annual Report of the Earth Simulator Center

April 2013 – March 2014




Center for Earth Information Science and Technology
Japan Agency for Marine-Earth Science and Technology

Annual Report of the Earth Simulator Center

April 2013—March 2014

Center for Earth Information Science and Technology
Japan Agency for Marine-Earth Science and Technology

CONTENTS

Outline of the Earth Simulator Project

Earth Simulator Research Projects

Chapter 1 Earth Science

Chapter 2 Visualization

Outline of the Earth Simulator Project

1. Mission and Basic Principles of the Earth simulator

The Earth Simulator was developed for the following aims. The first aim is to ensure a bright future for human begins by accurately predicting variable global environment. The second is to contribute to the development of science and technology in the 21st century. Based on these aims, the principles listed below are established for the projects of the Earth Simulator.

1) Each project should be open to researches in each research field and to the public, rather than it is confined within the limited research society.
2) In principle, the research achievements obtained by using the Earth Simulator should be promptly published and returned to the public.
3) Earth project should be carried out for peaceful purposes only.

2. Earth Simulator Research Project

The allocation of the Earth Simulator resources for each research field in FY2013 was decided to be as shown in Fig. 1. There are three project categories in the Earth Simulator resource allocation. The projects are shown in Table 1 and 2.

1) Proposed Research projects:
   We accept and select applications for the research projects of the earth science field which is included Climate Change, Solid Earth, Natural Disasters, etc.
2) Contract Research projects:
   The projects using the Earth Simulator focus on research commissioned by public organizations such as the government.
   - The Program for Risk Information on Climate Change (SOUSEI).
   - The Program for Creating Innovation by Sharing Advanced Research Facilities (The Strategic Industrial Use)
   - Consignment Study (JST/CREST, KAKENHI, etc.)
3) JAMSTEC Research projects:
   The Earth Simulator is also used for research projects organized by JAMSTEC, international and domestic collaboration projects and the execution of urgent jobs in the time of natural disasters. In addition, fee-based usage of the Earth Simulator is included in this category.

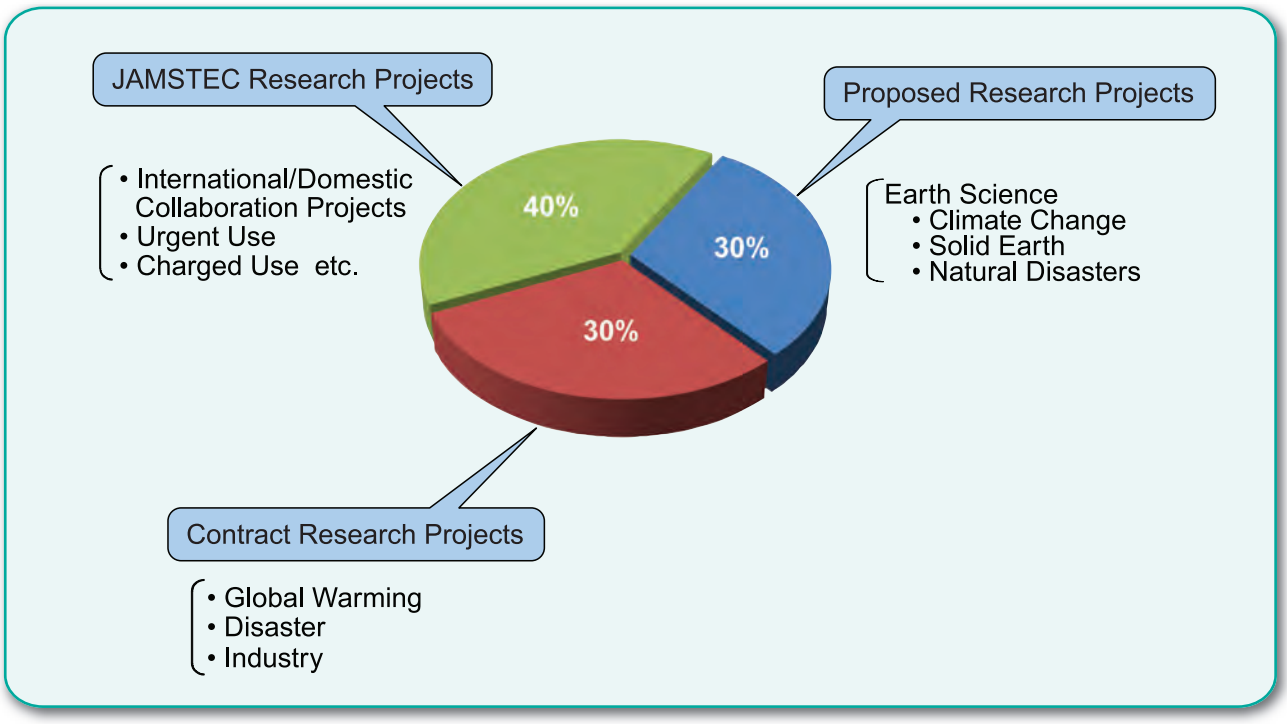

Fig. 1 The Allocation of Resources of the Earth Simulator in FY2013

Table 1 Proposed Research Projects in FY2013

Earth Science (24 projects)

	Project Name	Name of Project Representative	Professional Affiliation of Project Representative
1	Understanding Roles of Oceanic Fine Structures in Climate and its Variability	Hideharu Sasaki	ESC, JAMSTEC
2	Simulations of Adaptation-Oriented Strategy for Climate Variability	Keiko Takahashi	ESC, JAMSTEC
3	Development of a High-quality Climate Model for Global Warming Projection Study	Akira Noda	RIGC, JAMSTEC
4	Simulations of Atmospheric General Circulations of Earth-like Planets by AFES	Yoshiyuki Hayashi	Graduate School of Science, Kobe University
5	Study on the Diagnostics and Projection of Marine Ecosystem Change Associated with Global Change	Sanae Chiba	RIGC, JAMSTEC
6	Study of Cloud and Precipitation Processes Using a Global Cloud-system Resolving Model	Masaki Sato	RIGC, JAMSTEC / Atmosphere and Ocean Research Institute, The University of Tokyo
7	Study on the Predictability of Climate Variations and Their Mechanisms	Yukio Masumoto	RIGC, JAMSTEC
8	Simulation and Verification of Tropical Deep Convective Clouds Using Eddy-permitting Regional Atmospheric Models	Kozo Nakamura	RIGC, JAMSTEC
9	Improved Ocean State Estimation by Using a 4D-VAR Ocean Data Assimilation System	Shuhei Masuda	RIGC, JAMSTEC
10	Global Elastic Response Simulation	Seiji Tsuboi	DrC, JAMSTEC
11	Simulation Study on the Dynamics of the Mantle and Core in Earth-like Conditions	Yozo Hamano	IFREE, JAMSTEC
12	Numerical Simulation of Seismic Wave Propagation and Strong Ground Motions in 3-D Heterogeneous Media	Takashi Furumura	Center for Integrated Disaster Information Research, Interfaculty Initiative in Information Studies, The University of Tokyo/Earthquake Research Institute, The University of Tokyo
13	Development of Advanced Simulation Tools for Solid Earth Sciences	Mikito Furuichi	IFREE, JAMSTEC
14	Numerical Simulations of the Dynamics of Volcanic Phenomena	Takehiro Koyaguchi	Earthquake Research Institute, The University of Tokyo
15	Space and Earth System Modeling	Kanya Kusano	Laboratory for Earth Systems Science, JAMSTEC
16	Numerical Experiments with Multi-models for Paleo-environmental Problems	Ayako Abe	Atmosphere and Ocean Research Institute, The University of Tokyo
17	Model-observation Integration Study of the Middle-atmosphere Dynamics using a High-resolution Climate Model and the Antarctic PANSY Radar	Shingo Watanabe	RIGC, JAMSTEC
18	Predictability Variation in Numerical Weather Prediction	Takeshi Enomoto	Disaster Prevention Research Institute, Kyoto University
19	Computational Science of Turbulence in Atmospheric Boundary Layers	Takashi Ishihara	Graduate School of Engineering, Nagoya University

	Project Name	Name of Project Representative	Professional Affiliation of Project Representative
20	A Large-Scale Self-Organizing Map for Metagenome Studies for Surveillance of Microbial Community Structures	Toshimichi Ikemura	Nagahama Institute of Bio-Science and Technology
21	Generation Mechanism of the Banded Structures Observed in the Jovian-type Planetary Atmospheres	Shin-ichi Takehiro	Research Institute for Mathematical Sciences, Kyoto University
22	Study on the Real-time Ensemble Seasonal Prediction System and its Application	Swadhin Behera	APL, JAMSTEC
23	Analysis of Global Ecosystem Ecology by Fragment Molecular Orbital(FMO) Method	Tadashi Maruyama	BioGeos, JAMSTEC
24	Mercury Magnetosphere Simulator Using Global 3D EM PIC Code for Bepi Colombo	Cai, DongSheng	Faculty of Engineering, Information and Systems, University of Tsukuba

JAMSTEC: Japan Agency for Marine-Earth Science and Technology
IFREE: Institute for Research on Earth Evolution
ESC: The Earth Simulator
RIGC: Research Institute for Global Change
DrC: Data Research Center for Marine-Earth Sciences
APL: Application Laboratory
BioGeos: Institute of Biogeosciences

Table 2 Collaboration Projects in FY2013

System/Application Optimizations of Hetero Super Computer System in JAMSTEC : RIKEN
Implementation Agreement between ESC/JAMSTEC and DOPS/IFREMER on Simulation Research Using the ES: IFREMER
ESC-NERSC Performance Evaluation for HPC : NERSC
Ultra High Resolution Simulation for the Safety of International Transportation on the Sea : Kobe University
Study on the Evaluation Techniques of Vortex-Induced Vibrations for the Design of Risers : The University of Tokyo, NME, MHI
Collaborative Research on the Sophistication of the Computational Simulation Software toward Constructing the Platform for the Leading Industrial Research and Development : Institute of Industrial Science, The University of Tokyo
Forecasting Thunder Cloud : JAXA
Rapid Change of the Arctic Climate System and its Global Influences : NIPR
Numerical Simulations of Scalar Transfer Across Wind-driven Air-water Interface : Kyoto University

3. System Configuration of the Earth Simulator

The Earth Simulator (ES2) is the upgrade system of the previous Earth Simulator, which has significantly contributed to the development of a simulation culture in the area of earth science and related technical fields, and introduces new features to bring accurate and high-speed analysis and projections of global-scale environmental phenomena. The current ES is also used to product numerical simulations for advanced research fields that are beyond the scope of other computing systems. By the examination at the time of procurement, the average performance of real application benchmarks exceeded the first system's twice (Table 3).

Table 3 Real Application Benchmarks Performance

Application	ES initial (# of CPUs)	ES current (# of CPUs)	Speed up
PHASE	135.3 sec (4096)	62.2 sec (1024)	2.18
NICAM-K	214.7 sec (2560)	109.3 sec (640)	1.97
MSSG	173.9 sec (4096)	86.5 sec (1024)	2.01
SpecFEM3D	96.3 sec (4056)	45.5 sec (1014)	2.12
Seism3D	48.8 sec (4096)	15.6 sec (1024)	3.13

Harmonic Mean of Speed up Ratio : 2.22

ES2 is in the independent network environment and can be used via the Internet under advanced security protection (Fig. 2). In the Earth Simulator network, there are ES2, Login Servers, User Disks, Terminals and other servers. The current ES2 is a highly parallel vector supercomputer system of the distributed-memory type, and consisted of 160 processor nodes connected by Fat-Tree Network. Each Processor nodes is a system with a shared memory, consisting of 8 vector-type arithmetic processors, a 128-GB main memory system. The peak performance of each Arithmetic processor is 102.4Gflops. The ES as a whole thus consists of 1280 arithmetic processors with 20 TB of main memory and the theoretical performance of 131Tflops. All of the software available on the ES2 system are designed and developed so that users can fully and readily exploit the outstanding performance of the world's largest vector-type computer. ES2 is basically a batch-job system. Network Queuing System II (NQSII) is introduced to manage the batch job. The L batch queue is majored for a production run. The nodes allocated to a L batch queue are used exclusively for that batch job to estimate the job termination time and to make it easy to allocate nodes for the next batch jobs in advance. The batch job is scheduled based on elapsed time instead of CPU time to an efficiency job execution. The job can use the nodes exclusively and the processes in each node can be executed simultaneously. As a result, the large-scale parallel program is able to be executed efficiently.

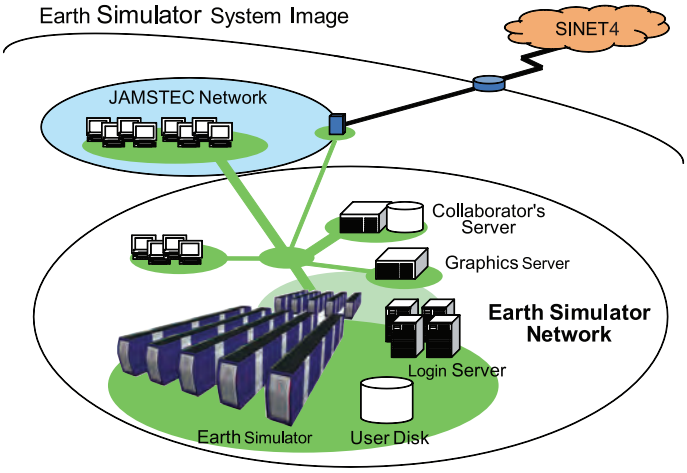

Fig. 2 ES System Outline

Earth Simulator Research Projects

Chapter 1

Earth Science

Understanding Roles of Oceanic Fine Structures in Climate and Its Variability

Project Representative
Hideharu Sasaki — Earth Simulator Center, Japan Agency for Marine-Earth Science and Technology

Authors
Hideharu Sasaki — Earth Simulator Center, Japan Agency for Marine-Earth Science and Technology
Masami Nonaka — Research Institute for Global Change, Japan Agency for Marine-Earth Science and Technology
Akira Kuwano-Yoshida — Earth Simulator Center, Japan Agency for Marine-Earth Science and Technology
Satoru Okajima — Research Center for Advanced Science and Technology, The University of Tokyo
Yoshikazu Sasai — Research Institute for Global Change, Japan Agency for Marine-Earth Science and Technology

We have been investigating roles of oceanic fine structures in climate and its variability by using high-resolution, primitive equation based, atmosphere, ocean and ocean-atmosphere coupled models, and a non-hydrostatic ocean-atmosphere coupled model. In this report, we present the following four topics, for all of which the oceanic fine structures play crucial roles. 1) Uncertainty in the Kuroshio Extension jet interannual variability, 2) Cyclogenesis response to the Kuroshio-Oyashio sea surface temperature (SST) front, 3) Large-scale atmospheric response to SST anomalies in the midlatitude North Pacific, and 4) Oceanic submesoscale variability and its impacts on the physical and biological fields.

Keywords: Oceanic fine structures, Sea surface temperature front, Kuroshio Extension jet, Cyclogenesis, Large-scale atmospheric response, Oceanic submesoscales, Oceanic biological field

1. Introduction

We have been leading researches on roles of oceanic fine scale structures in climate and its variations using atmosphere, ocean, and atmosphere-ocean coupled simulations on the Earth Simulator. Local air-sea interactions associated with oceanic fine structures such as fronts and eddies, which have significant potential impacts to modify local atmospheric and oceanic conditions and thus regional and larger scale climate systems, are observed in the world ocean. Oceanic fronts along the Kuroshio and Gulf Stream affect not only near-surface atmosphere but also entire troposphere, suggesting active roles of the mid-latitude ocean in the weather and climate. Furthermore, contributions of oceanic submesoscales smaller than mesoscale structures to large-scale oceanic field and oceanic ecosystems are implied in resent high-resolution satellite image and oceanic simulations. Oceanic surface wave and its dissipation should be considered to estimate surface momentum flux, which could reproduce realistic air-sea interactions with high surface wave.

We highlight in this report our recent progress in researches on the roles of oceanic fine structures in climate and its variability using simulations. In Section 2, uncertainty in the Kuroshio Extension jet interannual variability is discussed by conducting ensemble simulations of eddy-resolving ocean general circulation model (OGCM) hindcast experiment. In Section 3, a role of the Kuroshio-Oyashio sea surface temperature (SST) front on cyclogenesis is revealed by using atmospheric general circulation model (AGCM). In section 4, large-scale atmospheric response to SST anomalies in the midlatitude North Pacific is assessed by ensemble AGCM sensitivity experiments. Impacts of oceanic submesoscale variability on the physical and biological fields in a high-resolution coupled physical-biological ocean model are reported in Section 5.

2. Uncertainty in the Kuroshio Extension jet interannual variability

The Kuroshio and Kuroshio Extension (KE) transport huge amount of heat into midlatitude, and have significant impact in the climate system in the North Pacific sector. Further, recent studies have suggested that decadal changes in the speed of the Kuroshio and the upstream KE jet can influence natural mortality of infant Japanese sardine. Understanding of variability in the path and intensity of the KE jet is thus of social and scientific importance. It has been suggested that, on the one hand, interannual to decadal variability in the KE jet

is induced by large-scale atmospheric variability. On the other hand, numerical model studies have shown that such KE jet variability can appear as oceanic intrinsic variability under wind field without interannual variability. Then, in the present study, we examined oceanic intrinsic variability under interannually varying atmospheric field.

To investigate intrinsic variability in the North Pacific Ocean, we have conducted eddy-resolving OGCM ensemble hindcast experiment with slightly different conditions and an identical interannually varying atmospheric forcing. One can consider differences in the simulated fields are caused by oceanic intrinsic variability. In our experiment, slight differences in time step and/or in the initial conditions, which corresponds to just 10-day difference in a hindcast integration, induce remarkable differences not only eddy fields but also larger spatiotemporal scale fields. As shown in Fig. 1, interannual variability in the KE jet speed shows substantial difference among the members, indicating it is significantly influenced by the intrinsic variability. Also, so are the SST and salinity fields in their frontal zones in the western North Pacific. In contrast, interannual variability in the tropical Pacific is strongly governed by the external atmospheric forcing, and deterministic.

Although the number of ensemble members is quite limited in our experiment due to limited computational resources, the results indicate that interannual variability in the midlatitude western boundary current (WBC) and its extension region can include significant uncertainty. While it is, of course, impossible to examine uncertainty in the real ocean, our results based on a realistic OGCM imply that there is significant uncertainty in the real KE and we can observe just one realization of its variability. This means that for investigation of such variability with eddy-resolving OGCM hindcast simulations, multi ensemble integration is necessary to take account of the uncertainty. At the same time, it is expected that the uncertainty is model dependent, and multi-model experiment is also necessary as the next step. The strong dependence on the initial condition also suggests that for prediction of the WBC and its extension, initialization of the prediction model by assimilating observed data may not be sufficient, and multi ensemble prediction is necessary.

3. Cyclogenesis response to the Kuroshio-Oyashio SST front

To understand the role of SST fronts associated with the Kuroshio, Oyashio and their extensions, two AGCM experiments are conducted. AGCM for the Earth Simulator (AFES) with T239L48 is used. The control experiment (CNTL) is integrated for 20 years with high-resolution observed SST, while the sensitivity experiment (SMTH) is integrated with smoothed SST fronts (Fig. 2a). The local pressure tendency analysis suggests that in winter, rapid deepening of extratropical cyclones increases over the SST fronts in CNTL run compared

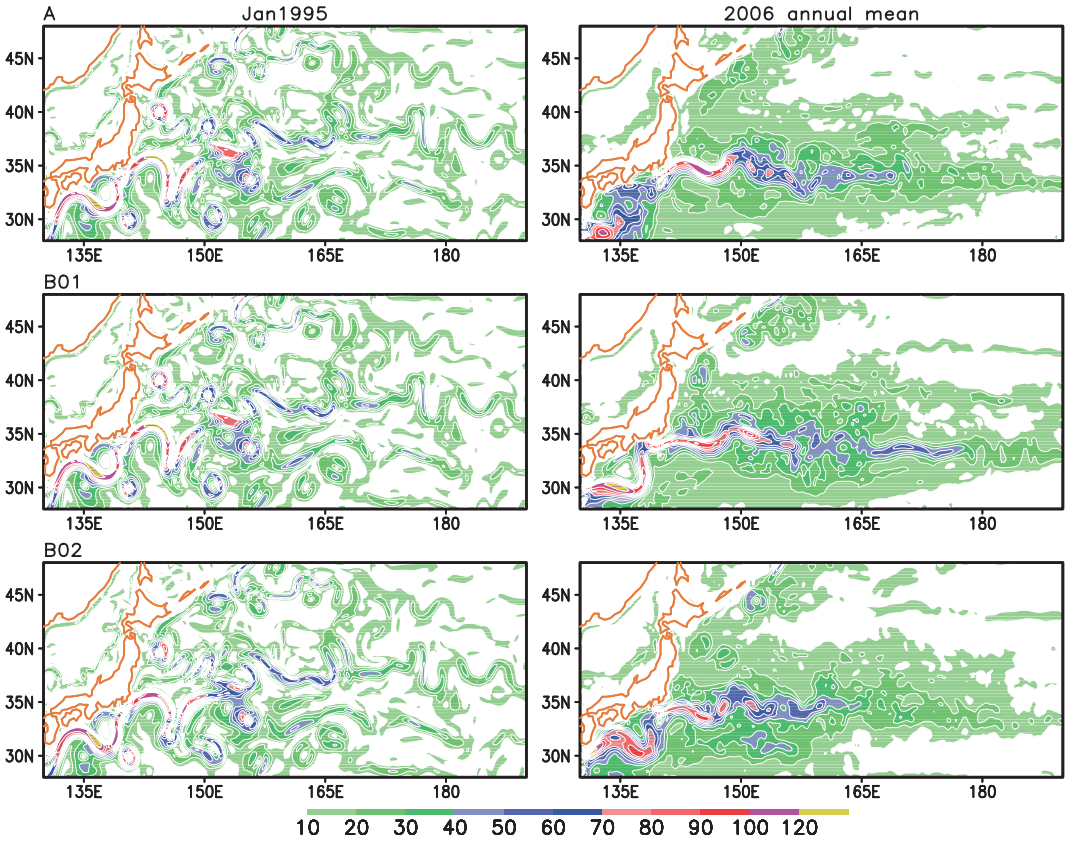

Fig. 1 100-m depth current speed (cm/s) in each member of the three-member ensemble hindcast experiment. (left panels) Monthly mean in January 1995, the first month of the experiment. (right panels) Annual mean in 2006.

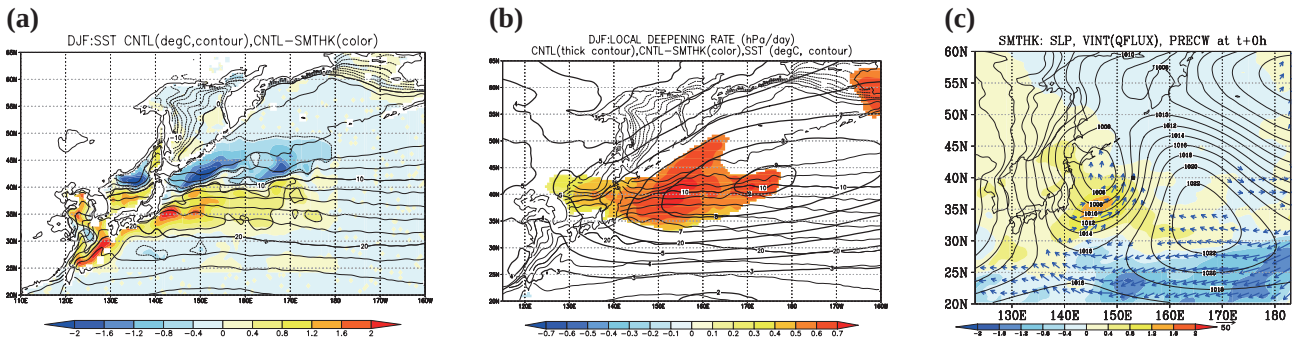

Fig. 2 (a) SST difference between CNTL and SMTH in DJF (°C, color), CNTL SST (°C, contour). (b) Pressure tendency rate difference between CNTL and SMTH with 95% significant level (hPa/day, color). Positive means pressure deepening. Bold contour is positive-only average of pressure tendency rate in CNTL. SST in CNTL (°C, thin contour). (c) Composites of SLP in CNTL (hPa, contour), and differences of vertical integrated moisture amount (mm, color) and vertical integrated moisture flux (mm m/s, vector) between CNTL and SMTH when pressure tendency rate is larger than 1 hPa/h at 153°E, 40°N (closed circle).

with SMTH run (Fig. 2b). The composite analyses for rapid deepening over the SST fronts suggest that moisture provided from Kuroshio along south coast of Japan flows into cyclones, and the enhanced latent heat release associated with precipitation leads to the more rapid deepening of cyclones (Fig. 2c).

4. Large-scale atmospheric response to SST anomalies in the midlatitude North Pacific in October

The influence of extratropical SST anomalies on large-scale extratropical atmospheric circulation has long been believed to be insignificant (e.g. Kushnir et al., 2002 [1]), based partly on results from sensitivity experiments with low-resolution AGCM. In this study (Okajima et al. 2014 [2]), their importance in forcing large-scale atmospheric anomalies is assessed through analysis of ensemble sensitivity experiments using AFES at higher resolution (~1° horizontal resolution and 56 vertical levels), focusing on the prominent warm SST anomalies observed in 2011 summer and autumn along a prominent oceanic frontal zone in the western North Pacific. Each of the experiments comprises 10 ensemble members integrated from June to October. The anticyclonic anomaly observed in October 2011 is well reproduced as a robust response of AGCM forced only with the warm SST anomaly associated with the poleward-shifted oceanic frontal zone in the midlatitude Pacific (Figs. 3a and 3b). The equivalent barotropic anticyclonic anomaly over the North Pacific is maintained under strong transient eddy feedback forcing associated with the poleward-deflected stormtrack (Fig. 4). Energy converted from the climatological-mean circulation also contributes substantially to the maintenance of the anticyclonic anomaly particularly in the model, indicative of its characteristic as a dynamical mode inherent to the co-existence of the extratropical climatological-mean flow and oceanic frontal zone (not shown). As the downstream influence of the anomaly, abnormal warmth and dryness observed over the northern U.S. and southern Canada in October are also reproduced to some extent (not shown). The corresponding AGCM response over the North Pacific to the tropical SST anomalies is in the same sense but substantially weaker and less robust (Fig. 3c), suggesting the primary importance of the prominent midlatitude SST anomaly in forcing the large-scale atmospheric anomalies observed in October 2011. Our results present another piece of evidence that a midlatitude SST anomaly has the potential to actively force large-scale atmospheric anomalies in the extratropics.

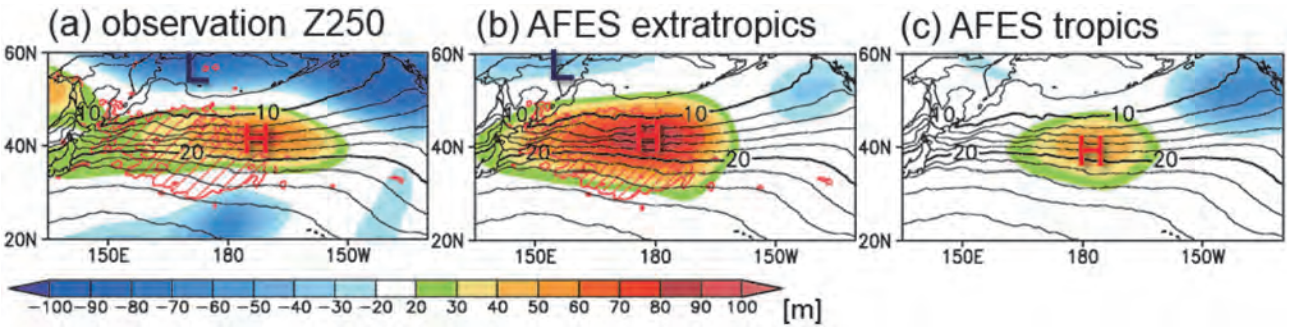

Fig. 3 (a) Map of monthly 250-hPa height anomalies (color) in October 2011 based on the JRA-25 data, superimposed on the climatological-mean SST in October (contour). Red hatches indicate SST anomalies warmer than the climatology by more than +1°C. (b)-(c) Same as in (a), respectively, but for the ensemble response of the sensitivity experiment for the SST anomaly in (b) the midlatitude North Pacific and (c) the Tropics.

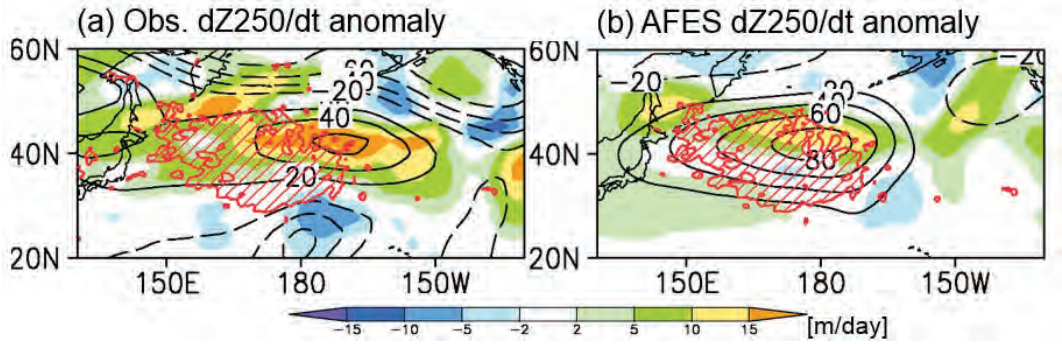

Fig. 4 (a) Anomalous geopotential height tendency at 250-hPa (m/day, color) induced by anomalous heat and vorticity fluxes associated with transient eddies, superimposed on 250-hPa height anomaly (contour, zero line is omitted). (a) is for October 2011 based on the JRA-25 data. Red hatches indicate SST anomalies warmer than the climatology by more than +1°C. (b) Same as in (a), but for the ensemble response of the sensitivity experiment for the SST anomaly in the midlatitude North Pacific.

5. Oceanic submesoscale variability and its impacts on the physical and biological fields

Ocean color satellite imagery reveals the smaller-scale variability (O(1-10km)) in the surface chlorophyll distribution. As a limited high quality ocean color satellite, we try to understand the submesoscale dynamics on the surface phytoplankton field using a high-resolution coupled physical-biological model. The model covers North Pacific (20˚S to 66˚N, 100˚E to 70˚W). The horizontal resolution is 1/30˚ and the vertical levels are 100. We also focus on the seasonality of submesoscale dynamics effects on the surface phytoplankton distribution. In the Kuroshio Extension, eddy activity is the highest and the seasonality of submesoscale dynamics is shown. In the south of the Kuroshio Extension, the model presents

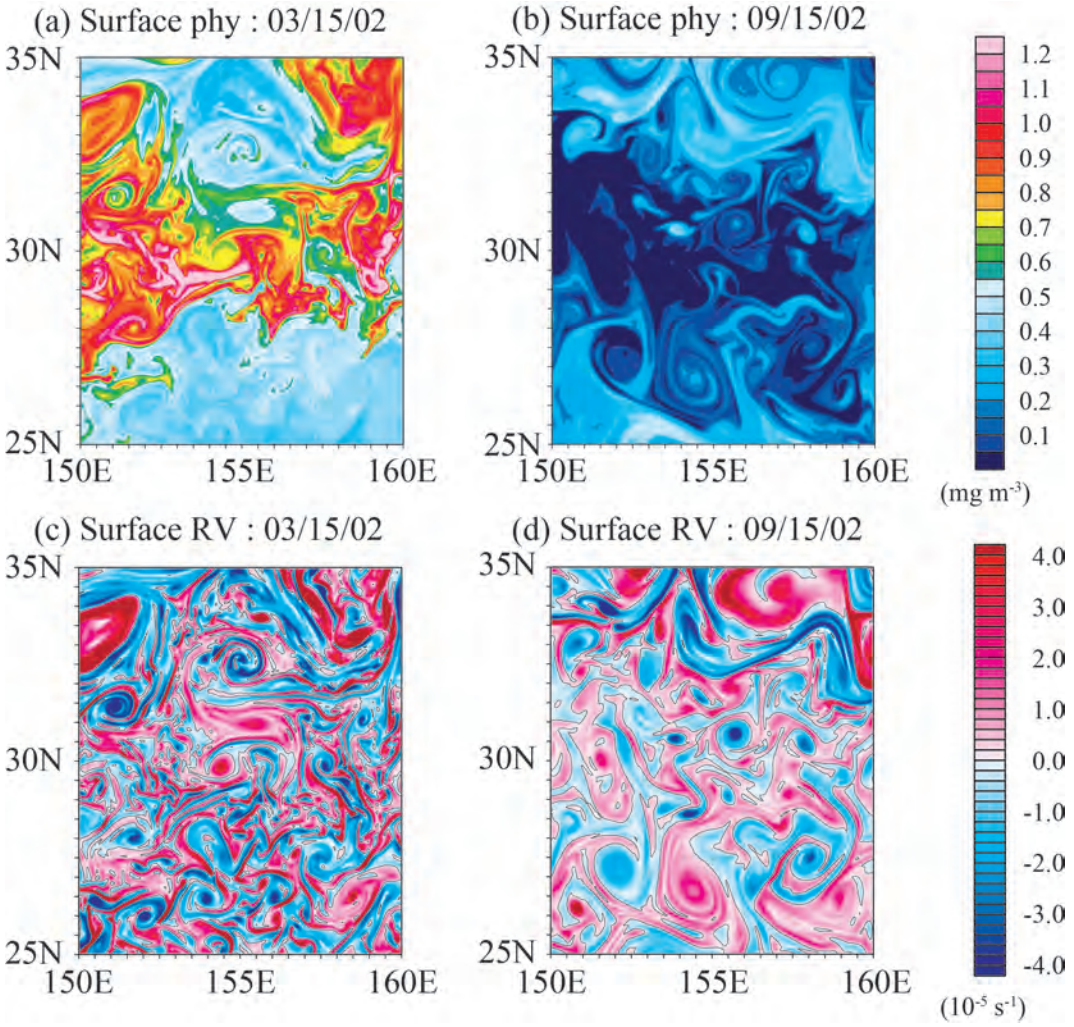

Fig. 5 Surface phytoplankton concentration (mg/m^3) (a-b), and surface relative vorticity (10^{-5} 1/s) (c-d) in the Kuroshio Extension region of 150˚E – 160˚E and 25˚N – 35˚N on March 15, 2002 and on September 15, 2002 in the model.

the similar pattern of submesoscale variability in the surface phytoplankton field in early spring, but in fall, this submesoscale pattern is weak because the mesoscale variability is dominant (Fig. 5). In winter, the energetic submesoscale variability is associated with the smaller scale of vertical velocity, which produces the submesoscale pattern of nitrate field. The submesoscale pattern of phytoplankton field in winter and early spring is formed by the submesoscale vertical injection of nitrate and the light intensity condition. The seasonality of submesoscale dynamics is significant to the phytoplankton production.

6. Conclusion

We have briefly reported research activities to investigate roles of oceanic fine structures in climate and its variability by using high-resolution, primitive equation based, atmosphere, ocean and coupled models. In this fiscal year, uncertainty in the Kuroshio Extension jet interannual variability are discussed, and the cyclogenesis response to the Kuroshio-Oyashio SST front and its mechanism are revealed. Large-scale atmospheric response to SST anomalies in the midlatitude North Pacific is investigated. In addition, large response of oceanic submesoscales on physical and biochemical fields are revealed.

References

[1] Kushnir, Y., W. A. Robinson, I. Bladé, N. M. J. Hall, S. Peng, and R. Sutton, “Atmospheric GCM response to extratropical SST anomalies: Synthesis and evaluation”, Journal of Climate, 15, 2233-2256, 2002.

[2] Okajima S., H. Nakamura, K. Nishii, T. Miyasaka, and A. Kuwano-Yoshida, “Assessing the importance of prominent warm SST anomalies over the midlatitude North Pacific in forcing large-scale atmospheric anomalies during 2011 summer and autumn”, Journal of Climate, 27, 3889-3903, 2014.

海洋の渦・前線とそれらが生み出す大気海洋現象の解明

課題責任者
佐々木英治　　海洋研究開発機構　地球シミュレータセンター
著者
佐々木英治　　海洋研究開発機構　地球シミュレータセンター
野中　正見　　海洋研究開発機構　地球環境変動領域
岡島　　悟　　東京大学　先端科学技術研究センター
吉田　　聡　　海洋研究開発機構　地球シミュレータセンター
笹井　義一　　海洋研究開発機構　地球環境変動領域

海洋の渦・前線などの空間的に小さいスケールの現象が、気候の形成やその変動に及ぼす影響や役割について、大気、海洋、結合モデルを用いて研究を行っている。この報告書では、次の四つの研究成果を取り上げた。渦解像北太平洋海洋モデルを用い 1）黒潮続流ジェットの経年変動の不確実性を調べ、全球大気モデルを用い 2）黒潮・親潮続流の海面水温フロントに対する低気圧発達の応答と、3）中緯度北太平洋域の海面水温偏差に対する大規模大気循環場の応答を示し、それぞれのメカニズムを明らかにした。さらに、高解像度北太平洋海洋生態系モデルを用い 4）海洋のサブメソスケール現象が物理場と生態系に大きな影響を及ぼしていることを示した。

キーワード:海洋の微細構造, 海面水温フロント, 黒潮続流ジェット, 低気圧の発達, 大規模大気応答,
海洋のサブメソスケール現象, 海洋生態系

Adaptation Oriented Simulations for Climate Variability

Project Representative

Keiko Takahashi Earth Simulator Center, Japan Agency for Marine-Earth Science and Technology

Authors

Keiko Takahashi[*1], Ryo Ohnishi[*1], Yuya Baba[*1], Shinichiro Kida[*1], Keigo Matsuda[*1], Li-Feng Lu[*1], Youngjin Choi[*1], Koji Goto[*2] and Hiromitsu Fuchigami[*3]

*1 Earth Simulator Center, Japan Agency for Marine-Earth Science and Technology

*2 NEC Corporation

*3 NEC Informatec Systems LTD

A coupled atmosphere-ocean-land model MSSG has been developed in the Earth Simulator Center, which is designed to model multi-scale interactions among the atmosphere, the ocean and the coupled system. Aiming to seamless simulation to understand mechanisms of radiation micro-physics, impacts of ocean effects to urban environment and heavy rain which are suffer in the future, models and simulations results with the model are introduced in this report.

Keywords: Coupled atmosphere-ocean model, urban cities, heat island phenomena, heavy rain, adaptation

1. Introduction

Multi-Scale Simulator for the Geoenvironment (MSSG), which is a coupled atmosphere-ocean-land global circulation model, has been developed for seamless simulation based on multi-scale multi-physics modeling strategy in order to predict not only weather but climate variability. MSSG is optimized to be run on the Earth Simulator with high computational performance and it is designed to be available with flexibility for different space and time scales [1, 2, 3, 4, 5]. In this report, summarizes a part of results of this project in FY2013 that focus on the following themes to execute seamless simulations with MSSG.

- In order to improve radiation process model for cloud process and urban scale distribution of temperature, three-dimensional direct numerical simulation was introduced and development of the improved three dimensional radiation model was promoted.
- In order to understand the effect of sea surface temperature in Tokyo Bay, investigation of impact to sea surface temperature from the wind distribution and resolution.
- Impact of roughness length to heavy rain representation is studies considering special deviation of buildings in urban area.

2. Improvement in radiation physics

The influence of turbulent clustering and entrainment of cloud droplets on the radar reflectivity factor is investigated. A three-dimensional direct numerical simulation of particle-laden isotropic turbulence is performed to obtain turbulent clustering data (Fig. 1). The clustering data is then used to calculate the power spectra of droplet number density fluctuations, which show a dependence on the Taylor microscale-based Reynolds number Re_λ and the Stokes number St. The Reynolds number dependency of the turbulent clustering influence is investigated for $127<Re_\lambda<531$. The spectra for this wide range of Re_λ values reveal that $Re_\lambda=204$ is sufficiently large to be representative of the whole wavenumber range relevant for radar observations of atmospheric clouds (Fig. 2). We then investigate the Stokes number dependency for $Re_\lambda=204$ and propose an empirical model for the turbulent clustering influence assuming power laws for

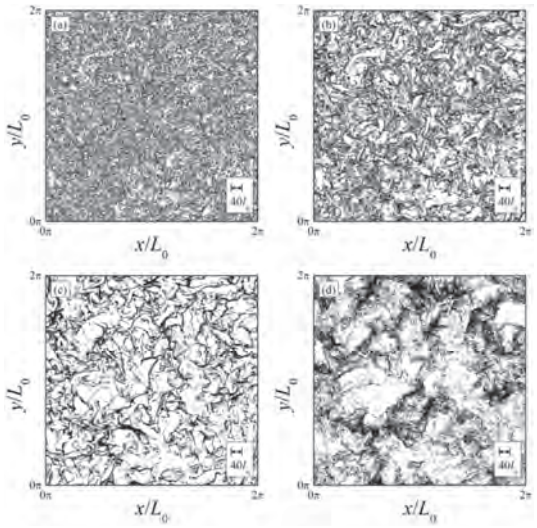

Fig. 1 Spatial distributions of droplets obtained by DNS for (a) St = 0.05, (b) 0.2, (c) 1.0 and (d) 5.0 at Re_λ = 204. Only droplets in the range $0 < z < 4l_\eta$ are drawn.

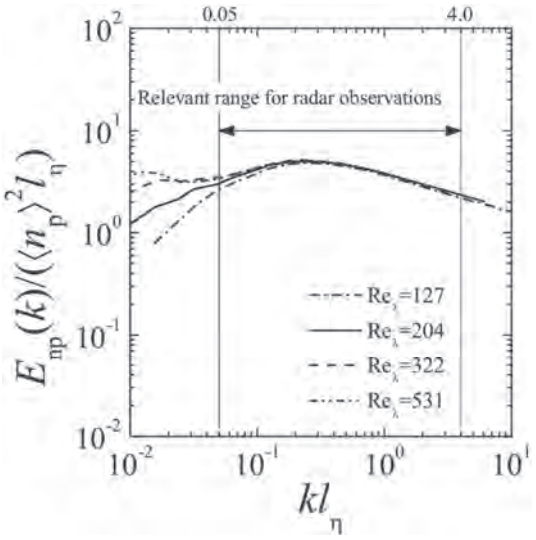

Fig. 2 Power spectra of droplet number density fluctuation obtained from DNS data for St = 1 at Re_λ = 127, 204, 322 and 531.

the number density spectrum. For Stokes numbers less than 2, the proposed model can estimate the influence of turbulence on the spectrum with an RMS error less than 1 dB when calculated over the wavenumber range relevant for radar observations. For larger Stokes number droplets, the model estimate has larger errors, but the influence of turbulence is likely negligible in typical clouds. This showed that the radar reflectivity factor model, which was developed before, is modified based on the DNS data for higher turbulent Reynolds number. As a result, the accuracy of the model is improved so that the model can estimate the radar reflectivity factor within 1 dB error [6].

3. Improvement in radiation physics for urban city planning

Improvement in radiation physics plays an important role to control atmospheric temperature in urban area. A reduction effect of temperature by planting trees in parks and the facilities site is likely to be one of the measures to decrease of heat island effect. However, the mechanism that a green tract of land has an influence on the temperature on surface is still unclear.

In this study, the temperature-reduction mechanism of green spaces is investigated. For the simulations of the heat transfer surrounding trees, the three-dimensional radiation scheme for surface-to-surface radiation is improved to consider the tree crowns as volume elements in ideal experiments (Fig. 3) By using the improved radiation scheme, we can obtain the leaf area temperature distributions inside the tree crowns more accurately. Then the heat transfer simulations for tree canopies are conducted, and analyzed the effect of the transpiration effect, tree volume and leaf area density (Fig. 4).

Furthermore, in order to validate MSSG including this radiation model, we apply the model to represent distribution of temperature and wind in Marunouchi Park Building area. As the results, the distribution of temperature and wind was comparable to observation data and validity of the model was shown (data not shown).

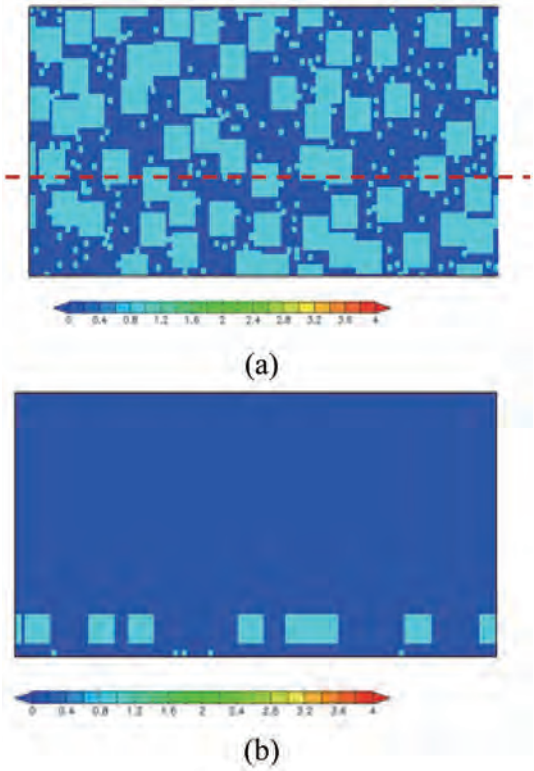

Fig. 3 Distributions of leaf area density on (a) the horizontal cross section at z=1.5m and (b) vertical cross section at y=29.5m.

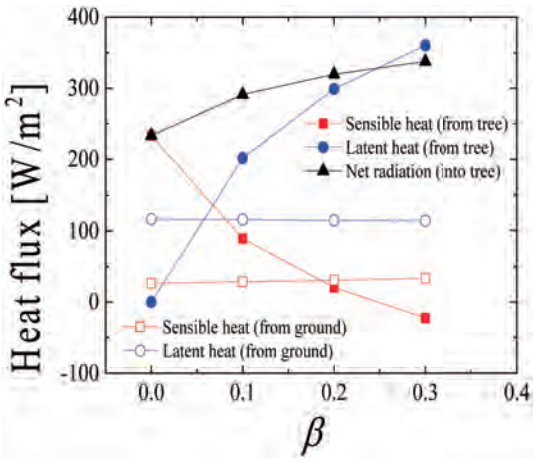

Fig. 4 Effect of the evaporation efficiency on the sensible, latent and radiative heat fluxes on the tree leaves and the ground surface.

4. Toward improvement of adaptation in urban city

4.1 Impacts of downscaling in atmosphere and ocean

Environment of mega cities located near the sea such as Tokyo is influence from condition of costal area. On the contrary, surface atmospheric forcing plays a significant role in controlling the dynamics in Tokyo Bay, in the form of surface fluxes of heat, momentum. Interaction mechanisms between the atmosphere and the ocean in urban area should not be neglected to adapt climate variability and climate change.

Previous observational and numerical studies have shown that the sea surface temperature is highly sensitive to the surface

forcing including surface heating and cooling processes and the variation of the wind. Therefore, highly resolved representation in Tokyo Bay was promoted in this study.

Two sets of simulations have been carried out with low resolution of NCEP and high resolution of MSM data. Even driving by a low-resolution atmospheric forcing, the model can reveal the seasonal variation of SST reasonably. Nevertheless, refinements in resolution of atmospheric forcing are preferable in improving the model performance (Fig. 5) [7,8].

Figure 6 shows the monthly mean sea surface temperature and surface currents for the two experiments. Results show that the variable wind field has a pronounced influence to both circulation and SST in Tokyo Bay. When applying monthly mean wind, two strong anti-clockwise circulations are formed at bay head and middle bay respectively. At the same time, a strong northward coastal current is formed along east coast of the bay. However, when variably wind field is apposed, the anti-clockwise circulations are vanished, and northward coastal currents are formed along both east and west coasts. In both cases, the SST shows a high value at bay head and east coast, and a low value near bay mouth and southwest coast. When a variable wind field is adopted, the sea surface temperature decreased over the whole bay. As the results, wind distribution may significantly affect atmospheric condition in coastal area [7,8].

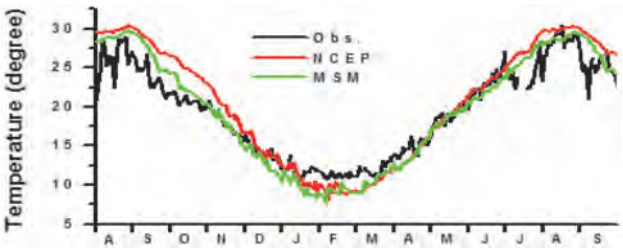

Fig. 5 Comparison of the modeled time serials of SST and the observation (Red line shows the result of the simulation using NCEP data, green line the results using MSM data).

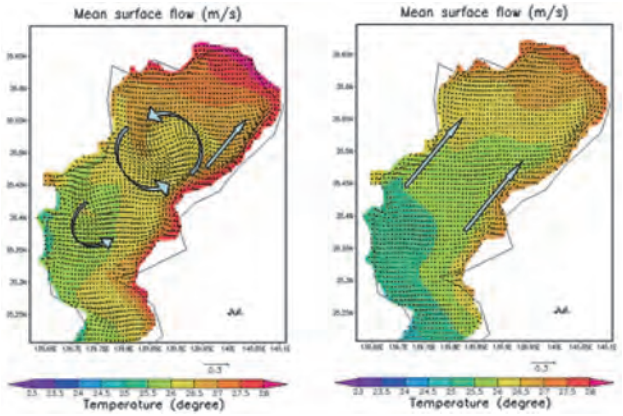

Fig. 6 Modeled SST and surface currents using monthly mean wind (left) and NCEP wind (right).

4.2 Impacts of urban building structure to heavy rain

In urban area, not only heat island phenomena but also heavy rain should be suffered for the adaptation. The mechanism of heavy rain in urban area has been still unclear, however, examinations for its prediction were tried and the result have been piled up. In reasons of of heavy rain in urban area, we focus on the roughness of urban cities. It was pointed out that roughness is becomes be larger not only the mean of building height but special deviation of buildings in urban area. Figure 7 shows special distribution of roughness for in Tokyo area in Japan considering with spatial distribution of buildings in substitution for conventional value which was calculated by land surface usage indexes. Difference of roughness for spatial distribution of buildings is shown in both Shinjuku-area and Otemchi area.

In Figure 8, simulation results of Zoshigaya-heavy rain phenomena which occurred on 5th August 2008. On the day,

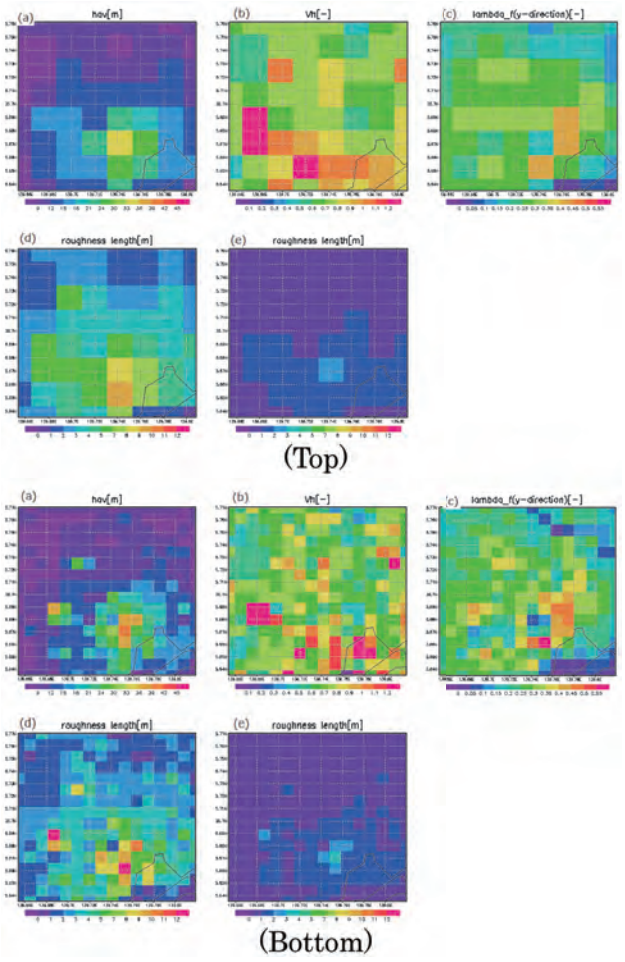

Fig. 7 Spatial distribution of roughness considering with spatial distribution of buildings in central of Totyo area. (Top) is the distribution for 2km horizontal resolution and (Bottom) shows it for 1km horizontal resolution, respectively. (a): mean building height, (b): ratio of standard deviation of the building height and the mean building height, Vh, (c): frontal area aspect ratio, λf, (d): roughness length distribution in consideration of only λf rough degree long z0, in consideration of Vh and λf, (e): z0 in consideration of λf.

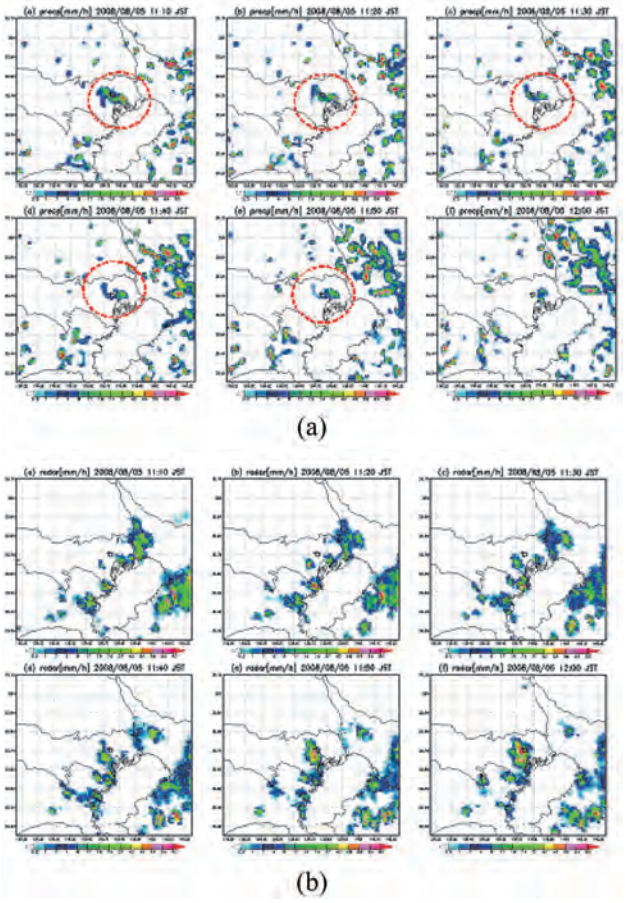

Fig. 8 Spatial distribution of rain every 10 minutes from 11:00 to 12:00 on 8th August 2008. (a) shows simulation result, (b) observation data with Radar reflection strength.

simulation results with 1km horizontal resolution using MSSG shows spatial distribution of rain every 10 minutes from 11:00 to 12:00. Representation of the heavy rain has improved.

5. Future work

Environment in urban area are composed of artificial elements such as buildings or exhaust heat energy and atmospheric or oceanic physical process c elements interact complicatedly. In this report, we introduced minute three dimensional radiation model and several simulation results with the radiation model. The model and validation is necessary for consideration of future adaptation to control increasing atmospheric temperature due to accumulation of heat energy in urban area. Furthermore, it is necessary to consider that cooling effects due to wind and heat transfer from coast. Not only increasing temperature but also heavy rain in urban area is considering to adapt future climate. Previous studies indicate heavy rain may be also effect from artificial elements such as characteristic structure in urban cities. Elemental technology to reproduce severe phenomena and predict future city environment has been prepared. Using those simulation techniques, we will investigate and identify key factors to adapt in the future.

References

[1] K. Takahashi, R. Onishi, Y. Baba, S. Kida, K. Matsuda, K. Goto, and H. Fuchigami, “Challenge toward the prediction of typhoon behavior and down pour”, Journal of Physics: Conference Series, Vol. 454, 012072 (2013).

[2] Keiko Takahashi, et al., “World-highest Resolution Global Atmospheric Model and Its Performance on the Earth Simulator”, Proceeding of SC ’11 State of the Practice Reports, Doi: 10.1145/2063348.2063376, 2011.

[3] Keiko Takahashi, et al., “Non-hydrostatic Atmospheric GCM Development and its computational performance”, http://www.ecmwf.int/newsevents/meetings/workshops/2004/ high_performance_computing-11th/presentations.html, 2004.

[4] Keiko Takahashi, et al., “Non-hydrostatic atmospheric GCM development and its computational performance”, Use of High Performance computing in meteorology, Walter Zwieflhofer and George Mozdzynski Eds., World Scientific, pp. 50-62, 2005.

[5] Yuya Baba and Keiko Takahashi, “Large-eddy simulation of convective boundary layer with density stratification”, Journal of the Meteorological Society of Japan, Vol.89, pp.105-117, 2011.

[6] K. Matsuda, R. Onishi, M. Hirahara, R. Kurose, K. Takahashi, and S. Komori, “Influence of microscale turbulent droplet clustering on radar observations”, Journal of the Atmospheric Science (accepted).

[7] L.-F. Lu, K. Takahashi, “Sensitivity of sea surface temperature in Tokyo Bay to the wind forcing”, Proc. of JOS fall meeting in 2013, Sapporo, Japan, September 17-21, 2013.

[8] L.-F. Lu, K. Takahashi, “A numerical study on the response of SST in Tokyo Bay to variable wind fields”, ECSA 53: Proc. Of Estuaries and coastal areas in times of intense change, Shanghai, China, October 13-17, 2013.

気候変動に適応可能な環境探索のための マルチスケールシミュレーション

課題責任者
高橋　桂子　　海洋研究開発機構　地球シミュレータセンター
著者
高橋　桂子 *1，大西　　領 *1，馬場　雄也 *1，木田新一郎 *1，松田　景吾 *1，Li-Feng Lu*1，
Youngjin Choi*1，後藤　浩二 *2，渕上　弘光 *3
*1 海洋研究開発機構　地球シミュレータセンター
*2 NEC 株式会社
*3 NEC インフォマティックシステム株式会社

A coupled atmosphere-ocean-land model MSSG has been developed in the Earth Simulator Center, which is designed to model multi-scale interactions among the atmosphere, the ocean and the coupled system. Aiming to seamless simulation, cloud micro-physics from the both view points of the accuracy of advection computation and high computational performance and oceanic part downscaling were improved and those results are summarized. In addition, three dimensional radiation scheme was developed and its impact was shown. The trial simulation for investigate regional climate variability was performed and its result was presented in this report.

都市域の気象・気候は、大気や海洋の物理的プロセスや要素だけでなく、構造物や人工排熱などの人為的な要因の影響を受ける。将来の気候変化や変動に対する適応策を考えるには、人が実現できる具体な施策、例えば緑化や水辺の確保などを提案していく必要がある。これまで開発してきた MSSG（大気海洋結合モデルコード）は、マルチスケール現象を再現および予測するためのシームレスシミュレーションが可能である。本年度は、MSSG の放射過程モデルを 3 次元的な精緻なモデルに拡張し、樹木、建物等の放射・輻射伝熱過程をモデル化した。その結果、緑化をする場合には、中低木ではなく高木の植樹のほうが周囲の大気の低温化の効果が高いことが定量的に明らかになった（図 1）。また、都市域の大気環境は、港湾域および湾内の海洋表面温度の影響があることから、東京湾を対象に超高解像度シミュレーションを行い、風の影響について解析した。その結果、風の統計的な扱いおよびシミュレーションの解像度によって、湾内の流れが変化することから、湾内の流れおよび表面温度分布は、風と密接な関係をもって構成されていることがわかった（図 2）。さらに、将来の適応策には、近年発生頻度が高くなってきているといわれる都市の局所的な豪雨の再現性について検討を行った。その結果、都市を特徴付ける建物群は、それらの高さの平均だけでなく高さ分布も大気の状態に影響を与えていることが示唆され、これら都市の構造物が豪雨をもたらす一因になっている可能性があることがわかった（図 3）。今後は、本年度までに構築した MSSG を活用して、都市域における将来の気象および気候の予測を行い、そこに緑化ベルトや水辺の構築などの人によるアクションと施策を導入したシミュレーションを実施して、適応可能性を定量的に評価する予定である。

キーワード：Coupled atmosphere-ocean model, MSSG, multi-scale, multi-physics, high performance computing, the Earth Simulator

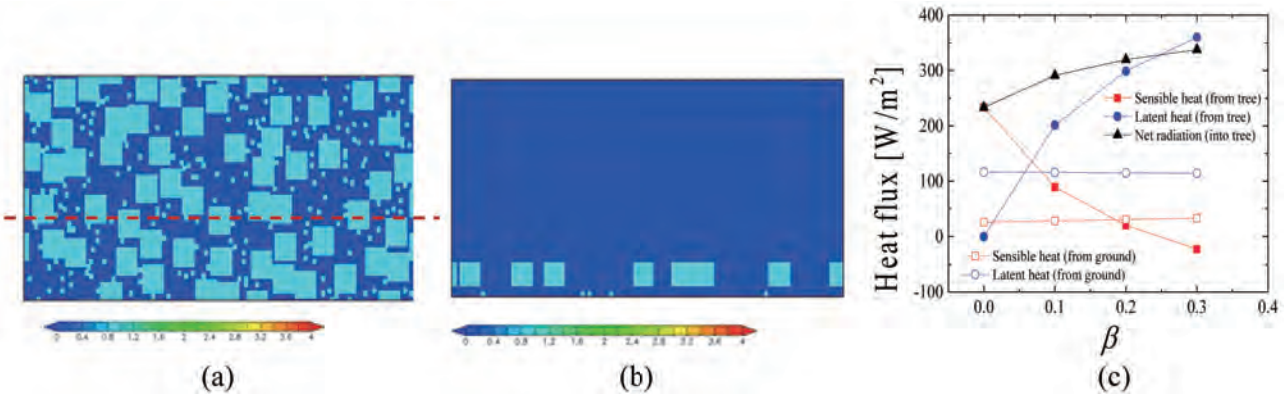

図 1　高木と中低木の 2 種類の樹木とその配置分布を設定した理想実験の概要。(a) 高さ z=1.5m の水平配置、(b) (a) 上の赤点線 y=29.5m の鉛直断面図。(c) 蒸発効率の変化による顕熱、潜熱および放射熱フラックスの変化。

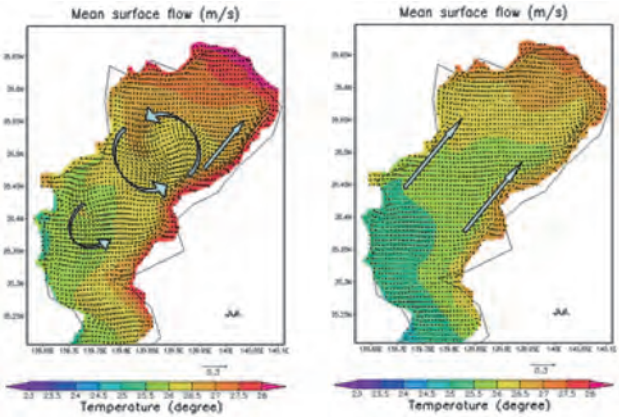

図 2　MSSG-O（MSSG の海洋大循環モデルコンポーネント）により再現された表面温度分布。左図：月平均風速を境界値として与えた場合の海表面温度分布と流れ場、右図：NCEP 風速データを与えた場合の海表面温度分布と流れ場。

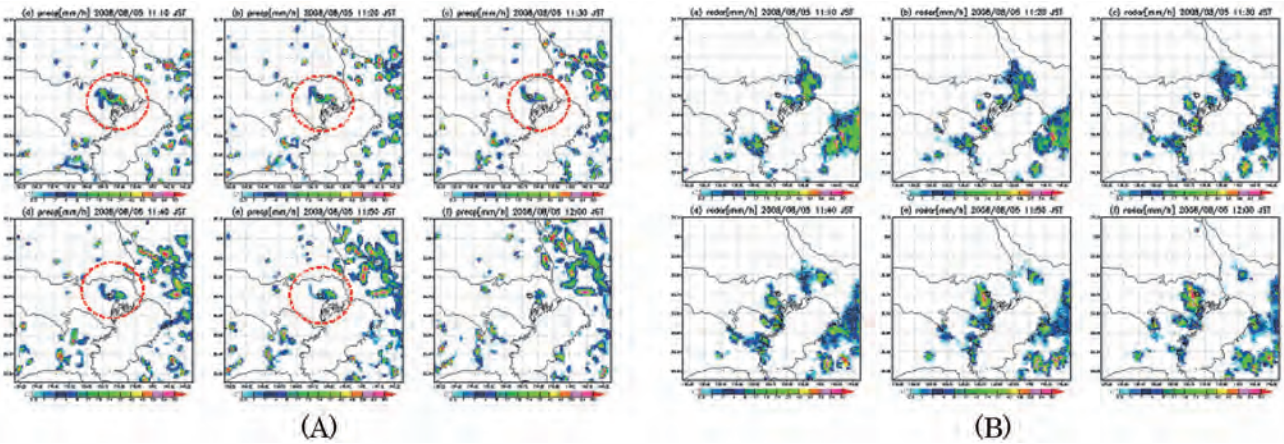

図 3　2008 年 8 月 8 日 11：00 ～ 12：00 降雨の時間変化。(A) 水平解像度 1km で MSSG を使用したシミュレーションによる 10 分ごとの積算降雨量分布。(B) レーダー反射強度から得られた 10 分ごとの降雨分布。

Development of a High-Resolution Coupled Climate Model for Global Warming Projection Study

Project Representative

Akira Noda Research Institute for Global Change, Japan Agency for Marine-Earth Science and Technology

Authors

Akira Noda[*1], Ayako Abe-Ouchi[*2, 1], Megumi O. Chikamoto[*1, 3], Minoru Chikira[*1], Yoshio Kawatani[*1], Rumi Ohgaito[*1], Fuyuki Saito[*1], Kunio Takahashi[*1] and Kumiko Takata[*1, 4]

*1 Research Institute for Global Change, Japan Agency for Marine-Earth Science and Technology

*2 Atmosphere and Ocean Research Institute, The University of Tokyo

*3 International Pacific Research Center, University of Hawaii

*4 National Institute of Polar Research

The purpose of this project is to further develop physical models for global warming simulations, and to investigate mechanisms of changes in global environment as a successor of a previous ES joint project. We have obtained the following results this year.

The weakening amplitude of the quasi-biennial oscillation (QBO) in the lower stratosphere was discovered by long-tern radiosonde observation and several climate model simulations. The results provide strong support for the existence of a long-term trend of enhanced upwelling near the tropical tropopause.

We analyzed the result of the Last Millennium experiment using MIROC-ESM and MIROC. The winter air temperature trend over the circum-arctic region shows unsynchronous variation over the arctic. A grounding-line flux parameterization was introduced to the parallel version of IcIES in order to better simulate transient behavior of grounding line migration and its performance was checked under some ideal configuration.

The advanced sub-grid snow fraction scheme (SSNOWD) was implemented in MIROC5.2. The expected reduction in the low bias of snow fraction was confirmed, but the cold biases in spring were enhanced in some regions. Further adjustment is needed for prolonged snow cover, besides inclusion of the improved soil physical properties.

Madden-Julian Oscillation represented by the Chikira-Sugiyama cumulus scheme was compared with observation and reanalysis. Furthermore, a new method to understand moisture variation associated with MJO was proposed. It was revealed for the first time that a vertical heating profile which maximizes moistening is selected.

Keywords: Atmosphere-Ocean-Land coupled model, offline biogeochemical model, stratospheric QBO, ice-sheet model, MJO

1. Introduction

This project is a successor of one of the previous ES-joint projects named “Development of a High-Resolution Coupled Climate Model for Global Warming Projection Study”. The purpose of this project is to further develop physical models for global warming simulations, and to investigate mechanisms of changes in global environment.

To achieve the purpose, we focus on the development of ice sheet model, permafrost model and sea ice model, improvement of subcomponent models for atmosphere, ocean and land-surface processes in the climate model MIROC, as well as sensitivity studies using climate models relevant to global warming and paleo-climate.

2. The weakening amplitude of the QBO by increased tropical upwelling

In the lowermost stratosphere, the vertical structure of the quasi-biennial oscillation (QBO) is linked to the mean upwelling. We analyzed 60 years of observational data, and discovered that the strength of the equatorial Quasi-Biennial Oscillation (QBO) has been weakening over the past several decades. Figure 1 shows time variation in the amplitude of observed and modelled QBO and in modelled annual mean tropical upwelling at 70 hPa. The QBO amplitudes are found to be dropped by about 30% over 60-years. This trend is also apparent in the global warming simulations of the CMIP5 models that realistically simulate the QBO and consistent our previous studies by MIROC-AGCM [1, 2]. The weakening is most reasonably explained as resulting from a trend of increased

mean tropical upwelling in the lower stratosphere. The discovery of a significant trend in the lower stratosphere QBO amplitude provides strong support for the existence of a long-term trend of enhanced upwelling near the tropical tropopause [3].

3. Improvement and development of an ice-sheet/ ice-shelf model IcIES

We analyzed the result of one of the experiments, the Last Millennium (LM) using MIROC-ESM (Sueyoshi et al. 2013) and MIROC, to verify the response of the cryosphere to the century-scale climate change. As preliminary results, winter warming during 20th century over the Eastern Siberia is clear. Signatures are shown in rise of temperature in February, decrease in snow amount, and increase in runoff during spring. We have also analyzed the winter air temperature trend over the circum-Arctic region, which shows unsynchronous variation over the Arctic. Variability is large in North Europe and Alaska, small in Siberia and Greenland. It also shows an anti-phase response to the volcanic forcing between Alaska and North Europe.

Simulating position of grounding-line is a key issue for ice-sheet modeling especially for Antarctic ice sheet. Following Schoof (2007 [4]), we introduced a grounding-line flux parameterization into the parallel version of IcIES. We performed a series of experiment presented in Marine ice-sheet model intercomparison project (MISMIP, Pattyn et al 2012 [5]) using the new version of IcIES and check the efficiency of the parameterization method (Fig. 2). Under this configuration (linear down-slope bedrock toward the ocean), the grounding line positions are expected be reversible along the changes

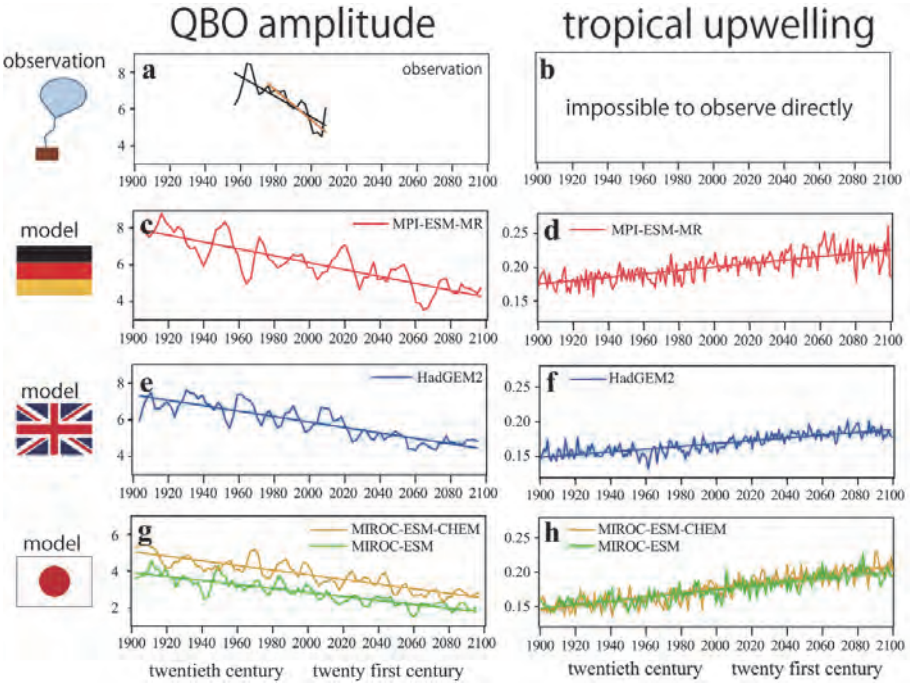

Fig. 1 Changes at altitude of about 19 km in (left) QBO and (right) equatorial upwelling. (a,b) are monitoring data; (c,d), (e,f), and (g,h) are German, British, and Japanese modeling results, respectively. The larger the value of the vertical axis, the larger the speed of westerly and easterly winds that accompany QBO (left) as well as the upwelling (right). From the 20th to 21st century, the QBO has weakened and the equatorial upwelling strengthened.

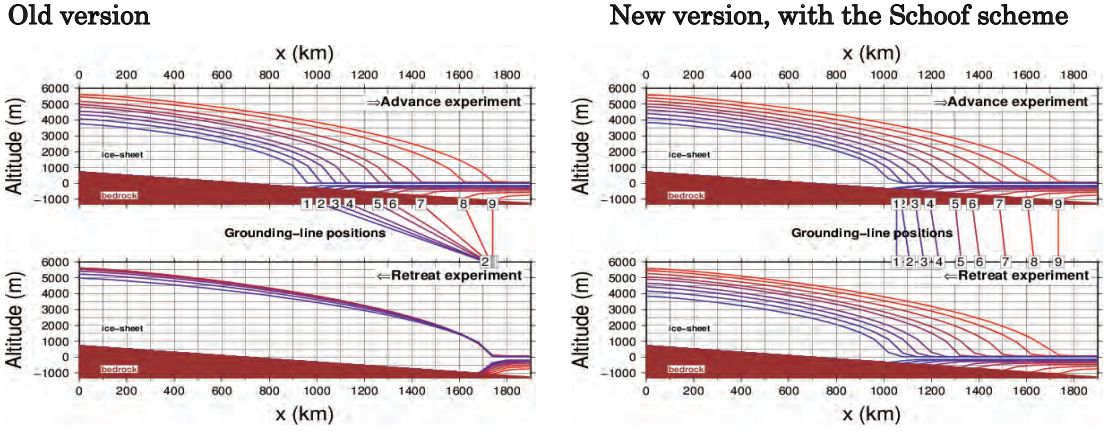

Fig. 2 An idealized ice-sheet/shelf/grounding line simulation following MISMIP (Pattyn et al. 2012). Left panels are results using the old model (before implementation of the Schoof parameterization scheme) and right are those using the new model. There are nine configuration for ice rate-factor (inverse of viscosity), from 1 to 9 which are expected to have reversible grounding positions when advance case (1 to 9) and retreat case (9 to 1). Grouding line retreat cannot be simulated using the old version.

in the environment. Upper panels are simulated ice-sheet topography along some environment change (number from 1 to 9) and the boxes are corresponding grounding line positions. Lower panels are simulated ice-sheet topography starting from the environment 9 to 1 and their grounding positions. Without the grounding line parameterization, the reversibility cannot be achieved, while it is successfully simulated with the parameterization. Although we implement this method using MPI parallel method, we only examine on serial case. Parallel efficiency of the new implementation is being examined.

4. Evaluation and improvement of the land-surface scheme

The advanced sub-grid snow fraction scheme (SSNOWD), which has been validated in MIROC5, was implemented in MIROC5.2. The expected improvement in snow fraction was confirmed, which has been underestimated in early winter in the regions with small snow amount. That led to reduction in the warm biases in mid-latitudes in early winter, but led to enhancement in the cold biases in some regions in spring. That could be related to the prolonged snow cover, which should be adjusted in the next step. The improved schemes for the soil thermal property including the organic layer have been tested in MIROC3.2, and are in preparation to be implemented in MIROC5.2. The dependence of soil surface albedo to soil moisture was coded, and realistic parameters were examined.

5. Understanding moisture variation in MJO represented by MIROC5 with the use of the Chikira cumulus scheme

Madden-Julian Oscillation (MJO) is a major variation of the atmospheric system in the tropics. However, the understanding of its mechanism has been remaining to be a challenging issue for decades. This fiscal year, a thorough analysis of the MJO represented by MIROC5 with the use of the Chikira-Sugiyama cumulus scheme was made digging into the mechanism of MJO (Chikira 2014 [6]) as well as a detailed comparison with observations and a reanalysis dataset (Chikira and Sugiyama 2013 [7]).

In particular, the work of this fiscal year includes a

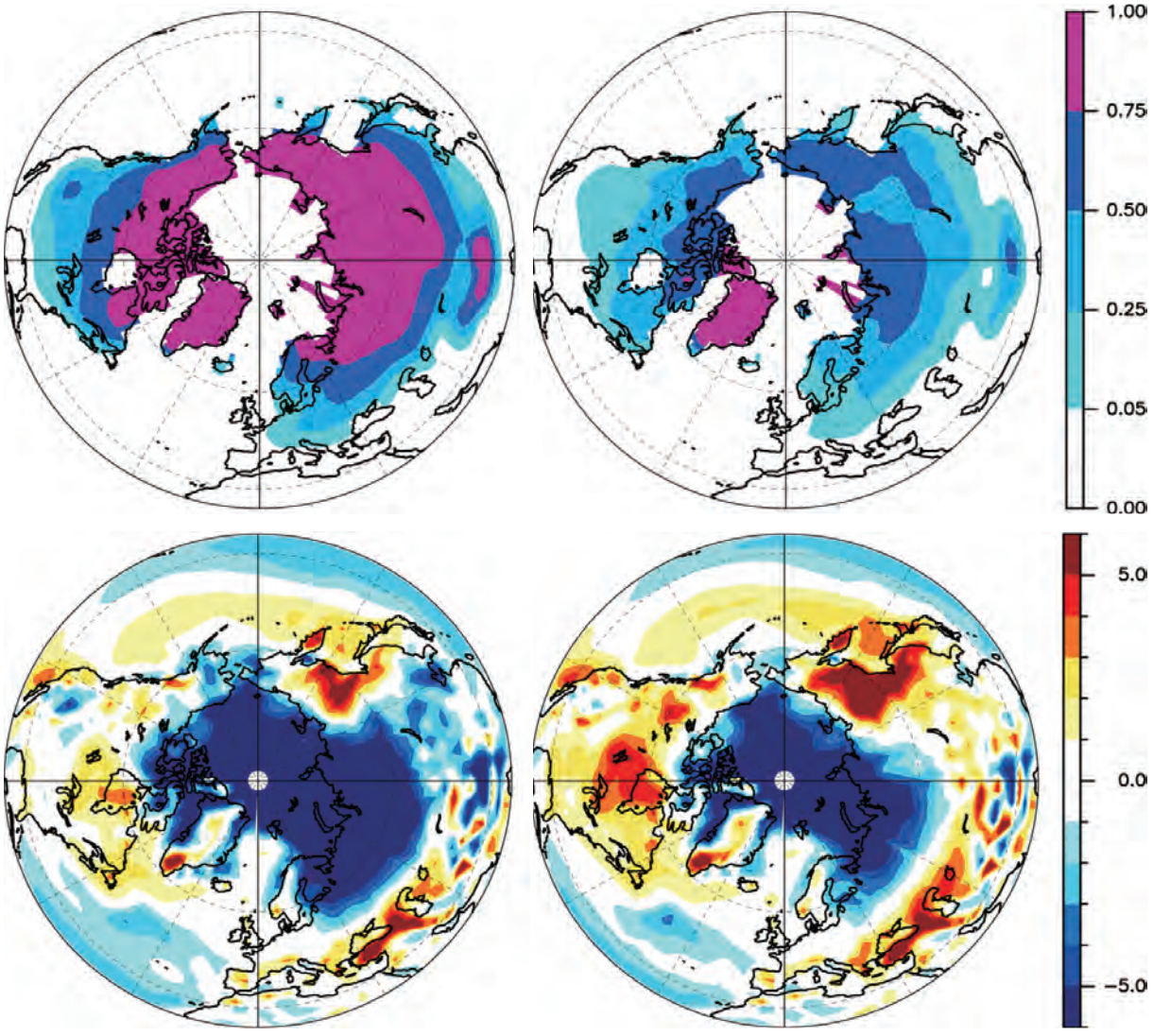

Fig. 3 Snow cover (upper) and surface air temperature (lower) in Oct.-Dec. with (left) and without (right) SSNOWD by MIROC5.2.

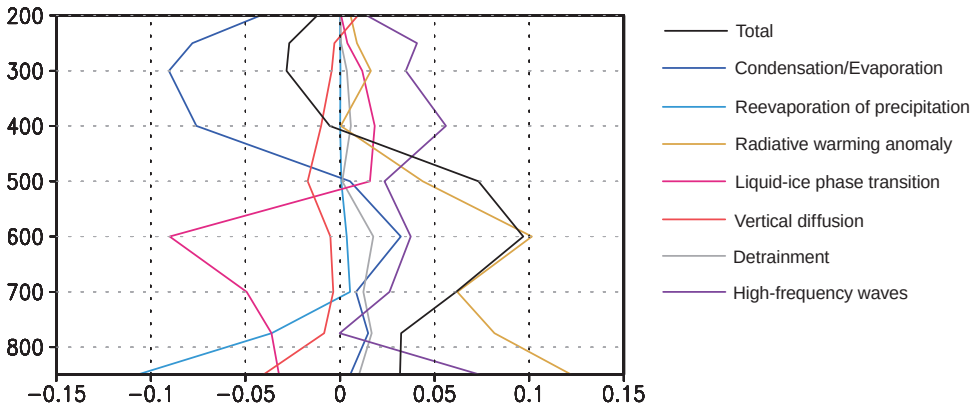

Fig. 4 Contribution of each factor to the amplification of the moisture over the convective area of the model MJO. Ordinate is pressure (hPa). Unit of abscissa is g $kg^{-1}day^{-1}$.

quantitative evaluation of physical factors which contribute to amplification of moisture (Fig. 4). The analysis showed that a primary factor for the amplification in the middle and lower troposphere is radiative warming anomaly. Besides, it was pointed out for the first time that the snow melting and the reevaporation of the precipitation suppress the moistening, and a cumulus heating profile which maximizes the moistening is selected

References

[1] Kawatani, Y., K. Hamilton, and S. Watanabe, “The Quasi-biennial oscillation in a double CO_2 climate”, J. Atmos. Sci., 68, 265-283, 2011.

[2] Kawatani, Y., K. Hamilton, and A. Noda, “The effects of changes in sea surface temperature and CO2 concentration on the quasi-biennial oscillation”, J. Atmos. Sci., 69, 1734-1749, 2012.

[3] Kawatani, Y. and K. Hamilton, “Weakened stratospheric Quasibiennial Oscillation driven by increased tropical mean upwelling”, Nature, 497, 478-481, doi:10.1038/nature12140, 2013.

[4] Schoof, C., Ice sheet grounding line dynamics: Steady states, stability, and hysteresis. J. Geophys. Res., 112, F03S28, 2007.

[5] Pattyn, F. et al., “Results of the Marine Ice Sheet Model Intercomparison Project, MISMIP”, The Cryosphere 6, 573-588, 2012.

[6] Chikira, M., “Eastward-propagating intraseasonal oscillation represented by Chikira-Sugiyama cumulus parameterization. Part II: Understanding moisture variation under weak temperature gradient balance”, J. Atmos. Sci., 71, 615-639, doi:10.1175/JAS-D-13-038.1, 2014

[7] Chikira, M. and M. Sugiyama, “Eastward-propagating intraseasonal oscillation represented by Chikira-Sugiayama cumulus parameterization. Part I: Comparison with observation and reanalysis”, J. Atmos. Sci., 70, 3920-3939, doi:10.1175/JAS-D-13-034.1, 2013.

地球温暖化予測研究のための高精度気候モデルの開発研究

課題責任者
野田　彰　海洋研究開発機構　地球環境変動領域
著者
野田　彰 *1，阿部　彩子 *2, 1，大垣内るみ *1，河谷　芳雄 *1，齋藤　冬樹 *1，高田久美子 *1, 3，
高橋　邦生 *1，近本めぐみ *1, 4，千喜良　稔 *1
*1 海洋研究開発機構　地球環境変動領域
*2 東京大学　大気海洋研究所
*3 国立極地研究所
*4 ハワイ大学　国際太平洋研究センター

本研究は、数年から数千年に及ぶ気候変動を再現できる大気・海洋・陸面結合大循環モデルを改良するとともに、氷床モデル等の開発を行い、最先端の気候システム研究を実施する。より具体的には（1）氷床モデル・凍土モデル・海氷モデルの開発、(2）大気、海洋、陸面の物理過程の評価と改良、(3）地球温暖化予測ならびに古気候再現に関わる気候モデルの感度実験、を行う。

本年度は以下の成果を得た。

重力波抵抗パラメタリゼーションのない気候モデルを用いて、温暖化時の赤道準 2 年振動（QBO）を再現させた成果を参考に、本年度は観測データと気候モデルを組み合わせた考察を行った。地球温暖化時に成層圏子午面循環が強まる事と下部成層圏の QBO 振幅が弱まる事の関連性を明らかにし、現実大気でも子午面循環が強まっている事を立証した。

MIROC-ESM を用いた過去 1000 年実験の解析を行い、100 年スケールの気候変動に対する寒冷圏の変化を調査した。その結果、北極圏における冬の気温応答は、場所により異なることが分かった。昨年度に引き続き、氷床モデルの改良と並列化を進めた。今年度は、棚氷と氷床の境界（grounding line）の parameterization を導入した。実装した過程を理想的な条件下で試験運用し、grounding line 位置の時間発展がよく再現されることを確認した。

陸面モデルの積雪過程については，これまで MIROC5 で検証・感度実験を進めてきたサブグリッド積雪被覆率スキームを MIROC5.2 に実装し、冬季前半に降雪量が小さい地域での積雪被覆率の過小評価が軽減することを確認し、秋から冬の中緯度での高温バイアスは改善したが、低温バイアスが増大する地域や季節もあった。今後、土壌の熱物性値やアルベドの改良、有機層の導入と合わせてパラメタ調整を進める。

MJO に関しては、Chikira-Sugiyama 積雲対流スキームによって表現された MJO を観測・再解析データと詳しく比較するとともに、MJO に伴う自由大気の水蒸気変動の鉛直構造を精確に理解することを可能にする新しい方法を提案した。大気の湿潤化を最大化する鉛直加熱モードが選択されていること等が初めて示された。

キーワード:大気海洋陸面結合モデル, オフライン地球生態化学モデル, 成層圏準二年振動 (QBO), 氷床モデル, MJO

Simulations of Atmospheric General Circulations of Earth-like Planets by AFES

Project Representative
Yoshi-Yuki Hayashi — Department of Earth and Planetary Sciences, Kobe University

Authors
Yoshi-Yuki Hayashi — Department of Earth and Planetary Sciences, Kobe University
Yoshiyuki O. Takahashi — Department of Earth and Planetary Sciences, Kobe University
Norihiko Sugimoto — Research and Education Center for Natural Sciences, Keio University
Masahiro Takagi — Faculty of Science, Kyoto Sangyo University
Hiroki Kashimura — Institute of Space and Astronautical Science, Japan Aerospace Exploration Agency
Masaki Ishiwatari — Department of Cosmosciences, Hokkaido University
Masatsugu Odaka — Department of Cosmosciences, Hokkaido University
Kensuke Nakajima — Department of Earth and Planetary Sciences, Kyushu University
George L. Hashimoto — Department of Earth Sciences, Okayama University
Yoshihisa Matsuda — Faculty of Education, Tokyo Gakugei University

High resolution simulations of the Venus and Mars atmospheres have been performed by using a General Circulation Model (GCM) based on AFES (Atmospheric GCM for the Earth Simulator). Our aim is to have insights into the dynamical features of small and medium scale disturbances in the Earth-like atmospheres and their roles in the general circulations. As for the simulation of the Venus atmosphere, a superrotation is reasonably reproduced with a realistic solar heating. Spectral analyses of the horizontal kinetic energy are performed for the high-resolution case (T159L120). The results suggest that small-scale gravity waves might be more important in Venus than in Earth. In addition, the structure of a polar vortex in a simulation is investigated to compare with observations. The "S-shaped" horizontal structure and vertical profile of the polar vortex is successfully reproduced. Based on the previous linear stability analyses, the dependence of the appearance of baroclinic instability on the meridional profile of zonal flow and the vertical profile of static stability is investigated. The results suggest that the realistic vertical distribution of static stability and a sufficiently high horizontal resolution are crucial for the occurrence of baroclinic instability. The results also indicate that baroclinic instability contributes significantly to the general circulation of the Venus atmosphere when the zonal mean flow, as is often observed, is characterized by the appearance of the mid-latitude jets. As for the simulation of the Martian atmosphere, the nature of dust lifting in the model is investigated by performing multiple runs with several horizontal resolutions from T79 to T639. The model demonstrates a variety of disturbances whose horizontal scales range from synoptic scales to tens of kilometers. The analyses of dust lifting events in terms of probability distribution function indicate that dust lifting amount, in general, increases with the increase of the resolution owing to the better representation of small scale disturbances in the higher resolution model. However, especially in the mid- and high-latitudes, dust lifting amount in the lower resolution model is sometimes larger than that in the higher resolution model. This inverse dependence of dust lifting amount would be a reflection of the large variability of synoptic eddies in those latitudes compared to the small scale disturbances in the lower latitudes.

Keywords: planetary atmospheres, superrotation, dust storm, Earth, Mars, Venus

1. Introduction

The structure of the general circulation differs significantly in each of the planetary atmospheres. For instance, the atmospheres of the slowly rotating Venus and Titan exemplify the states of superrotation where the equatorial atmospheres rotate faster than the solid planets beneath, while the equatorial easterly and the strong mid-latitude westerly jets form in the Earth's troposphere. The global dust storm occurs in some years on Mars, but a similar storm does not exist in the Earth's atmosphere. Understanding physical mechanisms causing such a variety of features in the general circulations of the planetary atmospheres is one of the most interesting and important open questions of the atmospheric science and fluid dynamics.

The aim of this study is to understand dynamical processes that characterize the structure of each planetary atmosphere by performing simulations of those planetary atmospheres by

using GCMs with a common dynamical core of AFES [1]. Appropriate physical processes are adopted for each planetary atmosphere. In the followings, the particular targets of each simulation, the physical processes utilized, and the results obtained will be described briefly.

2. Venus simulation

2.1 Targets of simulations

Low-resolution general circulation models have been used to simulate the superrotation of the Venus atmosphere in precedent studies, such as Yamamoto and Takahashi [2]. This is mainly due to the extremely long spin-up time needed to generate a superrotation from a motionless initial state. Furthermore, most of previous GCM studies included unrealistically intense solar heating and large static stability to generate a superrotation. In the present study, we construct a new model based on AFES for realistic high-resolution simulations of the Venus atmosphere.

Kinetic energy spectra have been utilized to explore properties of disturbances of a wide range of scales both in observational and numerical studies of the Earth atmosphere [3, 4]. As for the Venus atmosphere, it is suggested from observational studies such as Leroy and Ingersoll [5] that small-scale gravity waves play important roles at the cloud levels. However, kinetic energy spectra of the Venus atmosphere have not been well described yet. At the polar region of the Venus atmosphere, a strong polar vortex having “S-shaped” structure has been frequently observed by VIRTIS onboard Venus Express [6]. However, there has been no numerical simulation which reproduces such a polar vortex with a good agreement with observational studies so far. Our Venusian AFES with realistic solar heating and static stability profiles has successfully reproduced a reasonable superrotation. In this fiscal year, we perform simulations with very high resolutions to investigate properties of disturbances in a wide range of scales in the Venus atmosphere. The “S-shaped” structure of the Venus polar vortex is one of the targets which a high resolution model may represent. We conducted several sensitivity tests on baroclinic instability by AFES in the last year [7]. In this fiscal year, we investigate, consulting the previous linear stability analyses [8, 9], dependence of baroclinic instability on the choice of the basic state, i.e. the meridional profile of zonal flow and the vertical profile of static stability.

2.2 Model and experimental settings

Venus simulations are performed with simplified physical processes adopting the values of physical constants appropriate for Venus. The experimental settings basically follow those of the previous linear stability analysis [9] and the AFES simulations conducted last year [7]. The highest resolution used in the present simulations is T159L120, which is equivalent to about 79 km horizontal grid size. The vertical domain extends from the ground to about 120 km with almost the constant grid spacing of 1 km. Simulations with T63L120 and T42L60 resolutions, which are equivalent to about 198 km horizontal grid size and 120 vertical layers and about 297 km horizontal grid size with 60 vertical layers, respectively, are also performed.

The physical processes adopted in the model are vertical eddy diffusion with a constant diffusion coefficient of 0.15 m^2/s, a dry convective adjustment, the Newtonian cooling, and the Rayleigh friction at the lowest level representing the surface friction. In the upper region above about 80 km, a sponge layer is assumed; the friction increasing gradually with altitude acts to damp the eddy component only. In addition, the model includes a 4th-order horizontal diffusion (∇^4) with an e-folding time for the maximum wavenumber of about 0.01 days for T159, 0.03 days for T63, and 0.1 days for T42 simulations. The coefficients of the Newtonian cooling are based on the previous study [10]. The equilibrium temperature distribution toward which temperature is relaxed by the Newtonian cooling is the initial field described below. We adopt a realistic profile of solar heating. The vertical profile of solar heating is based on the previous works [10, 11]. Several solar heating distributions are used for simulations: a zonally averaged solar heating distribution, a diurnally varying solar heating distribution, and no solar heating.

For almost all simulations described below, the vertical temperature profiles of the initial conditions are constructed based on the observed vertical distribution of static stability [12]. In this temperature profile, the lower atmosphere near the ground is weakly stable. Below the cloud layer, static stability has a maximum at around 45 km. A layer with almost neutral stability exists from 55 to 60 km representing the cloud layer influenced by solar heating. Above the cloud layer (above 70 km), it is strongly stratified. Meridional temperature gradient from equator to pole is about 5 K on the model level, i.e., constant sigma surface, at the top of cloud layer. The initial condition for wind velocity is zonally symmetric, solid-body superrotating flow, which is determined by the gradient wind balance; zonal velocity at the equator linearly increases from zero at the ground up to 100 m/s at the altitude of 70 km, and above there the atmosphere is in a solid-body rotation with the same speed as that at 70 km. From this initial condition, time integration is performed for four Earth years.

In addition, for the investigation of dependence of baroclinic wave intensity on the basic state, we prepare a relatively realistic profile of zonally uniform zonal flow with mid-latitude jets near the cloud levels.

2.3 Results

In the results of the numerical simulation in which solar heating is excluded for simplicity, the zonal wind velocity decreases a little from the initial condition in the cloud layer (50-70 km) due to unstable modes of growing vortices. The preliminary results without solar heating are summarized in

Sugimoto et al. [7].

Fig. 1 shows snapshots of vorticity deviation from its zonal mean (left) and temperature (right) at 54 km altitude at 1422 days from the initial condition of the T159L120 simulation with the diurnally varying solar heating. A vortical structure appears at the mid-latitudes where meridional temperature gradient is large. Small filament structures of vorticity appear around the large-scale vortices. In addition, small-scale vortical disturbances are produced by the intense thermal forcing around the equatorial region. The temperature gradient produced by the thermal forcing enhances meridonal circulation and then the strong mid-latitude jets appear. On the other hand, strong meridional gradients of velocity and temperature generate baroclinic and barotropic unstable waves continuously. These instabilities would be the source of small-scale disturbances.

We calculate the horizontal kinetic energy spectrum [13] for the result of T159L120 simulation with the diurnally varying solar heating. Fig. 2a shows the horizontal kinetic energy spectra at eight sigma levels averaged over the last one year of the integration. The energy spectra obey −5/3 power law in the range of $10 < n < 40$, where n is the total wavenumber. Further, the horizontal kinetic energy is decomposed into a rotational component showing the contribution of balanced motion (e.g., Rossby waves) and a divergent component showing that of unbalanced motion (e.g., gravity waves); both components are displayed in Figs. 2b and c. The spectrum of the rotational component at $\sigma = 0.03$ (~ 40 km) shows −3 power law for $n < 20$; whereas the spectra in the other levels are gentler than −3 power law but steeper than −5/3 one. The divergent component in the upper two levels shows −5/3 power law extending to very small wavenumbers (planetary scales). The ratios of the divergent component to the rotational one for each level are also examined. For $n > 10$, the divergent component is comparable to rotational component or dominant. The dominance of the divergent component even in low wavenumbers might be a unique feature of the Venus atmosphere.

Fig. 3 shows time evolution of vorticity at 62 km altitude in the polar region for the T42L60 simulation with the diurnally varying solar heating. The “S-shaped” structure is successfully reproduced. The dominant wavenumber varies from two to three. We also investigate the vertical structure of phase for the wavenumber one component. The phase is anti-symmetric about

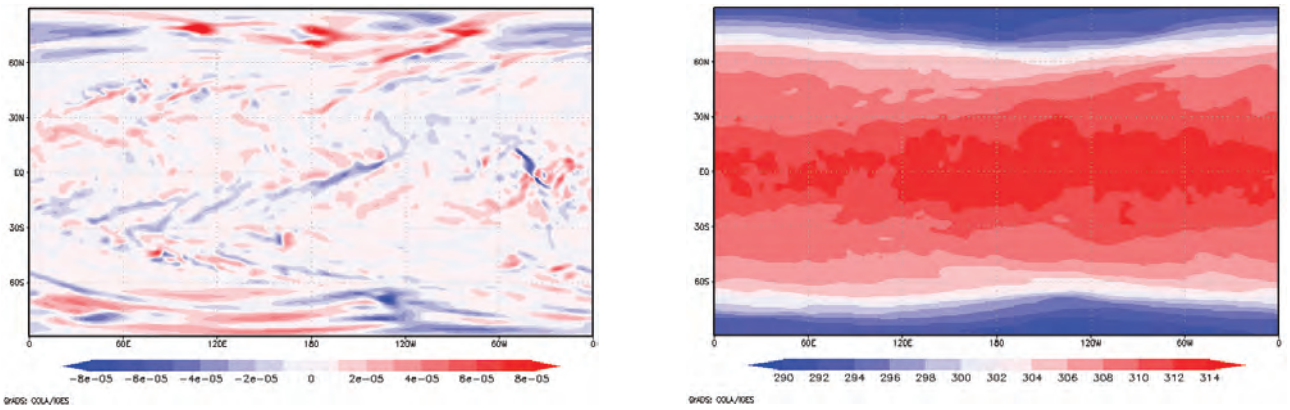

Fig. 1 Snapshots of distributions of vorticity deviation from its zonal mean (left) and temperature (right) at 54 km altitude and at 1422 days from the initial condition of the T159L120 simulation with the diurnally varying solar heating.

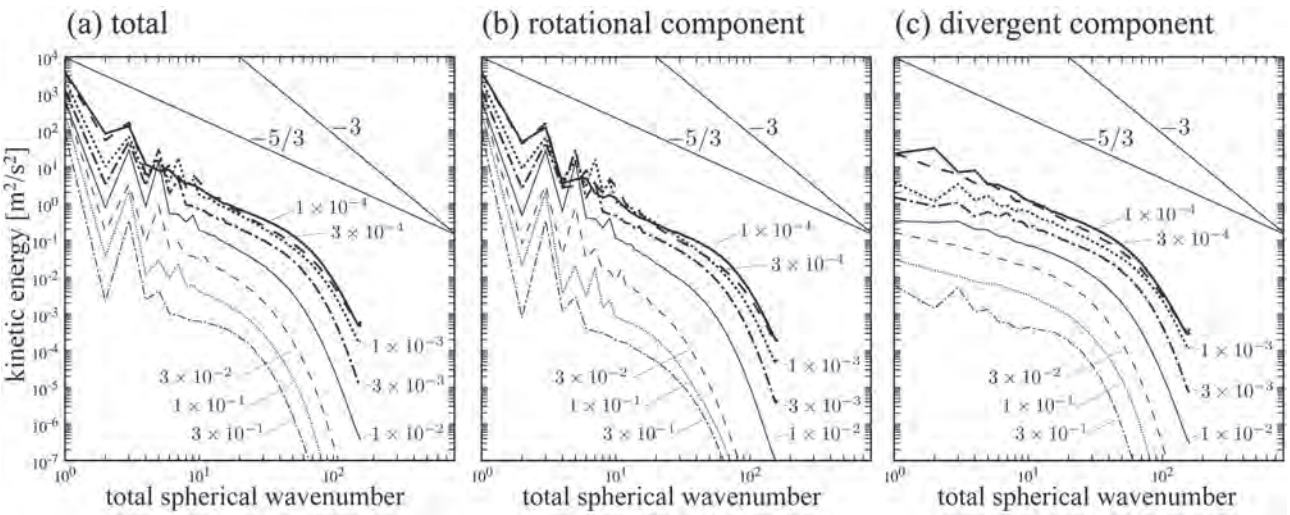

Fig. 2 Horizontal kinetic energy spectra of (a) total, (b) rotational component, and (c) divergent component. Two straight lines in each panel show slopes of −3 power law and −5/3 power law, respectively.

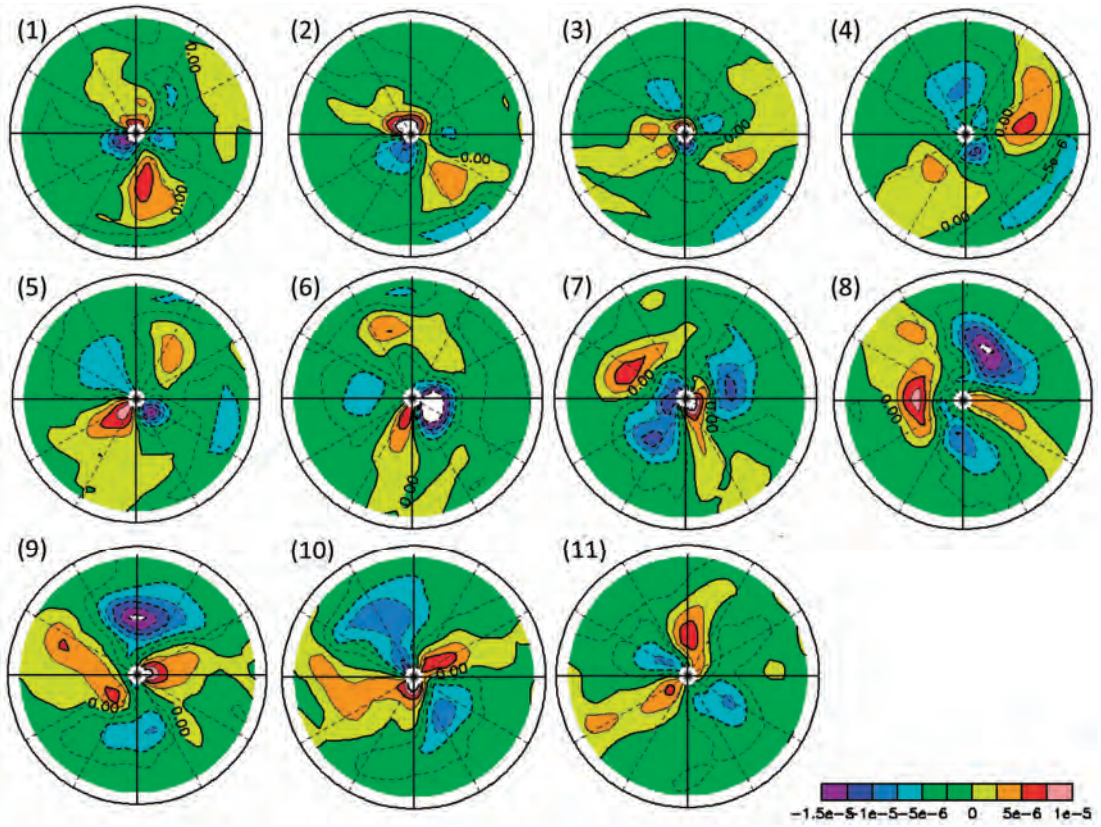

Fig. 3 Time evolution of vorticity at 62 km altitude in the polar region (60°N−90°N) from (1) t = 1365 days to (11) t = 1375 days. Time interval between panels is 12 hours.

at 62 km altitude (figures are not shown here) where the static stability and the vertical shear change strongly. These results agree well with observational studies. Our model can reproduce the polar vortex of the Venus atmosphere self-consistently; and further analysis will reveal dynamics of the polar vortex.

We also conduct sensitivity tests to explore the dependence of baroclinic instability on the initial meridional profile of zonal flow, on the vertical profile of static stability for the Newtonian cooling, and on the model resolution. The results indicate that the realistic vertical distribution of static stability and a sufficiently high resolution are crucial for the occurrence of baroclinic instability (figures are not shown here). The results also indicate that baroclinic instability contributes significantly to the general circulation of the Venus atmosphere when the zonal mean flow, as is often observed, is characterized by the appearance of the mid-latitude jets. The results of the sensitivity tests are summarized in Sugimoto et al. [14].

3. Mars simulation

3.1 Targets of simulations

Radiative effect of dust suspended in the Martian atmosphere has important impacts on the thermal and circulation structure of the Martian atmosphere. However, it has not been well understood what kind of dynamical phenomena play important roles in lifting dust from the ground into the atmosphere. A previous study by using a Mars GCM [15] suggests that the effects of subgrid scale wind fluctuations caused by small and medium scale disturbances would be important for the dust lifting processes. However, the features of small and medium scale disturbances which may contribute to the dust lifting have not been revealed yet. Disturbances of these scales are not easy to be observed and to be resolved in numerical models. In order to examine the disturbances in the Martian atmosphere and its effects on dust lifting, we have been performing medium and high resolution simulations of Martian atmosphere by using our Martian AFES. In this fiscal year, properties of dust lifting are analyzed in terms of probability distribution function.

3.2 Model and experimental settings

Mars simulations are performed with the AFES including physical processes introduced from the Mars GCM [16, 17] which has been developed in our group, and with the values of physical constants appropriate for the Mars. The implemented physical processes are radiative, turbulent mixing, and surface processes. By the use of this model, several simulations are performed. Resolutions of simulations are T79L96, T159L96, T319L96, and T639L96, which are equivalent to about 89, 44, 22, and 11 km horizontal grid sizes, respectively. In the simulations, the atmospheric dust distribution is prescribed, and the dust is uniformly distributed in horizontal direction with an amount corresponding to visible optical depth of 0.2. However, the dust lifting parameterization [18] is included in the model to diagnose the possible amount of dust lifting.

3.3 Results

Fig. 4 and 5 show snapshots of distribution of relative vorticity at 4 hPa pressure level and dust lifting flux during the northern fall from the T639L96 simulation. It is shown that a lot of disturbances with a variety of horizontal scales are responsible for dust lifting in the model. Most intense dust lifting occurs associated with synoptic scale eddies around the northern polar cap edge. At the same time, small scale eddies also contribute to dust lifting. Some of those are associated with small and medium scale orographic variations, but others are not.

Here, the nature of resolution dependence of dust lifting events in the model is examined in terms of probability distribution function. Fig. 6 shows the probability distribution function of dust lifting flux as a function of surface stress. It is found that dust lifting flux, in general, increases with increasing resolution over almost all surface stress values. However, as is shown in Fig. 6, in our simulation, the dust lifting flux from T159L96 simulation is larger than that in T319L96 simulation. Fig. 7 and 8 show the same as Fig. 6, but for two latitudinal bands. It is shown that dust lifting flux increases with increasing resolution in the region from 60ºS to 30ºN, where small scale vortices appear. But, in the region south of 60ºS and north of 30ºN, the dust lifting flux from T159L96 simulation is larger than those from the higher resolution simulations. The dust lifting events in mid- and high-latitudes are mainly caused by synoptic eddies as is shown in Fig. 4. It is implied that a variability of synoptic eddies in mid- and high-latitude would contaminate the resolution dependence of dust lifting.

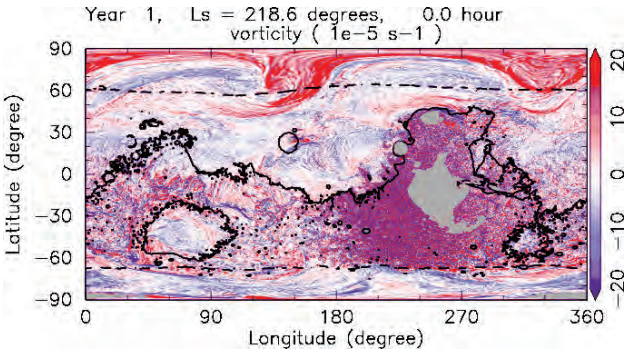

Fig. 4 Global distribution of vorticity at 4 hPa pressure level at northern fall with the resolution of T639L96. Unit of vorticity is 10^{-5} s^{-1}. Also shown is the areoid (solid line) and low latitude polar cap edge (dashed line). Gray areas represent mountains at the 4 hPa pressure level.

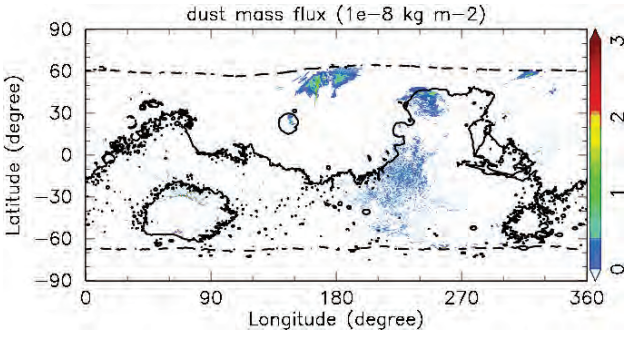

Fig. 5 Same as Fig. 4, but for dust lifting flux at the ground. Unit of dust lifting flux is arbitrary.

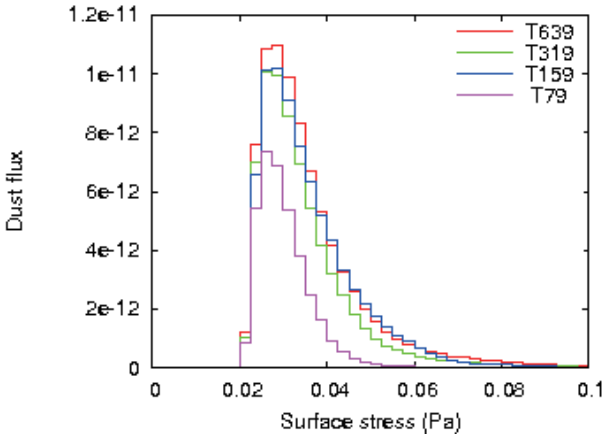

Fig. 6 Probability distribution function of dust lifting flux as a function of surface stress at northern fall with the resolutions of T639L96, T319L96, T159L96, and T79L96.

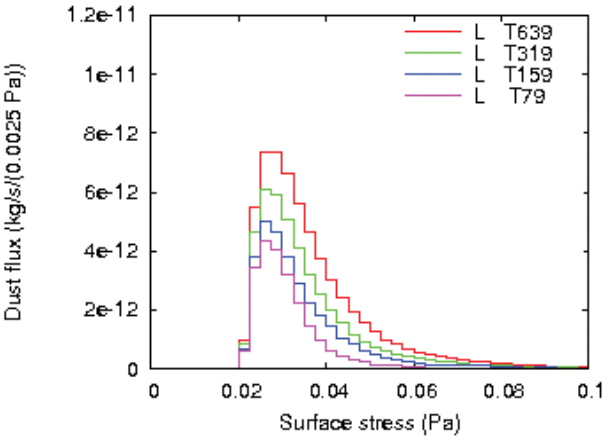

Fig. 7 Same as Fig. 6, but for probability distribution function at the region from 60ºS to 30ºN.

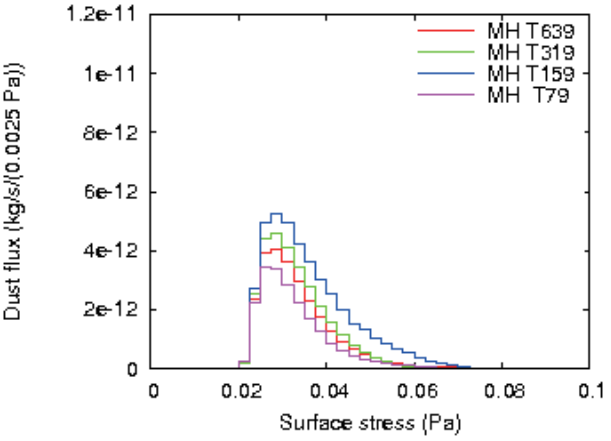

Fig. 8 Same as Fig. 6, but for probability distribution function at the region south of 60ºS and north of 30ºN.

References

[1] Ohfuchi, W., H. Nakamura, M. K. Yoshioka, T. Enomoto, K. Takaya, X. Peng, S. Yamane, T. Nishimura, Y. Kurihara, and K. Ninomiya, "10-km Mesh Meso-scale Resolving Simulations of the Global Atmosphere on the Earth Simulator - Preliminary Outcomes of AFES (AGCM for the Earth Simulator) –", Journal of the Earth Simulator, 1, 8, 2004.

[2] Yamamoto, M. and M. Takahashi, "The fully developed superrotation simulated by a general circulation model of a Venus-like atmosphere", J. Atmos. Sci., 60, 561-574, 2003.

[3] Nastrom, G. D. and K. S. Gage, "A climatology of atmospheric wavenumber spectra of wind and temperature observed by commercial aircraft", J. Atmos. Sci., 42, 950–960, 1985.

[4] Takahashi, Y. O., K. Hamilton, and W. Ohfuchi, "Explicit global simulation of the mesoscale spectrum of atmospheric motions", Geophysical Research Letters, 33, L12812, doi:10.1029/2006GL026429, 2006.

[5] Leroy, S. S. and A. P. Ingersoll, "Radio scintillations in Venus's atmosphere: application of a theory of gravity wave generation", J. Atmos. Sci., 53, 1018-1028, 1996.

[6] Piccioni, G. et al., "South-polar features on Venus similar to those near the north pole", Nature, 450, 637-640, 2007.

[7] Sugimoto, N., M. Takagi, Y. Matsuda, Y. O. Takahashi, M. Ishiwatari, and Y.-Y. Hayashi, "Baroclinic modes in the atmosphere on Venus simulated by AFES", Theoretical and Applied Mechanics Japan, 61, 11-21, 2013.

[8] Young, R. E., H. Houbel, and L. Pfister, "Baroclinic instability in the Venus atmosphere", J. Atmos. Sci., 41, 2310–2333, 1984.

[9] Takagi, M. and Y. Matsuda, "A study on the stability of a baroclinic flow in cyclostrophic balance on the sphere", Geophysical Research Letters, 33, L14807, doi:10.1029/2006GL026200, 2006.

[10] Crisp, D., "Radiative forcing of the Venus mesosphere: I. solar fluxes and heating rates", Icarus, 67, 484-514, 1986.

[11] Tomasko M. G., L. R. Doose, P. H. Smith, and A. P. Odell, "Measurements of the flux of sunlight in the atmosphere of Venus", J. Geophys. Res., Vol. 85, 8167-8186, 1980.

[12] Gierasch P. J., R. M. Goody, R. E. Young, D. Crisp, C. Edwards, R. Kahn, D. Rider, A. Del Genio, R. Greeley, A. Hou, C. B. Leovy, D. McCleese, and M. Newman, "The General Circulation of the Venus Atmosphere: an Assessment", In Venus II: Geology, Geophysics, Atmosphere, and Solar Wind Environment. University of Arizona Press, p.459, 1997.

[13] Koshyk, J. N. and K. Hamilton, "The horizontal kinetic energy spectrum and spectral budget simulated by a high-resolution troposphere-stratosphere-mesosphere GCM", J. Atmos. Sci., 58(4), 329–348, 2001.

[14] Sugimoto, N., M. Takagi, and Y. Matsuda, "Baroclinic instability in the Venus atmosphere simulated by GCM", J. Geophys. Res., under revision. (2014JE004624)

[15] Wilson, R. J. and K. Hamilton, "Comprehensive Model Simulation of Thermal Tides in the Martian Atmosphere", J. Atmos. Sci., 53, 1290-1326, 1996.

[16] Takahashi, Y. O., H. Fujiwara, H. Fukunishi, M. Odaka, Y.-Y. Hayashi, and S. Watanabe, "Topographically induced north-south asymmetry of the meridional circulation in the Martian atmosphere", J. Geophys. Res., 108, 5018, doi:10.1029/2001JE001638, 2003.

[17] Takahashi, Y. O., H. Fujiwara, and H. Fukunishi, "Vertical and latitudinal structure of the migrating diurnal tide in the Martian atmosphere: Numerical investigations", J. Geophys. Res., 111, E01003, doi:10.1029/2005JE002543, 2006.

[18] Newman, C. E., S. R. Lewis, and P. L. Read, "Modeling the Martian dust cycle 1. Representation of dust transport processes", J. Geophys. Res, 107, 5123, doi:10.1029/2002JE001910, 2002.

AFES を用いた地球型惑星の大気大循環シミュレーション

課題責任者
林　祥介　神戸大学　大学院理学研究科

著者
林　祥介　神戸大学　大学院理学研究科
高橋　芳幸　神戸大学　大学院理学研究科
杉本　憲彦　慶應義塾大学　自然科学研究教育センター
高木　征弘　京都産業大学　理学部
樫村　博基　宇宙航空研究開発機構　宇宙科学研究所
石渡　正樹　北海道大学　大学院理学研究院
小高　正嗣　北海道大学　大学院理学研究院
中島　健介　九州大学　大学院理学研究院
はしもとじょーじ　岡山大学　大学院自然科学研究科
松田　佳久　東京学芸大学　教育学部

大気大循環モデル AFES（AGCM (Atmospheric General Circulation Model) for the Earth Simulator）に基づく GCM を用いて、金星および火星大気の高解像度大気大循環シミュレーションを実施した。我々の研究の目的は、地球型惑星大気における中小規模擾乱の力学的特徴と、その大気大循環への影響を調べることである。金星大気シミュレーションでは、現実的な太陽加熱を用いて長時間スーパーローテーションを維持することができた。その高解像度計算（T159L120）の結果を用いて水平運動エネルギーのスペクトル解析を行い、金星大気では小規模重力波が地球大気に比べてより重要である可能性を示唆した。また、モデル中に現れた極渦の構造を観測と比較し、S 字構造や鉛直構造が整合的であることを示した。さらに、基本場の安定度の鉛直構造と速度の水平構造に対する線形不安定解析の結果を基に、傾圧不安定の発現の依存性も調べた。その結果、傾圧不安定波の発達には現実的な安定度の鉛直分布とこれを表現する十分な解像度が必要であることを示し、観測で見られるような中緯度ジェットをもつ東西風の下では傾圧不安定波が金星大気大循環においてより重要な働きをもたらすことを予想させる結果を得た。火星大気シミュレーションでは、T79 から T639 までの複数の水平解像度の計算結果を用いてダスト巻き上げ過程の特性を調べた。これらの計算では、総観規模から小規模までの様々な種類の擾乱が表現されている。ここでは、分布関数を用いてこれらの擾乱に伴うダスト巻き上げを調べ、一般に、解像度が高くなるほどダスト巻き上げ量が大きくなることを示した。これは高い解像度のモデルほど小規模擾乱をより良く表現できることに起因しているものと考えられる。しかし、特に中高緯度においては、低解像度のモデルの方でダスト巻き上げ量がより多い場合があることも示された。これは中高緯度における総観規模擾乱の変動性が低緯度の擾乱の変動性に比べて大きいことによるものと考えられる。

キーワード:惑星大気, スーパーローテーション, ダストストーム, 地球, 火星, 金星

Study on the Diagnostics and Projection of Ecosystem Change Associated with Global Change

Project Representative

Sanae Chiba Research Institute for Global Change, Japan Agency for Marine-Earth Science and Technology

Authors

Eiji Watanabe[*1], Maki Aita-Noguchi[*1], Naomi Harada[*1], Akio Ishida[*1, 2], Michio J. Kishi[*1, 3] and Toshiro Saino[*1]

*1 Research Institute for Global Change, Japan Agency for Marine-Earth Science and Technology

*2 Department of Social and Environmental Studies, Tokoha University

*3 Faculty of Fisheries Sciences, Hokkaido University

The future conditions of Arctic sea ice and marine ecosystems are of interest not only to climate scientists but also to economic and governmental bodies. However, the lack of widespread, yearlong biogeochemical observations remains an obstacle to understanding the complicated variability of the Arctic marine biological pump. Here we address an early winter maximum of sinking biogenic flux in the western Arctic Ocean and illustrate the importance of shelf-break eddies to biological pumping from wide shelves to adjacent deep basins using a combination of yearlong mooring observations and three-dimensional numerical modeling. The sinking flux trapped in the present study included considerable fresh organic material with soft tissues and was an order of magnitude larger than previous estimates. We then predicted that further reductions in sea ice would promote the entry of Pacific-origin biological species into the Arctic basin and accelerate biogeochemical cycles connecting the Arctic and subarctic oceans.

Keywords: pan-Arctic ice-ocean model, biological pump, mesoscale eddy, sea ice reduction

1. Marine biological pump in the western Arctic basin

Evaluating the responses of biogeochemical cycles to decreasing sea ice is important to predict long-term trends in fishery resources. Improved summer light conditions have been reported to enhance planktonic photosynthesis in the Eurasian pelagic area of the Arctic Ocean. Furthermore, the accumulation of nutrient-poor freshwater suppressed the primary production of phytoplankton in the central Canada Basin during the 2000s. Biological pump of particulate organic carbon (POC), which is one of the sequestration mechanisms of atmospheric CO_2 to deep sea, has been reported to be ineffective in the cryopelagic Canadian Arctic deep basins [1]. Whereas primary productivity of phytoplankton could be modest even under sea ice cover, low abundance of ballast particles such as shell-bearing micro-planktons might have prevented biological materials from sinking toward deep layers. On the other hand, lateral transport of resuspended bottom sediments played a role in oceanic carbon sink in the western Arctic off-shelf regions. These findings were obtained by time series sediment trap measurements in the deep Canada Basin, the Canadian Beaufort shelves, the northern Laptev Sea, and the Nordic seas (Fig. 1). However, there are many gaps to fill to achieve a comprehensive explanation of the spatial and temporal variability of biological pump processes under rapid environmental changes of the Arctic Ocean. The relative contribution of the lateral transport of shelf-origin materials to basin interiors remains uncertain. The western Canada Basin and the Chukchi Borderland, which have experienced a remarkable reduction of sea ice and substantial biological shifts during the early 21st century, are located downstream of Pacific-origin water that obtains heat, nutrients, and organic material over the shallower Chukchi shelf. Thus, further investigations of the physical and biogeochemical properties along the Pacific water pathway will provide valuable information regarding communication between the Bering Sea and the central Arctic.

We detect a significant amount of sinking biogenic materials with particulate organic nitrogen (PON) using measurements from sediment traps deployed in the Northwind Abyssal Plain (NAP; Fig. 1) since autumn 2010. We then address the background mechanisms and possible future conditions of the biological pump from the viewpoint of shelf water transport using an eddy-resolving (5-km grid size) framework in a pan-Arctic sea ice-ocean model [2]. Our findings reveal the effective role of Beaufort shelf-break eddies in biological pumping from the Chukchi shelf to the Canada Basin. Because these eddies are generated in summer immediately after shelf blooms of phytoplankton, biological activity can continue even during

eddy migration towards the central Arctic. Whereas the so-called "lateral biological pump" have meant the resuspension and eddy-induced transport of bottom sediments composed of old carbon, the presented process may sustain marine ecosystems in seasonal ice zones of the Arctic basins.

2. Roles of shelf-break eddies in sinking biogenic fluxes

A seasonal experiment using our pan-Arctic sea ice-ocean model demonstrated that the PON flux at Station NAP initially increased in July and reached summer and early winter peaks at depths of 180 and 1,300 m (Fig. 2). These modelled fluxes were larger than those derived from our shallow sediment trap data, but the modelled flux values at the greater depth were similar to the corresponding trap data. The carbon sink derived from the simulated PON flux at a 180 m (1,300 m) depth was 258 (59) mgC m^{-2} from May to December. Because shelf bottom water is considered to be the crucial nutrient source for biological production in the basin area, its pathway was addressed using a colored passive tracer in the model experiment. The tracer signal clearly indicated that the shelf bottom water reached Station NAP at the peak timing of PON flux in this case. Moreover, a distinct minimum-temperature layer, which was isolated from the surface mixed layer, appeared at a depth of 100–200 m from

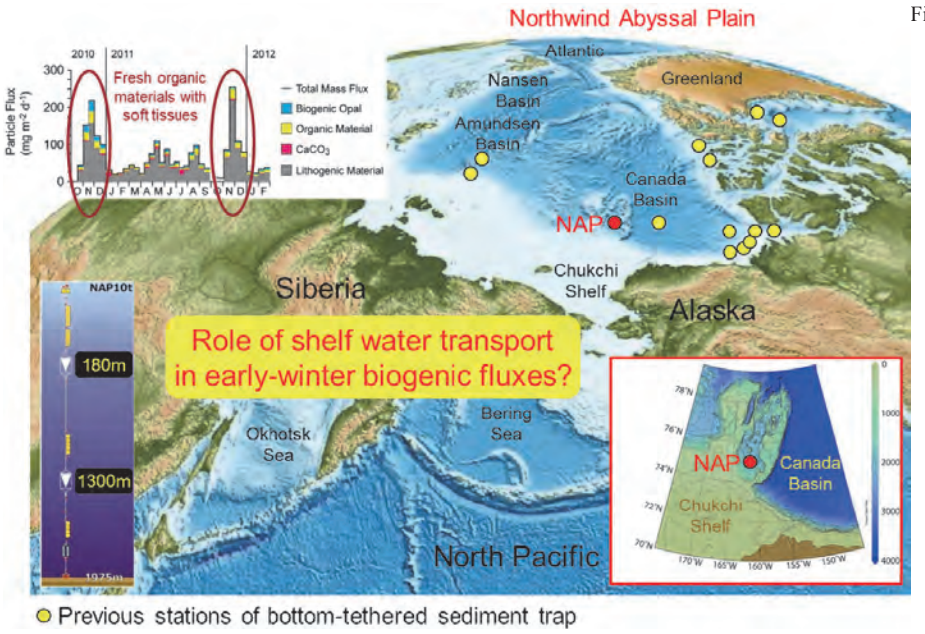

Fig. 1 Topography map in the Arctic-subarctic regions. Red dots show the location of Station NAP, where our sediment trap has been deployed since October 2010. Yellow dots show the locations of previous yearlong bottom-tethered sediment traps (See also Fig.1 in Honjo et al. [2010]). The inset shows the time series of observed sinking particle fluxes. Modified from Watanabe et al. [2014].

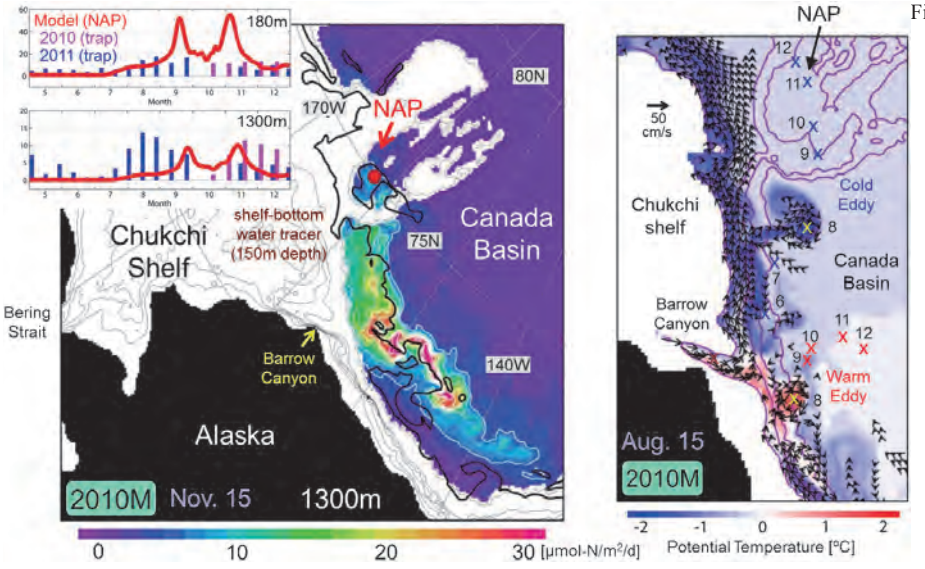

Fig. 2 (left) PON flux at a depth of 1,300 m on November 15 in the 2010M case [μmol-N m^{-2} d^{-1}]. The modeled tracer concentration of shelf bottom water at 150 m depth is 0.1 along black contours. Inset figures show the flux time series at 180 and 1,300 m depths; Pink and blue bars represent the observed fluxes in 2010 and 2011, respectively. The modeled fluxes in the 2010M case at Station NAP are shown by solid lines, respectively. (right) Potential temperature [°C] (color shade) and ocean horizontal velocity at a 100 m depth on August 15 in the 2010M case. The unit vector is 50 cm s^{-1}, and vectors of velocity less than 5 cm s^{-1} are hidden. Blue (red) crosses indicate the locations of cold (warm) eddy centres in each month (e.g., "6" denotes June 15, "7" denotes July 15, and so on). Modified from Watanabe et al. [2014].

October to December. This cooling event was detected by the sediment trap sensors and indicated the lateral advection of cold water mass.

Here, we propose that mesoscale eddies originating in the vicinity of the Beaufort shelf break play an important role in biological pumping in the western Arctic basin. Our model reproduced both cold and warm shelf-break eddies. One such cold eddy migrated westward along the pathway of basin-wide Beaufort Gyre circulation and passed Station NAP in November. This eddy, generated in June, carried near-freezing shelf water and retained its cold core at least until December. Due to phytoplankton bloom and zooplankton grazing, the PON concentration within the cold eddy increased from June to August in most of the water column and exceeded 10 μmol-N m^{-3} until the eddy passed Station NAP in November. Because the PON concentration within the cold eddy was higher than that in the surrounding basin water, the second peak of PON flux occurred in early winter at Station NAP. Warm eddies generated after sea ice retreat in late summer had greater contribution to PON flux compared with cold eddies produced under sea ice in early summer. A higher PON flux was localized in part of the southern Canada Basin, where baroclinic eddies traced the anti-cyclonic Beaufort Gyre. As well as cold eddies, the hydrographic and biogeochemical properties of warm eddies reflected the environment of Barrow Canyon during their generation [3]. In the case of warm eddies, the PON concentration exceeded 100 μmol-N m^{-3} from the eddy generation period in August. The higher water temperatures in the ocean surface layer of warm eddies kept their pathways away from the sea ice cover; thus, both the warmer conditions and the greater light intensity favoured phytoplankton photosynthesis and subsequent zooplankton grazing. We checked the PON flux north of Barrow Canyon (NBC), where a warm eddy passed on November 15. The peak fluxes of 150 and 38 μmol-N m^{-2} d^{-1} at 180 and 1,300 m, respectively, were several times larger than those within the cold eddy at Station NAP. In the Mackenzie shelf region, it has been reported that the resuspension of shelf bottom sediments and cross-shelf transport of POC were induced by buoyancy-driven convection following winter sea ice formation [4] and by baroclinic eddies [5]. In contrast, our results showed that high plankton activity was accompanied by the development and migration of summer eddies in the downstream region of the Pacific water pathway.

3. Impact of sea ice reduction

The eddy-induced early-winter biological pump would be enhanced by sea ice retreat. To address the impact of sea ice reduction on the early winter PON flux, we performed two additional experiments in which the sea ice thickness given as the initial condition on March 1 was multiplied by 2.0 or 0.5 in the entire model domain (named as Ice2.0 and Ice0.5 cases, respectively). The total sea ice extent on October 1 was 6.9 (3.9) × 10^6 km^2 in the Ice2.0 (Ice0.5) cases (Fig. 3). The average summer sea ice extent during the 1990s was similar to the Ice2.0 case, and the 2012 sea ice margin was located farther north than that seen in the Ice0.5 case. The modeling results indicate that the magnitude of the biological pump might have doubled over the last two decades in the southwestern Canada Basin. This trend arose because the eddy-driven transport of shelf-origin nutrients and biological materials towards the Canada Basin

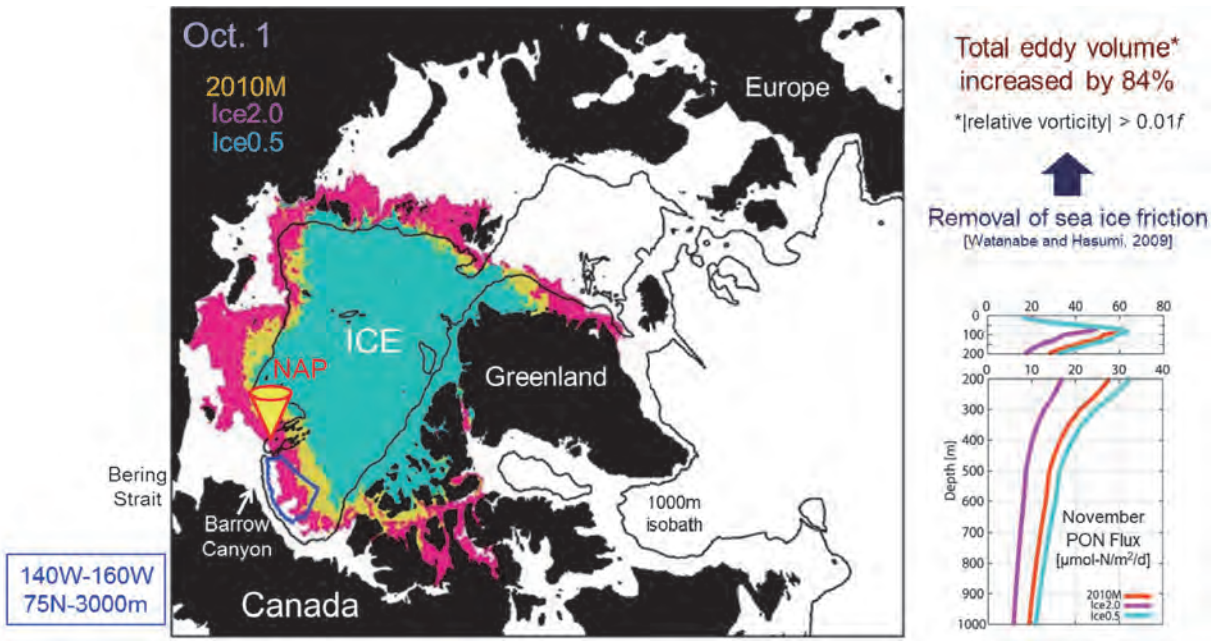

Fig. 3 (left) Sea ice distribution on October 1 in the (orange) 2010M, (pink) Ice2.0, and (sky blue) Ice0.5 cases. Black contours represent 1,000 m isobaths. The location of Station NAP is shown by a yellow cone. (right) The vertical profile of November mean PON flux in each case [μmol-N m^{-2} d^{-1}]. The average region is the southwestern Canada Basin, which is outlined by a blue contour in the left figure. Modified from Watanabe et al. [2014].

was promoted. The factor for this difference could be attributed to changes in shelf bloom and eddy activity, respectively. The improved light conditions owing to sea ice reduction increased phytoplankton biomass in early summer. The earlier shelf bloom hastened nutrient depletion and rapidly reduced the PON content per each eddy from summer to autumn. On the other hand, the removal of sea ice drag increased the Barrow Canyon outflow and eddy kinetic energy [6]. Additionally, the enhanced eddy generation and development promoted greater PON export to the deep basin under less sea ice condition. We can indicate that eddy-induced lateral nutrient supplies to the euphotic zone have favored the increasing phytoplankton growth in the Canada Basin, whereas the deepening nutricline in part caused by sea ice reduction may suppress primary productivity. Thus, the environmental transition for lower trophic ecosystems in the marginal Beaufort Gyre, including the NAP area, differs from the situation in the central gyre. In addition, the recent acceleration of Beaufort Gyre was reported by drifting buoy measurements. The faster gyre circulation is expected to reinforce the westward transport of Chukchi shelf water and to induce earlier peaks of PON flux at Station NAP. Now, we need to consider how far the area of high biological activity will spread in the near future and how ocean dynamics will contribute to the pan-Arctic marine ecosystem. Because mesoscale eddies have been detected in multiple shelf-basin boundary regions of the Arctic Ocean, the ecological function of laterally transported organic materials is likely to gain more importance as a food source for plankton and higher-trophic organisms in the basin interior.

Acknowledgements

This work was funded by the Grants-in-Aid for Scientific Research (S) of Japan Society for the Promotion of Science (JSPS) JFY2010–2014, No. 22221003, “Catastrophic reduction of sea ice in the Arctic Ocean: its impact on the marine ecosystems in the polar region”. The authors appreciate continuous support from the Earth Simulation Center.

References

[1] Honjo, S., et al. Biological pump processes in the cryopelagic and hemipelagic Arctic Ocean: Canada Basin and Chukchi Rise. *Prog. Oceanogr*., **85**, 137-170 (2010).

[2] Watanabe, E., et al. Enhanced role of eddies in the Arctic marine biological pump. *Nature Comm*., **5**:3950, doi:10.1038/ncomms4950 (2014).

[3] Watanabe, E., M. J. Kishi, A. Ishida, and M. N. Aita. Western Arctic primary productivity regulated by shelf-break warm eddies. *Journal of Oceanography*, **68**, pp703-718, doi:10.1007/s10872-012-0128-6 (2012).

[4] Forest, A., et al. Particulate organic carbon fluxes on the slope of the Mackenzie Shelf (Beaufort Sea): Physical and biological forcing of shelf-basin exchanges. *J. Mar. Sys*., **68**, 39-54 (2007).

[5] O’Brien, M. C., Melling, H., Pedersen, T. F., and Macdonald, R. W. The role of eddies on particle flux in the Canada Basin of the Arctic Ocean. *Deep Sea Res.-I*, **71**, 1-20 (2013).

[6] Watanabe, E. and Hasumi, H. Pacific water transport in the western Arctic Ocean simulated by an eddy-resolving coupled sea ice-ocean model. *J. Phys. Oceanogr*., **39**, 2194-2211 (2009).

地球環境変化に伴う生態系変動の診断と予測に関する研究

課題責任者
千葉　早苗　　海洋研究開発機構　地球環境変動領域
著者
渡邉　英嗣 *1，相田（野口）　真希 *1，原田　尚美 *1，石田　明生 *1, 2，岸　　道郎 *1, 3，才野　敏郎 *1
*1 海洋研究開発機構　地球環境変動領域
*2 常葉大学　社会環境学部
*3 北海道大学　水産科学研究院

北極海における近年の急激な海氷減少は大気・海洋場への影響も含めて社会的関心事の１つとなっている。ベーリング海峡から流入する太平洋起源水は北極海の熱・淡水・栄養塩の主要な供給源であり、その輸送は西部北極海の海氷変動や海洋生態系と密接な関係にある。独立行政法人・海洋研究開発機構では、太平洋側北極海のノースウィンド深海平原（NAP）にセディメントトラップ係留系を設置し、2010 年 10 月から現在に至るまで沈降粒子の時系列観測を実施している。セディメントトラップによる現場観測は北極海でもこれまでにカナダ側のマッケンジー陸棚縁やロシア側のラプテフ海北部で行われてきたが、太平洋起源水の下流域にあたる NAP 周辺で複数年に渡って実施されたのは今回が初めてである。その時系列観測結果からは、植物プランクトンの光合成が活発化する夏季に加えて、極夜が始まる 10 月以降に新鮮な珪藻や二枚貝幼生を多く含む沈降粒子量極大が捉えられており、沈降粒子の中には泥質の鉱物粒子も存在することから、陸棚域からの有機物の水塊輸送（移流）が関与していることが推察される。そこで本課題では北極海全域を対象にした海氷海洋物理モデル COCO に低次海洋生態系モデル NEMURO を結合させた数値実験を行い、陸棚海盆境界域で生成される海洋渦が北極海盆域の生物ポンプにとって重要な役割を担っていることが示唆された。この水平数十 km スケールの海洋渦は夏季に太平洋起源水がバロー峡谷からカナダ海盆域に流入する際に生成されるものであり、動植物プランクトンが自身の生物活動によって渦内部で増え続けることもモデル計算の結果から示されている。また海氷の条件を変える感度実験の結果では、北極海で海氷の減少が進むと渦生成も促進されることから、北極海盆域における極夜時の生物ポンプは徐々に活発化していることが示唆された。ノースウィンド深海平原において魚類の餌となる動植物プランクトンの生息環境が向上していることが本研究で示唆されたことで、将来的には北極海盆域が水産資源のターゲットになり得ると考えられる。今後も当海域において時系列観測を継続するとともに、高精度な数値モデリングを組み合わせることで、より詳細な北極海洋生態系プロセスが明らかになっていくことが期待される。

キーワード:北極海物理生態系結合モデル, 生物ポンプ, 中規模渦, 海氷減少

Study of Cloud and Precipitation Processes using a Global Cloud Resolving Model

Project Representative

Masaki Satoh Research Institute for Global Change, Japan Agency for Marine-Earth Science and Technology
Atmosphere and Ocean Research Institute, The University of Tokyo

Authors

Masaki Satoh[*1, 2], Hirofumi Tomita[*1, 3], Tomoe Nasuno[*1], Akira T. Noda[*1], Shin-ichi Iga[*3], Hiroaki Miura[*1, 4], Kazuyoshi Oouchi[*1], Hiroshi Taniguchi[*5], Yohei Yamada[*1], Wataru Yanase[*2], Chihiro Kodama[*1], Masayuki Hara[*1], Kazuaki Yasunaga[*1, 6], Tatsuya Seiki[*1], Masanori Yoshizaki[*1, 7], Masuo Nakano[*1], Tomoki Miyakawa[*1], Hisashi Yashiro[*1, 3], Tsuyoshi Yamaura[*3], Hiroyasu Kubokawa[*2], Mikiko Ikeda[*1], Masahiro Sawada[*2] and Ying-Wen Chen[*1]

*1 Research Institute of Global Change, Japan Agency for Marine-Earth Science and Technology
*2 Atmosphere and Ocean Research Institute, The University of Tokyo
*3 Advanced Institute for Computational Science, RIKEN
*4 School of Science, The University of Tokyo
*5 Department of Science, Kobe City College of Technology
*6 Department of Earth Science, University of Toyama
*7 Faculty of Geo-environmental Science, Rissho University

The goal of this project is to better understand cloud and precipitation processes on the Earth and to improve their treatment in climate models by global cloud-resolving approach. To achieve this goal, we performed series of numerical experiments using Nonhydrostatic Icosahedral Atmospheric Model (NICAM) with horizontal mesh sizes of 3.5 to 14 km. The major achievements of the FY2013 are as follows: (1) The extended simulation of the tropical convective disturbance, Madden-Julian Oscillation (MJO) for the Cooperative Indian Ocean experiment on intraseasonal variability in the year 2011 (CINDY2011) / Dynamics of the Madden-Julian Oscillation (DYNAMO) intensive observation period was conducted. The results suggested the potential ability of the global 7-km mesh model to reproduce the regulation of the MJO. (2) The impacts of the newly proposed modification in the cloud microphysical scheme on the simulated cloud and precipitation properties were examined by the 3.5-km mesh sensitivity experiments. The results show significant improvements in the statistics of the simulated cloud properties compared with the satellite observations. A pilot study of a near real-time operation of the global cloud-resolving simulation for a field campaign was also conducted.

Keywords: cloud and precipitation processes, global cloud-resolving model

1. Introduction

Recent improvements in observational technology allow high-resolution multi parameter measurements of the earth system. In particular, progress in cloud and precipitation observations by satellite missions is remarkable, which is based on the recognition of its broad impacts on global climate prediction, as well as daily weather forecasts. In JAMSTEC, the *in situ* observations including research cruise (e.g., MISMO, CINDY2011, PALAU project) have been successively conducted. The utilization of the up-to-date observation data in validating the numerical models, and to obtain deeper understanding of the processes are the necessary steps to make model predictions more reliable.

In this project, numerical experiments using Nonhydrostatic Icosahedral Atmospheric Model (NICAM, Satoh et al. 2008[1]) have been conducted to improve our understating of global cloud and precipitation processes. NICAM is unique in explicitly calculating cloud and precipitation processes on the whole globe. The simulations using the Earth Simulator derived innovative research results (e.g., Tomita et al. 2005[2]; Iga et al. 2007[3]; Miura et al. 2007[4]; Oouchi et al. 2009[5]; Noda et al. 2010[6]; Yamada et al. 2010[7]). In particular, series experiments targeted to the observation periods of the JAMSTEC field programs were executed and analyzed in

comparison with in-situ observation and satellite data (Satoh et al. 2010[8], 2011[9], 2012[10], 2013[11]).

In the FY2013, one of our targets was the recently observed Madden-Julian Oscillation (MJO; Madden and Julian 1971[12], 1972[13]) events that occurred during the CINDY2011/DYNAMO period (Yoneyama et al. 2013[14]). As the extension from the results obtained by the FY2012, we challenged the problem of the regulation of the MJO convective organization over the Indian Ocean and its eastward migration toward the Western Pacific. Another series of simulations with the 3.5-km mesh size had been performed to investigate TC genesis process that was observed during the field program PALAU2008. The simulation data was also quantitatively evaluated in comparison with satellite data (Hashino et al. 2013[15]). In the FY2013, a new method of cloud microphysics modeling (Roh and Satoh 2014[16]; hereafter, RS2014) was implemented and tested. A pilot study of extended-range forecasts was also conducted during the field campaign PALAU2013.

2. Extended simulation of the CINDY2011/DYNAMO

The international observation campaign CINDY2011/DYNAMO was operated over the Indian Ocean in 2011–2012 to investigate physical processes of the MJO. The MJO is characterized by a large-scale, O(1,000 km) wide, packet of organized cloud systems that moves eastward at an average speed of about 5 m s^{-1}. The MJO accompanies strong winds and severe precipitations, and thus, impacts socioeconomic activity in the tropics especially. Besides its importance on human society, the physical mechanisms of the MJO has not been revealed yet and accurate predictions of the MJO evens are still a challenge. It should be emphasized that JAMSTEC was one of the leading players of the CINDY2011/DYNAMO. Three packets of organized systems of the MJO were observed during the campaign, each called as “MJO-1”, “MJO-2” and “MJO-3”, respectively (Yoneyama et al. 2013 [14]).

It is thought that one of the reasons for insufficient understandings of the MJO is due to the difficulty in simulating the MJO by numerical weather prediction and climate models. If the MJO were simulated realistically, we could perform sensitivity studies by changing model parameters to identify the essential processes of the MJO. The simulation of the MJO is also being challenges for a high-resolution atmospheric model. It has been demonstrated that NICAM reproduced the eastward movement from the Indian Ocean to the maritime continent and the initiation of convection on the Indian Ocean (Miura et al. 2007[4]; Oouchi et al. 2009[5]; Miyakawa et al. 2014[17]), but it is still uncertain if NICAM has an ability to reproduce an observed 30–90-day cycle of the MJO events. Thus, using the Earth Simulator, we run NICAM for 60 days that includes MJO-1 and MJO-2 to test whether NICAM simulates MJO-2 or not.

We run NICAM on the Earth simulator, using the horizontal grid spacing of about 7 km. The time increment of the integration was 30 seconds. The initial fields of the atmospheric variables were generated by spatial interpolations of National Centers for Environmental Prediction (NCEP) final analyses. The realistic time evolution of the sea surface temperature was given by spatial and temporal interpolations of National Oceanic and Atmospheric Administration (NOAA) Optimum Interpolation Sea Surface Temperature (OI SST) data. The ocean-mixed layer was not used. The initial date was 16 October 2011 and the duration of the integration was 60 days.

Figure 1 shows the simulated outgoing longwave radiation (OLR). The onset, eastward movement, and decay of the MJO-1 are reproduced marginally. Interestingly, the onset and eastward movement of the MJO-2 are also captured although the timing of the onset is about five days earlier than the observed MJO-2. This result seems to suggest that the cause of the MJO-2 is

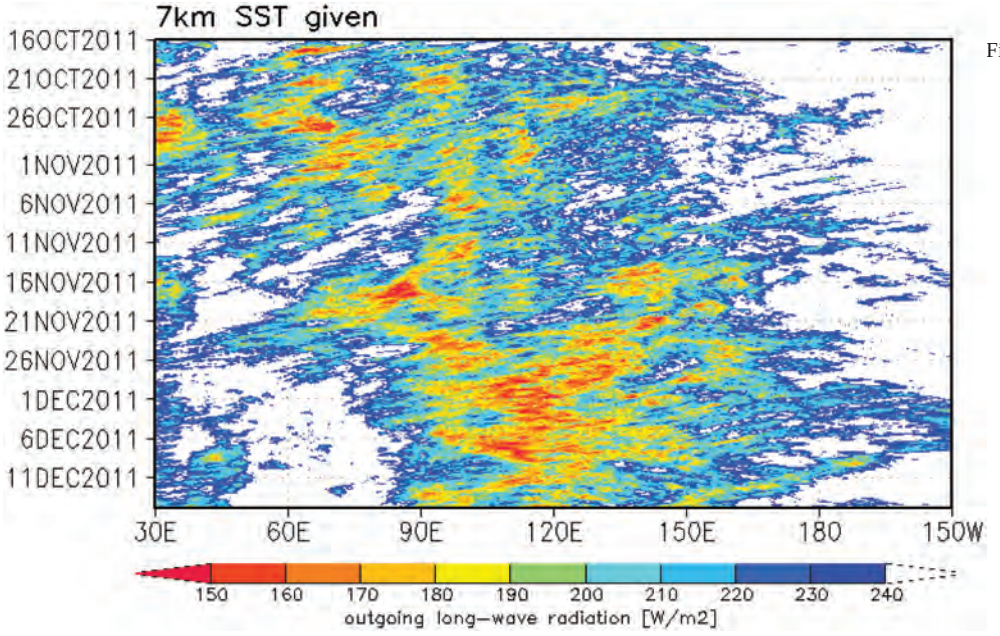

Fig. 1 Longitude-time cross section of outgoing longwave radiation simulated in the 7-km mesh run.

already included somewhere in the initial condition or in the SST time series. We cannot, of course, defy the possibility that the MJO-2 in the simulation is just an artifact. We will perform ensemble runs using the horizontal grid spacing of about 14 km, which is lower than about 7 km and allows us more simulation cases, to test if MJO-2 is a realistic one or not. In addition, sensitivity runs with different SST settings will be performed to investigate impacts of the SST evolution.

3. Evaluation and improvement in cloud microphysics

The clouds play important roles on the energy budget of the atmosphere and precipitation. The evaluation of cloud properties in General Circulation Models (GCMs) and cloud resolving models is important for analysis of the atmosphere and to overcome the limitations of observations. In this project, cloud properties simulated in the global 3.5-km mesh simulation using NICAM have been evaluated using a satellite simulator and model biases were discussed (Satoh

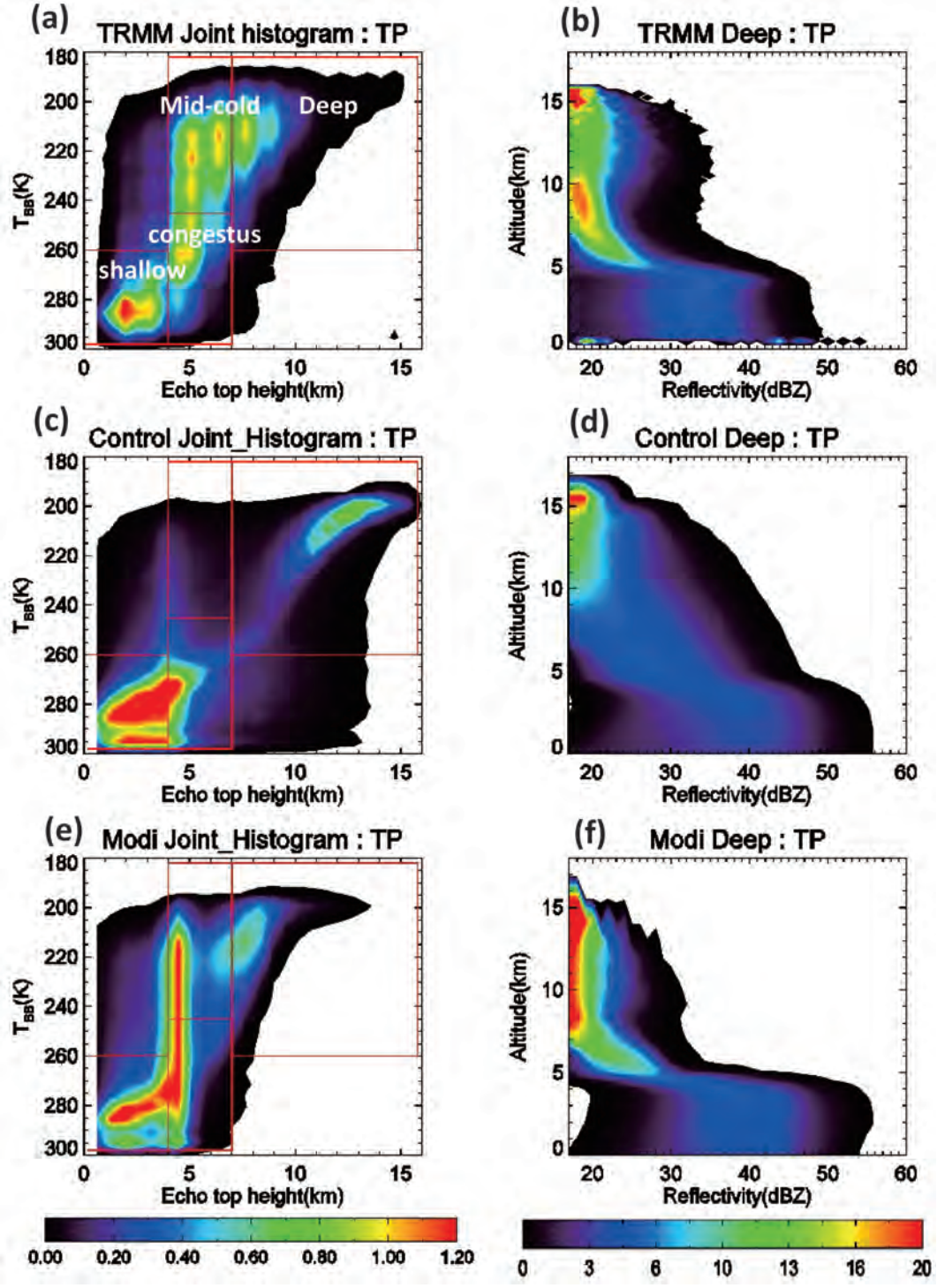

Fig. 2 The ETH–TBB joint histogram (left) and CFADs of deep clouds (right) for the TRMM observation (top), CON (middle), and MODI (bottom) in the whole tropics (20°S–20°N).

et al. 2011[9], 2012[10]; Hashino et al. 2013[15]). Recently, RS2014 proposed a new method to improve the model biases, based on the close examination of the numerical experiments using the regionally stretched version of NICAM (Tomita 2008a[18]) and the Tropical Rainfall Measuring Mission (TRMM) data. Their analysis was limited to the central Pacific domain, and global statistics were uncertain. Therefore, we applied the proposed modifications in the cloud microphysical scheme to the global 3.5-km mesh NICAM, and evaluated their impacts on (1) the echo top height (ETH) – 11μm brightness temperature (TBB) joint histograms and (2) the Contoured Frequency by Altitude Diagrams (CFADs) of deep clouds using the Satellite Data Simulator Unit (SDSU; Masunaga et al. 2010[19]). The experimental settings for the control run (CON) was documented by Satoh et al. (2010[9]) and Hashino et al. (2013[15]). A single moment bulk cloud microphysics scheme NSW6 (Tomita 2008b[20]) was used. The sensitivity tests with the modification by RS2014 (MODI) was conducted exactly the same way as CON except for the cloud microphysics scheme.

Figure 2 shows the ETH–TBB joint histogram and the CFADs of deep clouds for TRMM, CON, and MODI in the whole tropics (20°S–20°N). Deep clouds are defined as the ETH of TRMM higher than 7 km with the TBB lower than 260 K. The observed joint histogram shows the similar structure to those in RS2014 and Matsui et al. (2009[21]) (Fig 2a). Since a large part of the tropics is covered with the ocean, the overall structure of the joint histogram is similar to that of ocean cases in previous studies. The population of shallow precipitation clouds is overestimated in CON with high frequencies above the 10 km ETH, whereas there are few populations of clouds with the 5–7 km ETH and the TBB lower than 245 K (Fig. 2c). MODI reduced the biases of CON in shallow clouds and deep clouds above the 10 km ETH, and improved the frequencies of congestus clouds (Fig. 2e). The observed CFADs of deep clouds have concentrated frequencies with the range of radar reflectivity between 17 and 23 dBZ above the 5 km altitude (Fig. 2b). The maximum radar reflectivity above the 7 km height is almost 35 dBZ. In CON, widespread distributions of frequencies above the 5 km altitude and the overestimation of average and maximum radar reflectivity of the CFADs of deep clouds are found (Fig. 2b, d). In MODI realistic structure of CFADs is reproduced (Fig. 2b, f). However, maximum radar reflectivity in MODI is 32 dBZ, slightly lower than that in the observation. One of possible reasons for the lower maximum radar reflectivities is the absence of hail category in NSW6. The extreme precipitation in convective systems is often accompanied with large ice particles with high density like hails. Inclusion of hail category may be important to representation of extreme cases. In conclusion, the modified microphysics significantly improved the statistical properties of cloud and precipitation in the model. A satellite simulator and satellite observations are good tools for the evaluation and improvement of microphysics in a global high-resolution model.

4. A 15-day forecast during the PALAU2013

In the FY2013, the field campaign PALAU2013 was operated during May to July. The sounding network was deployed in Palau and Philippines, and on the research vessel Mirai (135°E, 12°N; MR-1303). Week-long near real-time forecasts using the regionally stretched grid version of NICAM have been daily operated during the observation period in support of the field operation. However, the nonuniform grid system is not suitable to extended-range forecasts. Therefore, a 15-day long forecast using the global 14-km mesh grid NICAM was executed for the

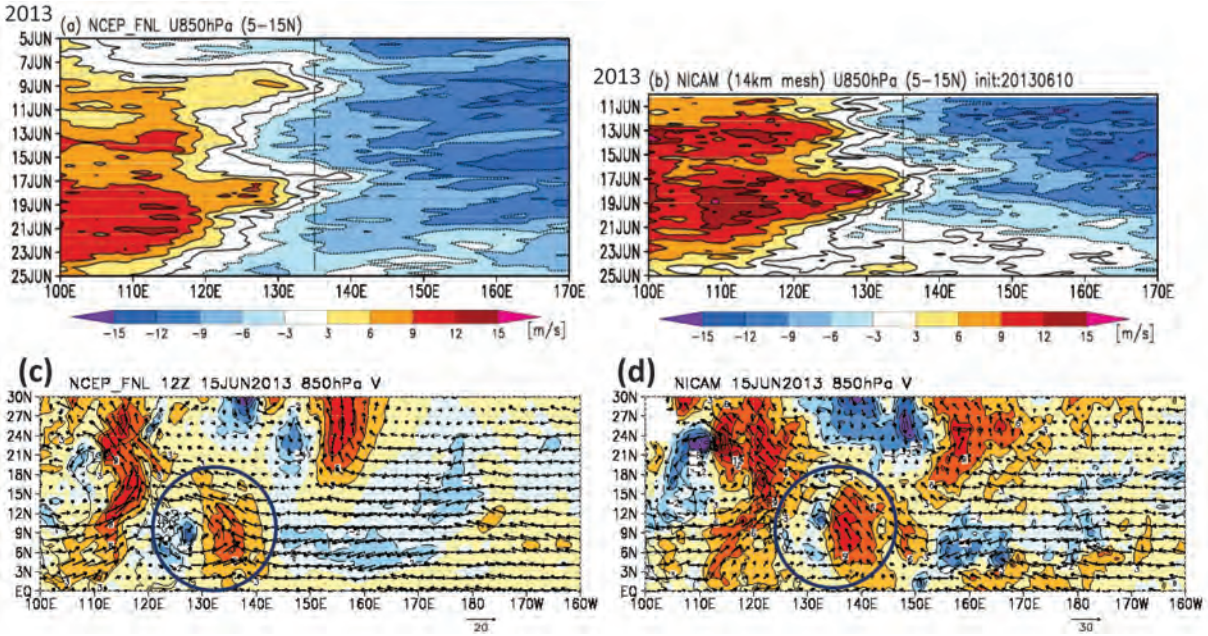

Fig. 3 Time-longitude plots of zonal wind at 850 hPa in (a) NCEP final analyses and (b) the 15-day NICAM forecast, averaged in 5°–15°N. Meridonal velocity (color) and wind vector at 850 hPa on 15 June 2013 in (c) NCEP final analyses and (d) the NICAM forecast.

first time.

Figure 3 show the time-longitude sections of observed and simulated low-level winds. Convective burst associated with the development of typhoon Yagi (TY1303) occurred on 7 June around the observation site, which led to South China Sea (SCS) monsoon onset, as seen in the abrupt acceleration of westerlies (Fig. 3a). After the passage of Yagi, the active period of intraseasonal variability (ISV) set in. The simulation was initialized on 10 June with an intention to gain information on the ongoing atmospheric variations and possible weather events. The forecasts captured the weakening of westerlies due to the inactive period of ISV/MJO in the second half of June (Fig. 3a, b). This suggests the potential ability of the model for subseasonal forecasts of large-scale disturbances, such as ISV or MJO (Miura et al. 2007[4]; Miyakawa et al. 2014[17]). The forecast also reproduced westward-propagating wave disturbances and its development into TY1304 close to the observation site around 17 June (Fig. 3c, d).

Since deterministic forecast has an intrinsic limitation in the predictability of mesoscale weather events, ensemble forecasts using the ES is planned as the next step, as well as the physically based sensitivity tests to understand the multi-scale interaction between convection and large-scale fields, as observed during the PALAU2013 field campaign.

CINDY2011: Cooperative Indian Ocean experiment on intreaseaonal variability in the year 2011 (http://www.jamstec.go.jp/iorgc/cindy/index_e.html)
DYNAMO: Dynamics of the Madden-Julian Oscillation (http://www.eol.ucar.edu/projects/dynamo/)
MISMO: Mirai Indian Ocean cruise for the Study of the MJO-convection Onset (http://www.jamstec.go.jp/iorgc/mismo/index-e.html)
PALAU: Pacific Area Long-term Atmospheric observation for Understanding of climate change (http://www.jamstec.go.jp/iorgc/palau/index.html)

Acknowledgements

Mr. Woosub Roh in Atmosphere and Ocean Research Institute / University of Tokyo is acknowledged for providing the modified NSW6 scheme and the analysis of the 3.5-km mesh experiments using the SDSU. ECMWF YOTC analysis is used for the initial data of the 3.5-km mesh experiment.

References

[1] Satoh, M., T. Matsuno, H., Tomita, H., Miura, T. Nasuno, and S.-I., Iga, “Nonhydrostatic Icosahedral Atmospheric Model (NICAM) for global cloud resolving simulations,” J. Comput. Phys., doi:10.1016/j.jcp.2007.02.006, the special issue on Predicting Weather, Climate and Extreme events. 2008.

[2] Tomita, H., H. Miura, S.-I., Iga, T. Nasuno, and M. Satoh, “A global cloud-resolving simulation: Preliminary results from an aqua planet experiment,” Geophy. Res. Lett., 32, L08805, doi:10.1029/2005GL022459, 2005.

[3] Iga, S.-I., H. Tomita, Y. Tsushima, and M. Satoh, “Climatology of a nonhydrostatic global model with explicit cloud processes,” Geophys. Res. Lett., 34, L22814, doi:10.1029/2007GL031048, 2007.

[4] Miura, H., M. Satoh, T. Nasuno, A. T. Noda, and K. Oouchi, “A Madden-Julian Oscillation event realistically simulated by a global cloud-resolving model,” Science, 318, 1763–1765, 2007.

[5] Oouchi, K., A. T. Noda, M. Satoh, H. Miura, H., Tomita, T. Nasuno, and S.-I. Iga, “A simulated preconditioning of typhoon genesis controlled by a boreal summer Madden-Julian Oscillation event in a global cloud-system-resolving model,” SOLA, 5, 65-68, doi:10.2151/sola.2009–017, 2009.

[6] Noda, A. T., K. Oouchi, M. Satoh, H. Tomita, S.-I. Iga, and Y. Tsushima, “Importance of the subgrid-scale turbulent moist process: Cloud distribution in global cloud-resolving simulations,” Atmos. Res., 96, 208–217, doi: “10.1016/j.atmosres.2009, 2010.

[7] Yamada, Y., K. Oouchi, M. Satoh, H. Tomita, and W. Yanase, “Projection of changes in tropical cyclone activity and cloud height due to greenhouse warming: Global cloud-system-resolving approach,” Geophy. Res. Lett., 37, doi:10.1029/2010GL042518, 2010.

[8] Satoh, M., H. Tomita, T. Nasuno, A. T. Noda, S.-I. Iga, H. Miura, K. Oouchi, H. Taniguchi, Y. Yamada, W. Yanase, C. Kodama, M. Hara, Y. Wakazuki, K. Yasunaga, and T. Seiki, “Study of cloud and precipitation processes using a global cloud-system resolving model,” Annual Report of the Earth Simulator Center, April 2009-March 2010, 49–53, 2010.

[9] Satoh, M., H. Tomita, T. Nasuno, A. T. Noda, S.-I. Iga, H. Miura, K. Oouchi, H. Taniguchi, Y. Yamada, W. Yanase, C. Kodama, M. Hara, Y. Wakazuki, K. Yasunaga, T. Seiki, and M. Yoshizaki, “Study of cloud and precipitation processes using a global cloud-system resolving model,” Annual Report of the Earth Simulator Center, April 2010-March 2011, 43–49, 2011.

[10] Satoh, M., H. Tomita, T. Nasuno, A. T. Noda, S.-I. Iga, H. Miura, K. Oouchi, H. Taniguchi, Y. Yamada, W. Yanase, C. Kodama, M. Hara, Y. Wakazuki, K. Yasunaga, T. Seiki, M. Yoshizaki, M. Nakano, and T. Miyakawa, “Study of cloud and precipitation processes using a global cloud resolving model,” Annual Report of the Earth Simulator Center, April 2011-March 2012, 51–58, 2012.

[11] Satoh, M., H. Tomita, T. Nasuno, A. T. Noda, S.-I. Iga, H. Miura, K. Oouchi, H. Taniguchi, Y. Yamada, W. Yanase, C. Kodama, M. Hara, Y. Wakazuki, K. Yasunaga, T. Seiki, M. Yoshizaki, M. Nakano, T.

Miyakawa, H. Yashiro, and T. Yamaura, “Study of cloud and precipitation processes using a global cloud resolving model,” Annual Report of the Earth Simulator Center, April 2012-March 2013, 47–53, 2013.

[12] Madden, R. and P. Julian, “Detection of 40-50 day oscillation in the zonal wind in the tropical Pacific,” J. Atmos. Sci., 28, 702–708, 1971.

[13] Madden, R. and P. Julian, “Description of global-scale circulation cells in the tropics with a 40-50 day period,” J. Atmos. Sci., 29, 1109–1123, 1972.

[14] Yoneyama, K., C. Zhang, and C. N. Long, “Tracking pulses of the Madden-Julian Oscillation,” Bull. Amer. Meteor. Soc., 94, 1871–1891, 2013.

[15] Hashino, T., M. Satoh, Y. Hagihara, T. Kubota, T. Matsui, T. Nasuno, and H. Okamoto, “Evaluating cloud microphysics from NICAM against CloudSat and CALIPSO,” J. Geophys. Res., 118, 7273–7292, 2013.

[16] Roh, W. and M., Satoh, “Evaluation of precipitating hydrometeor parameterizations in a single-moment bulk microphysics scheme for deep convective systems over the tropical open ocean,” J. Atmos. Sci., 71, 2654–2673, 2014.

[17] Miyakawa, T., M. Satoh, H. Miura, H. Tomita, H. Yashiro, A. T. Noda, Y. Yamada, C. Kodama, M. Kimoto, and K. Yoneyama, “Madden-Julian Oscillation prediction skill of a new-generation global model,” Nature Commun., 5, 3769, 2014.

[18] Tomita, H., “A stretched icosahedral grid by a new grid transformation,” J. Meteorol. Soc. Jpn., 86, 107–119, 2008a.

[19] Masunaga, H., T. Matsui, W.-K. Tao, A. Y. Hou, C. D. Kummerow, T. Nakajima, P. Baeur, W. S. Olson, M. Sekiguchi, and T. Y. Nakajima, “Satellite data simulator unit : a multisensor, multispectral satellite simulator package,” Bull. Amer. Meteorol. Soc., 91, 1625–1632, 2010.

[20] Tomita, H., “New microphysical schemes with five and six categories by diagnostic generation of cloud ice,” J. Meteorol. Soc. Jpn., 86, 121–142, 2008b.

[21] Matsui, T., X. Zeng, W.-K. Tao, H. Masunaga, W. S. Olson, and S. Lang, “Evaluation of long-term cloud-resolving model simulations using satellite radiance observations and multifrequency satellite simulators,” J. Atmos. Oceanic Technol., 26, 1261–1274, 2009.

全球雲解像モデルを用いた雲降水プロセス研究

課題責任者
佐藤　正樹　　海洋研究開発機　地球環境変動領域
　　東京大学　大気海洋研究所

著者
佐藤　正樹 *1,2，富田　浩文 *1,3，那須野智江 *1，野田　　暁 *1，伊賀　晋一 *3，三浦　裕亮 *1,4，
大内　和良 *1，谷口　　博 *5，山田　洋平 *1，柳瀬　　亘 *2，小玉　知央 *1，原　　政之 *1，安永　数明 *1,6，
清木　達也 *1，吉崎　正憲 *1,7，中野満寿男 *1，宮川　知己 *1，八代　　尚 *1,3，山浦　　剛 *3，
久保川陽呂鎮 *2，池田美紀子 *1，沢田　雅洋 *2，Ying-Wen Chen*1
*1 海洋研究開発機構　地球環境変動領域
*2 東京大学　大気海洋研究所
*3 理化学研究所　計算科学研究機構
*4 東京大学　理学部
*5 神戸高専　一般科（理科）
*6 富山大学　理学部
*7 立正大学　地球環境科学部

本プロジェクトは、地球上の雲降水プロセスの理解を深め、それらの気候モデルにおける扱いを改善することを目的とする。全球雲解像モデルによる数値計算を研究手法として用いる。平成 25 年度の主な成果として（1）国際集中観測プロジェクト Cooperative Indian Ocean experiment on intraseasonal variability in the year 2011 (CINDY2011) / Dynamics of the Madden-Julian Oscillation (DYNAMO) 期間のマッデン・ジュリアン振動（MJO）を対象とする 7-km 格子を用いた延長計算を行い、MJO サイクルの再現に成功した。（2）新しい雲微物理スキームの改善手法を実装して 3.5-km 格子を用いた感度実験を行い、衛星観測との比較により雲降水特性のバイアスの大幅な軽減を確認した。また、熱帯集中観測を対象とする 15 日間の予測計算を試験的に運用した。

キーワード:雲降水プロセス,全球雲解像モデル

Study on the Predictability of Climate Variations and Their Mechanisms

Project Representative

Yukio Masumoto Research Institute for Global Change, Japan Agency for Marine-Earth Science and Technology

Authors

Takeshi Doi[*1, 2], Yushi Morioka[*1], Wataru Sasaki[*2], Swadhin Behera[*1, 2], Ratnam Venkata Jayanthi[*1, 2], Chaoxia Yuan[*2], Hirofumi Sakuma[*1, 2], Sebastien Masson[*4], Antonio Navarra[*3], Silvio Gualdi[*3], Simona Masina[*3], Alessio Bellucci[*3], Annalisa Cherchi[*3], Pascal Delecluse[*5], Gurvan Madec[*4], Claire Levy[*4], Marie-Alice Foujols[*4], Arnaud Caubel[*4], Eric Maisonnave[*5], Guy Brasseur[*6], Erich Roeckner[*6], Marco Giorgetta[*6], Luis Kornblueh[*6], Monika Esch[*6], Toshio Yamagata[*2] and Yukio Masumoto[*1]

*1 Research Institute for Global Change, Japan Agency for Marine-Earth Science and Technology

*2 Application Laboratory, Japan Agency for Marine-Earth Science and Technology

*3 Centro Euro-Mediterraneo per i Cambiamenti Climatici, INGV

*4 Laboratoire D'oceanographie et du Climat (LOCEAN)

*5 Centre Européen de Recherche et de Formation Avancée en Calcul Scientifique

*6 Max Planck Institute for Meteorology

The SINTEX-Frontier coupled general circulation model version 1 (SINTEX-F1) has been developed under the EU-Japan collaborative framework to study the variability in global climate and its predictability. The seasonal prediction system on a basis of the SINTEX-F1 GCM has so far demonstrated high performance in predicting the occurrences of El Niño-Southern Oscillation (ENSO) and the Indian Ocean Dipole Mode (IOD) events in the tropics. However, it is still very challenging to predict their teleconnections and the occurrences of subtropical climate variations such as the Indian Ocean Subtropical Dipole (IOSD) and the Atlantic Ocean Subtropical Dipole (AOSD) by the SINTEX-F1 seasonal prediction system.

In order to overcome those challenges in predictions, we successfully developed a new high-resolution SINTEX-F2 model, with sea ice processes, and implemented it on the Earth Simulator. Using results from a long-term simulation of the new model, we explored three topics in this fiscal year: 1) roles of tropical SST variations on the formation of the subtropical dipoles, 2) the influence of ENSO on the equatorial Atlantic precipitation through the Walker circulation, and 3) impacts of the equatorial Atlantic sea surface temperature on the tropical Pacific. Those outcomes contribute to deepen our understanding of and to improve prediction skill of the Atlantic-Pacific teleconnection patterns and the occurrence of the subtropical climate variations.

In addition to conduct those process studies, we developed a proto-type system of the real-time seasonal climate predictions with the new SINTEX-F2. Preliminary analyses showed that the new seasonal prediction system improves the prediction skill of the subtropical dipoles, ENSO-Modoki, and the Ningaloo Niño relative to the SINTEX-F1 seasonal prediction system.

Keywords: SINTEX-F2 GCM, Seasonal Prediction, Subtropical Dipole Modes, Tropical Atlantic-Pacific Teleconnection

1. Introduction

We have been conducting seasonal predictions every month using the SINTEX-F1 seasonal prediction system on the Earth Simulator and providing a real-time outlook of seasonal to interannual climate predictions on JAMSTEC website (http://www.jamstec.go.jp/frcgc/research/d1/iod/e/seasonal/outlook.html). In this fiscal year, these real-time seasonal prediction experiments were conducted by another new project (Project representative: Swadhin K. Behera, APL/JAMSTEC; "Study on the real-time ensemble seasonal prediction system and its application") so as to focus on the process studies and model development parts under this project.

The SINTEX-F1 seasonal prediction system has demonstrated its outstanding performance of predicting El Niño-Southern Oscillation (ENSO) and the Indian Ocean Dipole Mode (IOD). In addition, Doi et al (2013) recently showed that the SINTEX-F1 prediction system is also highly skillful in predicting regional climate phenomenon known as the Ningaloo Niño/Niña off the west coast of Australia.

While the model has done extremely well to predict the

tropical climate phenomena, it is still a challenge to predict the teleconnections arising from ENSO and IOD in addition to the subtropical climate variations such as the Indian Ocean Subtropical Dipole (IOSD) and its Atlantic counterpart, the Atlantic Ocean Subtropical Dipole (AOSD). To tackle those difficulties, we had successfully developed a new high-resolution version of SINTEX-F with an embedded sea-ice model, the SINTEX-F2. Some preliminary works show that the SINTEX-F2 GCM is better in reproducing realistic mean atmosphere/ocean conditions, tropical/subtropical climate variations and extreme events, including tropical cyclones, relative to the SINTEX-F1. We are hence expecting significant contributions of the SINTEX-F2 for better understanding of finer-scale climate processes, mid-latitude climate variations, and interactions among climate modes in tropics and mid-latitude regions.

In the following sections, we introduce several important results obtained from our research activities in the fiscal year of 2013. In Section 2, three process studies with SINTEX-F2 sensitivity experiments are discussed. In Section 3, we show that preliminary results with a proto-type of new SINTEX-F2 seasonal prediction system.

2. Climate process studies with SINTEX-F2 experiments

2.1 Role of tropical SST variability on the formation of subtropical dipoles

The subtropical dipole is an interannual climate phenomenon over the mid-latitude ocean basin in the Southern Hemisphere, which accompanies in its positive phase a warmer-than-normal sea surface temperature (SST) in the southwestern part of each basin and a colder-than-normal SST in the northeastern part. The subtropical dipole develops typically during austral summer (December-February) and causes a rainfall increase in

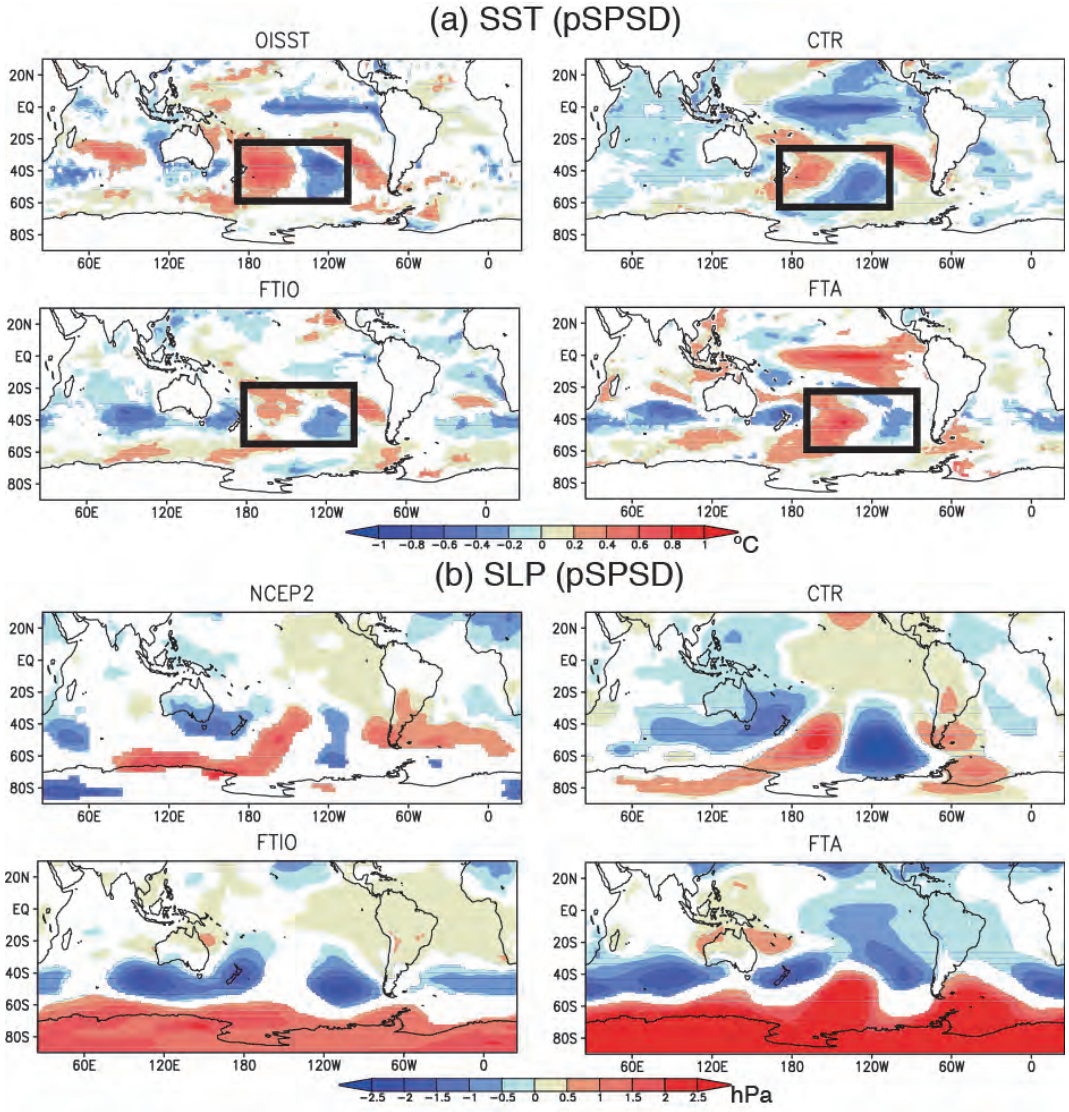

Fig. 1 (a) Composite SST anomalies (in ºC) during December-February of the positive South Pacific subtropical dipole (pSPSD). The OISST, the CGCM (CTR, FTIO, and FTA) experiments are shown. In the FTIO (FTA) experiment, the interannual SST variation in the tropical Indian (Atlantic) Ocean is suppressed. The boxes indicate positions of the dipole SST anomalies associated with the pSPSD. (b) Same as in (a), but for the sea level pressure anomalies during November-January. The NCEP Reanalysis-2 (NCEP2) is shown in the top left panel.

the southern Africa, the southeastern Brazil, and New Zealand. Since prediction of the rainfall variations are closely linked to natural disaster prevention, major crop yield management, and water resources management, detailed understanding of generation mechanisms of the subtropical dipole and improvement of their prediction skills are essential.

The generation mechanism of the subtropical dipole has been identified in our previous studies. During October-December when the subtropical dipole starts to develop, the subtropical high anomalously strengthens in its southern part. Over the northeastern part of the subtropical high, anomalously dry southeasterly wind from the high latitude enhances evaporation. This results in colder-than-normal SST, causing the surface water to mix with water underneath and hence deepening the surface mixed-layer. Although the solar radiation acts to warm the mixed-layer, its contribution becomes smaller due to the thicker-than-normal mixed-layer depth. This leads to development of the northeastern pole with the colder-than-normal mixed-layer temperature. The mechanism for the southwestern pole development is found to be a mirror image to that for the northeastern pole.

However, the variation of the subtropical high during the development of the subtropical dipole remains unclear. Previous studies suggest that ENSO in the tropics and the climate phenomenon in the higher latitudes of the Southern Hemisphere, called the Antarctic Oscillation (AAO), may contribute to the interannual variation in the subtropical high. To investigate the relative role of the lower and higher latitude climate phenomena in the formation of the subtropical dipole, we have conducted a series of experiments by using a coupled general circulation model (SINTEX-F2) that is executed on the Earth Simulator (Morioka et al. 2014[1]). In the experiment, where the interannual SST variation in each tropical basin is suppressed, the subtropical dipole occurs in association with the strengthening of the subtropical high in its southern part (see Fig. 1a for the South Pacific subtropical dipole case). The occurrence frequency and amplitude of the subtropical dipole do not significantly change compared to the case with the interannual SST variation. In addition, the variation in the subtropical high is found to be strongly related to the AAO (Fig. 1b). These results imply that even in the absence of the tropical climate phenomena, the AAO induces the variation in the subtropical high and hence the subtropical dipole.

Detailed understanding of generation mechanisms of the subtropical dipole contributes to better prediction skill of the phenomenon. Results obtained in this study suggest that accurate representations of climate phenomena in the higher latitudes of the Southern Hemisphere, as well as in the tropics, need to be included in prediction models. Since the higher latitude climate phenomena are in turn influenced by other processes such as sea-ice distribution and the ozone amount over Antarctica, it is also important to incorporate these elements appropriately in a climate model. Efforts to provide reliable prediction information to international communities by developing such a climate model are in progress.

2.2 The influence of ENSO on the equatorial Atlantic precipitation

The link between ENSO and the equatorial Atlantic precipitation during boreal spring (March–April–May) is explored using the SINTEX-F2 GCM (Sasaki et al. 2014a[2]). Simulated interannual variability of the equatorial Atlantic SST in the SINTEX-F2 is excluded by nudging the modeled SST toward the climatological monthly mean of observed SST in the equatorial Atlantic, but full air–sea coupling is allowed elsewhere. We found that the equatorial Atlantic precipitation is reduced (increased) during El Niño (La Niña) event, although the interannual variability of the equatorial Atlantic SST is disabled in the model. The precipitation anomalies in the equatorial Atlantic during ENSO are not strongly associated with the meridional migration of the Atlantic Intertropical Convergence Zone (ITCZ). We found that the reduced precipitation in the equatorial Atlantic during El Niño is due to an enhanced Atlantic Walker circulation associated with strengthened low-level easterlies and anomalous dry, downward winds over the equatorial Atlantic, while the Pacific Walker circulation is weakened. The upper-level anomalous westerlies over the equatorial Atlantic are consistent with a *Matsuno–Gill-type* response to heating in the eastern equatorial Pacific. Our results of the CGCM experiments suggest that changes to the Walker circulation induced by ENSO contribute significantly to changes in precipitation over the equatorial Atlantic (Fig. 2).

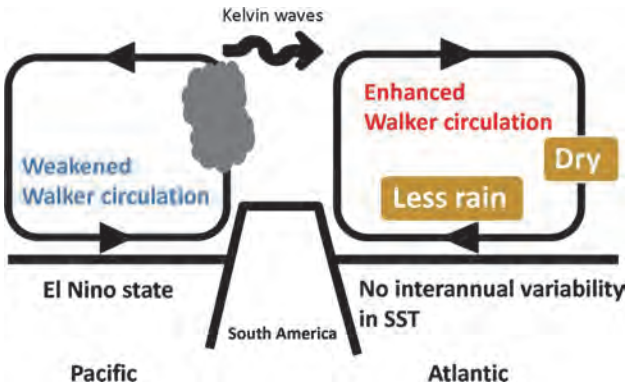

Fig. 2 Schematic diagram of the El Niño impact on the equatorial Atlantic precipitation in the SINTEX-F2 without interannual variability of the equatorial Atlantic SST (Fig. 10 in Sasaki et al. 2014a[2]).

2.3 Impact of the equatorial Atlantic SST on the tropical Pacific

Many CGCMs suffer from serious model bias in the zonal gradient of SST in the equatorial Atlantic. The bias of the equatorial Atlantic SST (EASST) may affect the interannual variability of the equatorial Atlantic, which in turn may

influence the state of the tropical Pacific. Therefore, we explore the impact of the EASST bias and the interannual variability of the EASST on the tropical Pacific by the SINTEX-F2 GCM (Sasaki et al. 2014b[3]). To determine the impact of the interannual variability of the EASST on the tropical Pacific, we compare a run in a fully coupled mode (CTL run) and a run in which the EASST is nudged toward the climatological monthly mean of the SST in the CTL run, but full air-sea coupling is allowed elsewhere (AT_m run). We found that, when the interannual variability of the EASST is excluded, the thermocline depth in the eastern equatorial Pacific is deepened, and the amplitude of the ENSO is reduced by 30% relative to the CTL run (Fig. 3).

The impact of the bias of the EASST on the tropical Pacific is investigated by comparing the AT_m run and a run in which the EASST is nudged toward the observed climatological monthly mean SST (AT_o run). It is found that, when the bias of the EASST is removed (i.e. AT_o run), the *Matsuno–Gill type* response to the warm SST anomalies in the western equatorial Atlantic induces low-level cyclonic anomalies in the eastern South Pacific, which leads to a deeper thermocline and colder SST in the South Pacific through the Ekman pumping relative to AT_m. The colder SST in the South Pacific reduces the precipitation along the South Pacific convergence zone (Fig. 4).

Our results of the model experiments demonstrate the importance of the EASST to the tropical Pacific climate.

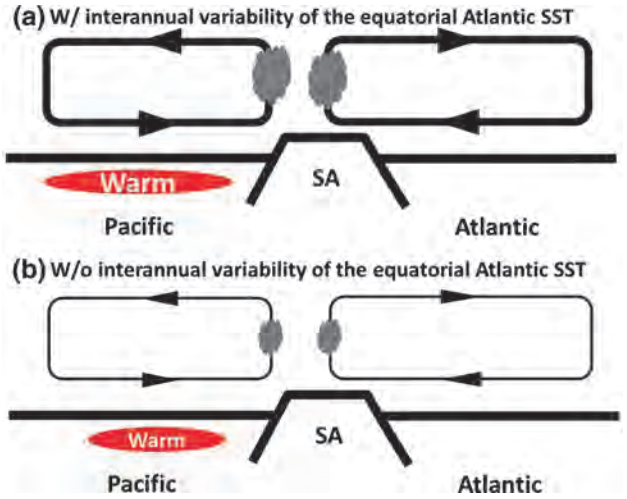

Fig. 3 Schematic diagram showing the difference in the atmosphere–ocean response to the inter-Pacific-Atlantic SST gradient caused by the presence or absence of the interannual variability in the equatorial Atlantic in the SINTEX-F2. (Fig. 13 in Sasaki et al. 2014b[3])

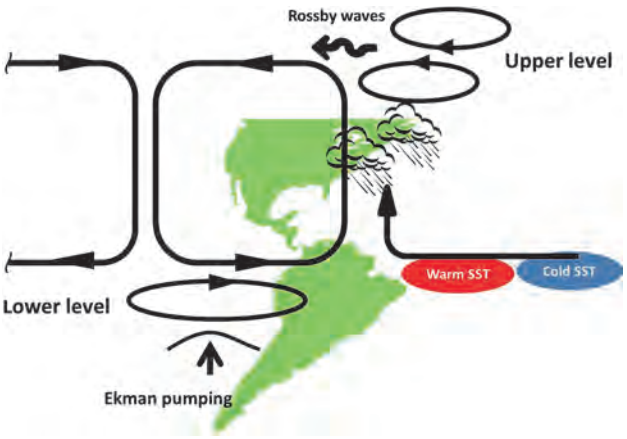

Fig. 4 Schematic diagram showing the atmosphere–ocean response when the equatorial Atlantic SST bias is reduced in the SINTEX-F2. Observed SST in the equatorial Atlantic is warmer (colder) in the west (east) compared to the SST in the CTL run of the SINTEX-F2. (Fig. 14 in Sasaki et al. 2014b[3])

3. A proto-type of new SINTEX-F2 seasonal prediction system

3.1 Differences between SINTEX-F1 and SINTEX-F2 seasonal prediction system

We developed the SINTEX-F2 GCM for better representation of several physical processes and to resolve relatively fine-scale phenomena in the ocean. Table 1 briefly summarizes major differences between the SINTEX-F1 and the new SINTEX-F2 GCMs (there are also some differences in numerical schemes and parameterizations). Owing to these differences, model biases in climatological fields are much reduced in SINTEX-F2 compared with those in SINTEX-F1, particularly in mid-latitudes. As a next step, we have been trying to develop a new seasonal prediction system on the basis of SINTEX-F2. In this fiscal year, we successfully developed a proto-type of the new SINTEX-F2 seasonal prediction system and similar to the SINTEX-F1 system, a SST-nudging coupled initialization scheme is adopted. 6 ensemble members with 6-month lead are now available for the SINTEX-F2 seasonal prediction experiments (Table 2).

Table 1 Main differences between SINTEX-F1 and SINTEX-F2

	AGCM	OGCM	Coupling	Sea Ice
SINTEX-F1	ECHAM4.6 T106L19	OPA8.2 2×2 L31	Every 2 hour No flux correction	No
SINTEX-F2	ECHAM5 T106L31	OPA9 0.5×0.5 L31	Same as F1	Yes

Table 2 A proto-type of seasonal prediction system with SINTEX-F1 and F2

	Initialization	Ensemble size	Lead time	Period
SINTEX-F1	SST-nudging, every month	9~27	1~2yr	1982~
SINTEX-F2	Same as F1	6	6mo	2000~

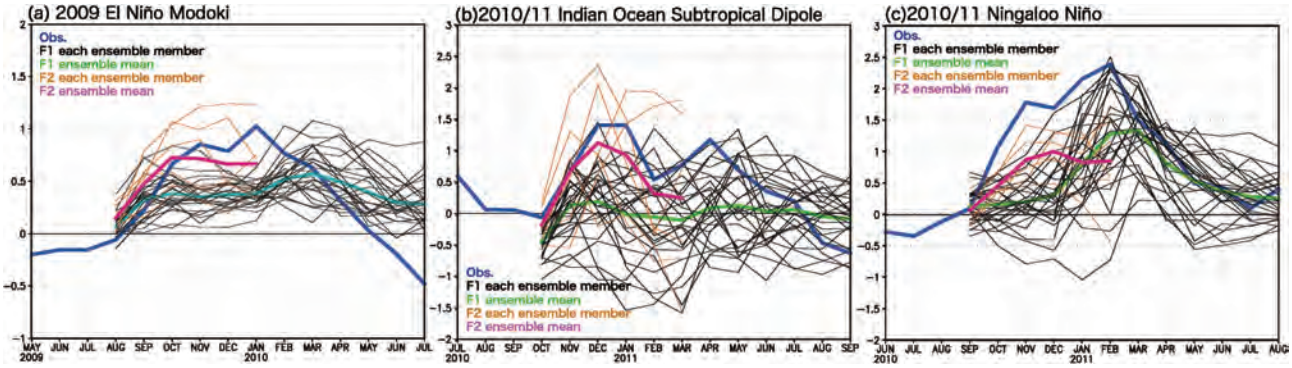

Fig. 5 (a) Monthly El Nino Modoki Index in 2009, defines as SST anomaly in 165°E-140°W, 10°S-10°N minus the half of SST anomaly in 110°W-70°W, 15°S-5°N minus the half of SST in 125°E-145°E, 10°S-20°N. (b) Monthly Indian Ocean Subtropical Dipole Index in 2010/11, defined as SST anomaly in 55ºE-65ºE, 37ºS-27ºS minus SST anomaly in 90ºE-100ºE, 28ºS-18ºS. (c) Monthly Ningaloo Niño Index in 2010/11, defined as SST anomaly in 108º-116ºE, 28º-22ºS.

3.2 Preliminary results with the SINTEX-F2 seasonal prediction system

The preliminary results from the SINTEX-F2 seasonal prediction experiments are shown in Fig. 5. The predicted indices are the ENSO-Modoki, IOSD, and the Ningaloo Niño. It is noted that the SINTEX-F2 system has better skill to predict 2009 El Nino-Modoki and 2010/11 IOSD (Figs. 5a and b). This might be due to the better simulation of the mean state in the mid-latitude and interactions between the tropics and subtropics in the SINTEX-F2 CGCM. Fig. 5c shows the prediction of a newly identified regional climate phenomena off the west coast of Australia, the Ningaloo Niño. The early development stage of the 2010/11 Ningaloo Niño was better predicted by the SINTEX-F2 system relative to the SINTEX-F1 system. This might be due to the high-resolution of the ocean component of the SINTEX-F2 that better resolves the coastally trapped ocean current such as the Leeuwin Current, and its local air-sea feedback - key to develop the Ningaloo Niño. Further analysis is necessary for deep understanding why the SINTEX-F2 successfully improved their prediction skills relative to the SINTEX-F1.

Acknowledgement

We appreciate the support extended by the Earth Simulator in achieving our project goals. Also, we are grateful to Dr. Jing-Jia Luo, Dr. Sebastien Masson and our European colleagues of INGV/CMCC and L'OCEAN for their contribution to developing the prototype of the prediction model.

References

[1] Y. Morioka, S. Masson, P. Terray, C. Prodhomme, S. K. Behera, and Y. Masumoto, 2014: Role of tropical SST variability on the formation of subtropical dipoles, J. Climate, DOI: 10.1175/JCLI-D-13-00506.1, in press.

[2] W.Sasaki, T. Doi, K. J. Richards, and Y. Masumoto, 2014a: The influence of ENSO on the equatorial Atlantic precipitation through the Walker circulation in a CGCM. Clim. Dyn., DOI: 10.1007/s00382-014-2133-5.

[3] W.Sasaki, T. Doi, K. J. Richards, and Y. Masumoto, 2014b: Impact of the equatorial Atlantic sea surface temperature on the tropical Pacific in a CGCM. Clim. Dyn., DOI: 10.1007/s00382-014-2072-1.

Published news articles

(1) The Hindu, Business Line, May 31, 2013
http://www.thehindubusinessline.com/industry-and-economy/agri-biz/japanese-climate-body-waves-red-says-monsoon-could-be-below-normal/article4769747.ece?homepage=true

(2) Oryza, May 31, 2013
http://www.oryza.com/content/japan-weather-agency-predicts-below-normal-2013-monsoon-rains-india

(3) The Wall Street Journal, India, May 29, 2013
http://blogs.wsj.com/indiarealtime/2013/06/05/india-monsoon-cheer-may-fade-in-july/

(4) WeatherZone, Forum, "ENSO discussion 2013"
http://forum.weatherzone.com.au/ubbthreads.php/topics/1152950/15/ENSO_Discussion_2013

(5) Green Media, June 4 2013
http://cmsenvis.cmsindia.org/newsletter/enews/NewsDetails.asp?id=46086

大気海洋結合モデルを用いた短期気候変動のプロセス研究とその季節予測可能性研究

課題責任者
升本　順夫　　海洋研究開発機構　地球環境変動領域

著者
土井　威志 *1, 2，森岡　優志 *1，佐々木　亘 *2，スワディン ベヘラ *1, 2，Ratnam Venkata Jayanthi*1, 2，Chaoxia Yuan*2，佐久間弘文 *1, 2，Sebastien Masson*4，Antonio Navarra*3，Silvio Gualdi*3，Simona Masina*3，Alessio Bellucci*3，Annalisa Cherchi*3，Pascal Delecluse*5，Gurvan Madec*4，Claire Levy*4，Marie-Alice Foujols*4，Arnaud Caubel*4，Eric Maisonnave*5，Guy Brasseur*6，Erich Roeckner*6，Marco Giorgetta*6，Luis Kornblueh*6，Monika Esch*6，山形　俊男 *2，升本　順夫 *1

∗1　海洋研究開発機構　地球環境変動領域

∗2　海洋研究開発機構　アプリケーションラボ

∗3　Centro Euro-Mediterraneo per i Cambiamenti Climatici, INGV

∗4　Laboratoire D’oceanographie et du Climat (LOCEAN)

∗5　Centre Européen de Recherche et de Formation Avancée en Calcul Scientifique

∗6　Max Planck Institute for Meteorology

数ヶ月から数年スケールで発生する気候変動の理解ならびにその予測可能性研究のため、SINTEX-F 大気海洋結合大循環モデルを日欧研究協力に基づき開発および改良してきた。その第一版である SINTEX-F1 は、リアルタイムの季節・経年変動予測実験に長く用いられており、近年発生したインド洋ダイポールモードやエルニーニョ・南方振動（ENSO）現象のほとんどを現実的に予測している。今年度は、このリアルタイム季節・経年変動予測実験の計算は新規課題（課題責任者 : JAMSTEC/APL スワディヒン・ベヘラ）で行うこととし、本課題では更なる気候変動プロセスの研究と、高度化させた第二版 SINTEX-F2 の開発を中心に実施した。

従来の SINTEX-F1 では、特に中緯度の気候変動現象である亜熱帯ダイポールモード現象の予測や、熱帯海盆を跨いだ気候変動現象同士の相互作用の予測に問題があった。そこで、新しく開発に成功した SINTEX-F2 を用いて、1）亜熱帯ダイポールモード現象の発生プロセスに熱帯域の気候変動がどの程度重要なのか、2）太平洋の ENSO 現象はどのように大西洋の気候変動現象に影響を与えるのか、3）大西洋の気候変動現象やモデルバイアスが太平洋の気候にどの程度影響を与えるのか、を調べた。その結果、1）亜熱帯ダイポールモード現象は ENSO などの熱帯域の現象が無くても発生しうること、2）大気のウォーカー循環を通じて ENSO が大西洋上の降水過程に影響を及ぼしていること、3）大西洋の海面水温バイアスは松野 – ギルパターンの形成を通じて太平洋の風系と海洋表層の変動をもたらしていることが明らかになった。これらの成果は国際誌で発表され、世界の気候変動研究を先導するモデルとして SINTEX-F の地位を確立する礎となっている。

更に新しい高度化モデル SINTEX-F2 を用いたアンサンブル気候予測実験のプロトタイプを開発した。この SINTEX-F2 予測システムでは、近年頻発してきたエルニーニョモドキ現象や、亜熱帯に現れるインド洋亜熱帯ダイポール現象、オーストラリア西岸に現れる地域気候変動現象であるニンガルーニーニョ現象等の予測精度が向上していることが確認できた。SINTEX-F2 での高解像度化や海氷モデルの導入により、中緯度域や海洋の比較的小さな現象の再現性が SINTEX-F1 より向上していることが主な原因と考えられる。

キーワード:SINTEX-F2, 新季節予測システム , 亜熱帯ダイポールモード , 熱帯太平洋 – 大西洋テレコネクション

Simulation and Verification of Tropical Deep Convective Clouds using Eddy-Permitting Regional Atmospheric Models III

Project Representative

Kozo Nakamura Research Institute for Global Change, Japan Agency for Marine-Earth Science and Technology

Authors

Kozo Nakamura[*1], Masayuki Hara[*1], Akira T. Noda[*1], Hirofumi Tomita[*2, 1], Seiya Nishizawa [*2], Hisashi Yashiro[*2] and Yasutaka Wakazuki[*3, 1]

*1 Research Institute for Global Change, Japan Agency for Marine-Earth Science and Technology

*2 Advanced Institute for Computational Science, RIKEN

*3 College of Geoscience, School of Life and Environmental Sciences, University of Tsukuba

The objective of this project is to develop an eddy-permitting regional atmospheric model, which can simulate turbulent motion with deep moist convection. We develop a regional model called diamond NICAM, whose simulation domain consists of one diamond (two triangles in an icosahedron for the whole globe). In this fiscal year, we performed a series of one-month simulations to validate the regional NICAM. The diurnal cycle of the simulation by the diamond NICAM shows same characteristics as the one of the original global NICAM and other simulations. We also performed large-eddy simulation of stratocumulus clouds in order to determine the responses of typical marine stratocumulus cloud to perturbed boundary layer states. The results show that the most important factors controlling the boundary layer cloud behavior are the amplitude of gaps in vapor and temperature across a boundary layer top.

Keywords: LES, regional atmospheric model, NICAM, cloud resolving model, boundary layer clouds

1. Introduction

Deep convection in tropics is one of the most important heat sources for the planetary-scale atmospheric circulation. Although the convection system occurs in synchronization with a diurnal cycle, the diurnal cycle, i.e., intensity and space distribution of deep convection, is not well simulated in most of GCMs. Therefore, it is an important task to understand the dynamical aspects of such deep convective systems in relation with the diurnal cycle and local circulation. The purpose of this project is as follows;

- to develop an eddy-permitting regional atmospheric model, which can simulate turbulent motion with deep moist convection, by the use of a grid resolution on the order of a hundred meters, in order to represent explicitly the cloud-scale processes,
- to perform several Large-Eddy Simulation (LES)s for tropical convection using this model, and to improve the model by comparing the results with observation and performing some sensitivity studies, and
- to investigate the generation and maintenance mechanism of convective systems based on the simulated data, which can be fundamental for improving cumulus parameterization schemes used in larger-scale atmospheric models including GCMs.

In order to develop the eddy-permitting regional atmospheric model efficiently, we adopted a model using similar dynamical and physical frameworks to those of a global cloud-resolving model called NICAM (Nonhydrostatic ICosahedral Atmospheric Model, Satoh et al., 2008[1]). Based on NICAM, we have developed two kinds of models. One is a regional model called a diamond NICAM, whose simulation domain consists of one diamond (two triangles in an icosahedron), although the original NICAM global domain consists of ten diamonds (twenty triangles). The results of some test experiments are shown in section 2. Although the diamond NICAM can be used for a very small region, because the model is based on a spherical-coordinate it cannot be used for the case of cyclic boundary conditions, which is often adopted in small-scale numerical simulation study for convection. Therefore, another model called a plain-coordinate NICAM is also developed which can be used for the case of cyclic boundary conditions. Some results of simulating boundary layer clouds relating to such boundary conditions are shown in section 3.

2. Diamond NICAM for regional climate simulations

This regional atmospheric model is developed for conducting realistic regional climate simulations, targeted onto a certain limited area. Stretched horizontal grid version of a regional model based on the global cloud-resolving model, NICAM, had developed and used by Tomita (2008) [2] and Satoh et al. (2010) [3]. In these simulations, inhomogeneity of horizontal grid sizes causes inconsistency of physical parameterizations such as cumulus convection. The simulation domain of the newly developed regional model (hereafter diamond NICAM) consists of one diamond (two triangles in an icosahedron), although the original NICAM global domain consists of ten diamonds (twenty triangles). We modified the original NICAM to enable the limited area simulation with minimum modification of source code.

In this fiscal year, we performed a series of one-month simulations to validate the regional NICAM. We performed three numerical simulations, i.e., (1) stretched grid global simulation without nudging, (2) stretched grid global simulation with nudging, and (3) diamond NICAM simulation. The initial and nudging data used are the simulation results of Glevel-9 global NICAM performed in Yamada et al. 2010 [4].

Figure 1 shows domains of numerical simulations. Figure 1(a) is grid location for stretched grid global simulation (simulations 1 and 2) as one of the control experiments. Figure 1(b) shows grid location of numerical simulation by diamond NICAM (simulation 3). Duration of the simulations is from 00Z 2 June 2004 to 00Z 1 July 2004. We validate the simulations with global Glevel-9 NICAM simulation (Yamada et al., 2010)[4]. Difference of the experiment setting between (simulation 2) and (simulation 3) is only numerical domain. The results of (simulation 2) and (simulation 3) should be same if the diamond NICAM works correctly.

Figure 2 shows one-month averaged 6-hourly precipitation for each simulation. The figure shows the simulated diurnal cycle of precipitation over a large island. i.e., the precipitation is weak from 06 to 17 LST over the island, and in the nighttime, the maximum appears over the northwestern ocean and the band from northeast to south west of the island along the mountain ranges. This diurnal cycle of precipitation well agrees to the one observed, which is not well simulated by a usual global model with coarse grid interval (Hara et al. 2009)[5]. The diurnal cycle of the simulation by the diamond NICAM in (d) shows same characteristics as the one of the original global NICAM and other simulations.

3. Large-eddy simulations of stratocumulus cloud

Marine stratocumulus clouds are one of the most important climatic elements, especially with respect to their influence on the Earth's radiative budget through their high solar albedo and significant coverage. Consequently, a realistic representation of stratocumulus clouds in global climate models (GCMs) is required for an accurate prediction of future climate change. However, at present, such boundary-layer (BL) clouds are poorly represented in GCMs and their low-accuracy prediction prevents a better understanding of future climate change. The reason for this difficulty arises not only from the complexity associated with modeling BL processes, but also from model biases, such as in the predicted thermodynamic and dynamic structure in and around the BL used to generate clouds within their BL scheme. It remains unclear which of these biases within the large-scale conditions are crucial to the accurate reproduction of BL clouds. To develop a better understanding of the effects of variations in the simulated large-scale conditions, we use large-eddy simulations to evaluate the effects of the fluctuation based on the latest GCM ensemble data on the prediction of a Californian stratocumulus under perturbed environments.

The case chosen was initially conducted in the DYCOMS-II model intercomparison study (Ackerman et al., 2009[6]; herein, A09). The horizontal and vertical grid lengths were 50 and 5 m, respectively, following A09. The domain size was 6.5 × 6.5 km^2 horizontally, and 1.5 km vertically. In this study, the setting of the control experiment (herein, CTL) from the A09 was modified in two aspects. First, for simplicity, the wind velocity at the initial state was modified to (u, v) = (8.0 m s^{-1}, 0 m s^{-1}) over the domain to examine the sensitivity of wind and the associated vertical shear. The wind velocity of 8.0 m s^{-1} corresponds to the approximate average of the initial wind

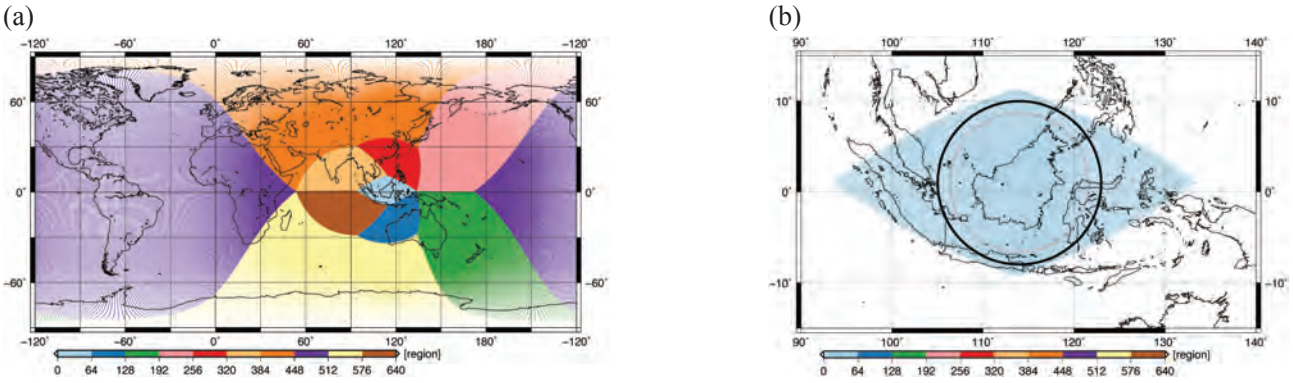

Fig. 1 Domains of numerical simulations of (a) grid location of stretched grid global NICAM, and (b) grid location of diamond NICAM.

velocity in A09. The geostrophic wind was set to 8.0 m s^{-1} over the entire domain during the simulation with a Coriolis parameter of 7.62 × 10^{-5} s^{-1} (A09). Second, the surface fluxes were computed based on Monin–Obukhov's similarity theory (Kondo, 1975)[7] to examine cloud behavior under different stability conditions near the surface. In addition, the definition of the height of the BL top, z_i, was modified from that in A09 to the average of heights where the vertical gap in the total water mixing ratio, $q_t=q_v+q_l$, was at a maximum in each column.

To determine the extent of any differences caused by the slight modification of CTL from A09, we also conducted an experiment that followed A09 for reference (herein, ORG). We examined the responses of simulated clouds by assigning possible errors in GCMs to each factor of the BL states. We

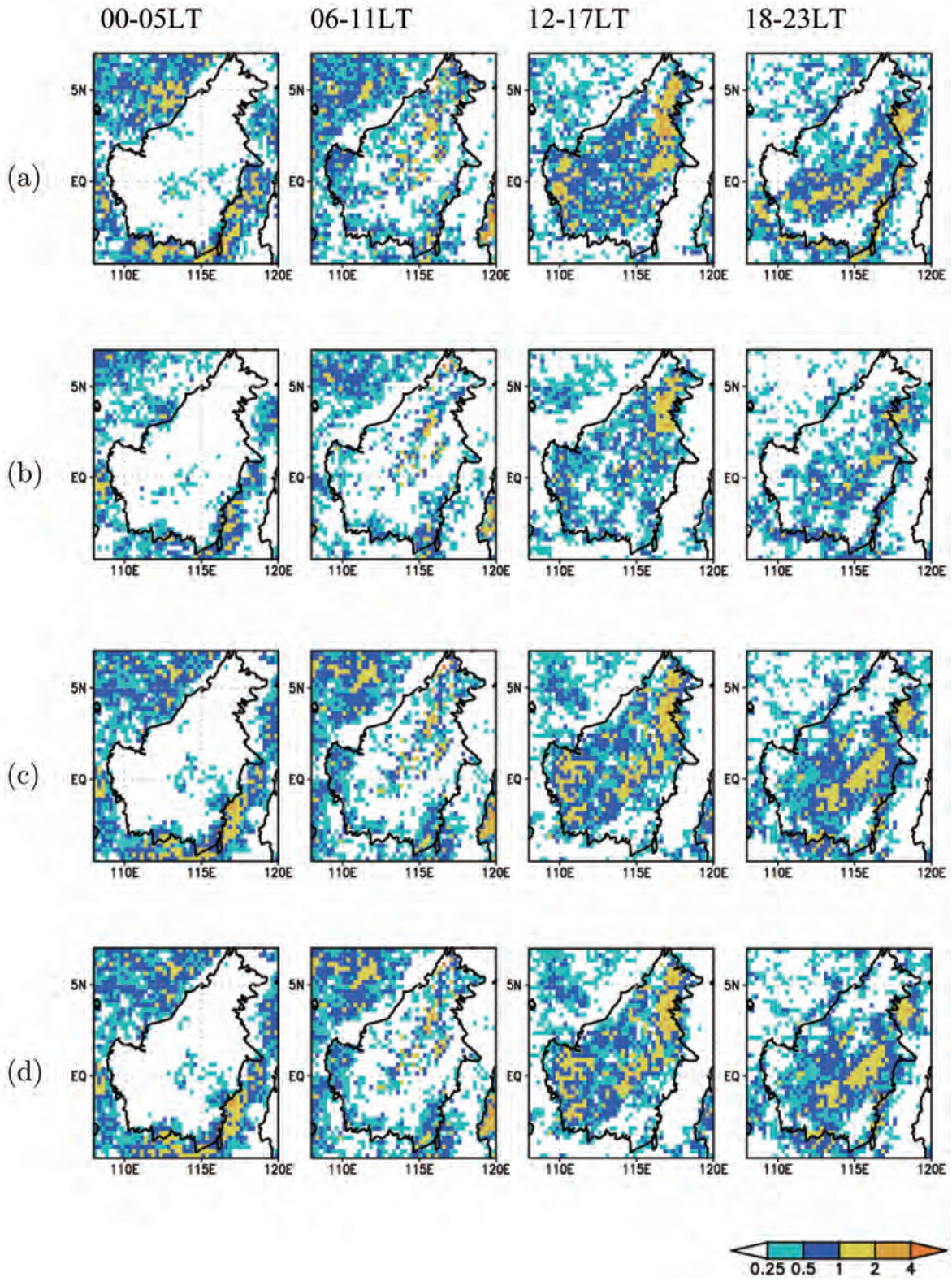

Fig. 2 One-month averaged diurnal cycle of precipitation by (a) global NICAM simulation, (b) stretched grid global simulation without nudging, (c) stretched grid global simulation with nudging, and (d) diamond NICAM simulation. From left to right 00-05LT, 06-11LT, 12-17LT, 18-23LT.

first considered six factors as possible major elements affecting the behavior of stratocumulus cloud: gaps in vapor and in temperature across z_i, the strength of wind velocity (and its vertical shear near z_i), the strength of subsidence, and surface sensible and latent heat fluxes (SHF and LHF, respectively). For these experiments, we examined cases in which low-resolution models, including GCMs, predict each component with a 20% bias. This threshold was selected based on the variance of the large-scale environment over regions of Californian (USA) stratocumulus clouds in the current GCMs within the present climate simulations of CMIP5 (Coupled Model Intercomparison Project Phase 5). Time integration was performed for six hours for these experiments, and averages for the last two hours were analyzed.

Figure 3 compares the liquid water path (LWP) in CTL with the sensitivity experiments. First, we will consider the difference between CTL and ORG. The LWP in CTL shows the result similar to that in ORG, although the former is smaller by ~3% compared with ORG. A possible major reason for this slight difference is increased entrainment of overlying dry air in CTL during an earlier stage of the simulation. In fact, z_i in CTL is slightly higher than that in ORG (not shown). Thus, we conclude that the slight modification of CTL from ORG does not cause significant issues in the behavior of the typical stratocumulus cloud (DYCOMS-II).

Comparing CTL with the other experiments, there are two major factors that change LWP: gaps in vapor and temperature across z_i. For the temperature gap, the result is consistent with previous findings that the temperature stratification of the lower atmosphere strongly controls BL clouds (Wood and Bretherton, 2006)[8]. In addition, our results indicate that, in predicting LWP, the error of the gap in vapor in the GCMs causes a greater error than the gap in temperature, if the predicted percentages of both errors are similar.

The importance of the other factors investigated was of a similar magnitude in all cases, but this was less than the impact of the vapor and temperature gaps across z_i. For the strength of wind velocity, a stronger (weaker) initial wind velocity leads to more (fewer) LWP. The magnitude of the LWP change is more pronounced when wind velocity is increased. The decrease (increase) of the subsidence strength results in the increase (decrease) of LWP. Changes in LHF and SHF also affect the prediction of LWP. LWP increases when SHF increases. The decrease in SHF does not alter LWP greatly in this case. The decrease (increase) in LHF results in the increase (decrease) of LWP.

The results indicate the relative importance of each component, and the most important factors controlling cloud behavior are the amplitude of jumps in vapor and temperature across a BL top. The given variations in wind velocity and its vertical shear, large-scale subsidence, and surface heat fluxes have a lesser effect. This suggests that to reduce model biases predicted in GCMs, greater attention should be paid to the stratification structure across the BL top. The details of this study are written in Noda et al (2014)[9].

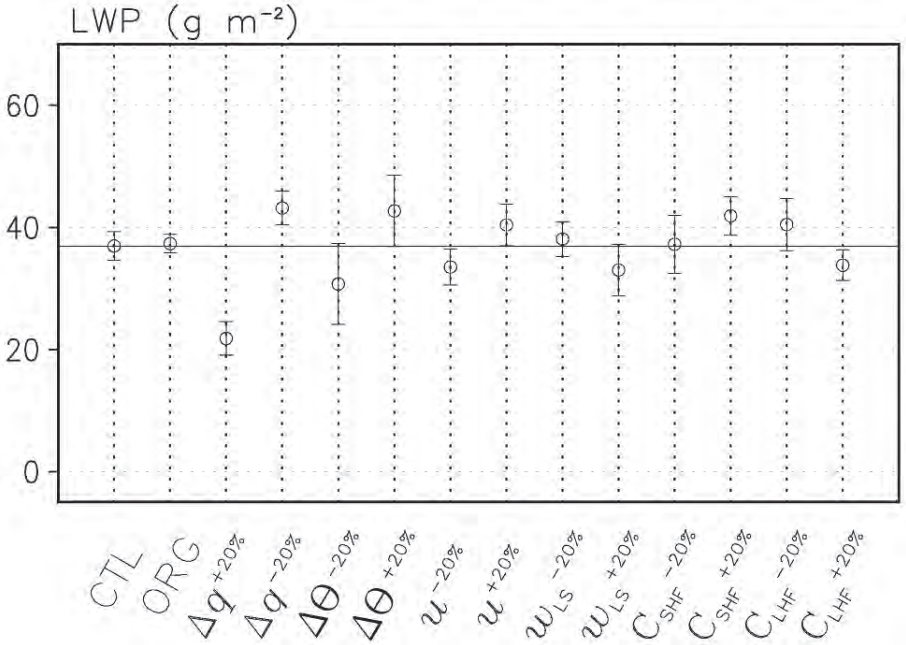

Fig. 3 LWP (g m^{-2}) averaged over the last two hours of the simulations. Error bars are computed using data collected at intervals of 60 s during this period. CTL, ORG, Δq, $\Delta\theta$, u, w_{LS}, C_{SHF}, C_{LHF} mean the control experiment, the experiment following the setting in Ackerman et al. (2009), experiments changing vapor and liquid water potential temperature across inversion, BL mean wind velocity, subsidence, sensible and latent heat fluxes from the surface. Subscripts of "+20%" ("-20%") mean the results in which each quantity is increased (decreased) by 20%. The horizontal line shows the value of CTL.

References

[1] Satoh, M., T. Matsuno, H. Tomita, H. Miura, T. Nasuno, and S. Iga, Nonhydrostatic icosahedral atmospheric model (NICAM) for global cloud resolving simulations, 2008; Journal of Computational Physics, 227, 3486-3514, DOI: 10.1016/jjcp.2007.02.006.

[2] Tomita, H., 2008: A stretched icosahedral grid by a new grid transformation. J. Meteor. Soc. Japan, 86A, 107-119.

[3] Satoh, M., T. Inoue, and H. Miura, 2010: Evaluations of cloud properties of global and local cloud system resolving models using CALIIPSO/CloudSat simulators, J. Geophys. Res., 115, D00H14, doi:10.1029/2009JD012247.

[4] Yamada, Y., K. Oouchi, M. Satoh, H. Tomita, and W. Yanase, 2010: Projection of changes in tropical cyclone activity and cloud height due to greenhouse warming: Global cloud-system-resolving approach, Geophys. Res. Lett., 37, L07709, DOI:10.1029/2010GL042518.

[5] Hara, Masayuki, T. Yoshikane, H. G. Takahashi, F. Kimura, A. Noda, and T. Tokioka, 2009: Assessment of the Diurnal Cycle of Precipitation over the maritime Continent Simulated by a 20km Mesh GCM Using TRMM PR Data. J. Meteor. Soc. Japan, 87A, 413-424.

[6] Ackerman, A. S., M. C. Vanzanten, B. Stevens, V. Savic-Jovcic, C. S. Bretherton, A. Chlond, J. C. Golaz, H. L. Jiang, M. Khairoutdinov, S. K. Krueger, D. C. Lewellen, A. Lock, C. H. Moeng, K. Nakamura, M. D. Petters, J. R. Snider, S. Weinbrecht, and M. Zulauf, 2009: Large-Eddy Simulations of a Drizzling, Stratocumulus-Topped Marine Boundary Layer. Mon. Wea. Rev., 137, 1083-1110, DOI: 10.1175/2008MWR2582.1.

[7] Kondo, J., 1975: Air-sea bulk transfer coefficients in diabatic conditions, Bound.-Layer Meteor., 9, 91–112.

[8] Wood, R. and C. Bretherton, 2006: On the relationship between stratiform low cloud cover and lower-tropospheric stability, J. Climate, 19, 6425–6432.

[9] Noda, A. T., K. Nakamura, T. Iwasaki, and M. Satoh, 2014: Responses of subtropical marine stratocumulus cloud to perturbed lower atmospheres. SOLA, 10, 34-38.

渦解像可能な領域大気モデルを用いた深い対流のシミュレーションとその検証（その３）

課題責任者
中村　晃三　　海洋研究開発機構　地球環境変動領域

著者
中村　晃三 *1，原　　政之 *1，野田　　暁 *1，富田　浩文 *2, 1，西澤　誠也 *2，矢代　　尚 *2，
若月　泰孝 *3, 1

*1 海洋研究開発機構　地球環境変動領域
*2 理化学研究所　計算科学研究機構
*3 筑波大学　生命環境学群地球学類

本プロジェクトの目的は、十分に細かい格子を用い、深い湿潤対流を解像できるモデルを開発することである。効率的な開発のため、全球雲解像モデル（NICAM、Nonhydrostatic ICosahedral Atmospheric Model）と共通の力学／物理フレームワークを用いた２つの NICAM モデルを開発した。領域版 NICAM は全球版 NICAM の一部を用いるもので、今年度は、その有効性の確認のため１か月再現実験を行った。領域版 NICAM によって再現された日変化の様子は、全球 NICAM などの結果とよく一致した。一方、周期境界条件のケースとして、境界層にできる雲の外部条件の変動に対する応答を調べた。その結果、境界層雲の振る舞いには、境界層上部の温度と湿度のジャンプが大きな影響を持つことがわかった。

キーワード:LES, 領域大気モデル, NICAM, 雲解像モデル, 境界層雲

Estimated State of Ocean for Climate Research by Using a 4 Dimensional Variatinal Approach (ESTOC)

Project Representative
Shuhei Masuda Research Institute for Global Change, Japan Agency for Marine-Earth Science and Technology

Authors
Shuhei Masuda[*1], Nozomi Sugiura[*1], Satoshi Osafune[*1] and Toshimasa Doi[*1]
*1 Research Institute for Global Change, Japan Agency for Marine-Earth Science and Technology

A 4-dimensional variational data assimilation system has been used to better define the 53-year global ocean state estimation for climate research. The synthesis of available observations and general circulation model with a pelagic ecosystem model based on nitrogen cycle yields a dynamically self-consistent dataset. Obtained ocean state estimation possibly has greater information than do models or data alone. We here present the properties of the analysis fields and some results of climate study by using this state estimation named ESTOC. This report implies that our synthesis scheme as a dynamical interpolation for sparse observations including bio-geochemical parameters is possibly promising and useful for climate researches.

Keywords: Ocean, Data assimilation, Hydrological cycle

1. Introduction

Ocean state estimation is a coherent picture of the global ocean circulation by synthesizing data from observational tools of a very wide diversity of type and is usually capable of being used for global-scale energy, heat, and water cycle budgets (*Wunsch and Heimbach, 2013*)[1]

It is getting widely recognized that dynamical state estimation is a promising tool for ocean climate change research (*e.g., Masuda et al., 2010*)[2].

In this study, we have conducted a global ocean synthesis on the basis of available ocean observations, satellite data and a global circulation model through a 4-dimensional variational (4D-VAR) data assimilation to obtain a comprehensive 4-dimensional integrated dataset. The dataset includes an estimate of the global biogeochemical variables toward an Integrated Earth System Analyses (*Rienecker et al., 2010*)[3].

2. Model

The background dynamical ocean state is derived from ocean data assimilation system, based on ocean general circulation model (OGCM); version 3 of the GFDL Modular Ocean Model (MOM) (*Pacanowski and Griffies, 1999*)[4] with major physical parameter values determined through a variational optimization procedure (*Menemenlis et al., 2005*)[5]. The horizontal resolution is 1 degree in both latitude and longitude, and there are 46 vertical levels for the global ocean basin.

Biogeochemical model we used is a NPDZC-model. This model is the pelagic ecosystem model based on nitrogen cycle and is optimized for the Earth Simulator. Our system is summarized in Fig. 1.

3. Optimization

In our 4D-VAR approach, optimized 4-dimensional analysis fields are sought by minimizing a cost function on the basis of adjoint method for physical parameters (*e.g., Sasaki 1970*)[6] and Green's function approach (*Menemenlis et al., 2005*)[5] for biogeochemical ones. The assimilated elements are temperature and salinity based on EN3 dataset provided by Met Office Hadley Centre, sea surface height anomaly form AVISO, nitrate from WOA05, and chlorophyll-a from WOA98 and SeaWiFS. We carried out a data synthesis experiment on the Earth Simulator, which covers 53-year period for 1957-2009.

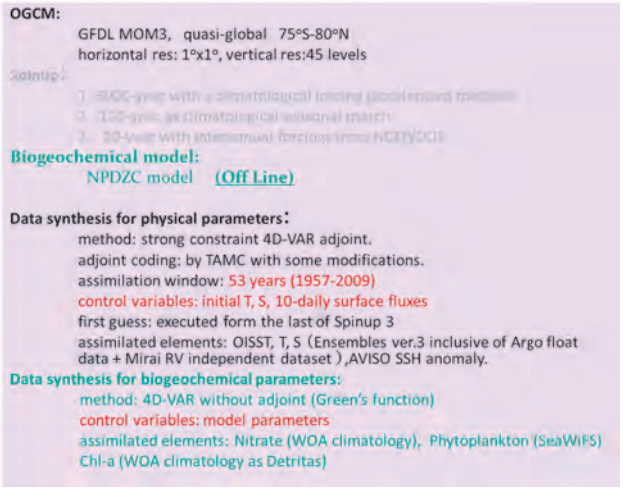

Fig. 1 Overview of the ocean data synthesis system.

4. Results

The obtained synthesis results were compared with Grid Point Value of the Monthly Objective Analysis using the Argo data (MOAA GPV) (WOCE Hydrographic Program) (*Hosoda et al., 2008*)[7]. Figures 2 show the distribution of temperature and salinity at 1000-m depth. These panels illustrate the synoptic patterns in ESTOC are by and large consistent with observations.

Figure 3 shows salinity anomaly for 2003-2007 above 100-m depth. It is implied that positive (negative) anomalies tend to appear in the high (low) salinity regions. This result is in basic agreement with *Hosoda et al*., (*2009*)[8]. Some positive anomalies are caused by change in the surface fresh water flux (not shown), which support the hydrological cycle intensification hypothesis made by *Hosoda et al*., (*2009*)[8].

5. Concluding Remarks

Our ocean data synthesis system is a powerful tool to better understand ocean climate change and will possibly contribute to the resolution of scientific issues, for instance, on global hydrological cycle in conjunction with global warming. This report implies that further work along these lines may enable us to obtain new scientific findings and also identify the optimal requirements for measurement instruments to be deployed in the future.

Acknowledgement

We thank Dr. Y. Ishikawa and Dr. K. Fukuda for construction of data service system for ESTOC.

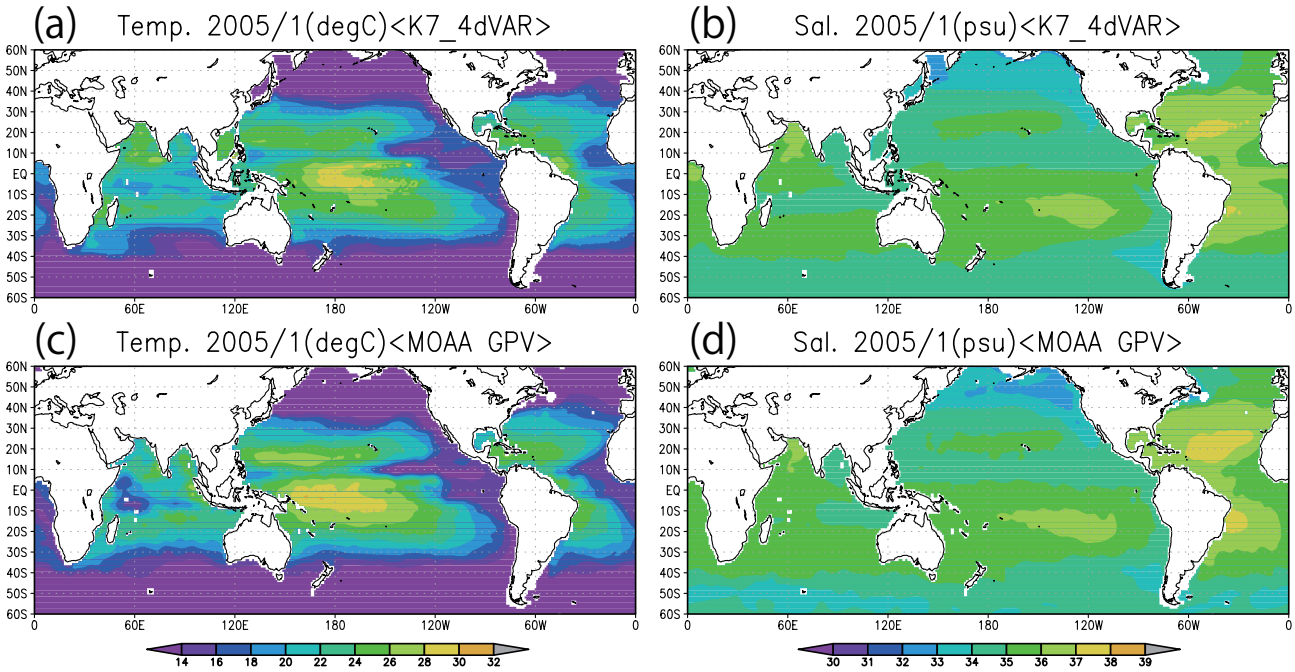

Fig. 2 (a), (b) Temperature and salinity distribution at the depth of 1000 m in ESTOC. (c), (d) The same as (a) and (b) but for MOAA GPV.

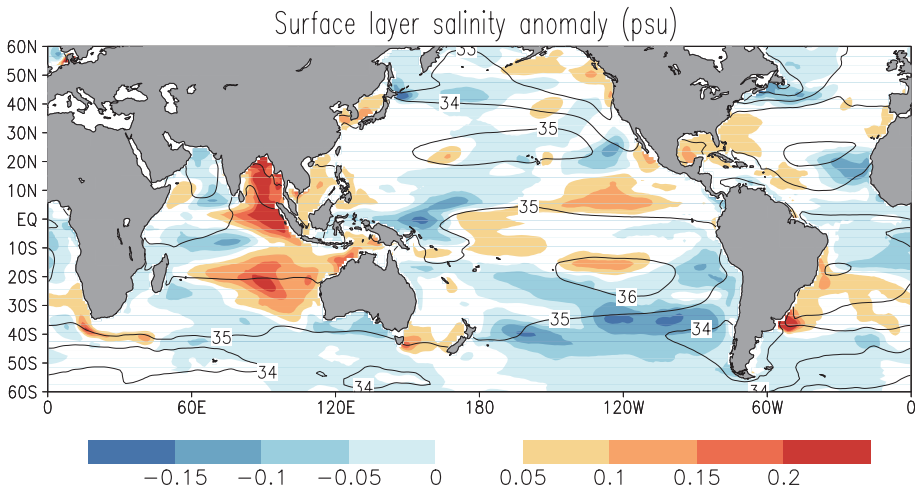

Fig. 3 Surface-layer salinity anomaly (color shade) with climatological salinity (contour).

References

[1] Wunsch, C. and P. Heimbach, "Dynamically and kinematically consistent global ocean circulation and ice state estimates," in *Ocean Circulation and Climate 2nd Edition*, Siedler et al., Eds, 2013.

[2] Masuda, S., T. Awaji, N. Sugiura, J. P.Matthews, T. Toyoda, Y. Kawai, T. Doi, S. Kouketsu, H. Igarashi, K. Katsumata, H. Uchida, T. Kawano, and M. Fukasawa, Simulated Rapid Warming of Abyssal North Pacific Waters, *Science*, 329, 319-322, DOI: 10.1126/science.1188703, 2010.

[3] Rienecker, M., T. Awaji, M. Balmaseda, B. Barnier, D. Behringer, M. Bell, M. Bourassa, P. Brasseur: L.-A. Brevik, and J. Carton, "Synthesis and Assimilation Systems - Essential Adjuncts to the Global Ocean Observing System" in *Proceedings of OceanObs'09: Sustained Ocean Observations and Information for Society (Vol. 1)*, Venice, Italy, 21-25, 2010.

[4] Pacanowski, R. C. and S. M. Griffies, *The MOM 3 manual*, report, 680 pp., Geophys. Fluid Dyn. Lab., Princeton, N. J, 1999.

[5] Menemenlis, D., I. Fukumori, and T. Lee, Using Green's functions to calibrate an ocean general circulation model, *Mon. Wea. Rev*., 133, 1224-1240, 2005.

[6] Sasaki, Y., Some basic formalisms in numerical variational analysis, *Mon. Wea. Rev*., 98, 875-883, 1970.

[7] Hosoda, S., T. Ohira, and T. Nakamura, A monthly mean dataset of global oceanic temperature and salinity derived from Argo float observations, *JAMSTEC Rep. Res. Dev*., 8, 47-59, 2008

[8] Hosoda, S., T. Suga, N. Shikama, and K. Mizuno, Global surface-layer salinity changes have been investigated and related to the intensification of the global hydrological cycle, *J. Oceanogr*., 65, 579–586, 2009

四次元変分法を用いた海洋環境再現（Estimated State of Ocean for Climate Research: ESTOC）

課題責任者
増田　周平　　海洋研究開発機構　地球環境変動領域

著者
増田　周平 *1，杉浦　望実 *1，長船　哲史 *1，土居　知将 *1
*1　海洋研究開発機構　地球環境変動領域

数年から数十年の時間スケールを持つ気候変動現象の包括的な理解を深めるためには海洋の状態を正確に把握することが重要である。そのための手段として海洋観測と数値シミュレーション結果を力学的整合性を保持しながら統合する海洋環境再現が注目されている。（独）海洋研究開発機構では水温、塩分などの物理データ、溶存化学物質、植物プランクトン色素などの生物化学データ等、異なる時空間スケールを持つ様々な海洋観測データを数値モデルを活用して時空間的に矛盾なく統合したデータセット（Estimated State of Ocean for Climate Research: ESTOC）を作成した。本研究ではESTOC の概要とそれを用いた海盆規模での淡水循環変動研究への応用可能性を示す。

キーワード:海洋, データ同化, 淡水循環

Global Elastic Response Simulation

Project Representative
Seiji Tsuboi — Data Research Center for Marine-Earth Sciences, Japan Agency for Marine-Earth Science and Technology

Authors
Satoru Tanaka — Institute for Research on Earth Evolution, Japan Agency for Marine-Earth Science and Technology
Seiji Tsuboi — Data Research Center for Marine-Earth Sciences, Japan Agency for Marine-Earth Science and Technology

We compute theoretical seismic waves for realistic three dimensional (3-D) Earth models and recent large earthquake using Spectral-Element Method (SEM) and compare them with the observed seismic waves. We calculate synthetic seismic waveform for 2013 Sea of Okhotsk deep earthquake (Mw8.3) using fully 3-D Earth model. Our results indicate that the earthquake source mechanism of this event can be modeled by a rupture along low-dip fault. We also have calculated synthetic seismograms for Fiji deep earthquake and compared with the observed seismograms recorded in Europe. The results demonstrate that current performance of SEM is insufficient for the outermost core study using velocity seismograms and higher frequency contents up to at least 0.5 Hz are required, which we hope to be realized with the next generation Earth Simulator.

Keywords: Synthetic seismograms, 3-D velocity structure of the Earth, Spectral Element Method, Core-mantle structure

1. May 24, 2013 Sea of Okhotsk deep earthquake (Mw8.3)

May 24, 2013 Sea of Okhotsk earthquake (Mw 8.3, depth 640km NEIC) was not only one of the largest events in this general region but one of the largest deep earthquakes ever recorded (Fig. 1). We apply the waveform inversion technique to obtain slip distribution in the source fault of this earthquake in the same manner as our previous work (Nakamura et al., 2010 [1]). We use 57 broadband seismograms of IRIS GSN seismic stations with epicentral distance between 30 and 100 degrees. The broadband original data are integrated into ground displacement and band-pass filtered in the frequency band 0.002-1 Hz. We use the velocity structure model IASP91 to calculate the wavefield near source and stations. We assume that the fault is squared with the length 135 km. We obtain source rupture model for both nodal planes with high dip angle (81 degree) and low dip angle (10 degree) and compare the synthetic seismograms with the observations to determine which source rupture model would explain the observations better. We calculate broadband synthetic seismograms with this source propagation model for a realistic 3D Earth model using the spectral-element method (SEM) (Komatitsch and Tromp, 2002 [2]). The simulations are performed using 1014 processors, which require 127 nodes of the Earth Simulator 2. We use a mesh with 200 million spectral-elements, for a total of 13 billion global integration grid points. This translates into an approximate grid spacing of 2.0 km along the Earth's surface. On this number of nodes, a simulation of 30 minutes of wave propagation accurate at periods of 3.5 seconds and longer requires about 7 hours of CPU time. Comparison of the synthetic waveforms with the observation shows that source rupture model with the low dip angle fault plane explains the observation better specifically at stations, which locate south of the epicenter. These results demonstrate that the source rupture

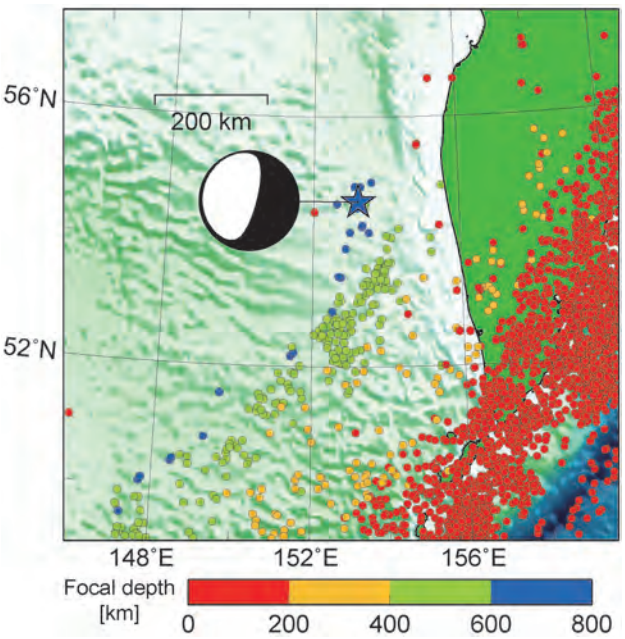

Fig. 1 Global CMT solution of 2013 Okhotsk deep earthquake and seismic activity of surrounding region. Epicenters are the earthquakes,which occurred during 1973 and September 2013 (Tsuboi et al., 2013 [3]).

of this deep earthquake occurred along the horizontal fault plane inside the subducting pacific plate.

We also have computed broadband synthetic seismograms using point source Global CMT solution and compared with the observation. Figures 2 show comparison of the synthetics with the observation for low-pass filtered traces and band-pass filtered traces. Synthetics for GCMT solution match the observation well in low frequencies but do not match well in

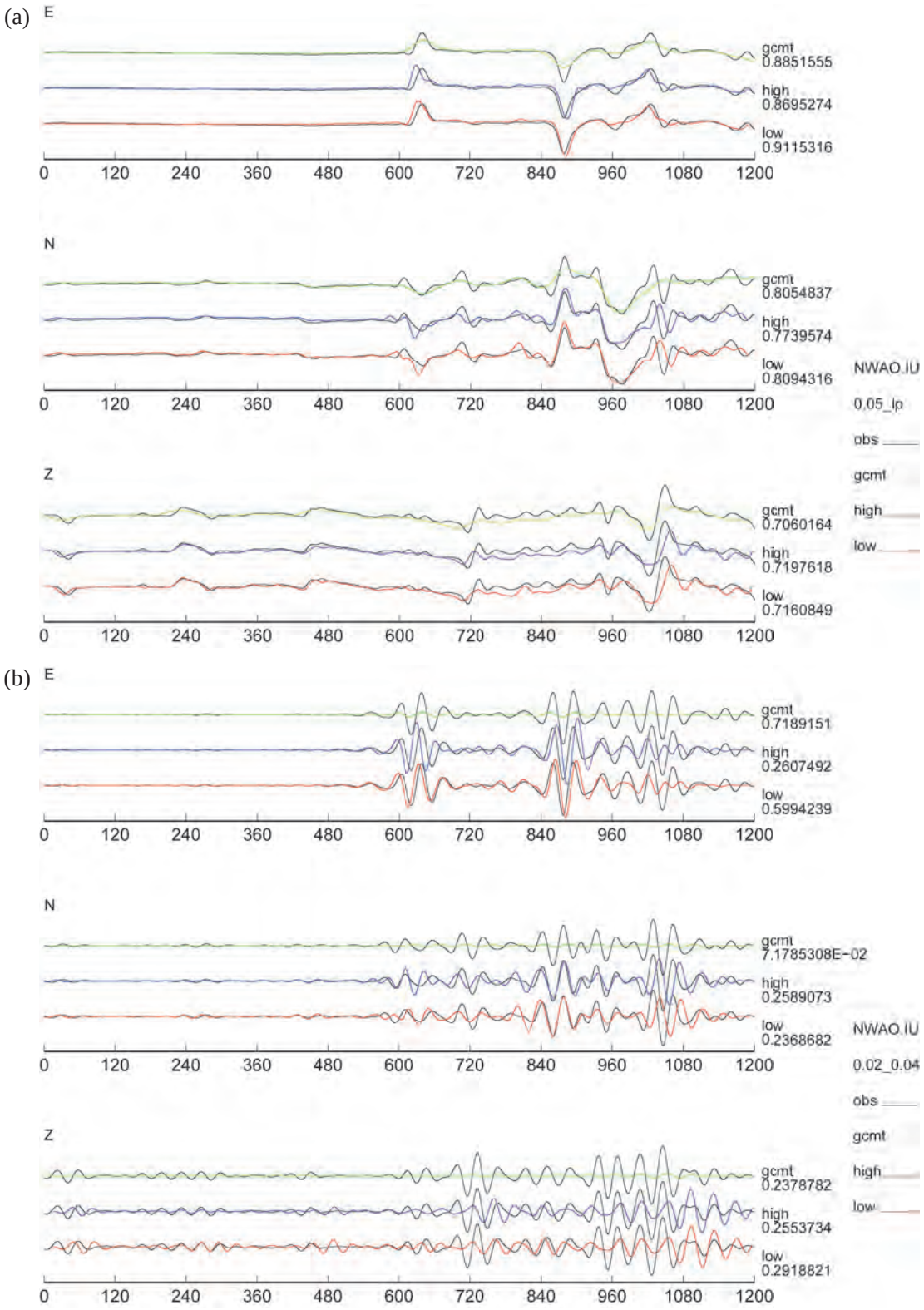

Fig. 2. (a) Comparison of synthetic seismograms for global CMT solution and finite fault model with observed seismograms. These traces are lowpass filtered at 20 second. Comparisons are displayed for EW components, NS components and vertical components from top to bottom. For each component, black traces are observed seismograms. Green traces are for global CMT solution, blue traces are for high-dip angle fault model and red traces are for low-dip angle fault model (Tsuboi et al., 2013) [3]). (b) Same as (a) but traces are bandpass filtered between 25 second and 50 second (Tsuboi et al., 2013 [3]).

high frequencies, which implies that this source mechanism contain much high frequency components. This may be consistent to the limited rupture area and large rupture velocity due to high rigidity (Tsuboi et al., 2013 [3]).

2. Seismological structure at the top of the Earth's outer core

Seismic structure at the top of the Earth's core is quite important to elucidate a stable stratification in the outermost part of the Earth's core. SmKS waves are most suitable for the observational constraints (Tanaka, 2007 [4]; Alexandrakis and Eaton, 2010 [5]; Helffrich and Kaneshima, 2010 [6]; Kaneshima and Helffrich, 2013 [7]; Fig. 3). Although the differential travel times between SmKS waves are analyzed to reduce the structural effect at the base of the mantle, it has been thought that the strong and unknown structure in the D" region certainly gives a bias in the estimation of the outer core structure (Garnero and Helmberger, 1995 [8]). For further studies, a relevant waveform modeling is required to find how to distinguish the structures above and below the core-mantle boundary.

To date, reflectivity method (RM) has been frequently used, which can easily synthesizes SmKS waves down to the period of 2 s at distances from 150-160° with 1-D structure, and can reproduce S5KS on velocity seismograms as previously noted by Helffrich and Kaneshima (2010) [6]. To fully incorporate 3D mantle heterogeneity, the spectral element method (SEM) can be used on Earth Simulator 2, which enables us to achieve the shortest period of about 3.5 s with 127 nodes (1014 CPUs). We adopt these setting and conduct the waveform modeling for PREM incorporating ETOPO5 and CRUST2.0 to simulate seismograms from a South Fiji earthquake observed by European seismic networks as a single large array (Fig. 4; Tanaka (2013) [9]). The phase-weighted stack is applied and the differential travel times are picked. Comparing between displacement seismograms from RM (only PREM is used) and SEM, differential travel times of S4KS–S3KS and S3KS–S2KS are coincides within 0.1 s that is two sampling intervals (Figs. 5 and 6; Tanaka (2014) [9]). However, the differential travel time of S4KS–S3KS on velocity seismogram with SEM was 0.5 s larger than that with RM. Furthermore, S5KS phase is not identified on velocity seismogram with SEM (Figs. 7 and 8; Tanaka (2013) [9]). These suggest that the current setting of SEM is insufficient for the outermost core study using velocity seismograms and higher frequency contents up to at least 0.5 Hz are required, which we hope to be realized with the next generation Earth Simulator.

Additionally we have conducted another runs incorporating the 3D mantle models of S20RTS with the spherical harmonics coefficients at the base of the mantle modified to be 3 times and an approximated SB4L18. These results clearly show that there are strong effects of heterogeneity in the lowermost mantle on the differential travel times of S4KS–S3KS and S3KS–S2KS (Figs 7, 8, and 9; Tanaka (2014) [9])

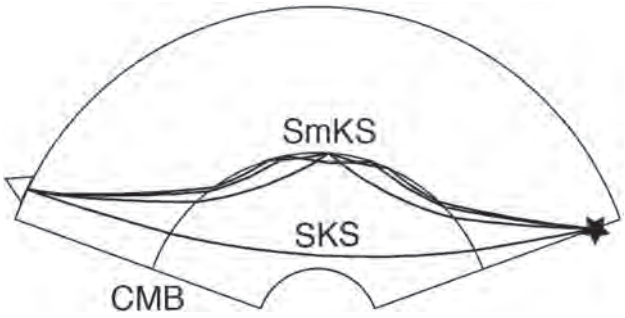

Fig. 3 Seismic ray paths of SKS, SmKS waves.

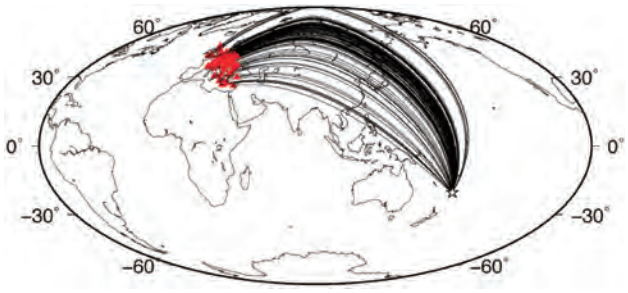

Fig. 4 Geographical distribution of epicenter and stations used for the calculation of synthetic waveforms.

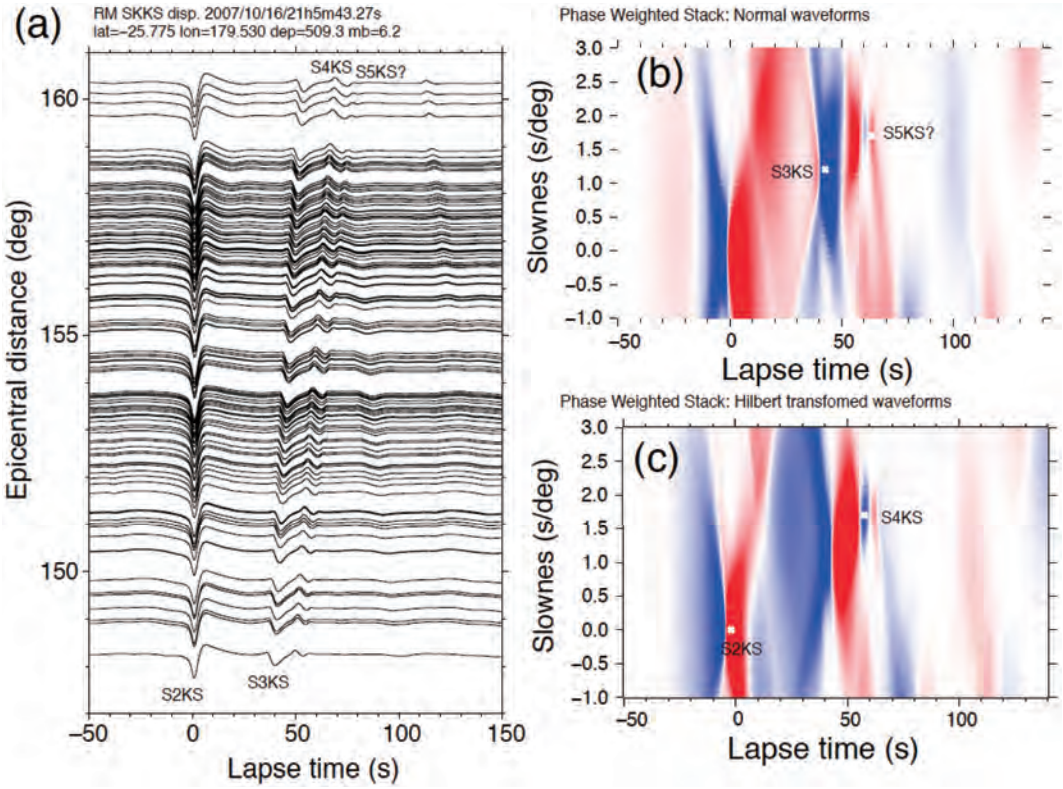

Fig. 5 (a) Displacement waveforms of S2KS and later phases synthesized by reflectivity method. PREM is used. (b) Vespagram by phase weighted stack with power index of 2 using original waveforms, in which the peak of S3KS is marked by a white cross. (c) Vespagram by phase weighted stack using Hilbert transformed waveforms, in which the peaks of S2KS and S4KS are marked by white crosses.

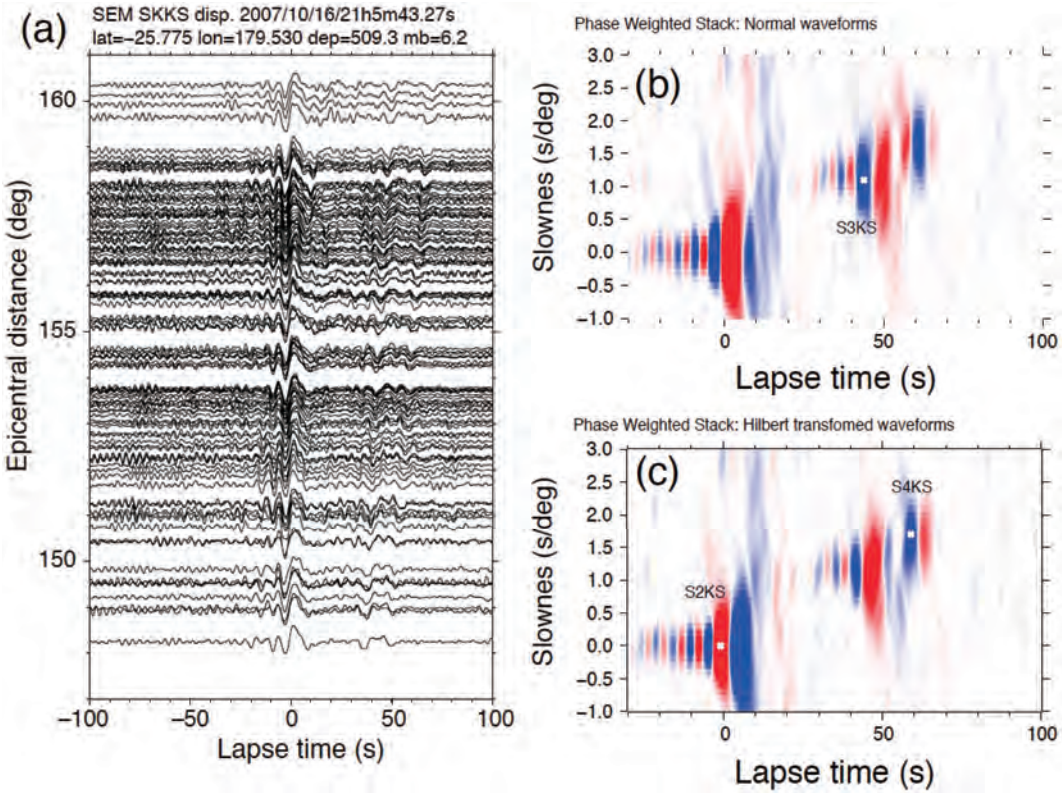

Fig. 6 Same as Fig. 5 except that spectral element method is used for the waveform calculation.

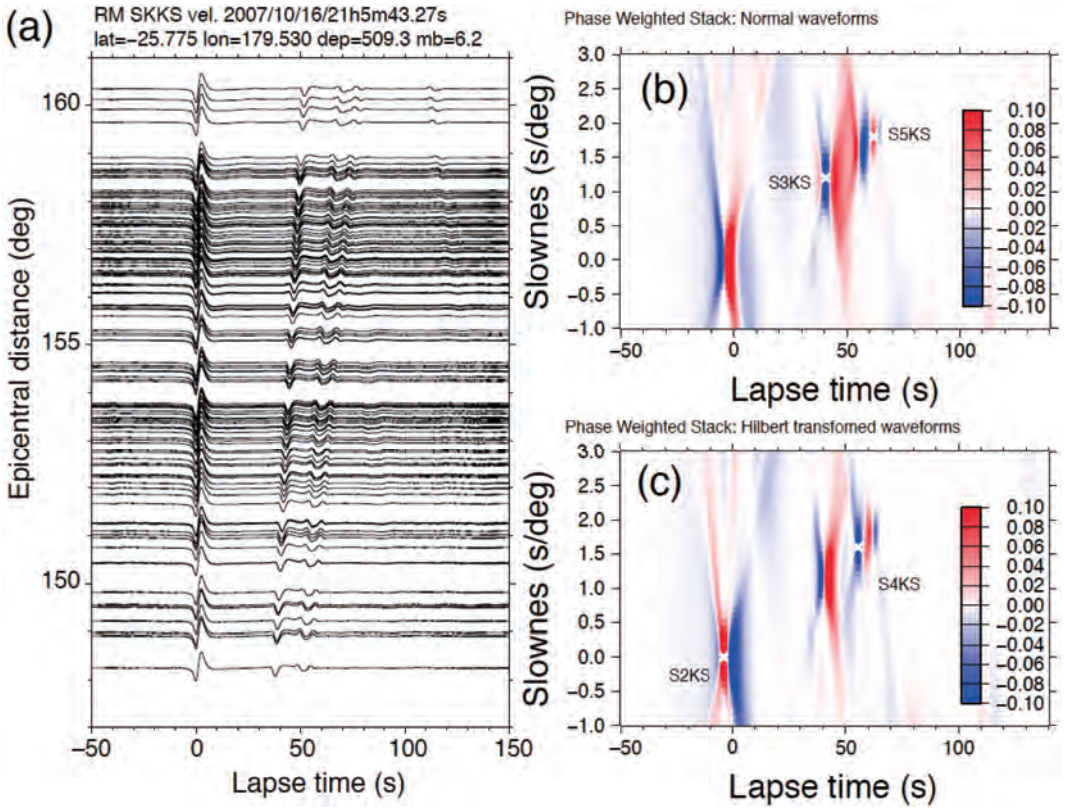

Fig. 7 Same as Fig. 5 except for velocity waveform.

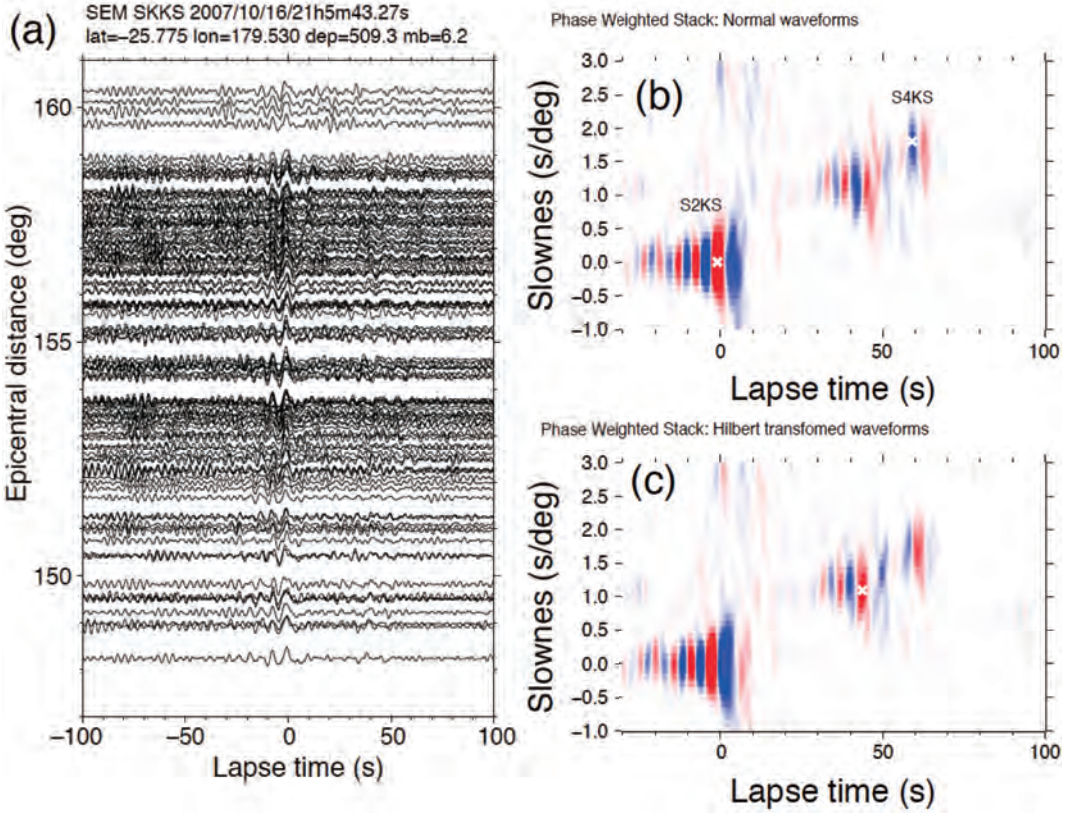

Fig. 8 Same as Fig. 6 except for velocity waveform.

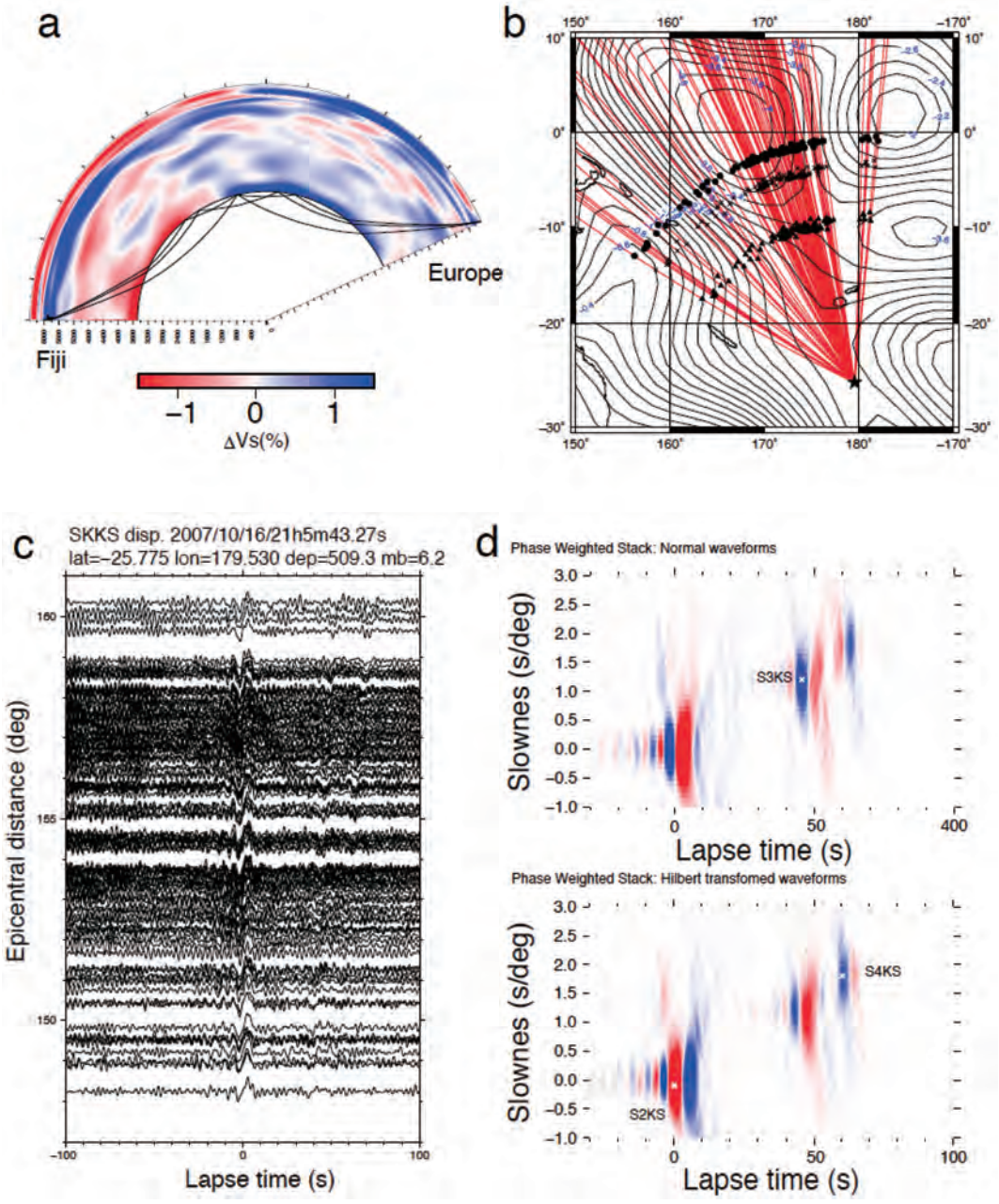

Fig. 9 (a) Vertical cross-section from the hypocenter to a station with seismic ray paths of SmKS. The background color indicates the heterogeneity in the mantle that is calculated with S20RTS but the coefficients at the base of the mantle are multiplied by factor 3. (b) Geographical distribution of SmKS piercing points at the core-mantle boundary beneath the hypocentral area. Triangles, crosses, and circles represent the points of S2KS, S3KS, and S4KS, respectively. (c) Displacement waveforms SmKS synthesiezed by spectral element method with S20RTS but the coefficients at the base of the mantle are multiplied by factor 3. (d) Vespagrams of S2KS and later phases.

References

[1] Nakamura, T., Tsuboi, S., Kaneda, Y., and Yamanaka, Y., 2010. Rupture process of the 2008 Wenchuan, China earthquake inferred from teleseismic waveform inversion and forward modeling of broadband seismic waves, Tectonophysics, 491, 72-84.

[2] Komatitsch, D. and Tromp, J., 2002. Spectral-element simulations of global seismic wave propagation-I. Validation. Geophys. J. Int. 149, 390-412.

[3] Tsuboi, S., Miyoshi, T., Nakamura, T., Obayashi, M., and Tono, Y., 2013. Source mechanism of May 24, 2013 Sea of Okhotsk deep earthquake (Mw8.3) estimated by broadband waveform modeling, AGU Fall meeting, S41-C07.

[4] Tanaka, S., 2007. Possibility of a low P-wave velocity layer in the outermost core from global SmKS waveforms, Earth Planet. Sci. Lett., 259, 486-499.

[5] Alexandrakis, C. and D. W. Eaton, 2010. Precise seismic-wave velocity atop Earth's core: No evidence for outer-core stratification, Phys Earth Planet In, 180(1-2), 59-65, doi:10.1016/j.pepi.2010.02.011.

[6] Helffrich, G. and S. Kaneshima, 2010. Outer-core compositional stratification from observed core wave speed profiles, Nature, 468(7325), 807-U896, doi:10.1038/nature09636.

[7] Kaneshima, S. and G. Helffrich, 2013. Vp structure of the outermost core derived from analysing large-scale array data of SmKS waves, Geophys J Int, 193(3), 1537-1555, doi:10.1093/gji/ggt042.

[8] Garnero, E. J. and D. V. Helmberger,1995. On seismic resolution of lateral heterogeneity in the Earth's outermost core, Phys. Earth Planet. Inter., 88(2), 117-130.

[9] Tanaka, S., 2014. Broadband waveform modeling with the spectral element method on Earth Simulator for the study of the structure at the top of the Earth's outer core, accepted, JAMSTEC-R.

全地球弾性応答シミュレーション

課題責任者
坪井　誠司　　海洋研究開発機構　地球情報研究センター
著者
田中　　聡　　海洋研究開発機構　地球内部ダイナミクス領域
坪井　誠司　　海洋研究開発機構　地球情報研究センター

スペクトル要素法により現実的な 3 次元地球モデルに対する理論地震波形記録を 2013 年千島沖地震（Mw8.3）に対して計算した。計算は地球シミュレータの 127 ノードを用いて、周期約 5 秒の精度で行った。理論地震波形は、低角逆断層と高角逆断層の震源過程モデルに対して計算し、それぞれを観測と比較した結果、低角逆断層の震源モデルが観測をより良く説明出来ることが分かった。また、点震源の GCMT 解を用いた理論波形との比較では、短周期側で観測を説明出来ないことが分かったが、これは、この地震の震源過程が短周期成分を多く含んでいる可能性があることを示している。

フィジーで起きた深発地震により励起された地震波をヨーロッパ大陸に展開された地震網で観測した波形に対してスペクトル要素法による理論地震波形計算を行った。計算した理論地震波形の精度は核マントル境界の詳細な構造を推定するためには十分ではなく、少なくとも周期 2 秒の精度が必要であることが分かった。

キーワード:理論地震波形記録, 3次元地球内部構造, スペクトル要素法, 核マントル境界

Numerical Simulations of Present and Ancient Dynamos in the Earth

Project Representative
Yozo Hamano — Institute for Research on Earth Evolution, Japan Agency for Marine-Earth Science and Technology

Authors
Futoshi Takahashi — Department of Earth and Planetary Sciences, School of Science and Engineering, Tokyo Institute of Technology
Kumiko Hori — Earthquake Research Institute, The University of Tokyo
Takatoshi Yanagisawa — Institute for Research on Earth Evolution, Japan Agency for Marine-Earth Science and Technology
Yozo Hamano — Institute for Research on Earth Evolution, Japan Agency for Marine-Earth Science and Technology

The core-mantle boundary (CMB) region is important to understand the generation mechanisms of the geomagnetic field and its secular variations, whereas convective motions in the Earth's outer core at present are driven by the buoyancy arising from thermal and chemical effects at the inner core boundary. To better understand the thermo-chemical buoyancy of the Earth's core, we performed numerical simulations of the geodynamo powered by double diffusive convection. We find three sorts of dynamos, that is, dipolar, non-dipolar and hemispherical dynamos. Flow dynamics in these dynamos can be characterized by the zonal flow and relative axial helicity. Then, dynamo simulations with a thin stably stratified layer imposed below the core-mantle boundary were run. It is found that dynamos can strongly be affected even with the slightly thin stable layer. While the present geodynamo is predominantly driven by inner core solidification, the ancient geodynamo probably operated without an inner core. It was thus exclusively driven by secular cooling and radiogenic heating. We also explore lateral CMB heat flux variations on dynamos with and without an inner core, by comparing dynamos driven by homogeneous internal sources and by bottom buoyancy sources. Our results indicate that the field intensity and morphology of the ancient geodynamo was more variable and more sensitive to the thermal CMB structure than that after onset of inner core growth.

Keywords: Geodynamo, Geomagnetic field, Core convection, Magnetohydrodynamics

1. Introduction

Internal activities of the Earth are the consequence of convective motions of the mantle and core. The convection of mantle and core also control Earth's surface environment through material circulations, volcanism, continental drift, geomagnetic field, and so on. The mantle convection, driven by both cooling of the Earth and internal radiogenic heating, takes the form of rigid-plate motions at the surface. As the mantle cools by the subducting plates, the underlying liquid metallic core becomes thermally unstable and the resulting convective motion causes generation of the geomagnetic field and its time variations. As a result of cooling of the liquid core containing some lighter elements, a solid denser inner core grows from below, causing compositional instability in the liquid outer core. Seismic studies have illuminated detailed structures inside of the Earth, such as subducting plate in the mantle and strong heterogeneity at the core-mantle boundary (CMB), and stratified layer in the outer core. The geomagnetic field has been monitored at the surface or from satellites. It contains information on both the core convection and the electrical conductivity of the mantle. Paleomagnetic records provide information on the long-term variation and the evolution of geomagnetic filed. The purpose of our group is to construct a comprehensive view on the structure and dynamics of the Earth's deep interior, by including the results of latest observations. We report here several topics on geodynamo.

2. Geodynamo simulations with double diffusive convection and stable stratification

The most likely source of the geomagnetic field generation and its secular variation is a dynamo action due to convective motions in the Earth's outer core. Convective motions in the Earth's core are driven by buoyancy force originating from thermal and compositional effects. Thermal convection is driven

by the super-adiabatic temperature difference across the core, release of latent heat upon inner core growth at the inner core boundary, and core secular cooling. Compositional convection is fueled by light element ejection into the outer core at the inner core boundary.

According to the molecular diffusivity, the thermal Prandtl number Pr^T is about 0.1, while the corresponding compositional Prandtl number Pr^C is of the order of 10^2. In spite of such a huge gap in the Prandtl numbers, an optimistic assumption of turbulent diffusivity due to turbulence in the core somehow allows us to adopt the same values of thermal and compositional Prandtl numbers. Then, temperature and composition can be treated simultaneously by using a new variable, codensity [1]. However, the codensity treatment is not fully verified because of our limited knowledge on turbulence in the core. Instead of introducing the codensity, we employ a double diffusive convection (DDC) model to investigate the effects of co-existence of two buoyancy sources with different diffusivity coefficients on the core convection and the geodynamo.

Using our numerical dynamo code [2-4], numerical simulations of DDC are performed at the Ekman number, $E = 3\times10^{-4}$, and 10^{-4}, whereas the two Prandtl numbers are fixed at $Pr^T = 0.1$, $Pr^C = 1$ and $Pm = 3$, where Pm is the magnetic Prandtl number. The Ekman number adopted here is not extremely low to allow us to perform a parameter survey. Varying the two Rayleigh numbers representing strength of thermal and compositional convection, we have obtained three types of dynamos: dipolar dynamo, non-dipolar dynamo and hemispherical dynamo [4]. In Fig. 1, the typical magnetic field morphology is exhibited. The non-dipolar and hemispherical dynamos tend to appear when thermal buoyancy prevails relative to compositional one. The opposite situation regarding the buoyancy force results in the dipolar dynamos.

Flow dynamics responsible for such distinct dynamos are then examined. Consequently, it is found that the dipolar dynamos and other non-dipolar and hemispherical dynamos are distinguished by strength of the zonal flows. The non-dipolar and hemispherical dynamos tend to have larger fractions of the zonal flow kinetic energy to the total kinetic energy than the dipolar ones. Figure 2a shows that the threshold value seems about 12%. Figure 2b represents the relative axial helicity, $|H^{rel}_z|$ defined by Soderlund et al. [5] with respect to the zonal flow. The relative axial helicity is defined by

$$\left|H_z^{rel}\right| = \frac{\left|\left\langle H_z\right\rangle_h\right|}{\left(\left\langle u_z u_z\right\rangle_h \left\langle \omega_z \omega_z\right\rangle_h\right)^{1/2}},$$

where $H_z = u_z\,\omega_z$ is the axial helicity, the product of the axial velocity u_z and the axial vorticity ω_z, and $\langle\rangle_h$ is the volumetric average taken in each hemisphere. It is evident that $|H^{rel}_z|$ is anti-correlated with the zonal flow, and the dipolar dynamos tend to have $|H^{rel}_z|$ larger than the non-dipolar dynamos as well as hemispherical dynamos. Such an anti-correlation suggests two possible mechanisms. One is that the columnar convection, which generates the axial helicity, is suppressed by the strong zonal flow, and the other is that the dipolar magnetic field forces the flow to enhance the helicity and to brake the zonal flow [6]. According to the results that fraction of the zonal flow kinetic energy is not so large that the columnar convection

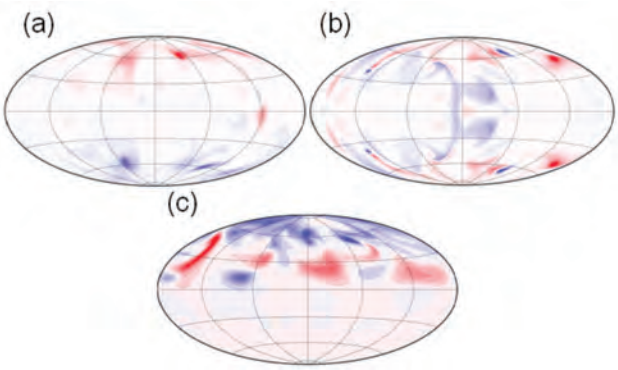

Fig. 1 Typical simulation results for (a) dipolar dynamo, (b) non-dipolar dynamo and (c) hemispherical dynamo. The radial magnetic field at the core surface is represented. Red regions denote the outward radial field and blue regions denote the inward field.

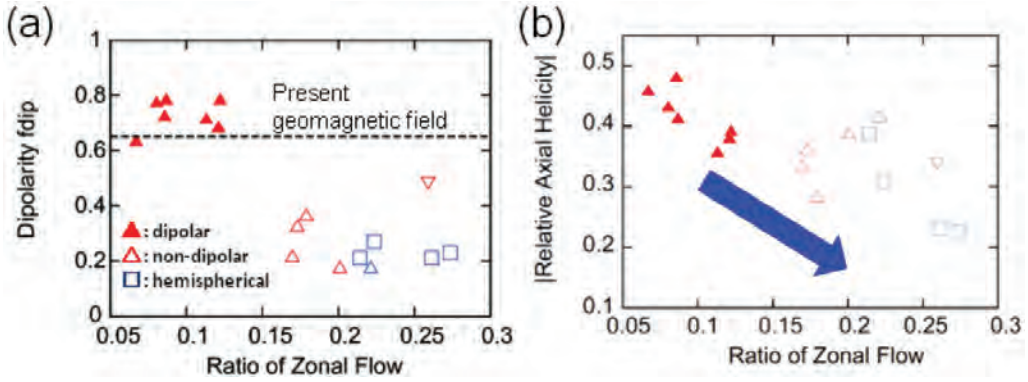

Fig. 2 (a) Dipolarity and (b) relative axial helicity as functions of the ratio of the zonal flow kinetic energy to the total kinetic energy. Results at Ekman number = 3×10^{-4} (10^{-4}) are drawn in red (blue). Axial dipolar (non-dipolar) dynamos are represented by filled (open) triangles. Equatorial dipolar dynamos are represented by down-pointing triangles. Hemispherical dynamos are denoted by squares. This figure was modified from [4].

is significantly affected, and that the enhanced anti-cyclones appear in dipolar dynamos, the latter case is more likely.

Then, we have also performed dynamo simulations with an imposed thin stably stratified layer beneath the outer boundary, which is implemented to mimic a stably stratified layer detected by seismic observations [7]. The Ekman number of 3×10^{-5} is adopted and layer thickness is 10% of the core radius (~350 km). It is apparent that magnetic field strength is much varied between the cases with and without the stable layer, although the dipolar morphology remains unchanged (Fig. 3a, c). Difference in spatial scale in the low-latitude region is also notable. The stable layer filters out the small-scale, short-period components through the skin effects. Comparing the results, the flow structure is substantially altered. The well-known thermal wind balance is found in the case without the stable layer (Fig. 3b), whereas the zonal flow structure in the corresponding case with the stable layer is almost invariant along the rotation axis (Fig. 3d). It is suggested that the flow is primarily controlled by the stable layer just below the outer boundary via the Taylor Proudman theorem.

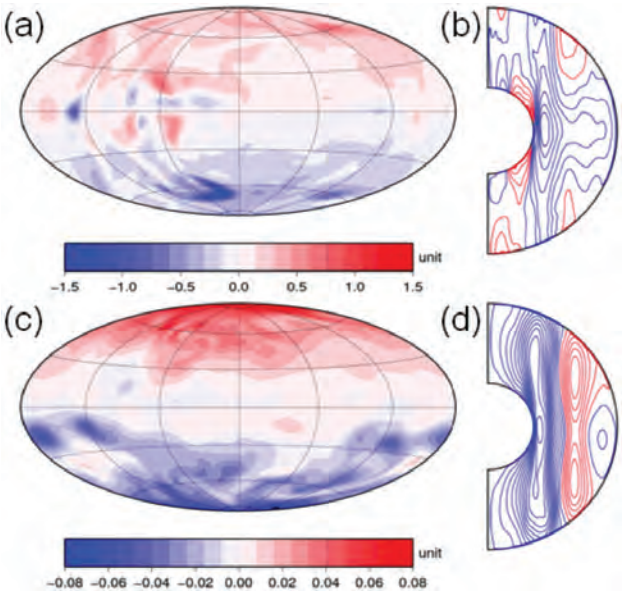

Fig. 3 (a, c) The radial component of the magnetic field at the outer boundary. (b, d) The zonal flow in the meridional plane. A case without stable layer is drawn in the top (a and b), while a case with stably stratified layer is displayed in the bottom (c and d). Positive (negative) values are represented by red (blue).

3. Ancient dynamos of Earth and Mars, without inner core growth

Paleomagnetic studies have been updating evidences for the geomagnetic field in ancient period, since approximately 3.5 Ga. Although the data seemingly show large variations, for instance, in virtual dipole moment and angular standard deviation, impacts of inner core growth on the field and paleomagnetic records has been extensively discussed. A recent convection-driven dynamo model, which was coupled with a thermal evolution model but included no lateral heterogeneity induced by mantle convection, proposed a rather minor impact of the inner core growth [8].

We found that, with lateral heterogeneity at the CMB, the impact could become sizable through the different sensitivity to the CMB between core convection with and without inner core growth [9]. When an inner core is growing, core convection and dynamos are driven by buoyancy sources associated with the inner core growth, such as latent heat and light element releasing from the inner core boundary (ICB), yielding the onset of the convection very close to the ICB. Without inner core growth, convection and dynamos should be driven predominantly by secular cooling and sinks from the CMB induce the convection, which occurs at a mid depth of a sphere/spherical shell. Secularly cooled dynamos thus respond more sensitively to CMB thermal conditions than dynamos driven by inner core growth-related sources (Fig. 4). The result implies that inner core age might be detectable through variability of the paleomagnetic data.

This also involves implications for the ancient dynamo of Mars. Mars has no active dynamo action at present but likely had one in the past, from the time of core formation to the late heavy bombardment, 4 Ga. Thermal evolution models suggest that the early Martian dynamo probably operated without an inner core being present and was exclusively driven by secular cooling. The situation can thus reinstate the early geodynamo before an inner core started to grow.

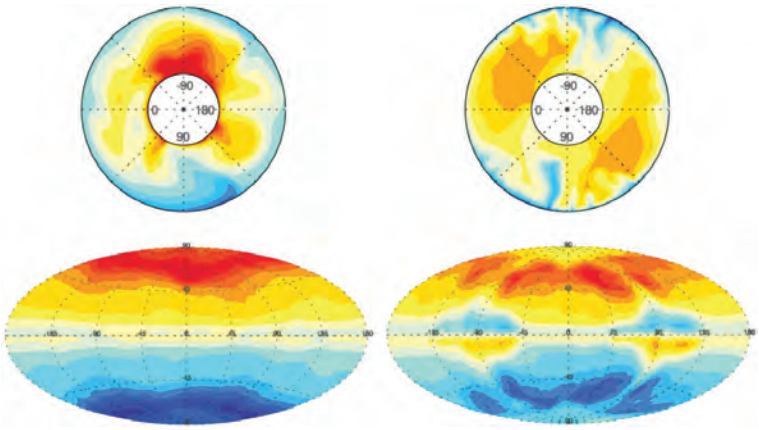

Fig. 4 Responses of convection and dynamos to a CMB thermal forcing with azimuthal wavenumber two (left) with and (right) without inner core growth. At $E=10^{-4}$, $Pm=3$ and $Pr=1$. (Top) temperature in the equatorial plane in snapshots and (bottom) time-averaged radial magnetic field at CMB. Red (blue) contours represent high (low) temperature and outward (inward) radial field. Larger impacts are found in the case without inner core growth (after [9]).

A challenging question is why and how the Martian dynamo ceased. Several scenarios have been proposed: for example, a result of natural cooling of the core, changes of the style of mantle convection, and subcritical dynamo action. While the subcriticality cannot explain the cessation of the Martian dynamo by itself, it can help to understand why the dynamo did not recover after some temporary effects stopped it operating. This possibility is expected through rotating magnetoconvection studies, but fully nonlinear dynamo simulations in spherical shells have reported rather narrow subcritical regimes [6,10], indicating that it may not play an important role for the cessation. By adopting a more appropriate model for the early dynamo driven by secular cooling, we found that the subcritical regime could become much wider than previously reported [11]. This supports that subcriticality may have played a role in the shutdown of the early Martian dynamo and that it would have been difficult to restart the dynamo once the magnetic field has decayed.

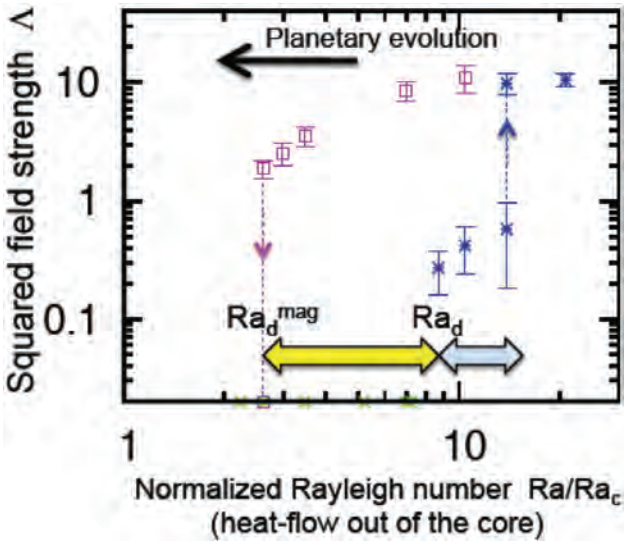

Fig. 5 Squared field strength Λ versus the Rayleigh number, Ra/Ra_c, normalized by the critical Rayleigh number Ra_c for the onset of the nonmagnetic convection. At $E=10^{-4}$, $Pm=3$ and $Pr=1$. Stars and squares represent dynamo runs started from a seed field and from a strong dipolar field, respectively. Failed dynamo runs are also represented by the symbols located at the base of the diagram. Possible thresholds for seed field growth and for strong field maintenance are indicated by Ra_d and Ra_d^{mag}, respectively, and the region between the two values presents the window for subcritical dynamos (after [11]).

References

[1] S. I. Braginsky and P. H. Roberts, "Equations governing convection in Earth's core and the geodynamo", *Geophys. Astrophys. Fluid Dyn*., 79, 1–97, 1995.

[2] F. Takahashi, "Implementation of a high-order combined compact difference scheme in problems of thermally driven convection and dynamo in rotating spherical shells", *Geophys. Astrophys. Fluid Dyn*., 106, 231–249, 2012.

[3] F. Takahashi and H. Shimizu, "A detailed analysis of a dynamo mechanism in a rapidly rotating spherical shell", *J. Fluid. Mech*., 701, 228–250, 2012.

[4] F. Takahashi, "Double diffusive convection in the Earth's core and the morphology of the geomagnetic field", *Phys. Earth Planet. Inter*., 226, 83–87, 2014.

[5] K. M. Soderlund, E. M. King, and J. M. Aurnou, "The influence of magnetic fields in planetary dynamo models", *Earth Planet. Sci. Lett*., 333-334, 9–20, 2012.

[6] B. Sreenivasan and C. A. Jones, "Helicity generation and subcritical behavior in rapidly rotating dynamos", *J. Fluid Mech*., 688, 5–30, 2011.

[7] G. Helffrich and S. Kaneshima, "Outer-core compositional stratification from observed core wave speed profiles", *Nature*, 468, 807–810, 2010.

[8] J. Aubert, S. Labrosse, and C. Poitou, "Modelling the paleo-evolution of the geodynamo", *Geophys. J. Int*., 179, 1414–1428, 2009.

[9] K. Hori, J. Wicht, and W. Dietrich, "Ancient dynamos of terrestrial planets more sensitive to core-mantle heat flows", *Planet. Space Sci*., 98, 30–40, 2014.

[10] W. Kuang, W. Jiang, and T. Wang, "Sudden termination of Martian dynamo?: implications for subcritical dynamo simulations", *Geophys. Res. Lett*., 35, L14204, 2008.

[11] K. Hori and J. Wicht, "Subcritical dynamos in the early Mars' core: Implications for cessation of the past Martian dynamo", *Phys. Earth Planet. Int*., 219, 21–33, 2013.

現在および過去の地球ダイナモに関する数値シミュレーション

課題責任者
浜野　洋三　　海洋研究開発機構　地球内部ダイナミクス領域
著者
高橋　　太　　東京工業大学　大学院理工学研究科　地球惑星科学専攻
堀　久美子　　東京大学　地震研究所
柳澤　孝寿　　海洋研究開発機構　地球内部ダイナミクス領域
浜野　洋三　　海洋研究開発機構　地球内部ダイナミクス領域

マントルとコアでの対流は、地球に生起する諸々の自然現象の原因をつかさどる根本的な物理プロセスであり、また両者の対流は様々な関係で結合している。コアの対流により地磁気が生成・維持されることで、表層環境が穏やかに保たれてきた一方、このコアの冷却を支配するのは周囲のマントルである。マントルとコアの結合の理解に重要なマントル最下層の構造が、地震学により詳細に明らかになってきた。さらには外核に安定な成層の存在も示唆されている。そして地球史をさかのぼった地磁気の変遷についての情報も蓄積されてきた。我々はこれまで、マントルとコアという2つの対流系を、より観測事実に則した条件のもとで、また一方では地球進化を想定して、数値的にモデリングする研究をおこなってきた。ここでは特にコアの対流に焦点を絞って、コア対流の駆動源、外核での成層構造、内核成長の役割、等のダイナモ作用への影響を報告する。また、それに基づき現在と古代の地球ダイナモの差異や、火星でのダイナモ作用の消失過程について議論する。

現在の外核の対流は、内核成長に伴い放出される潜熱や軽元素の放出によって駆動されている。加えて外核とマントルの境界は、地球磁場の生成や永年変化のメカニズムに重要な役割を果たす。これらをふまえて我々は、昨年度に続き熱対流と組成対流を二重拡散対流として同時に取り扱い、エクマン数を 3×10^{-4}、1×10^{-4}、熱プラントル数 0.1、組成プラントル数 1.0、磁気プラントル数 3.0 として、ダイナモシミュレーションを実施した。その結果、双極子的、非双極子的、半球的の3つの磁場形態が見出された。これら磁場の形態と帯状流の強さ、ヘリシティの大きさの間には相関があり、組成対流の寄与が 30-40% 程度あれば地球型の双極子磁場が維持されることを示した。さらに、外核の最上部に熱的な安定成層を置き、二重拡散対流ダイナモにおける効果を、エクマン数を 3×10^{-5} まで下げて調査した。この安定成層の有無は、生成される磁場の強度とパターンに大きな影響を与えることが確認された。

一方で地球史をさかのぼると、古代地球コアにおけるダイナモ作用は現在のものとは異なっていたかもしれない。内核成長が開始する前の古代ダイナモでは、地球形成時から続く永年冷却が主な駆動源であっただろうと考えられる。永年冷却により駆動される対流とそのダイナモの数値シミュレーションを行った結果、内核成長に伴う場合に比べて、コア－マントル境界における熱的境界条件に対し敏感に応答することがわかった。本結果は、古地磁気学的データのばらつきにより内核成長の開始時期が制約できる可能性を示唆する。また、同モデルは古代火星ダイナモへ拡張することも可能である。火星では約 40 億年前までコアダイナモが駆動されていたと示唆されており、そこでは内核成長が開始していなかったと見積もられている。上述の古代ダイナモモデルにおいて詳細なパラメータサーベイを行った結果、解の亜臨界的分岐が顕著となることがわかった。これは、古代火星ダイナモが急速に消失していった理由を説明し得ることを示すものである。

キーワード:地球ダイナモ, 地磁気, コア対流, 磁気流体力学

Finite Difference Method Simulation of Long-Period Ground Motion at the Northern Kanto Region, Japan, Using the Earth Simulator

Project Representative

Takashi Furumura — Center for Integrated Disaster Information Research, Interfaculty Initiative in Information Studies, The University of Tokyo / Earthquake Research Institute, The University of Tokyo

Authors

Shunsuke Takemura — Graduate school of Nanobioscience, Department of Material System Science, Yokohama City University

Kazuo Yoshimoto — Graduate school of Nanobioscience, Department of Material System Science, Yokohama City University

To conduct precise three-dimensional finite difference method (FDM) simulations of long-period ground motion in the Kanto basin, Japan, we investigate the characteristics of the *S*-wave velocity in the Kanto Basin and construct a realistic sedimentary structure model. The *S*-wave velocities derived from the vertical seismic profiling measurements in the Kanto Basin show smooth depth gradients rather than step-like increases and can be successfully modeled by an exponential asymptotically bounded velocity function. We conduct large-scale FDM simulation of long-period ground motion using constructed high-resolution sediment structure in the Kanto region. Our simulation using the modified Japan integrated velocity structure model by incorporating a sedimentary layer with *S*-wave velocity-depth gradients well reproduces the excitation and dispersion of the observed surface waves at northern Kanto. This result indicates that a realistic modeling of the impedance contrast at the sediment-bedrock interface is indispensable for the precise evaluation of surface wave excitation at the basin edge.

Keywords: long-period ground motion, surface wave excitation, sedimentary basin, Kanto Basin

1. Introduction

Long-period ground motion is generated by shallow moderate-to-large earthquakes and its dominant period is ranging from several to ten seconds. It often causes significant resonance and severe damage to large-scale man-made structures, such as high-rise buildings, oil-storage tanks, and suspension bridges, which are often located in large-scale sedimentary basins. Therefore, it is very important for the disaster mitigation of future large earthquakes to investigate characteristics of long-period ground motion in large complex basins.

In Kanto region, Japan, long-period ground motions are frequently observed for shallow local moderate-to-large earthquakes (e.g., Yamanaka et al., 1989 [1]; Kinoshita et al., 1992 [2]; Sato et al., 1999 [3]; Koketsu and Kikuchi, 2000 [4]). Such strong long-period ground motions are often caused by the surface wave excited at the edge of basin. The excitation of long-period surface waves at a sedimentary basin edge owing to the incidence of *S*-waves has been reported by many researchers (e.g., Kawase and Aki, 1989 [5]; Hatayama et al., 1995[6]). Furumura and Hayakawa (2007)[7] visualized that the surface waves excited at the northern edge of the Kanto Basin by the 2004 Niigata-ken Chuetsu earthquake (M_W 6.6) propagated toward the southern part of the basin and caused large long-period ground motions with a predominant period of approximately 7 s in Tokyo. This observation indicates that the study of surface wave excitation at the basin edge is important for the precise evaluation and prediction of the long-period ground motion and disaster mitigation in the Tokyo metropolitan area.

To precisely expect long-period ground motion for disaster mitigation from future large earthquakes, the study of the basin structure is necessary for gaining a better understanding of the observed phenomenon. However, the heavily urbanized state of the Tokyo metropolitan area and the complex shape of the bedrock (seismic basement) resulting from the active tectonics in the Kanto region have prevented the rapid advance of the related studies. Using extensive geophysical datasets from refraction/reflection experiments, gravity surveys, microtremor surveys, etc., Koketsu et al. (2008)[8] proposed the Japan

integrated velocity structure model (JIVSM) as a regional three-dimensional (3-D) velocity structure model of Japan, including the complex Kanto Basin structure. Although the JIVSM is one of the latest and most widely used structure models for the evaluation of strong and long-period ground motions of local and/or regional earthquakes, this model has scope for improvement, especially in the deterministic evaluation of the surface waves observed in the Kanto Basin.

In this report, we discuss the significant structural properties that control the surface wave excitation at a basin edge on the basis of a 3-D finite-difference method (FDM) simulation. In this process, we first investigate the characteristics of the *S*-wave velocity in the Kanto Basin and find that the *S*-wave velocity in the sediment shows a smooth depth gradient rather than a step-like increase assumed in a conventional layered structure modeling. Our analysis indicates that the *S*-wave velocity-depth gradient is well represented by an exponential asymptotically bounded velocity function (Ravve and Koren, 2006 [9]). Adopting this function, we modify the JIVSM and propose a 3-D structure model. By using the Earth Simulator, we demonstrate that the simulation of long-period ground motion using our model accurately reproduces the amplitudes and dispersions of the surface waves observed in the northern edge of the Kanto Basin.

2. Realistic velocity structure model of the Kanto Basin

The Kanto Basin spreads over an area of approximately 10000 km^2 in central Japan, with a sediment-bedrock interface locally deeper than 4 km (Fig. 1a). The characteristics of seismic wave propagation in the sediment in this basin have been investigated at the seismological observation wells of the National Research Institute for Earth Science and Disaster Prevention (NIED) by use of the vertical seismic profiling (VSP) method (e.g., Yamamizu, 1996 [10]; Yamamizu 2004 [11]). Fig. 1b shows the one-way travel time of *S*-waves from the surface to a certain depth (depth-time curve) obtained at 14 wells of the NIED. The slopes of the depth-time curves correspond to the reciprocals of *S*-wave velocity. Despite the local variation in the depth-time curves, this figure shows that the curves are smooth enough to suggest a continuous increase in *S*-wave velocity with depth at all sites. This observation indicates that the conventional layered structure modeling of *S*-wave velocity is not appropriate for the Kanto Basin.

In this report, we adopt a simple analytical velocity function, the exponential asymptotically bounded velocity function (Ravve and Koren, 2006)[9], for the expression of *S*-wave velocity in the Kanto Basin. This function assumes that the *S*-wave velocity $V(z)$ at a depth z is given by the equation

$$V(z) = V_0 + \Delta V\left[1 - \exp\left(-\alpha z / \Delta V\right)\right], \quad (1)$$

where V_0 is the *S*-wave velocity at $z = 0$, ΔV is the increment of the *S*-wave velocity at infinite depth, and α is the positive constant for adjusting the velocity-depth gradient. The velocity-depth gradient, which is controlled by the nonlinear exponential term in this equation, gradually decreases with increasing depth. For this function, the one-way travel time of *S*-waves $t(z)$ from $z = 0$ to a certain depth z is analytically calculated by the following equation:

$$t(z) = \frac{\Delta V}{\alpha\left(V_0 + \Delta V\right)} \ln \frac{\left(V_0 + \Delta V\right)\exp\left(\alpha z / \Delta V\right) - \Delta V}{V_0}. \quad (2)$$

Equation (2) can be directly applied to the results of the VSP measurements in the *S*-wave velocity structure modeling. Because the *S*-wave velocity in the sediment approaches the value in the bedrock as depth increases, we assumed ΔV = 3.2 km s^{-1} by referring to the JIVSM in our least-squares regression analysis. Figure 1c shows the best-fitting functions for the three wells close to the northern edge of the Kanto Basin. The result well explains the observed depth-time curves, except for the very shallow part of the Isesaki well. Similar results obtained at other wells (shown in Fig. 1d) confirm that the exponential asymptotically bounded velocity function is practically useful for modeling the *S*-wave velocity structure of the sedimentary basin. Figure 1e shows the depth variations of *S*-wave velocities at all wells analyzed in this study. Nonlinearity in the *S*-wave velocity increase with depth can be clearly seen in this figure.

Based on the above findings, we construct an *S*-wave velocity model in the Kanto Basin. We adopt a linear interpolation method to estimate sedimentary *S*-wave velocities over the target area. Figures 2a and 2b respectively show the local variation in V_0 and α estimated for the northern edge of the Kanto Basin. The values in the area are characterized mainly by the VSP observations at the Isesaki, Iwatsuki, and Mohka wells. An artificial boundary seen at southwestern part of Fig. 2b are due to the coarse distribution of VSP observation wells and may not affect our discussions in this report.

To construct a velocity structure model for 3-D FDM simulations, we modify the JIVSM by discarding three sedimentary layers and incorporating a sedimentary layer with the *S*-wave velocity-depth gradients estimated above. *P*-wave velocity and the density of the sediment are estimated by using empirical relations given by the Ministry of Education, Sports, Culture, Science and Technology (MEXT) (2007)[12] and Shiomi et al. (1997)[13], respectively. Anelastic attenuation Q-values of the sediment are taken from the JIVSM as it is, allowing depth dependent anelastic attenuation. Other structures beneath the sediment, including the bedrock, subducted oceanic plates, and mantle, are also taken from the JIVSM. We hereafter refer to the velocity structure model constructed in this study as the modified JIVSM.

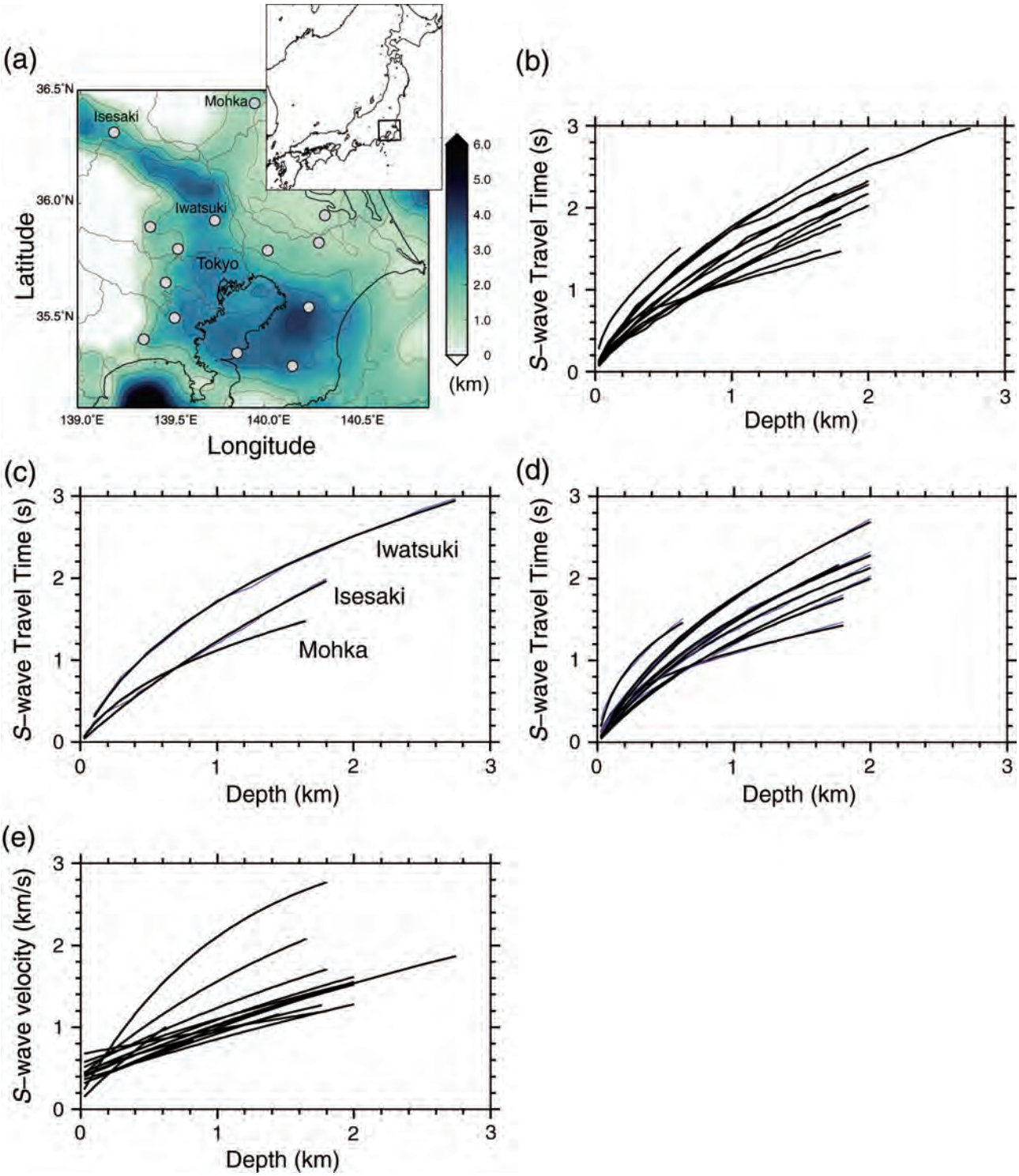

Fig. 1 (a) Map showing Kanto Basin and the locations of 14 seismic observation wells (gray circles), where VSP measurements were carried out. Local variation of sediment-bedrock interface depths from the JIVSM [8] is shown by color gradations. (b) One-way travel time of S-waves from the surface to certain depths obtained by VSP measurement at 14 wells (Yamamizu, 1996 [10]; Yamamizu, 2004 [11]). (c) Best-fitting exponential asymptotically bounded velocity functions (black lines) to the VSP observations at the Isesaki, Iwatsuki, and Mohka wells (blue lines). (d) Best-fitting exponential asymptotically bounded velocity functions (black lines) to the VSP observations at other wells (blue lines). (e) Depth variations of S-wave velocities at 14 wells evaluated by the best-fitting exponential asymptotically bounded velocity functions.

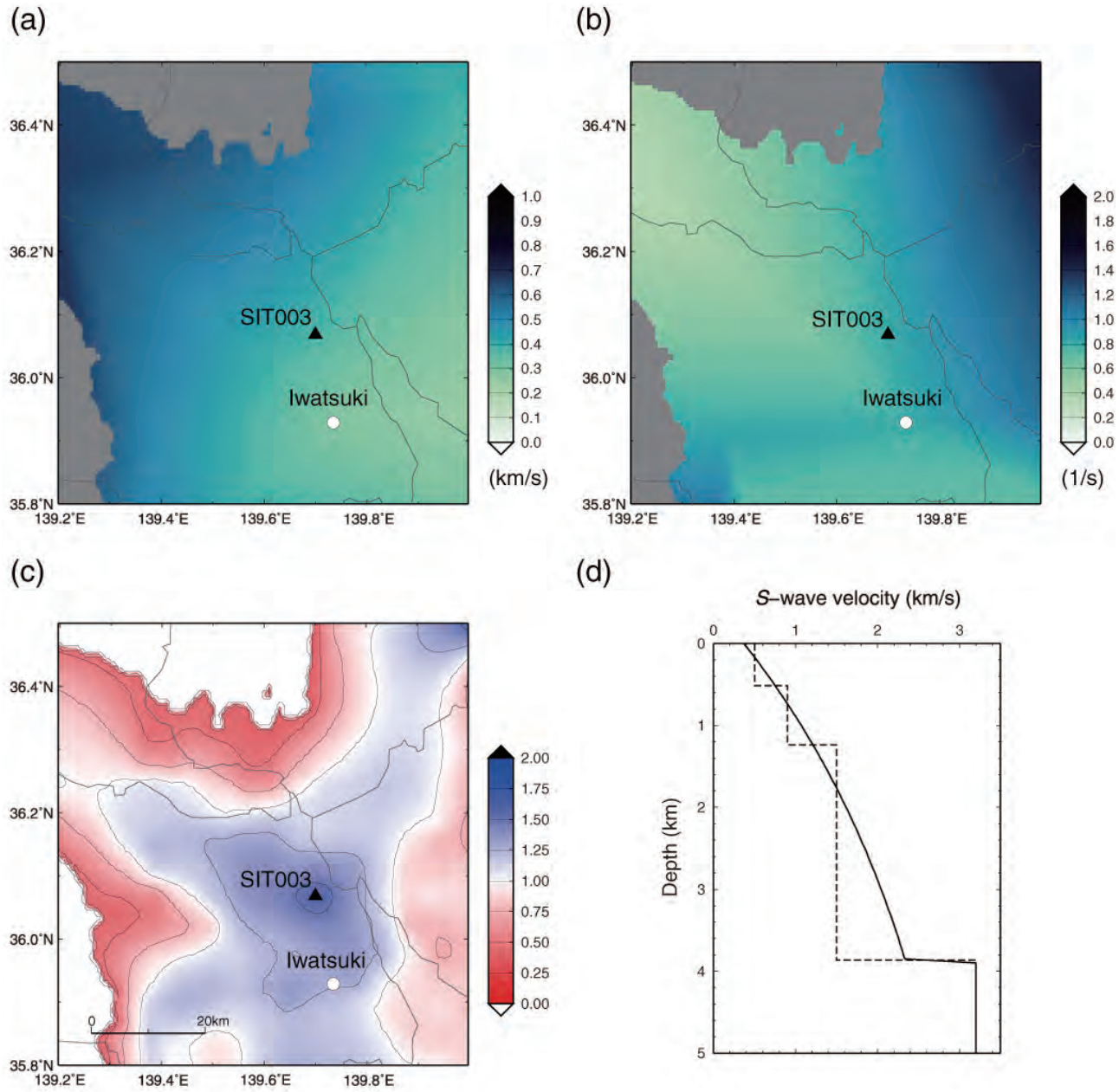

Fig. 2 (a) Local variations in V_0 estimated around the northern edge of the Kanto Basin. (b) Local variations in α. (c) Local variations in ratio of sedimentary *S*-wave velocity just above the bedrock of the modified JIVSM to that of the JIVSM. (d) *S*-wave velocity structure models beneath SIT003 from the JIVSM (broken line) and modified JIVSM (solid line).

3. 3-D FDM simulation of long-period ground motion around the northern Kanto

Using the velocity structure model constructed in the previous section, we conduct 3-D FDM simulation of long-period ground motion to examine the influence of the sedimentary velocity structure on the surface wave excitation at the basin edge. To conduct precise simulation of long-period ground motion in model with smooth velocity gradient, the computations were conducted on the Earth Simulator at the Japan Agency for Marine-Earth Science and Technology.

The model of the 3-D simulation covers an area of 320 km × 220 km in horizontal directions and 64 km in depth, which is discretized by a grid interval of 0.1 km in the horizontal directions and 0.05 km in the vertical direction. To perform an effective simulation, we employ a parallel 3-D FDM simulation code based on a domain-partitioning procedure that utilizes a large number of processors with the message passing interface (MPI) (e.g., Furumura and Chen, 2004 [14]; Maeda and Furumura, 2013 [15]).

The seismic source at the northern Tochigi Prefecture, corresponding to the seismic activity that occurred on February 25, 2013, at a depth of 8 km, is used in this simulation. A focal mechanism of strike/dip/rake = 168/86/-10° and moment magnitude of M_W = 5.8 are assumed by referring to the centroid moment tensor (CMT) solution of F-net. A source time function represented by the asymmetric cosine function (Ji et al., 2003 [16]) with t_s = 0.3 and t_e = 2.7 is adopted for a point seismic source. After the calculation, the value of seismic moment is

adjusted to 77% of CMT estimation to explain the observed waveform amplitude of a rock site (TCG011 shown in Fig. 3c).

Figure 3 shows record sections of transverse (T) component seismograms derived from simulations and dense-array observation. A band-pass filter with a pass-band of 0.125–0.25 Hz is applied to extract surface waves with a predominant period of approximately 7 s, and each trace is multiplied by the hypocenter distance to enlarge seismogram amplitudes at far stations. Because of the strong *SH*-wave source radiation in the direction of the Kanto Basin, large-amplitude *SH* waves are expected in the T component.

At hypocenter distances of less than 60 km, simulation results from the JIVSM and the modified JIVSM well reproduce waveforms observed by the KiK-net and K-NET of the NIED. This ability indicates that the modeling of the source and the velocity structure of the crust and uppermost mantle are appropriate for calculating the seismic wave propagation in this frequency range. As the hypocenter distances exceed 70 km, source-radiated body waves enter the Kanto Basin, and excitation of surface waves (Love waves) occurs at the edge of the basin. The simulated and observed seismic waves show strong amplification by the low-velocity sediment as they propagate toward the inner part of the Kanto Basin.

The amplitude of the Love waves derived from the simulation using the JIVSM (Fig. 3a) is much larger than that from observation (Fig. 3c). The JIVSM predicts strong excitation and development of the Love waves, and an unrealistically large wave packet appears at SIT010. Meanwhile, the amplitude of the Love waves derived from the simulation using the modified JIVSM (Fig. 3b) is much closer to that from observation, though it is still far from perfect fitting.

Figure 4 shows a comparison of horizontal-component waveforms at SIT003 as obtained from simulations and observations. SIT003 is located in the Kanto Basin and at 30 km from the basin edge. It is clear that a dominant wave packet of Love waves in the T component appears significantly earlier in the simulation using the JIVSM than in the observation. The simulation result using the modified JIVSM (Fig. 4b) drastically minimizes this inconsistency. Moreover, the amplitude and dispersion of the surface waves in both the T and the radial (R) components are well reproduced.

To examine the effect of velocity gradient model on the level of long-period ground motion in the Kanto basin, we calculated peak ground velocity (PGV) for frequency of 0.125–0.25 Hz using two horizontal component seismograms. Figure 5 shows PGV distributions derived from simulation results and observations. PGV from original JIVSM (Fig. 5a) was overestimated around the deeper basement region, such as southern Saitama, eastern Tokyo and Chiba. By introducing a velocity gradient model (Fig. 5b), the gap of PGV between simulations and observations became smaller. Thus, we conclude that the impedance contrast at the sediment-bedrock boundary in modified JIVSM may be more suitable compared to original JIVSM.

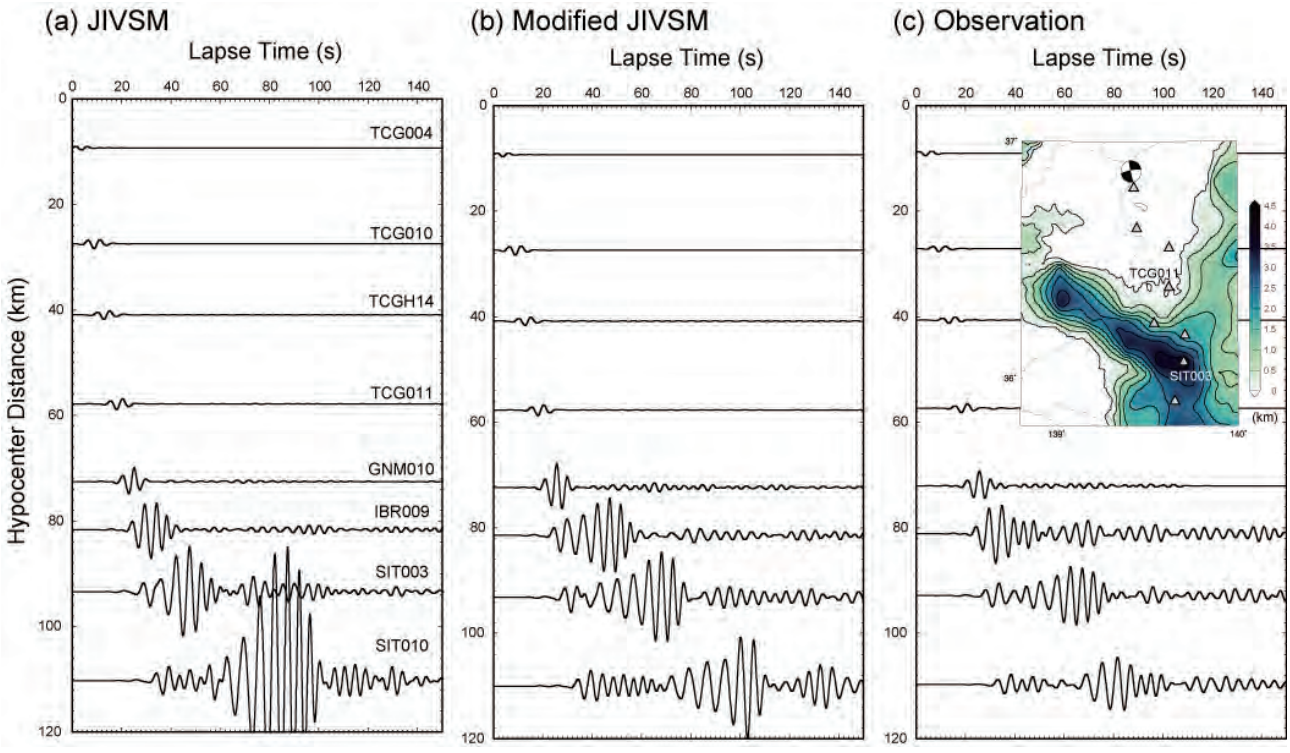

Fig. 3 Comparison between simulated and observed velocity seismograms of transverse component: (a) JIVSM, (b) modified JIVSM, and (c) observations. A band-pass filter with a pass-band of 0.125–0.25 is applied. Each trace is magnified by a factor proportional to the hypocenter distance to enlarge seismogram amplitudes at far stations. An inset map in (c) shows the locations of the epicenter and the observation stations, and the local variation of sediment-bedrock interface depths from the JIVSM.

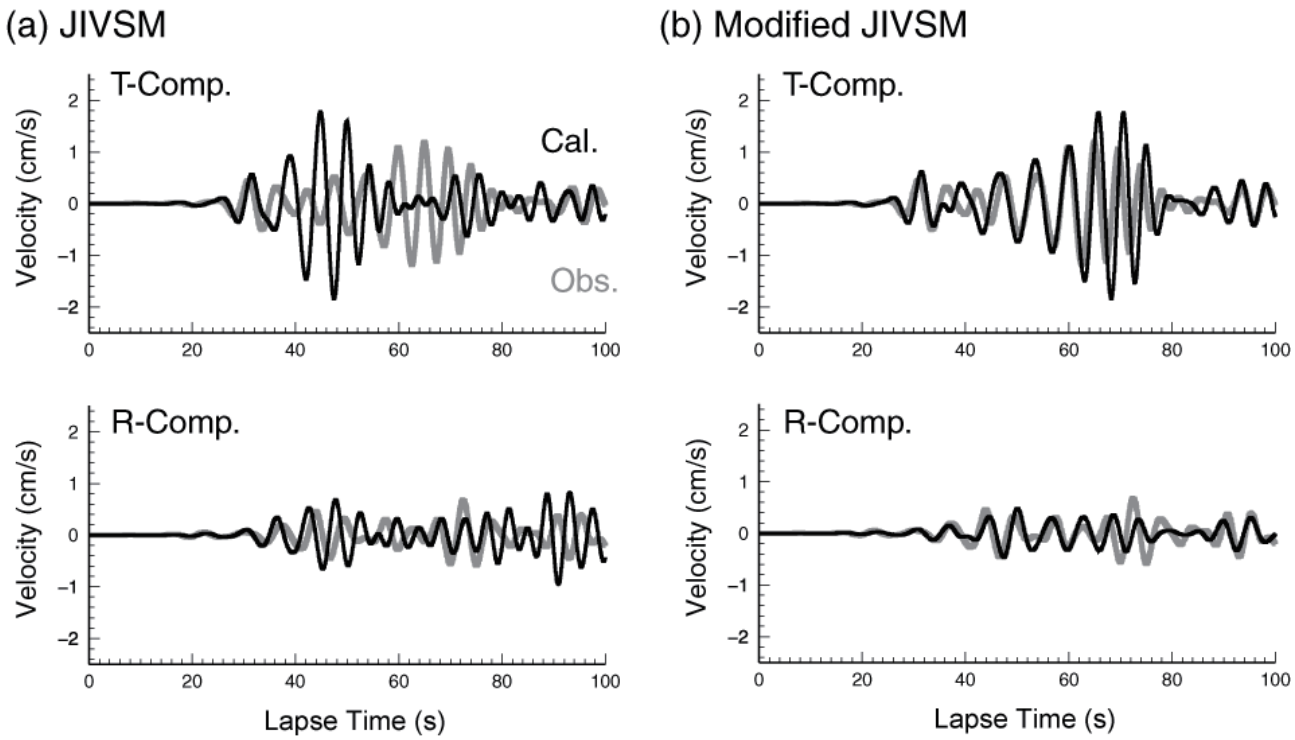

Fig. 4 Comparison of horizontal seismograms recorded at SIT003 between simulations and observation: (a) JIVSM and (b) modified JIVSM. The black and gray lines represent the simulation results and observations, respectively.

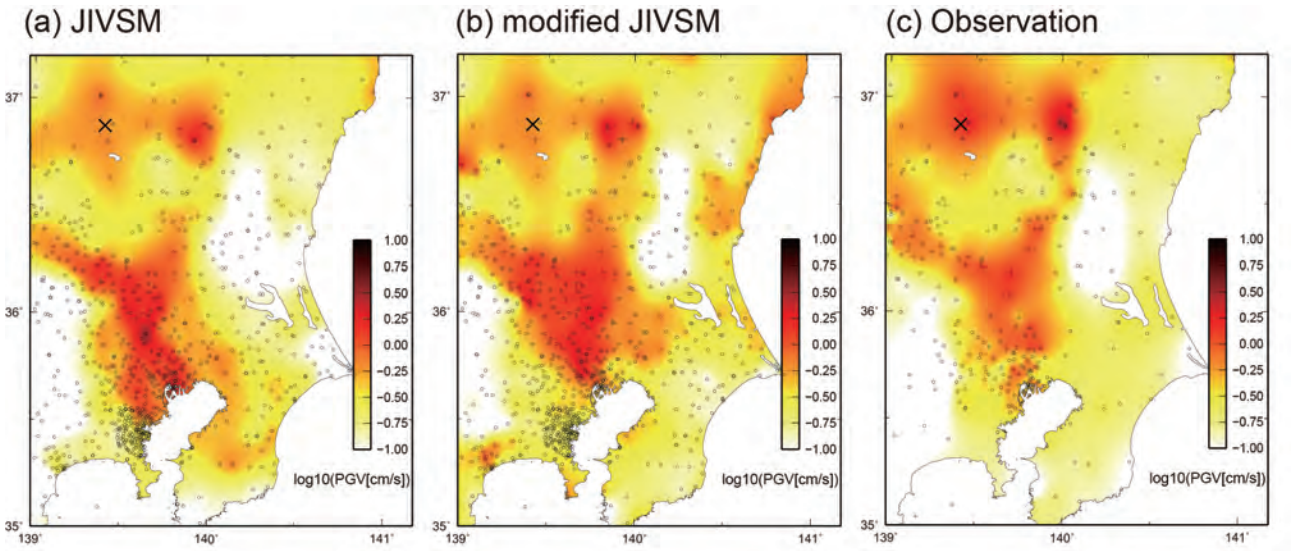

Fig. 5 Peak ground velocity (PGV) distributions derived from horizontal seismograms for 0.125-0.25 Hz: (a) JIVSM, (b) modified JIVSM, and (c) observation.

4. Discussion and Conclusion

Our 3-D FDM simulation using the modified JIVSM well reproduced the characteristics of the surface waves observed at the northern edge of the Kanto Basin in the frequency range of 0.125–0.25 Hz. In particular, the appearance of the dominant wave packet of Love waves was satisfactorily reproduced by introducing the velocity gradient of sediment into the JIVSM. Because the depth of the bedrock, which is supposed to be well constrained in the refraction/reflection experiments (e.g., Hamada et al., 1990)[17], was not modified in our simulations, the improvement in the reproducibility can be attributed solely to the modeling of the sedimentary structure.

The dominant wave packet of Love waves recorded at SIT003 shows clear normal dispersion, indicating the propagation of this packet over a certain distance where arrival-time differences of 40 s can be expected between the direct *S*-waves and the Love waves. However, the simulated Love wave packet at SIT003 using the JIVSM precedes the corresponding wave packet in the observation by 20 s and shows very weak dispersion, implying Love wave excitation close to this station. Because the surface wave is excited by the trapping of the body-wave energy in a low-velocity surface structure, the abovementioned discrepancy

is most probably the result of inexact modeling of the impedance contrast at the sediment-bedrock interface. Figure 2c shows the local variation in the ratio of the sedimentary *S*-wave velocity just above the bedrock of the modified JIVSM to that of the JIVSM. This ratio is relatively small at the extreme edge of the basin (within 15 km of the border), where the bedrock is not deeper than approximately 2 km; the ratio is conversely large in the inner part of the basin, where SIT003 is located. This observation indicates that the modified JIVSM has a higher potential to excite Love waves at the extreme edge of the basin than does the JIVSM. Figures 3b and 4b show that the dominant wave packets of the observed Love waves are well explained by the simulation using the modified JIVSM. This result strongly suggests that the Love waves are excited at the extreme edge of the basin, and propagate toward the inner part of the basin with a group velocity of approximately 1 km/s.

To investigate the influence of the velocity gradient in the sediment on the surface wave propagation, we conducted additional 3-D FDM simulations using simple 1-D velocity structure models from the SIT003 site of the JIVSM and the modified JIVSM (Fig. 2d). Although the figures are not shown here owing to space constraints, they confirm that no apparent difference exists between the two models in terms of the group velocity and the dispersion of the Love waves in the frequency range of 0.125–0.25 Hz. This result implies that the incorporation of the velocity gradient affects the surface wave excitation much more strongly than it affects the surface wave propagation at the basin edge in the analyzed frequency range.

The results of this study indicate that a realistic velocity structure model is required to explain the excitation and propagation of the surface wave in the sedimentary basin. Our results also strongly suggest that the dominant wave packet of Love waves is excited at the extreme edge of the Kanto Basin and propagates toward the inner part of the basin. This finding indicates that the study of the surface wave excitation at the extreme edge of the basin, including dense-array observations, is quite important for the precise evaluation and prediction of the long-period ground motion in the Tokyo metropolitan area.

We showed a case study in which the realistic modeling of the sedimentary velocity structure improves the geophysical reproducibility of the surface wave excitation at basin edge, but the highly accurate modeling of the phase and amplitude of excited surface waves remains as a matter to be studied further. It is obvious that the number of the VSP measurements used in this study is insufficient to construct an accurate sedimentary structure model of the Kanto Basin. Concerning this matter, we should determine the local variation of the model parameter of the sedimentary structure (e.g, V_0 and α of the *S*-wave velocity) using geophysical analyses such as phase and group velocity analysis, spectral analysis and a waveform inversion of surface waves of local and/or regional earthquake. For the fully accurate modeling of the sedimentary structure, an additional consideration how to specify the relation among the structural parameters, including anelastic parameter, may be required.

Acknowledgments

We acknowledge the National Research Institute for Earth Science and Disaster Prevention (NIED), Japan, for providing the KiK-net and K-NET waveform data and CMT solutions from the F-net. The computations were conducted on the Earth Simulator at the Japan Agency for Marine-Earth Science and Technology (JAMSTEC) under the support of a joint research project entitled “Seismic wave propagation and strong ground motion in 3-D heterogeneous structure” of the Earthquake Research Institute, the University of Tokyo, and the Earth Simulator Center. Some figures in the present study were drawn using the Generic Mapping Tools (GMT) software package developed by Wessel and Smith (1998) [18].

References

[1] Yamanaka, H., K. Seo, and T. Samano (1989), Effects of sedimentary layers on surface-wave propagation, *Bull. Seismol. Soc. Am.*, 79, 631–644.

[2] Kinoshita, S., H. Fujiwara, T. Mikoshiba, and T. Hoshino (1992), Secondary Love waves observed by a strong-motion array in the Tokyo lowlands, Japan, *J. Phys. Earth*, 40, 99–116.

[3] Sato, T., R. W. Graves, and P. G. Somerville (1999), Three-dimensional finite-difference simulations of long-period strong motions in the Tokyo metropolitan area during the 1990 Odawara earthquake (MJ 5.1) and the great 1923 Kanto earthquake (MS 8.2) in Japan, *Bull. Seismol. Soc. Am.*, 89, 579–607.

[4] Koketsu, K. and M. Kikuchi (2000), Propagation of seismic ground motion in the Kanto basin, Japan, *Science*, 288(5469), 1237-1239, DOI: 10.1126/science.288.5469.1237.

[5] Kawase, H. and K. Aki (1989), A study on the response of a soft basin for incident S, P, and Rayleigh waves with special reference to the long duration observed in Mexico city, *Bull. Seismol. Soc. Am.*, 79, 1361–1382.

[6] Hatayama, K., K. Matsunami, T. Iwata, and K. Irikura (1995), Basin-induced Love waves in the eastern part of the Osaka basin, *J. Phys. Earth.*, 43, 131–155.

[7] Furumura, T. and T. Hayakawa (2007), Anomalous propagation of long-period ground motions recorded in Tokyo during the 23 October 2004 Mw 6.6 Niigata-ken Chuetsu, Japan, Earthquake, *Bull. Seismol. Soc. Am.*, 97, 863–880, doi: 10.1785/0120060166.

[8] Koketsu, K., H. Miyake, H. Fujiwara, and T. Hashimoto (2008), Progress towards a Japan integrated velocity structure model and long-period ground motion hazard map, *In Proceedings of the 14th World Conference on Earthquake Engineering*, S10–038.

[9] Ravve, I. and Z. Koren (2006), Exponential asymptotically bounded velocity model: Part I – Effective models and velocity transformations, *Geophysics*, 71, T35–T65, doi:10.1190/1.2196033.

[10] Yamamizu, F. (1996), Down-hole measurements of seismic wave velocities in deep soil deposits beneath the Tokyo metropolitan area, *Report of the National Research Institute for Earth Science and Disaster Prevention*, 56, 1–32.

[11] Yamamizu, F. (2004), Seismic wave velocity structures in Kanto area as revealed by the crustal activity observation well VSP, *Technical Note of the National Research Institute for Earth Science and Disaster Prevention*, 251, 1–75 (in Japanese with English abstract).

[12] Ministry of Education, Sports, Culture, Science and Technology, Japan (MEXT) (2007), Deep Seismic Exploration, *Annual report of Special Project for Earthquake Disaster Mitigation in Urban Areas, I. Regional characterization of the crust in metropolitan areas for prediction of strong ground motion*, 215–230.

[13] Shiomi, K., H. Sato, and M. Ohtake (1997), Broad-band power-law spectra of well-log data in Japan, *Geophys. J. Int.*, 130, 57–64, doi:10.1111/j.1365-246X.1997.tb00987.x.

[14] Furumura, T. and L. Chen (2004), Large scale parallel simulation and visualization of 3-D seismic wavefield using *Earth Simulator*. *Comput. Model. Sci*., 6, 153-168, doi:10.3970/cmes.2004.006.153.

[15] Maeda, T. and T. Furumura (2013), FDM simulation of seismic waves, ocean acoustics waves and tsunami based on tsunami-coupled equations of motion, *Pure Apple. Geophys*., 170, 109–127, doi:10.1007/s00024-011-0430-z.

[16] Ji., C., D.V. Helmberger, D.J. Wald, and K.F. Ma (2003), Slip distribution and dynamic implication of the 1999 Chi-Chi, Taiwan earthquake, *J. Geophys. Res*., 108, 2412, doi:10.1029/2002JB001764.

[17] Hamada, K., F. Kaneko, T. Yamada, and T. Doi (1990), Characteristics of medium-long period seismic motion based on the results of seismic prospecting in Saitama prefecture [in Japanese with English abstract], *Oyo Chishitsu Nenpo*, 12, 13–37.

[18] Wessel, P. and W. H. F. Smith (1998), New improved version of generic mapping tools released, *EOS, Trans. Amer. Geophys. Union*, 79 (47), 579, doi:10.1029/98EO00426.

地球シミュレータによる関東平野北部で励起した長周期地震動のシミュレーション

課題責任者
古村　孝志　　東京大学　大学院情報学環総合防災情報研究センター
　　東京大学　地震研究所
著者
武村　俊介　　横浜市立大学　生命ナノシステム科学研究科
吉本　和生　　横浜市立大学　生命ナノシステム科学研究科

より高精度な長周期地震動のシミュレーションを行うために、中深層の観測井による VSP 調査の結果から堆積層内の S 波速度構造の特徴を調査した。その結果、既往のモデルで用いられているような 3 層構造ではなく、深さに対してゆるやかに速度が増大するような構造により VSP 調査の結果を正確に表現できることを明らかにした。鉛直速度勾配を含んだ堆積層の速度構造を用いて栃木県北部の地震（Mw 5.8）の地震動シミュレーションを行った結果、関東平野北部における長周期地震動の励起・伝播を再現することに成功した。これらの結果から、地震基盤におけるインピーダンスコントラストを正確に表現することが長周期地震動を再現する上で重要であることが示唆された。

キーワード:地震, 表面波, 長周期地震動, 不均質構造, 堆積盆地構造

Development of Advanced Simulation Methods for Solid Earth Simulations

Project Representative

Mikito Furuichi Institute for Research on Earth Evolution, Japan Agency for Marine-Earth Science and Technology

Authors

Mikito Furuichi[*1], Akira Kageyama[*2], Takehiro Miyagoshi[*1], Masanori Kameyama[*3], Nobuaki Ohno[*4], Takashi Nakagawa[*1], Kensuke Yokoi[*5] and Daisuke Nishiura[*1]

*1 Institute For Research on Earth Evolution, Japan Agency for Marine-Earth Science and Technology

*2 Graduate School of System Informatics, Kobe University

*3 Geodynamics Research Center, Ehime University

*4 Graduate School of Simulation Studies, University of Hyogo

*5 Cardiff University

Geodynamo: We have performed numerical geodynamo simulations with length-of-day (LOD) variation associated with Milankovitch cycle by using the Yin-Yang geodynamo code which was developed in this project. We mainly investigated the period of twenty thousand years for LOD variation. We found that the LOD variation causes geomagnetic field variation. It strongly affects the fluid flow, the Joule heating, and so on. The change of the Joule heating is important for geomagnetic field variation.

Numerical planet: We have developed simulation code for a growing planet with core formation in 3D. In this FY, we have developed the implicit time stepping technique toward thermal convection simulation surrounded by sticky air. Our proposed method which deals with the material transport as a nonlinearity, is found as effective scheme to reduce the computational cost to obtain the numerically stable solution in comparison to the conventional explicit time stepping method.

Keywords: Geodynamo simulation, Length-of-Day variation, Yin-Yang grid, Mantle convection, Core formation, Stokes flow, mixed precision arithmetic, implicit time integration, inexact newton like nonlinear solver

1. Geodynamo simulation (Miyagoshi)

We have studied geomagnetic field variation associated with the Milankovitch cycle by magnetohydrodynamic (MHD) geodynamo simulations by using the Yin-Yang dynamo code which was developed and used in this project [1][2][3]. The geomagnetic field is not temporally constant and changes with various periods. By recent progresses of paleomagnetism, geomagnetic field variations with the periods of several tens of thousands years have been discovered [4]. For this variation, the relation to climatic changes is pointed out [5]. The relation is as follows. The cycle of ice and non-ice ages arises by the variation of the intensity of solar radiation caused by the Milankovitch cycle. The volumes of continental ice sheets also changes with the cycle. This causes redistribution of water mass on the Earth, thus changes of the inertial momentum of the Earth. It causes rotational speed changes or length-of-day (LOD) variations (Fig.1). The LOD variation may affect geomagnetic field variation through changes of convection of fluid iron in the Earth's outer core. However, there was no geodynamo model with LOD variation. We have investigated the mechanism of geomagnetic field variation with the period of twenty thousand years, which is close to one of the Milankovitch cycle.

The mechanism of geomagnetic field variation is found by the detail analysis of numerical simulation results. Our results

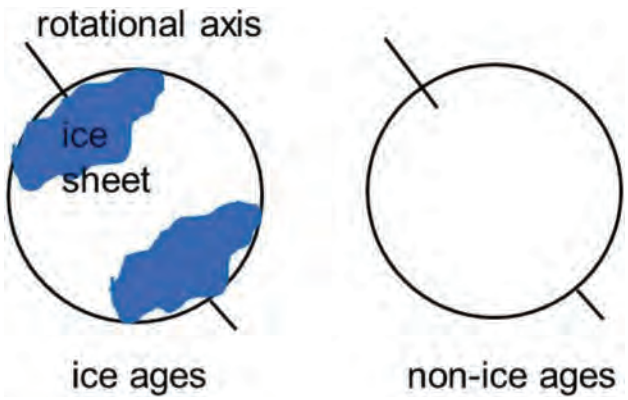

Fig. 1 The schematic picture of the LOD variation by the Milankovitch cycle. In ice ages the water mass concentrates near the polar region by the development of the continental ice sheet while there is no concentration in non-ice ages. This causes the LOD variation.

show that geomagnetic field changes with the amplitude of several tens of percent. We found that the important factor for geomagnetic field variation is the variation of the Joule heating. The LOD variation initially affects the fluid motion in the core. The Joule heating is strongly affected by the change of convection, thus it changes associated with LOD variation. We published the paper for detail results in this fiscal year [6]. The contents of the study were press released from Japan Agency for Marine-Earth Science and Technology (JAMSTEC).

2. Mantle convection simulation (Miyagoshi & Kameyama)

We have studied the mantle convection in super-Earths by the ACuTEMAN code [7-8]. Super-Earths are extra-solar terrestrial massive planets. The mass reaches ten times the Earth's at the maximum. The mantle convection affects the operation of plate tectonics, or the generation of the planet's magnetic field through influences to core convection. These factors are related to the habitability of the super-Earths. The mantle convection also affects the thermal evolution history of super-Earths. Our motivation is to understand the fundamental physical process of mantle convection in super-Earths and get keys to understand these problems.

One of the important factors for mantle convection in super-Earths is a strong adiabatic compression effect. The size of super-Earths is of course considerably large than that of the Earth, which means the adiabatic compression effect and the stratification of the density are important. The intensity of the adiabatic compression effect is measured by the dissipation number $D_i=\alpha gd/C_p$, where α is the thermal expansivity, g is the gravity, d is the thickness of the mantle, and C_p is the specific heat in constant pressure, respectively. In the Bousinnesq approximation which is often used in models of the mantle convection for the Earth, the adiabatic compression effect is neglected and D_i is regarded as zero. At the surface of massive super-Earths with ten times the Earth's mass, the D_i reaches about 5. We take 5 for the D_i.

Figure 2 shows one of the numerical simulation results. In this simulation, the Rayleigh number is 10^{10} and the temperature-dependent viscosity contrast between the top and the bottom is 10^3. One of the important results is that the activity of hot plumes is totally lowered while that of cold plumes remains strong. The reason is as follows. The adiabatic compression effect depends on the original temperature of plumes. The buoyancy force of hot plumes is weakened because of the increment of the adiabatic temperature gradient by the strong adiabatic compression effect. In contrast, the negative buoyancy of cold plumes is hardly weakened because the adiabatic compression effect depends on the original temperature of plumes. In addition, by the formation of the thick lithosphere due to the high viscosity contrast, the temperature of the isothermal core increases. This reduces the difference of the temperature between hot plumes and ambient materials so the buoyancy force of hot plumes is more and more lowered. The result is published in this fiscal year [9].

3. Core formation simulation: numerical planet (Furuichi)

We have been developed a numerical code for simulating global sinking of the dense metal-rich material over long time scale during the planetary core formation process. Our code named "Nplat", solves the Stokes flow motion with free surface under a self-gravitation by using the sophisticated algorisms designed for ES2 [10-13]. With this code, we can investigate the dynamical change of the internal structure owning to the compositional density anomaly during the core formation. Such dynamics might generate thermal and compositional heterogeneity on the CMB. The conventional explicit time stepping algorithm however is difficult for simulating a thermal evolution because a numerical oscillation problem arises in solving free surface motion.

To investigate an efficient solution strategy for such free surface thermal convection problem, we have developed the implicit time integration schemes. We deal with the material transport given by tracer makers as the nonlinearity coupled to the Stokes flow equations. As the nonlinear solver, we employ the inexact newton-like nonlinear solver implemented with Jacobian free newton Krylov (JFNK) and Picard preconditioner.

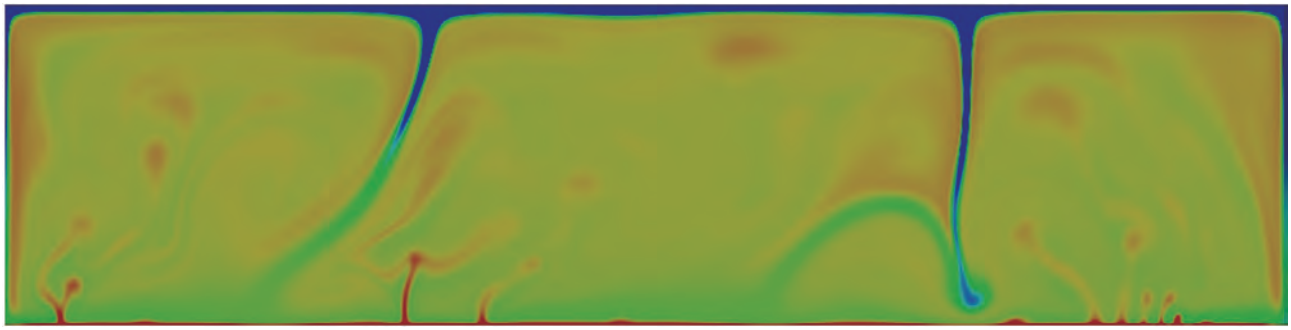

Fig. 2 One of the numerical simulation results for mantle convection in super-Earths. The color shows the potential temperature distribution. Red is large and blue is small, respectively.

In order to evaluate the performance by our solver, we solved thermal evolution problem surrounded by sticky air layers of Fig. 3a. Fig. 4a and Fig. 4b show the averaged velocity of the middle layer by the explicit and implicit time stepping methods, respectively. The explicit method requires the small time step size (CFL $\geqq$ 5.0e-3) to obtain the numerically stable solution, but implicit method is found to be unconditionally stable for time step size. Fig. 3b shows the computational cost and load balance by each solution method to reach t = 1.0e7. With the implicit time stepping technique (Imp), we could reduce 60% of CPU time compared with explicit method (Explicit). We also propose the semi-implicit method (Semi-imp) which uses grid based advection method to reduce the cost to evaluate the nonlinear residual. Our proposed semi-implicit method successfully reduces 90% of CPU time by the conventional explicit method.

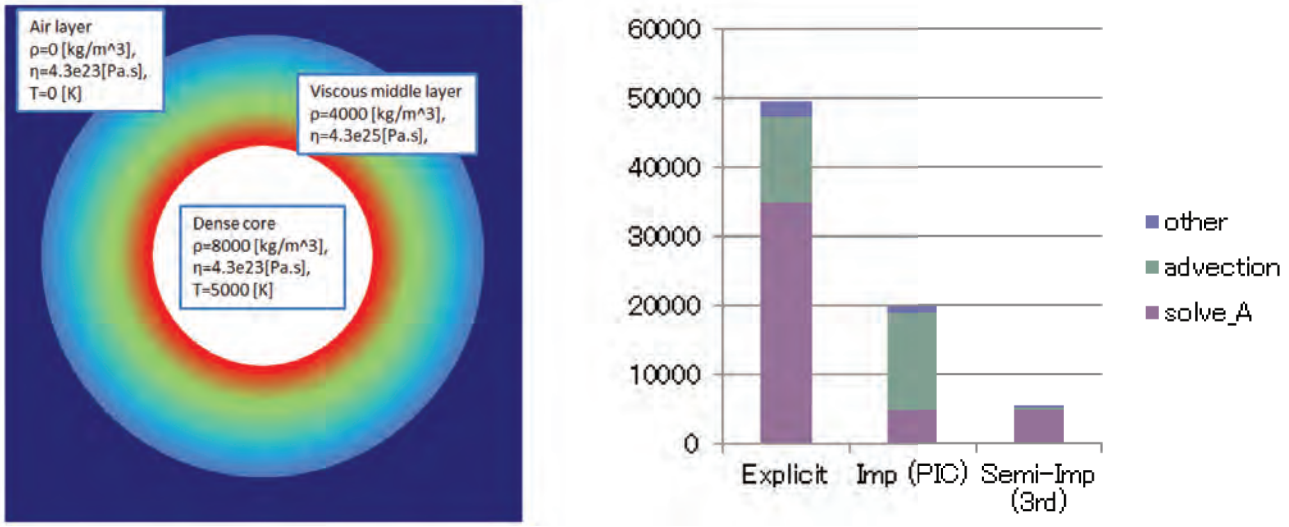

Fig. 3 Left:(a) initial temperature profile of three layers. Right:(b) CPU time and load balance to solve free surface thermal convection. Explicit, Imp (PIC) and Semi-imp (3rd) stand for the explicit, full implicit and semi-implicit time integration method, respectively.

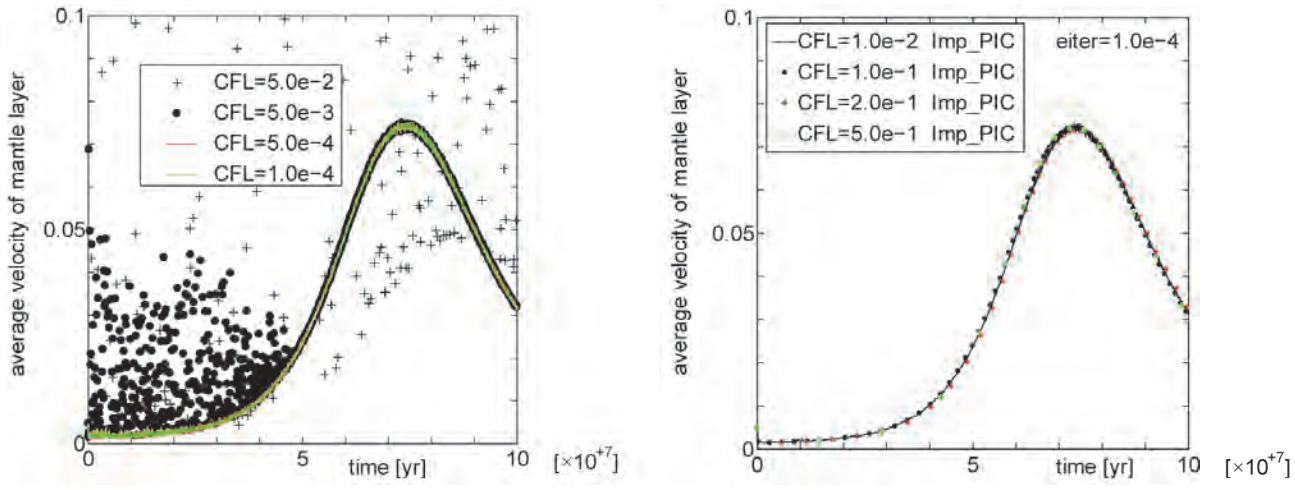

Fig. 4 Plot for averaged velocity of middle layer in free surface thermal convection test. Left :(a) Explicit time stepping method. Right :(b) Implicit material transport method

References

[1] A. Kageyama and T. Sato, Geochem. Geophys. Geosyst., 5, Q09005, 2004.

[2] Akira Kageyama, Takehiro Miyagoshi, and Tetsuya Sato, Nature, vol. 454, pp. 1106-1109, 2008.

[3] Takehiro Miyagoshi, Akira Kageyama, and Tetsuya Sato, Nature, vol. 463, pp. 793-796, 2010.

[4] Toshitsugu Yamazaki, (In Japanese) Journal of Geography, vol. 114, pp.151-160, 2005.

[5] Yozo Hamano, (In Japanese) Kagaku, vol.62, No.1, pp.14-18, 1992.

[6] Takehiro Miyagoshi and Yozo Hamano, Phys. Rev. Lett., 111, 124501, 2013.

[7] M. Kameyama, A. Kageyama, and T. Sato, J. Comput. Phys., 206, 162-181, 2005.

[8] M. Kameyama, J. Earth Simulator, 4, 2-10, 2005.

[9] Takehiro Miyagoshi, Chihiro Tachinami, Masanori Kameyama, and Masaki Ogawa, Astrophys. J. Lett., 780, L8, 2014.

[10] M. Furuichi, M. Kameyama, and A. Kageyama, J. Comput. Phys., 227, 4977–4997, 2008.

[11] M. Furuichi, M. Kameyama, and A. Kageyama, Phys. Earth Planet. Inter., 176, 44-53, 2009.

[12] M. Furuichi, D. A. May, P. J. Tackley, and J. Comput. Phys., 230, 8835-8851, 2011.

[13] M. Furuichi, proceedings of International Conference on Computational Science, ICCS 2011, 2011.

先端的固体地球科学シミュレーションコードの開発

課題責任者
古市　幹人　　海洋研究開発機構　地球内部ダイナミクス領域
著者
古市　幹人 *1，陰山　　聡 *2，宮腰　剛広 *1，亀山　真典 *3，大野　暢亮 *4，中川　貴司 *1，
横井　研介 *5，西浦　泰介 *1
*1 海洋研究開発機構　地球内部ダイナミクス領域
*2 神戸大学　大学院システム情報学研究科
*3 愛媛大学　地球深部ダイナミクス研究センター
*4 兵庫県立大学大学院　シミュレーション学研究科
*5 カーディフ大学

本プロジェクトでは、地球シミュレータ２を活用した先端的なシミュレーションコードを開発することにより、惑星の形成過程から地球ダイナモの生成並びにマントル対流の駆動といった固体地球科学ダイナミクスの諸問題の解決に取り組んでいる。さらにコード開発で得られた知見は積極的に他分野でも応用する事を目指している。

ダイナモ：本プロジェクトで開発された Yin-Yang ダイナモコードを用いて、気候変動による氷期―間氷期サイクルに伴う自転速度変動を考慮した地球ダイナモシミュレーションを行った。ミランコビッチサイクルの一つに極めて近い 2 万年周期の自転速度変動を考慮した計算を行った結果、コア内の経度方向の流れが強く変動する事、ジュール散逸の変動が磁場変動に重要な役割を果たしている事等が分かった。得られた成果を“Physical Review Letters”誌に成果を発表し、海洋研究開発機構よりプレスリリースも行われた。

マントル：本プロジェクトで開発された ACuTE 法を用いて、スーパーアースのマントル対流の数値シミュレーションを行った。その結果強い断熱圧縮の効果によりコア―マントル境界からのホットプルームがかなり弱められる事、対照的に惑星表面からのコールドプルームはあまり弱められない事等が分かった。得られた成果を“Astrophysical Journal Letters”誌に発表した。

数値惑星：コア形成時のグローバルスケールの金属層の落ち込みを再現する 3 次元シミュレーションコードを開発している。本年度は、隕石衝突イベントにより地球内部に持ち込まれる熱を変形する表面形状と共に追跡するための、ソルバーの改良を行った。具体的には移流解を陰的に取り扱うための大規模非線形ソルバーを開発し、時間ステップを用いて計算コストを大幅に削減する事に成功した。

キーワード:地球ダイナモ, インヤン格子, 地球回転変動, マントル対流, コア形成, ストークス流れ, 陰解法,
大規模非線形ソルバー

3D Numerical Simulations of Eruption Cloud Dynamics and Tephra Dispersal

Project Representative
Takehiro Koyaguchi Earthquake Research Institute, The University of Tokyo

Authors
Yujiro Suzuki Earthquake Research Institute, The University of Tokyo
Takehiro Koyaguchi Earthquake Research Institute, The University of Tokyo

We are developing a three-dimensional (3D) numerical model that reproduces the formation of volcanic plume, the tephra dispersal in the atmosphere and the deposition of tephra on the ground under various wind conditions. We have carried out simulations for two extreme cases: a weak plume in a strong wind field and a strong plume in a weak wind field. When the magma discharge rate is low and the wind speed in the atmosphere is high, the mixture of the volcanic gas and solid pyroclasts ejected from the vent is largely distorted by the wind. The tephra particles drift leeward at the neutral buoyancy level (NBL) where the cloud density is equal to the atmospheric density; as a result, the dispersal axis of main tephra fall deposits extends leeward. On the other hand, if the magma discharge rate is high and the wind speed is slow, the eruption cloud (the mixture of the ejected material and entrained air) rises almost vertically and forms a concentric umbrella cloud at the NBL. The tephra particles are transported radially and deposit in both leeward and windward regions. In this case, the distribution of fall deposits slightly elongates in the downwind direction owing to the wind effect. On the basis of the simulation results, the distribution of number density of marker particles and the size distribution on the ground are obtained. These distributions can be compared with the isomass and isopleth maps based on field observations.

Keywords: volcanic eruption, eruption column, ash dispersal, volcanic hazard

1. Introduction

Explosive volcanic eruptions can cause a widespread tephra dispersal. During explosive eruptions, a mixture of solid particles (pyroclasts) and volcanic gas is ejected from vents into the atmosphere. As the ejected material entrains ambient air by turbulent mixing, the entrained air expands rapidly owing to the heating from the hot pyroclasts. Consequently, the density of the cloud (i.e., the mixture of the ejected material and the entrained air) becomes lower than the atmospheric density and forms buoyant plume [1, 2]. The eruption cloud exhausts its thermal energy and loses its buoyancy within the stratified atmosphere. At the level where the cloud density is equal to that of the atmosphere (i.e., NBL), the eruption cloud spreads laterally. Tephra particles are lifted upward by buoyant plume and transported by laterally-spreading cloud.

The flow patterns of eruption cloud, and hence, the depositional patterns of tephra particles are controlled by the intensity of eruption and the strength of the atmospheric wind [3, 4]. At high eruption intensities and/or under weak wind speeds, plume trajectories are not wind-affected. In this case, a plume rises vertically, and subsequently it spreads radially as an umbrella cloud at the NBL. Tephra particles are separated from the vertically-rising plume or radially-spreading cloud; as a result, the tephra particles are distributed concentrically on the ground. In contrast, if eruption intensity is weak and/or wind speeds are high, volcanic plumes are highly distorted by the wind, leading to a bent-over trajectory. In this case, the tephra particles can be transported leeward and its depositional area can significantly deviate from concentric distribution.

Recent progress has been made on developing a more quantitative understanding of the wind-effects on the depositional patterns of tephra particles [e.g., 5]. However, in these studies, the distributions of tephra particles in eruption clouds are given as an initial conditions on the basis of one-dimensional models of volcanic plume [6, 7]. We attempt to directly simulate the motion of tephra particles ejected from the vent in the atmosphere and their deposits on the ground using a 3D numerical model.

2. Numerical model

Our numerical model is designed to simulate the behavior of a gas-particle mixture ejected into the stratified atmosphere with one-way coupling between fluid and particle motions [8]: marker particles do not have any effect on the fluid, whereas the particle motion depends on the fluid motion. During fluid dynamics calculations, we ignore the separation of solid

pyroclasts from the eruption cloud, treating an eruption cloud as a single gas with a density calculated using a mixing ratio between ejected material and entrained air [9]. The governing equations are solved numerically by a general scheme for compressible flow. For the calculations of particle motion, our model employs Lagrangian marker particles of ideal sphere. The density of particles is assumed to be 1000 – 2500 kg m^{-3}, and about 200 marker particles are ejected from the vent every 2 sec at the same velocity as the pseudo-gas. Particle grain sizes are randomly selected within a range of 0.0625 to 64 mm. The terminal velocity is added to the vertical velocity of fluid motion at every time step, until the marker particle ceases its motion and settles as sediment when it reaches the ground surface.

3. Simulation results

In order to understand the wind-effects on the tephra dispersal, we carried out numerical simulations for two cases: a weak plume in a strong wind field and a strong plume in a weak wind field.

3.1 Weak plume in strong wind field

Magma discharge rate is set to be 2.5×10^6 kg s^{-1}. The speed of horizontal wind linearly increases with height, reaching 80 m s^{-1} at Z = 10 km. The wind speed is assumed to be horizontally uniform at each height, with vertical wind velocity assumed to be zero. The volatile content (H_2O) and magma temperature are 2.84 wt% and 1000 K, respectively. The mid-latitude atmosphere is applied to calculate the atmospheric density, pressure, and temperature.

A computational domain extends 13 km vertically (Z– direction) and 30 km × 12 km horizontally (X– and Y– directions, respectively). The boundaries are located at X = –3, 27 km (YZ – plane) and Y = –6, 6 km (XZ – plane). Grid sizes are set to be D_0/16 near the vent, where D_0 is the vent diameter, and to increase at a constant rate (by a factor of 1.02) with distance from the vent up to D_0/2.

Our simulation successfully reproduced fundamental features of typical weak plumes in the strong wind fields (Fig. 1). The plume near the vent is largely distorted by wind. A distal horizontally moving cloud develops at the NBL (6 – 8 km a.s.l.). Our simulations also reproduce particle separation and sedimentation from the volcanic plume (Fig. 1c). The marker particles ejected from the vent are lifted upward by the bent-over plume, and leave from the cloud because their density is higher than that of the gas phases. Fine particles (shown by red points) are transported to the top of the plume, are carried by the horizontally moving cloud, and spread leeward. In contrast, coarse particles (blue points) leave from the volcanic plume and fall to the ground near the vent. Medium-sized particles (light blue points) show intermediate features between the fine and coarse particles; they are lifted up to higher level than the coarse particles, but do not reach the top of the plume.

On the basis of the simulation results of marker particles settled on the ground, we obtain the distribution of tephra deposits (Fig. 2a) and their particle size distribution (Fig. 2b). The results show the general features that the dispersal axis of main fall deposits extends leeward and that the number and the maximum size of particles decreases with distance from the vent.

3.2 Strong plume in weak wind field

Magma discharge rate is set to be 1.0×10^9 kg s^{-1}. The speed of horizontal wind is given as $U_{wind} = 15\tanh(Z/1000)$ m s^{-1}. The volatile content (H_2O) and magma temperature are 4 wt% and 1053 K, respectively. The tropical atmosphere is applied to calculate the atmospheric density, pressure, and temperature.

A computational domain extends 58 km vertically (Z-direction) and 456 km × 456 km horizontally (X- and Y-directions, respectively). The boundaries are located at X = –192, 264 km (YZ – plane) and Y = –228, 228 km (XZ – plane). Grid sizes is set to be D_0/20 near the vent, and to increase at a constant rate with distance from the vent up to 300 m.

Typical features of the developments of an eruption column and an umbrella cloud in the weak wind field are reproduced in the present simulation (Fig. 3). The buoyant plume rises vertically and is not largely affected by wind. The plume overshoots the NBL (20 – 25 km) and reaches the height of 40 km. The umbrella cloud at the NBL spreads radially with diameter of ~400 km at 5500 s. The center of the umbrella cloud is located at 40 km leeward from the vent, which approximately coincides with the position of the maximum height. Pattern of ash dispersion is different from that from the weak plume ejected in the strong wind field (Fig. 3c). Fine particles (shown by red points) are transported radially by the umbrella cloud, whereas coarse particles (blue points) leave from the volcanic plume near the vent. Medium-sized particles (light blue, yellow, and orange points) separate from the umbrella cloud. Between the umbrella cloud and the ground, all the particles are drifted leeward by the wind to considerable extent.

The distribution of number density of marker particles (Fig. 4a) and the size distribution (Fig. 4b) on the ground show that the particles are dispersed almost concentrically. However, the distribution of fall deposits slightly elongates in the downwind direction.

4. Concluding remarks

We have developed a 3D numerical model of volcanic plumes in wind fields to simulate the dispersal and deposition of volcanic ash particles. The present model can reproduce the typical features of flow patterns of eruption cloud such as buoyant plume distorted by strong wind, umbrella cloud drifted by weak wind, and those of tephra deposits. The distribution of number density of marker particles settled on the ground can be compared with the isomass map based on field observations. In

addition, the size distribution of marker particles on the ground can be directly compared with the isopleth map based on field observations. The present model is considered to be useful for quantitative analyses of eruption cloud observations and geological data of tephra deposits in the future.

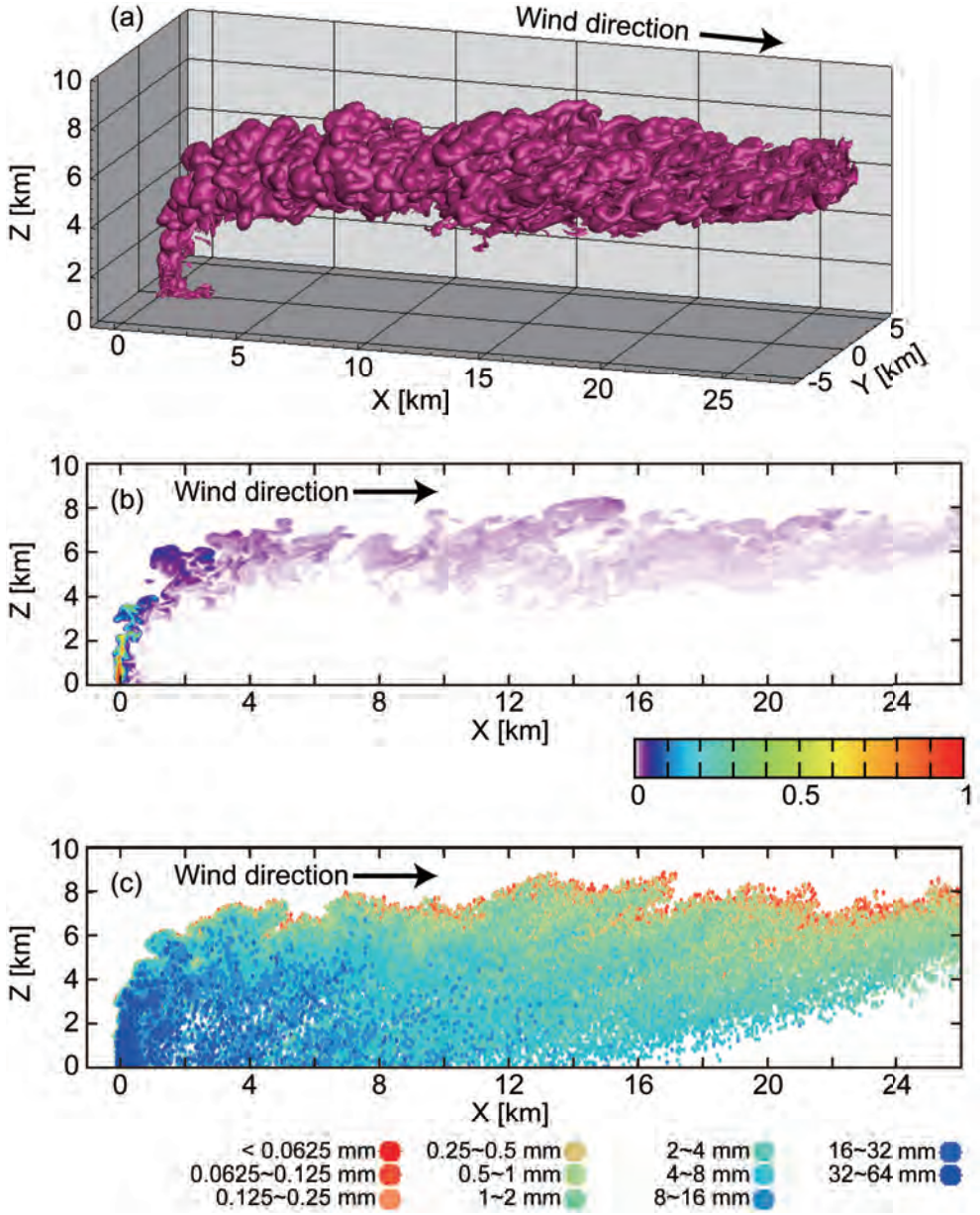

Fig.1 Results of 3D numerical simulation of a weak volcanic plume distorted by a strong wind at 700 s from eruption initiation. The wind blows rightward (for the wind profile see text). (a) Bird-eye view of the iso-surface of $\xi = 0.02$, where ξ is the mass fraction of the ejected material. (b) Cross-sectional distribution of ξ in X–Z space. (c) Side view of the distribution of marker particles. The colors in (c) represent the size of marker particles.

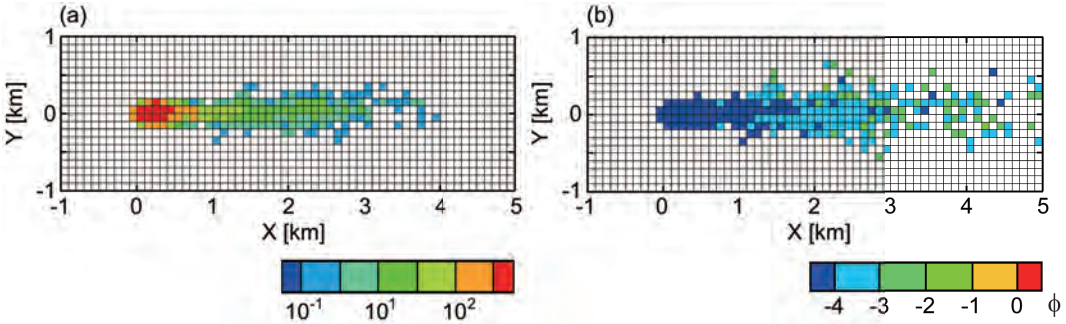

Fig.2 Depositional patterns of marker particles separated from a weak plume in a strong wind field. (a) The distribution of number density of marker particles at 700 s from the eruption initiation. (b) The distribution of maximum size of marker particles at 700 s from the eruption initiation.

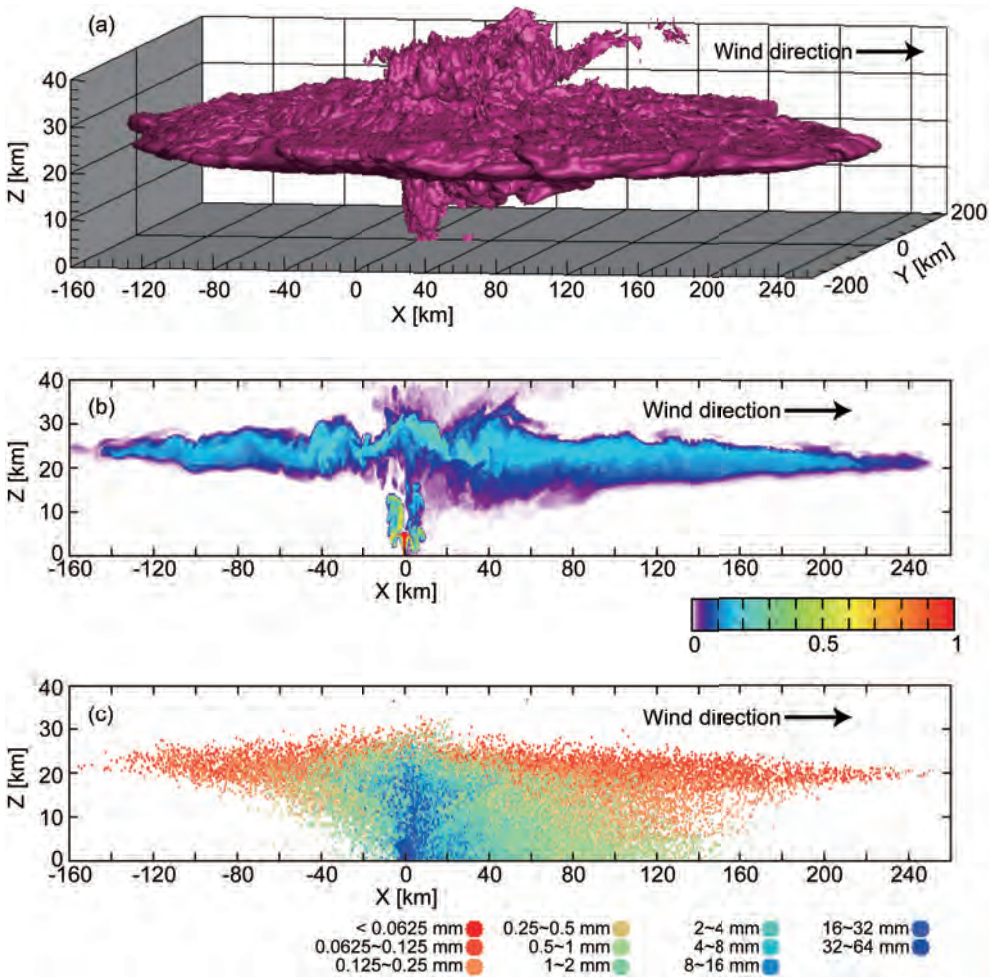

Fig.3 Results of 3D numerical simulation of a strong volcanic plume distorted by a weak wind at 5500 s from eruption initiation. The wind blows rightward (for the wind profile see text). (a) Bird-eye view of the iso-surface of $\xi = 0.02$. (b) Cross-sectional distribution of ξ in X–Z space. (c) Side view of the distribution of marker particles. The colors in (c) represent the size of marker particles.

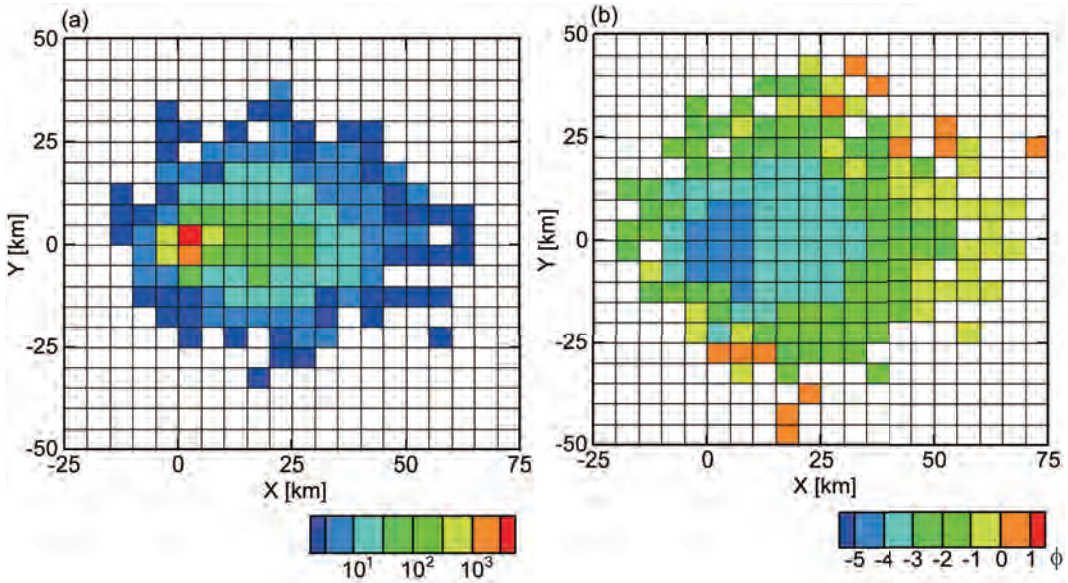

Fig.4 Depositional patterns of marker particles separated from a strong plume in a weak wind field. (a) The distribution of number density of marker particles at 5500 s from the eruption initiation. (b) The distribution of maximum size of marker particles at 5500 s from the eruption initiation.

Acknowledgments

Part of this study was supported by the ERI Cooperative Research Program and KAKENHI (Nos. 24244069 and 25750142).

References

[1] B. R. Morton, G. Taylor, and J. S. Turner, “Turbulent gravitational convection from maintained and instantaneous sources”, Proc. R. Soc. Lond. A, vol.234, pp.1-23, 1956.

[2] R. S. J. Sparks, “The dimensions and dynamics of volcanic eruption columns”, Bull. Volcanol, vol.48, pp.3-15, 1986.

[3] C. Bonadonna, J. C. Phillips, and B. F. Houghton, “Modeling tephra sedimentation from a Ruapehu weak plume eruption”, J. Geophys. Res., vol.110, B08209, 2005.

[4] S. Carey and R. S. J. Sparks, “Quantitative models of the fallout and dispersal of tephra from volcanic eruption columns”, Bull. Volcanol., vol.48, pp.109-125, 1986.

[5] A. Costa, G. Macedonio, and A. Folch, “A three-dimensional Eulerian model for transport and deposition of volcanic ashes”, Earth Planet. Sci. Lett., vol.241, pp.634-647, 2006.

[6] M. Bursik, “Effect of wind on the rise height of volcanic plumes”, Geophys. Res. Lett., vol.28, no.18, pp.3621-3624, 2001.

[7] A. W. Woods, “The fluid dynamics and thermodynamics of eruption columns”, Bull. Volcanol., vol.50, pp.169-193, 1988.

[8] Y. J. Suzuki and T. Koyaguchi, “3D numerical simulation of volcanic eruption clouds during the 2011 Shinmoe-dake eruptions”, Earth Planets Space, vol.65, pp.581-589, 2013.

[9] Y. J. Suzuki, T. Koyaguchi, M. Ogawa, and I. Hachisu, “A numerical study of turbulent mixing in eruption clouds using a three-dimensional fluid dynamics model”, J. Geophys. Res., vol.110, B08201, 2005.

火山灰輸送・堆積の３次元数値シミュレーション

課題責任者
小屋口剛博　　東京大学　地震研究所
著者
鈴木雄治郎　　東京大学　地震研究所
小屋口剛博　　東京大学　地震研究所

本プロジェクトでは、固体地球と地球表層・大気にまたがる火山現象について、大規模数値シミュレーションを用いた物理過程の理解と計算結果の防災への応用を目指している。特に、火山噴煙の到達高度や火山灰の降灰分布を定量的に正しく再現することに焦点をあて、噴煙ダイナミクスを支配する乱流混合や流体中の固体粒子沈降などの素過程の理解を進めている。

爆発的火山噴火では、高温の火山灰（マグマの破片）が水蒸気を主体とする火山ガスと混合した状態で火口から大気中へと噴出する。噴出した火山灰・ガスの混合物は、周囲の大気を取り込んで膨張させることで浮力を獲得して噴煙柱を形成する。成層大気中で噴煙（噴出物と混合大気の混合物）の密度と大気密度が釣り合うと、噴煙はその密度中立高度で水平方向へと拡大する。火山灰はこの噴煙上昇と水平移動によって運搬されるが、その輸送・堆積パターンは風の影響を受ける。平成 25 年度は、火山灰の移動を含めた噴煙の 3 次元数値シミュレーションを行い、火山灰輸送・堆積パターンへの風の影響を調べた。特に、(a) 風が強い大気中での弱い噴火、(b) 風が弱い大気中での強い噴火、の 2 種類の場合について、噴煙挙動と火山灰輸送・堆積過程を比較した。

(a) 風が強い大気中での弱い噴火は、新燃岳 2011 年噴火程度の噴火強度を想定し、噴出率を 2.5×10^6 kg s^{-1} とするシミュレーションを行った。大気中の風については、地表で 0 m s^{-1}、高度 10 km で 80 m s^{-1} まで高さとともに風速が直線的に増加する初期プロファイルを与えた。シミュレーションの結果、噴煙は風下方向に大きく曲がり、密度中立となる高度 6 〜 8 km で水平に流れた。火山灰はこの噴煙によって運搬され、風下側のみに堆積した。火山灰の輸送・堆積パターンは、粒子サイズによって大きく異なった。数 cm サイズの粒子は上昇中の噴煙柱から分離し、火口付近に堆積した。数 mm 〜 1cm サイズの粒子は噴煙柱上昇によって噴煙上部まで到達し、密度中立高度で噴煙とともに水平に移動するが、その後、水平移動する噴煙から徐々に分離して地表面へと降下した。非常に細かな粒子は噴煙から分離せず、水平移動する噴煙内を移動し続けた。

(b) 風が弱い大気中での強い噴火は、ピナツボ 1991 年噴火程度の噴火強度を想定し、噴出率を 1.0×10^9 kg s^{-1} とするシミュレーションを行った。大気中の風速については、高度 Z に対し、$U_{wind} = 15\tanh(Z/1000)$ m s^{-1} で与えた。シミュレーションの結果、噴煙柱は風の影響をほとんど受けずに鉛直方向に上昇し、密度中立高度でほぼ同心円状に拡大し、傘型噴煙を形成した。シミュレーション結果では、この傘型噴煙の中心が、風の影響で火口直上から風下側に徐々に移動する様子が観察された。火山灰は、同心円上に拡大する傘型噴煙から降下・分離し、風下側・風上側の両方に堆積するが、その分布は風の影響で風下側に偏向する。

以上のように、火山灰輸送と堆積に対する風の影響を定性的に捉えることができた。また、シミュレーション結果から地表における粒子密度分布と粒子サイズ分布を作成することができ、これらは実際の火山噴火における地質調査によって作成される堆積分布図と比較・検証することが可能である。

キーワード:火山噴煙, 降灰分布, 火山災害

Space and Earth System Modeling

Project Representative

Kanya Kusano Laboratory for Earth Systems Science, Japan Agency for Marine-Earth Science and Technology

Authors

Kanya Kusano[*1, 5], Wataru Ohfuchi[*2, 1], Shin-ichiro Shima[*3], Yusuke Chikaraishi[*4, 1], Ryohei Suzuki[*4, 1] Shigenori Maruyama[*4] and Daiko Shiota[*5]

*1 Laboratory for Earth Systems Science, Japan Agency for Marine-Earth Science and Technology

*2 Earth Simulator Center, Japan Agency for Marine-Earth Science and Technology

*3 Graduate School of Simulation Studies, University of Hyogo

*4 Tokyo Institute of Technology

*5 Solar-Terrestrial Environment Laboratory, Nagoya University

Solar activities may seriously impact terrestrial environment as well as our infrastructure in different manners. However, our predictability of solar activities and the influence upon the earth is substantially hindered, because the evolution mechanism of solar activities and the causal relationship between the solar variation and the climate change are not yet well understood. The objective of the Earth Simulator Project "Space and Earth System Modeling" is to advance our understanding for the variability of terrestrial environment caused by the dynamics in space including the sun. In FY 2013, we have continued the development of the several simulation models for space weather and space climate, respectively, for the prediction of coronal mass ejection as well as for understanding the influence of cloud microphysics onto the variability of weather and climate.

Keywords: space weather, space climate, multi-scale, multi-physics, plasma, cloud, aerosols, solar flares, solar eruptions, snowball earth, Earth Simulator

1. Introduction

Earth's environment is not isolated from the outside of the atmosphere as well as from the interior of the solid earth. In fact, the several evidences indicate that there is clear correlation between the climate variation and sunspot activity. Also it is widely believed that giant volcanic eruption may impact the worldwide climate. However, the mechanism whereby the solar activity may affect the climate is not well understood yet. On the other hand, giant solar eruptive events such as solar flares and coronal mass ejections (CMEs) may seriously impact the infrastructure of satellite, power grids, and communication facilities. Therefore, the improvement in the predictability of solar activities and our understanding of the sun and earth connection is crucially important not only from scientific point of view but also from the social and economic aspects.

Earth Simulator Project "Space and Earth System Modeling" was established in order to understand the mutual relationship between the surface environment and the activity in space including the solar activities. In FY 2013, we have continued the development of the several numerical models which will compose a space climate system simulation. They are the cloud simulation in terms of super-droplet method, the global circulation model for the study on the onset mechanism of snowball earth, and the magnetohydrodynamics simulation for solar eruptive events. In the following sections, we will explain about the detail of the each particular model.

2. Bifurcation analysis of the stratus-to-cumulus transition of maritime shallow clouds

Clouds play a crucial role in atmospheric phenomena. Since the galactic cosmic ray was suggested to induce the creation of cloud condensation nuclei (CCN) by various literatures, the mutual interaction between CCN and cloud is an important subject also for understanding the solar influence on climate. However, the numerical modeling of clouds remains somewhat primitive. We have developed a novel, particle-based, probabilistic simulation scheme of cloud microphysics, named the Super-Droplet Method (SDM), which enables accurate numerical simulation of cloud microphysics with less demand on computation (Shima et al. 2009). The SDM is implemented on the Cloud Resolving Storm Simulator (CReSS), which is a widely used cloud-resolving model developed by Tsuboki and Sakakibara (2002), and we call this new model the CReSS-SDM.

In 2013 FY, we investigated the behavior of marine stratocumulus near the stratus-to-cumulus transition point

using the CReSS-SDM. The simulations are carried out on an idealized meteorological system in which aerosols are formed continuously. We constructed the system by modifying the set-up based on the RICO composite case defined in van Zanten, et al. (2011). The equilibrium states of the system are compared changing the aerosol nucleation rate and the initial number density of aerosols. As a result, we confirmed the final steady state of this system is determined by the aerosol nucleation rate, and it is irrelevant to the initial number density of aerosols, even near the stratus-to-cumulus transition point (Fig.1). This suggests that bistability of stratus and cumulus does not occur for this system.

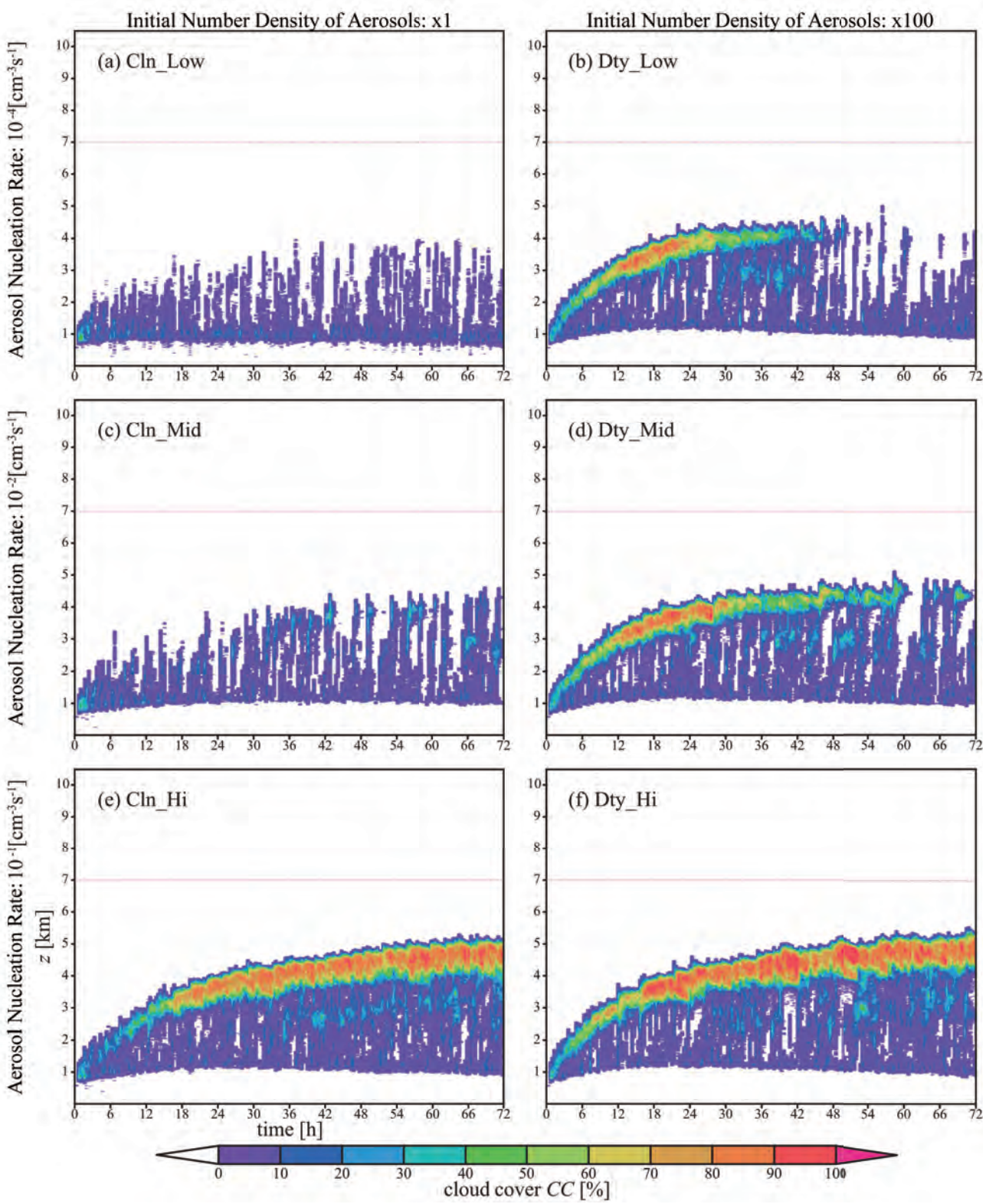

Fig. 1 Comparison of the time evolution of the cloud cover *CC*(*z*) defined on each height between 6 experiments. The graph shows the height on the vertical axis and the time on the horizontal axis. The system gradually evolves to reach its final steady state, which is not affected by the initial number density of aerosols. A transition of the final steady state from cumulus to stratus occurs when the aerosol formation rate is increased.

3. Response of a coupled GCM to sudden changes in solar luminosity

It is known that the Earth has experienced a globally ice-covered condition a few times through its history [e.g. 4]. There are some factors that might have caused the snowball Earth. One is an impact of gigantic meteorite that injects a huge amount of ash into the atmosphere, and the ash reflects the incoming solar radiation back to the outer space. In this case, the net solar radiation into the atmosphere should be reduced suddenly after the meteorite impact. In this study, we investigate the response of the climate system to a sudden reduction of total solar irradiance (TSI) using a couple atmosphere-ocean general circulation model (CGCM).

Our CGCM is a very low-resolution version of CFES (Cgcm For the Earth Simulator) [5]. The horizontal resolution is about 640 km and 320 km for the atmosphere and ocean, respectively. The vertical levels are not changed from the original CFES, and the numbers of levels are 48 for the atmosphere and 54 for the ocean. The "CFES-micro" uses two nodes of the Earth Simulator and needs about one hour for one-model-year integration.

A set of aqua planet simulation was conducted. The modeled planet is covered globally with the ocean with a constant depth of 4,000 m. Firstly we ran CFES-micro with a current TSI (Case100) from an initial condition taken from a quasi-equilibrium state in a long-term realistic simulation of the original CFES. After 100 years, we continued Case100 for another 100 years while ran also TSI suddenly reduced cases, Case90 (TSI is reduced to 90 % of the current value), Case80, Case70 and Case60.

Figure 2 shows the time series of global average of surface temperatures of the set of our simulations. It is clearly seen that, in Case80, 70 and 60, the temperatures rebound after quick drops while it decreases steadily in Case90. The rebound happens probably because quick cooling from the surface of the ocean induces convection, and relatively "warm" water wells up to the surface in a sudden manner when the sudden TSI reduction is large. This result suggests that the Earth may not be cooled steadily after a meteorite impact. This process makes the ocean vertically unstable. Case80 and 70 were aborted probably due to this instability at years 185 and 148, respectively. We plan to continue Case90 and Case60. Case90 may result in the snowball Earth.

4. Simulation study of solar eruptions

Solar eruptions, such as solar flares and coronal mass ejections, are the most catastrophic events in our solar system, and they sometimes impact the terrestrial environment and our infrastructure. Although the solar eruptions are widely believed to be driven by magnetic energy stored in the solar corona, what triggers their onset remains poorly understood. Hypotheses for the trigger mechanism include the emerging flux model, which proposed that the small magnetic flux emerging onto the solar surface may lead to the solar eruptions. However, what kind of the emerging flux is capable to trigger the eruptions is unclear. This severely limits our capacity to predict the occurrence of solar eruptions and forecast space weather.

Recently, we proposed that there are two types of magnetic field structures which favor the onset of solar eruptions. The first type is called the opposite polarity type, in which the small magnetic bi-pole opposite to the major magnetic polarity in an active region drives the solar eruption. The second type is called the reversed shear type, in which the cancellation of magnetic shear on the polarity inversion line may cause the onset of eruption. We have compared the simulation results and the data of Hinode solar observation satellite, and revealed that the four major flares observed by Hinode can be classified into these two types [7].

In FY 2013, based on this study, we extended the simulation to the whole solar corona in order to simulate not only flare onset

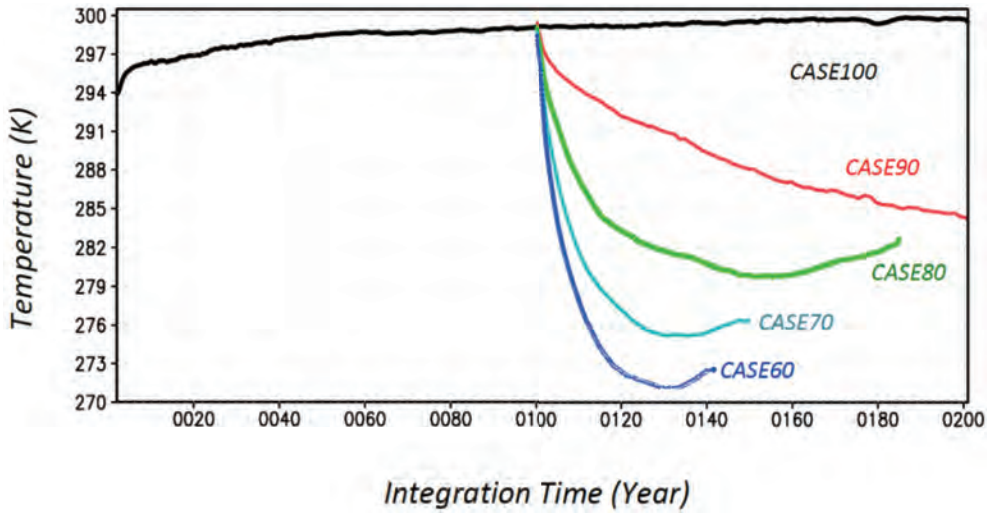

Fig. 2 Time series of global average surface air temperature from the set of CFES-micro aqua planet simulations. CaseN indicates the case of N % of the current TSI.

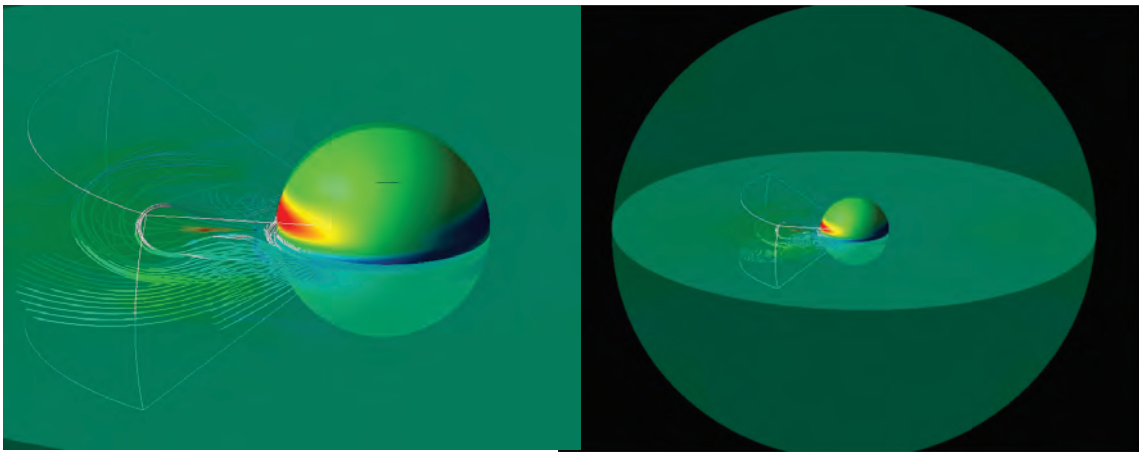

Fig. 3 The simulation results of solar eruption. The colored sphere corresponds to the sun, and color scale denotes the magnetic field on the solar surface. Thin strings show the three-dimensional structure of magnetic field lines connecting to an active region. Left panel is a zoom-in view of the whole simulation box (right).

but also the formation and propagation of coronal mass ejection. (CME). The simulation box covers the global solar corona, and we simulated the onset of solar eruption by imposing the rotation motion on a small portion in sheared magnetic field (see Fig. 3). As a result, we found that the sheared magnetic field becomes unstable when the rotation motion causes the opposite polarity type of magnetic structure, and the magnetic flux rope can be ejected out of the lower corona. Although the calculations are still preliminary, the results are consistent with our previous model [6], and suggest that some typical magnetic field structure in small scale may trigger a large-scale solar eruption.

References

[1] S. Shima, K. Kusano, A. Kawano, T. Sugiyama, S. Kawahara, The super-droplet method for the numerical simulation of clouds and precipitation: a particle-based and probabilistic microphysics model coupled with a non-hydrostatic model, Quarterly Journal of the Royal Meteorological Society, Vol. 135, 642, pp.1307–1320, 2009.

[2] K. Tsuboki and A. Sakakibara, large-scale parallel computing of cloud resolving srom simulator, High Performance Computing Lecture Notes in Computer Science, 2327, pp. 243-259, 2002.

[3] M. van Zanten, Controls on precipitation and cloudiness in simulations of trade-wind cumulus as observed during RICO, J. Adv. Model. Earth Sys., 3, 2, Art. M06001, Jun 2011.

[4] P. F. Hoffman, D. P. Schrag, The Snowball Earth hypothesis: testing the limits of global change, Terra Nova, 14, 129–155, 2002.

[5] N. Komori, A. Kuwano-Yoshida, T. Enomoto, H. Sasaki, and W. Ohfuchi, High-resolution simulation of global coupled atmosphere–ocean system: Description and preliminary outcomes of CFES (CGCM for the Earth Simulator). In *High Resolution Numerical Modelling of the Atmosphere and Ocean*, K. Hamilton and W. Ohfuchi (eds.), chapter 14, pp. 241–260, Springer, New York, 2008.

[6] K. Kusano, Y. Bamba, T. Yamamoto, Y. Iida, S. Toriumi, and A. Asai, Magnetic field structures triggering solar flares and coronal mass ejections, The Astrophysical Journal, 760, Issue 1, article id 31, 9pp., 2012.

[7] Y. Bamba, K. Kusano, T. T. Yamamoto, and T. J. Okamoto, Study on triggering process of solar flares based on Hinode/SOT observations, The Astrophysical Journal, 778, Issue 1, article id 48, 2013.

宇宙・地球表層・地球内部の相関モデリング

課題責任者
草野　完也　　海洋研究開発機構　システム地球ラボ
著者
草野　完也 *1, 5，大淵　　済 *2, 1，島　伸一郎 *3，力石　祐介 *4, 1，鈴木　遼平 *4, 1，丸山　茂徳 *4，
塩田　大幸 *5
*1 海洋研究開発機構　システム地球ラボ
*2 海洋研究開発機構　地球シミュレータセンター
*3 兵庫大学大学院シミュレーション学研究科
*4 東京工業大学　大学院理工学研究科
*5 名古屋大学　太陽地球環境研究所

地球環境システムは内部（地殻、マントル、コア）、表層（大気海洋）および外部（宇宙）が互いに影響を及ぼしながら変動進化する相関システムである。本プロジェクトは地球環境の大規模変動と太陽及び宇宙空間ダイナミクスの関係を探るために、先進的な相関モデルを開発する目的で 2009 年度より開始された。本プロジェクトでは、太陽活動と地球環境の関係に注目し、放射変動、宇宙線変動の影響を中心にそのメカニズム解明と予測を目指したシミュレーション研究を実施している。2013 年度はその結果、以下の３つの成果を得た。第 1 に、超水滴法を利用した積雲層雲遷移の双安定性に関する研究においては、超水滴法を利用した雲分解モデル CReSS-SDM を用いて、RICO プロジェクトの設定に基づいて熱帯積雲のシミュレーションを行った。特に、雲核生成率に対する雲の長期安定性を解析した結果、積雲層雲遷移に関する双安定状態が出現し難いことを示唆する結果を得た。第 2 に、大気海洋結合全球循環モデルを用いて全球凍結事象のような地球史における大規模環境変動が宇宙線の急激な増加に伴う雲凝結核の変化によって発生する可能性を調べるため、高効率の大気海洋結合全球循環モデルの開発を開始した。このモデルを用いて太陽放射の突然変動がその後の大気海洋結合システムにどのような影響を与えるかを、小型 CFES モデルを用いて調べた。その結果、太陽放射の変動量に対して表層温度の応答時間が大きく変化することを見出した。変動量がより小さい場合、平衡温度に達するためにはより長い緩和時間が必要であった。また、計算結果より太陽放射の 10% 減少によって全球凍結が可能であることが示唆された。第 3 に、地球環境に大きな影響を与える巨大な太陽面爆発のトリガ機構に関する３次元電磁流体シミュレーション研究を、全球コロナモデルを用いて実施した。その結果、コロナ全体の大規模爆発も我々が提唱すした太陽フレアトリガモデルと同様の太陽表面磁場によって発生することを示唆する結果を得た。このことは、太陽面磁場の詳細観測に基づいて地球に影響を与えるように大規模な太陽面爆発を予測できる可能性を意味するものである。

キーワード:宇宙天気, 宇宙気候, マルチスケール, マルチフィジックス, プラズマ, 雲, エアロゾル, 太陽フレア,
太陽面爆発, 全球凍結, 地球シミュレータ

Numerical Experiments with Multi-Models for Paleo-Environmental Problems

Project Representative

Ayako Abe-Ouchi Atmosphere and Ocean Research Institute, The University of Tokyo

Authors

Ayako Abe-Ouchi[*1], Masakazu Yoshimori[*1], Wing-Le Chan[*1], Akitomo Yamamoto[*1], Kazumi Ozaki[*1], Ryouta O'ishi[*2], Mika Ichino[*2], Yusuke Ozawa[*1], Takashi Obase[*1], Sam Sherriff Tadano[*1], Nitta Tomoko[*1] and Alexandre Laine[*2]

*1 Atmosphere and Ocean Research Institute, The University of Tokyo

*2 National Institute of Polar Research, Research Organization of Information and Systems

The MIROC4m AOGCM was used for several paleoclimate simulations of the mid-Pliocene Warm Period (mPWP, 3.3-3.0 million years ago), stadial states (millennial-scale cold period during the last glacial cycle), and the last millennium (850-2000 C.E.). MIROC4m mPWP simulations show that greenhouse gas emissivity dominates the tropical warming in all models, whereas clear-sky albedo is important in the high latitudes.

A higher resolution AGCM is used to simulate freshwater hosing to investigate stadial climate states and vegetation distribution. Initial analysis suggests that summer monsoonal changes indicated by proxy data are well-represented. Vegetation distribution shows a global pattern of decrease of forest which is similar to that of a reconstructed one. However, the intensity of decrease is underestimated.

In order to evaluate the impact of collapse of methane hydrate upon the climate, preliminary estimation has been done using MIROC3.2 quadrupled atmospheric CO_2 experiment. The result indicates that a huge amount of methane hydrate is decomposed throughout a timescale of several thousand years.

Several sensitivity experiments are conducted under time-varying forcing of the last millennium. The response pattern of the climate to extraordinarily large volcanic events suggests that the phase of the Pacific Decadal Oscillation appears to be locked to the event. This characteristic is commonly seen in different ensemble members whose integration started from different initial conditions.

Keywords: atmosphere-ocean GCM MIROC, paleoclimate modeling, mid-Pliocene, last millennium

1. Introduction

The mid-Pliocene warm period (mPWP), defined as the interval between 3.3-3.0 million years ago, was the most recent period with sustained warmth during the earth's history. Global mean temperatures were comparable to those predicted for the latter half of the 21st century, leading to the mPWP as being thought of as an analogue for future climate conditions. This particular interval was chosen for paleoclimate reconstruction for a variety of reasons, not least because there are multiple temperature proxies from extant fauna and flora and continental distribution was not unlike that of present day. The mPWP has thus become a period of particular interest within the paleoclimate community and includes potential targets, such as climate sensitivity and vegetation, for reducing uncertainties in future projections.

The Late Pleistocene age was characterized by abrupt climate change of millennial timescales, the Dansgaard-Oeschger Cycle. Within this age, MIS3 (60,000-30,000 years ago) was an important time for the dispersal of Modern Humans. To investigate the reason for the replacement of Neanderthals by Modern Humans, the reconstruction of environmental factors, especially climate and vegetation distribution, is important. In the current study we report on the progress of the reconstruction of climate and vegetation in the Late Pleistocene using GCMs.

Global warming could decompose methane hydrate and cause methane release into the ocean. This methane release is thought to affect climate and ocean biogeochemical cycle in future and past global warming, such as the Paleocene-Eocene Thermal Maximum (PETM) (about 56 million years ago) and Ocean Anoxic Events (OAEs) in the Mesozoic (252-66 million years ago). We estimated the methane hydrate inventory loss in response to global warming and discuss its potential impact on ocean oxygen depletion. Our study is a highly suggestive estimation for both future and past climate change.

The last millennium (LM) simulation (850 – 2000 A.D.), designed under the Paleoclimate Modelling Intercomparison

Project phase 3 and included in a suite of tier 2 experiments in the Coupled Model Intercomparison Project phase 5, is now being carried out by multiple climate modeling centers across the world and archived. In the current study, we focus on the response of the Pacific Decadal Oscillation upon volcanic forcing.

2. Mid-Pliocene Warm Period: model-model and model-data comparisons

The Pliocene Model Intercomparison Project (PlioMIP) was set up in 2010 to stimulate interest in the mid-Pliocene warm period by bringing international climate modeling groups together and assessing climate simulations of that period by both model-model and model-data comparisons [1,2]. The first phase recently produced many interesting results just as a possible time slice is being identified for the upcoming next phase [3]. The MIROC4m atmosphere-ocean model had previously been used to run simulations adhering to PlioMIP guidelines [4] and recent results focus on the various aspects of model inter-comparisons and data-model discrepancies.

The MIROC4m results, as with those from other individual models, show mostly warming in the mid-Pliocene sea surface temperatures (SST). There are only two locations where the mid-Pliocene multi-model-mean value is more than 3°C higher than the present day value [5]. Most models show slight warming in the tropical regions, in contrast to many of the PRISM3 proxy data there. On the other hand, the models do not show warming in the high latitudes of the Atlantic Ocean to be as high as that suggested by proxy data. Thus, although there is a polar amplification of SSTs in model data, it appears weaker than PRISM3 data set. It is difficult to explain this by changes in ocean heat transport since models show only small changes and no consistent increase in the strength of the Atlantic meridional overturning circulation (AMOC) [6]. Energy balance calculations show that greenhouse gas emissivity dominates the tropical warming in all models, whereas clear-sky albedo is important in the high latitudes [7]. Even though greenhouse gas warming is fairly consistent at all latitudes, it is partially offset at high latitudes by the cloudy sky impact on the planetary albedo. Comparisons with confidence-assessed temperature proxy data and biome reconstructions reveal a substantial cold bias in the model surface air temperatures of the northern hemisphere, especially Siberia [8]. A more robust evaluation of the capabilities of models to simulate mid-Pliocene warming may be achieved by removing the temporal constraints on the current PlioMIP proxy records.

3. Modeling climates of the Late Pleistocene with MIROC4m AOGCM and AGCM

The Late Pleistocene lasted from the end of the previous interglacial period to the start of the warm Holocene and was characterized mostly by widespread glacial ice. It is thought that melting sea ice or icebergs from the Laurentide ice sheet led to a large discharge of freshwater into the North Atlantic Ocean during Heinrich events and a weakening of the Atlantic meridional overturning circulation, coinciding with large fluctuations in temperature, as suggested by geochemical records of ice cores. This period also saw modern humans spread throughout the world and other remaining species of the same genus, such as the Neanderthals, become extinct. One hypothesis proposed to explain the extinction of the Neanderthals points to their inability to adapt to climate and environmental changes during oxygen isotope stage 3 (OIS-3), 58.9-27.6ka BP [9]. In order to better understand the role of climate and vegetation changes on the migration patterns of early modern humans and Neanderthals, climate models can be used to reconstruct past climates and, in particular, those of the cool stadials and warm interstadials. We analyzed the simulated climates for several versions of the MIROC model (and AOGCM, mid-resolution T42 AGCM and a high-resolution T106 AGCM) and also compared them with some proxy data.

Previous studies have shown that release of freshwater into the northern North Atlantic Ocean, akin to Heinrich events, can weaken the AMOC, affecting climate throughout Europe and beyond. To mimic this release, AOGCM simulations include 'freshwater hosing' whereby a freshwater flux had been applied over the northern North Atlantic [10,11]. In a mid-glacial experiment (Hosing), freshwater was released at a rate of 0.1Sv ($10^6 m^3/s$) for 500 years in MIROC. In a second experiment (Non-hosing), this hosing was then switched off, resulting in a recovery in the AMOC. Sea surface temperatures and sea ice from these two experiments were applied to the mid- and high-resolution AGCM to simulate climates depicting the cool stadials and warm interstadials. This is slightly different to previous analyzes where the stage before freshwater hosing is applied was taken to represent the interstadial case.

Figures 1 and 2 show the temperature and precipitation response to freshwater hosing and a weakening of the AMOC. SST biases inherent in the AOGCM are adjusted for the AGCM experiments, and cooling and warming is seen over the North and South Atlantic Oceans, respectively, although warming occurs over Siberia due to differences in the AGCM sea ice treatment. Drier conditions during the summer as inferred from proxy data (red circles in Fig. 2) are simulated better in the AGCM, for example, near the Philippines. In all experiments, there is a weakening of the South Asian summer monsoon, as seen in the weakening of the southwesterlies and the drier conditions over the northern Arabian Sea. Adjustments made to the sea ice, such as the inclusion of interannual variability, removes the warming over Siberia; the drier conditions over the western Pacific Ocean also extend inland into East Asia (Figs. 1d and 2d). Results from these climate simulations were applied to a global dynamical vegetation model to examine changes in the natural environment.

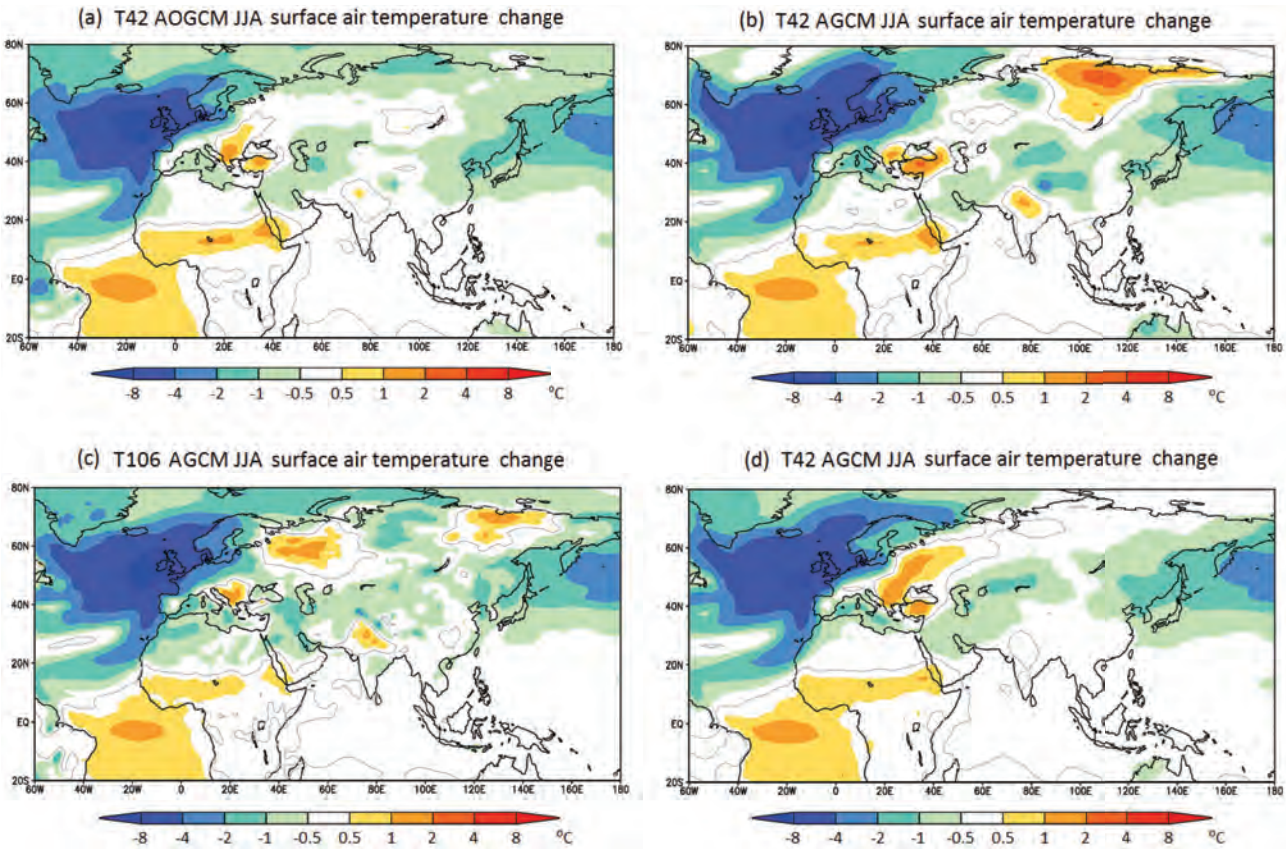

Fig. 1 Change in surface air temperature (Hosing - Non-hosing) during June-August for (a) T42 AOGCM, (b) T42 AGCM, (c) T106 AGCM and (d) T42 AGCM with adjustments made to the sea ice.

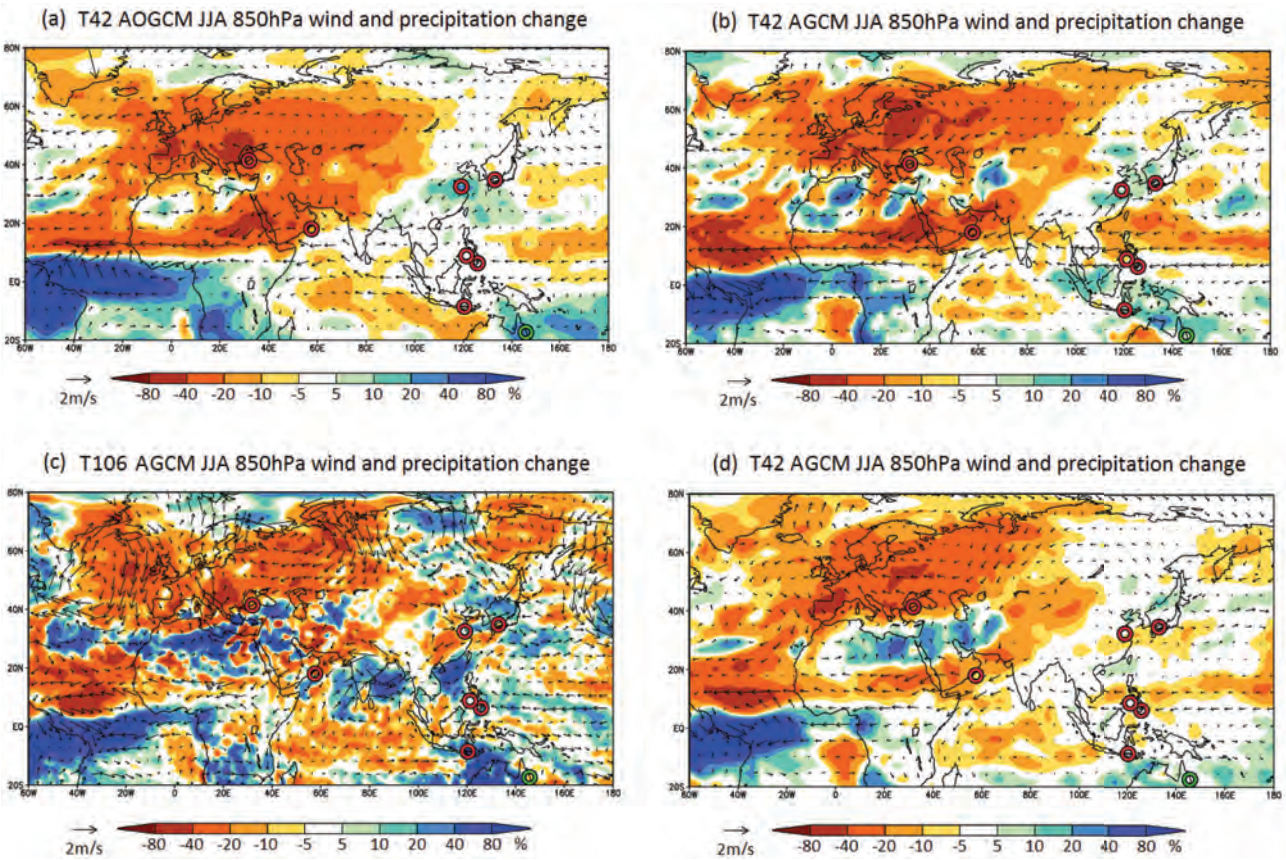

Fig. 2 Change in precipitation (Hosing/Non-hosing) and 850hPa wind (Hosing - Non-hosing) during June-August for the models as in Fig. 1. Orange and brown areas indicate drier conditions associated with freshwater hosing.

Changes in vegetation were investigated with a dynamic global vegetation model (DGVM), the Lund-Potsdam-Jena DGVM [12]. Surface air temperature and precipitation from the AOGCM were fed into the DGVM which simulates changes in plant functional types (PFT) - 8 woody/forest types and 2 herbaceous/grass types. Changes in these two are shown in Fig. 3 with bare ground as the residual. Freshwater hosing conditions tend to reduce forests throughout continental Europe, replacing them mainly with grassland. The reduction in temperature is the more dominant factor, with boreal PFTs generally surviving better in cooler conditions, but overcompensated by the decrease in temperate PFTs. There is loss of both forest and grassland over parts of Spain and northwest Africa where precipitation is greatly reduced. On the other hand, there is forest growth in the coastal regions of eastern Spain and western Italy, and across the islands in between, mainly in the form of temperate needle-leaved evergreen at the expense of grassland. This tendency of vegetation change is similar to the reconstructed vegetation change from proxies [13]. Moreover, the predicted intensity of vegetation change is the largest in Europe and less vegetation change is seen in East Asia, North America and Australia, as shown in the reconstruction. Hence, the global pattern of vegetation change is well predicted compared to the proxies. However, proxies show vegetation changes which are more significant than those of model results. This modelling framework still underestimates vegetation change.

4. Estimations of methane hydrate inventory loss and its potential impact on ocean oxygen depletion

Increases in bottom seawater temperature due to global warming could destabilize submarine methane hydrate and cause a release of methane into the water column. The release of several thousand GtC of methane from methane hydrate decomposition may have contributed to the past global warming (e.g. PETM [14]). The methane released from the seafloor consumes dissolved oxygen via methane oxidation in seawater. Thus, massive methane release is considered as a plausible cause for OAEs in the Mesozoic, which is warmer than present climate [15]. We projected the methane hydrate inventory loss in response to global warming and discuss its potential impact on global oxygen reduction for timescales of 10kyr.

A quasi-equilibrium experiment, in which 1% annual increase in the CO_2 concentration from preindustrial values was applied until stabilization at 4 × CO_2 level after 140 years, was conducted for 3650 years with MIROC3.2 [16]. The mean bottom seawater warming with respect to preindustrial conditions was 4.5˚C, and the temperature reached a quasi-

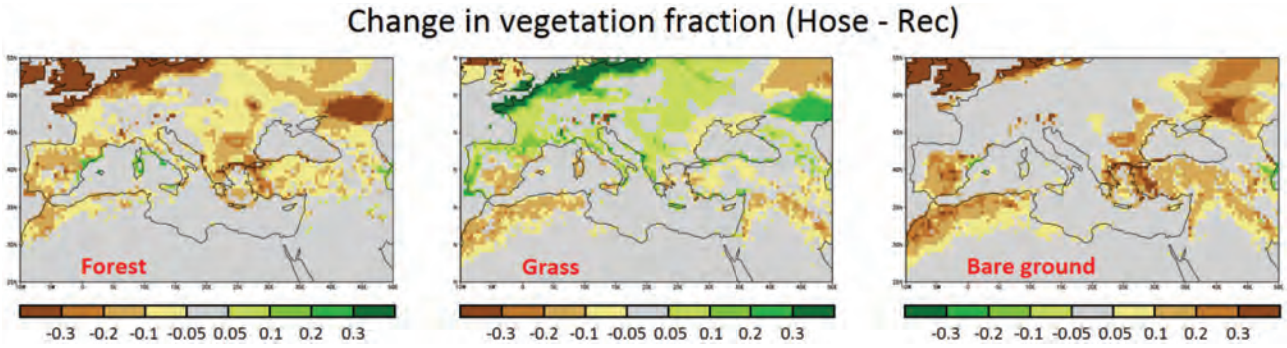

Fig. 3 The difference in vegetation fraction in LPJ dynamic global vegetation model experiments using surface air temperature and precipitation obtained from freshwater hosing and non-hosing AOGCM experiments.

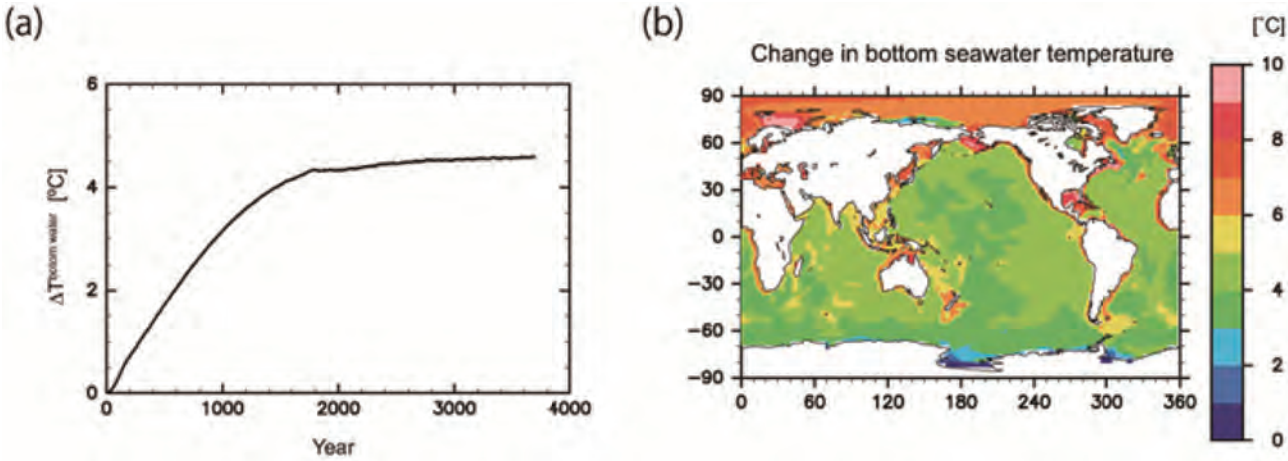

Fig. 4 (a) Temporal evolution of mean temperature changes in bottom seawater, relative to the preindustrial climate. (b) Distribution of change in the bottom seawater temperature at steady stare for 4 × CO_2 experiment.

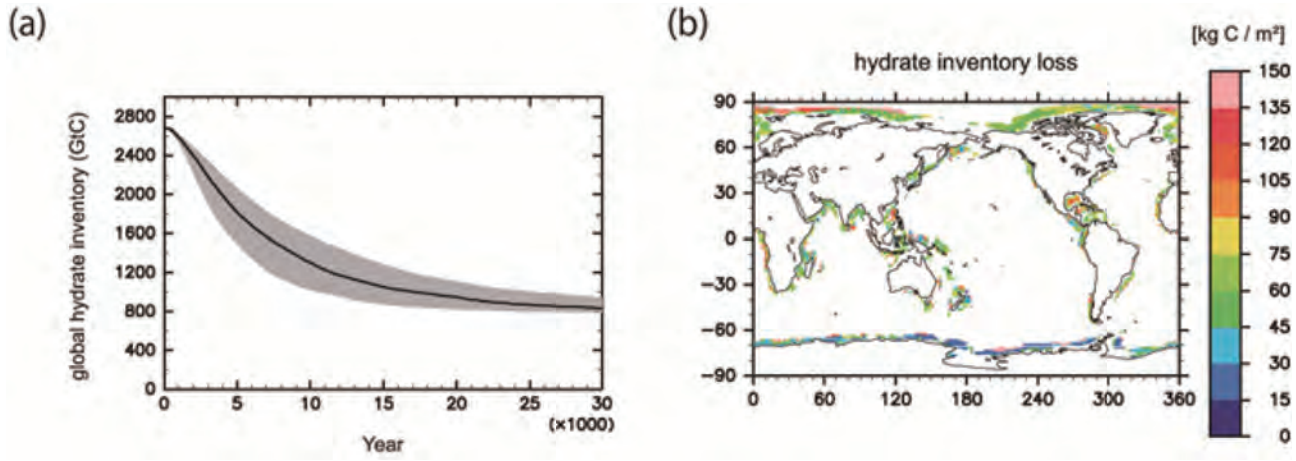

Fig. 5 (a) Temporal evolution of the global inventory of hydrates. The solid line represents the 4 × CO_2 experiment for hydrate evolution with thermal diffusivity of sediment of 3.0 × 10^{-7} m^2 s^{-1}. The evolution with thermal diffusivities of 1.86–4.2 × 10^{-7} m^2 s^{-1} is indicated by the gray shading. (b) Distribution of the column-integrated inventory loss of methane hydrates at the steady state of the 4 × CO_2 experiment.

steady state in around 2000 model years (Fig. 4a). The bottom seawater warming in the Arctic Ocean is 2-3˚C higher than that in other oceans because of polar amplifications (Fig. 4b).

We calculated the sediment warming and reduction in the global inventory of methane hydrate using calculated bottom seawater temperature, a one-dimensional thermal diffusion model and a transfer function [17]. The decomposition of methane hydrate begins to occur in the Arctic Ocean with 150 model years, and the majority of the adjustment of the hydrate inventory to the increased sediment temperatures occurs within the first 15kyr (Fig. 5a). This long timescale is primarily determined by thermal diffusion in the sediment. The global inventory of methane hydrates ultimately decreases by 1890 GtC. The hydrate inventory loss primarily occurs in the Pacific Ocean, where the hydrate inventory was found to be the greatest. A remarkable inventory loss occurs in the Arctic Ocean because the largest bottom seawater warming occurs here (Fig. 5b).

The oxidation of approximately 1200 GtC in the form of methane could potentially consume the entire oxygen content of present-day oceans. However, more than 8000 years are required to achieve a global inventory loss of 1200 GtC. Thus, because this timescale induced by slow thermal diffusion in the sediment is sufficiently longer than the timescale required for ocean ventilation (timescale of about a thousand years), the supply of oxygen from the atmosphere would be expected to prevent global ocean anoxia. The methane release in the Pacific Ocean, where present-day seawater has low oxygen concentration, would cause expansion of suboxic and hypoxic waters, having an adverse impact on marine organisms and ocean biogeochemical cycles.

5. Modeling the climate of the last millennium

Since the beginning of this project, a series of LM experiments have been carried out with the Model for Interdisciplinary Research on Climate, medium resolution version, MIROC3.2 and MIROC4m. The result of the MIROC3.2 last millennial simulation was published by Yiou et al. (2012) [19]. MIROC4m is essentially same as MIROC3.2[16], but is renamed after a minor bug-fix on surface flux treatment over ice sheets. This fiscal year, we added two LM experiments (named R11 and R12, 13 experiments in total) of only volcanic forcing with large amplitude [18]. The two experiments differ only in the initial conditions. We focus here on the Pacific Decadal Oscillation (PDO), the leading mode of climate variability on a decadal time scale in the North Pacific. It is timely to search for the model response of PDO to external forcing as proxy records for sea surface temperature near Japan apparently sensitive to PDO are becoming available.

Figure 6 shows that MIROC4m control simulation captures the basic feature of the PDO pattern. Figure 1a corresponds to the positive phase of the PDO characterized by a cold sea surface temperature (SST) anomaly located east of Japan and by a stronger Aleutian low pressure.

We investigated the relation between volcanic forcing and PDO by the following procedures: (1) subtract SST of the perpetual 850 C.E. climatology from the simulated LM SST at each grid; and (2) subtract concurrent SST of the North Pacific (20°N-60°N, 120°E-120°W) average from the SST anomaly (obtained after the first procedure) at each grid. The first procedure is aimed at removing the effect of geographical dependence of SST spatial pattern in the unforced simulation (e.g., colder at higher latitudes), and the second procedure is aimed at removing the effect of global-scale cooling in response to volcanic forcing. Without (2), the pattern may simply exhibit domain-wide cooling, and thus it is not easy to extract the spatial SST response pattern such as PDO. Figure 7 shows the SST response pattern after the largest volcanic eruption (1258C.E.). The patterns are similar in the two experiments with different initial conditions (R11 and R12, only R11 is shown). The same analysis for the large volcanic eruption (1762C.E.) also exhibits a similar response in the two runs.

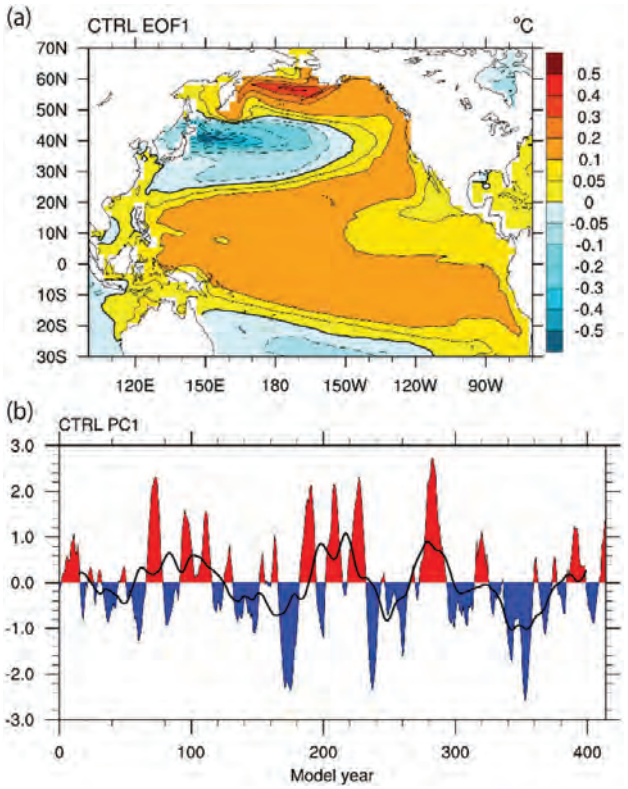

Fig. 6 The leading mode of North Pacific (20°N-60°N) sea surface temperature decadal variability in the control simulation: (a) spatial pattern; and (b) time series. Empirical orthogonal function analysis is applied after an 8-year running mean filter is imposed.

References

[1] A. M. Haywood, H. J. Dowsett, B. Otto-Bliesner, M.A. Chandler, A. M. Dolan, D. J. Hill, D. J. Lunt, M. M. Robinson, N. A. Rosenbloom, U. Salzmann, and L. E. Sohl, Pliocene Model Intercomparison Project (PlioMIP): experimental design and boundary conditions (Experiment1), Geosci. Model Dev., vol. 3, pp. 227-242, 2010; doi:10.5194/gmd-3-227-2010.

[2] A. M. Haywood, H. J. Dowsett, M. M. Robinson, D. K. Stoll, A. M. Dolan, D. J. Lunt, B. Otto-Bliesner, and M.A. Chandler, Pliocene Model Intercomparison Project (PlioMIP): experimental design and boundary conditions (Experiment 2), Geosci. Model Dev., vol. 4, pp. 571-577, 2011; doi:10.5194/gmd-4-571-2011.

[3] A. M. Haywood, A. M. Dolan, S. J. Pickering, H. J. Dowsett, E. L. McClymont, C. L. Prescott, U. Salzmann, D. J. Hill, S. J. Hunter, D. J. Lunt, J. O. Pope, and P. J. Valdes, On the identification of a Pliocene time slice for data-model comparison, Phil. Trans. R. Soc. A, vol. 371: 20120515, 2013; doi:10.1098/rsta.2012.0515.

[4] W.-L. Chan, A. Abe-Ouchi, and R. Ohgaito, Simulating the mid-Pliocene climate with the MIROC general circulation model: experimental design and initial results, Geosci. Model Dev., vol. 4, pp. 1035-1049, 2011; doi:10.5194/gmd-4-1035-2011.

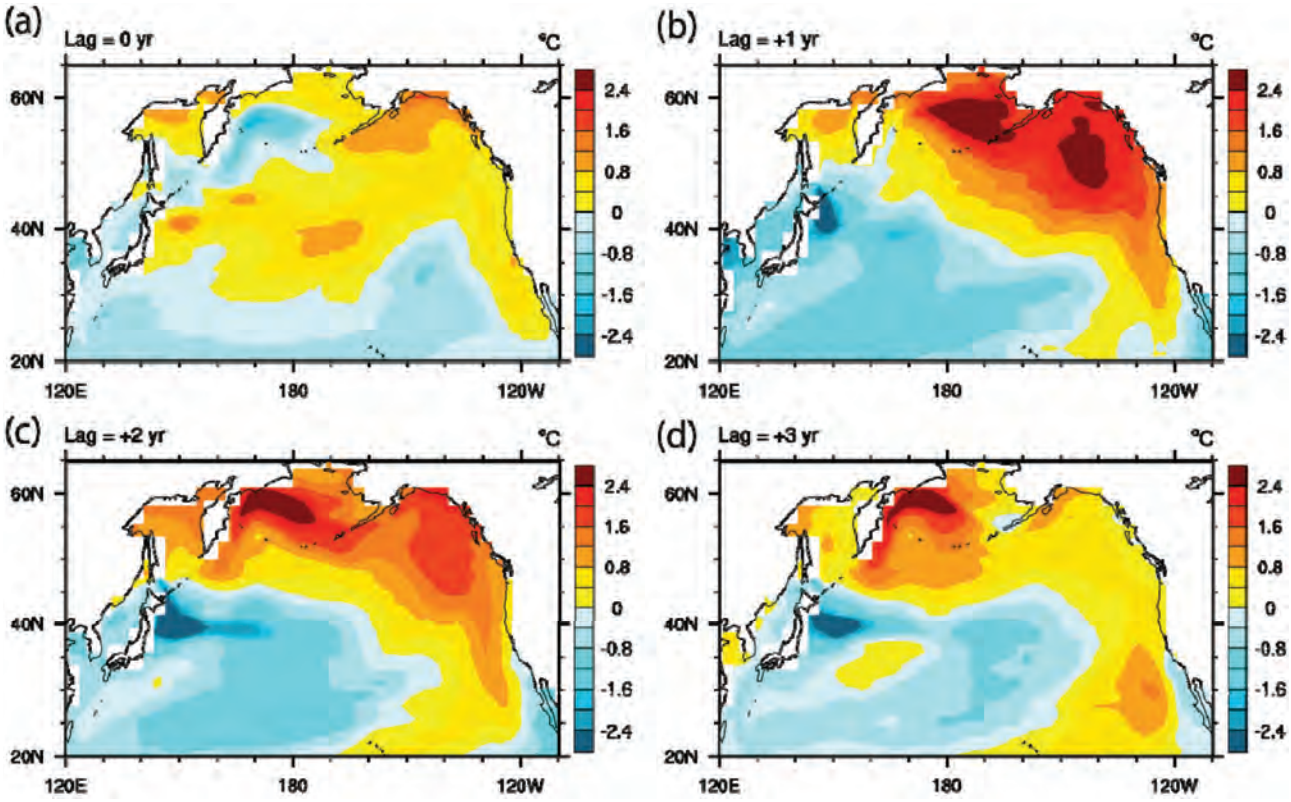

Fig. 7 Annual mean SST anomaly response pattern (R11 experiment) after the largest volcanic event (1258C.E.): (a) the year 1258; (b) 1 year later; (c) 2 years later; and (d) 3 years later. See text for the data process.

[5] H. J. Dowsett, K. M. Foley, D. K. Stoll, M. A. Chandler, L. E. Sohl, M. Bentsen, B. L. Otto-Bliesner, F. J. Bragg, W. L. Chan, C. Contoux, A. M. Dolan, A. M. Haywood, J. A. Jonas, A. Jost, Y. Kamae, G. Lohmann, D. J. Lunt, K. H. Nisancioglu, A. Abe-Ouchi, G. Ramstein, C. R. Riesselman, M. M. Robinson, N. A. Rosenbloom, U. Salzmann, C. Stepanek, S. L. Strother, H. Ueda, Q. Yan, and Z.-S. Zhang, Sea Surface Temperature of the mid-Piacenzian Ocean: A Data-Model Comparison, Sci. Rep., vol. 3, 2013; doi:10.1038/srep02013.

[6] Z.-S. Zhang, K. H. Nisancioglu, M. A. Chandler, A. M. Haywood, B. L. Otto-Bliesner, G. Ramstein, C. Stepanek, A. Abe-Ouchi, W.-L. Chan, F. J. Bragg, C. Contoux, A. M. Dolan, D. J. Hill, A. Jost, Y. Kamae, G. Lohmann, D. J. Lunt, N. A. Rosenbloom, L. E. Sohl, and H. Ueda, Mid-pliocene Atlantic Meridional Overturning Circulation not unlike modern, Clim. Past, vol. 9, 1495-1504, 2013b; doi:10.5194/cp-9-1495-2013.

[7] D. J. Hill, A. M. Haywood, D. J. Lunt, S. J. Hunter, F. J. Bragg, C. Contoux, C. Stepanek, L. Sohl, N. A. Rosenbloom, W.-L. Chan, Y. Kamae, Z.-S. Zhang, A. Abe-Ouchi, M. A. Chandler, A. Jost, G. Lohmann, B. L. Otto-Bliesner, G. Ramstein, and H. Ueda, Evaluating the dominant components of warming in Pliocene climate simulations, Clim. Past, vol. 10, 79-90, 2014; doi:10.5194/cp-10-79-2014.

[8] U. Salzmann, A. M. Dolan, A. M. Haywood, W.-L. Chan, J. Voss, D. J. Hill, A. Abe-Ouchi, B. Otto-Bliesner, F. J. Bragg, M. A. Chandler, C. Contoux, H. J. Dowsett, A. Jost, Y. Kamae, G. Lohmann, D. J. Lunt, S. J. Pickering, M. J. Pound, G. Ramstein, N. A. Rosenbloom, L. Sohl, C. Stepanek, H. Ueda, and Z.-S. Zhang, Nature Clim. Change, vol. 3, 969-974, 2013; doi:10.1038/nclimate2008.

[9] J. R. Stewart, The ecology and adaptation of Neanderthals during the non-analogue environment of Oxygen Isotope Stage 3, Quat. Int., vol. 137, pp. 35-46, 2005; doi:10.1016/j.quatint.2004.11.018.

[10] S. Manabe and R. J. Stouffer, Coupled ocean-atmosphere model response to freshwater input: Comparison to Younger Dryas event, Paleoceanography, vol. 12, pp. 321-336, 1997; doi: 10.1029/96pa03932.

[11] M. Kageyama, U. Merkel, B. Otto-Bliesner, M. Prange, A. Abe-Ouchi, G. Lohmann, R. Ohgaito, D. M. Roche, J. Singarayer, D. Swingedouw, and X. Zhang, Climatic impacts of fresh water hosing under Last Glacial Maximum conditions: a multi-model study, Clim. Past, vol. 9, pp. 935-953, 2013; doi:10.5194/cp-9-935-2013.

[12] S. Sitch, B. Smith, I. C. Prentice, A. Arneth, A. Bondeau, W. Cramer, J. O. Kaplan, S. Levis, W. Lucht, M. T. Sykes, K. Thonicke, and S. Venevsky, Evaluation of ecosystem dynamics, plant geography and terrestrial carbon cycling in the LPJ dynamic global vegetation model, Global Change Biol., vol. 9, pp. 161-185, 2003; doi:10.1046/j.1365-2486.2003.00569.x.

[13] S. P. Harrison and M. F. Sanchez Goñi, Global patterns of vegetation response to millennial-scale variability and rapid climate change during the last glacial period, Quat. Sci. Rev., vol29, 2957-2980, 2010; doi:10.1016/j.quascirev.2010.07.016.

[14] G. R. Dickens, J. R. O'Neil, D. K. Rea, and R. M. Owen, Dissociation of oceanic methane hydrate as a cause of the carbon isotope excursion at the end of the Paleocene, Paleoceanography, vol. 10, pp. 965–971, 1995.

[15] S. P. Hesselbo and G. Pienkowski, Stepwise atmospheric carbon-isotope excursion during the Toarcian Oceanic Anoxic Event (Early Jurassic, Polish Basin), Earth Plann. Res. Lett., vol. 301, p.365-372, 2011.

[16] K-1 model developers: K-1 coupled model (miroc) description. Tech. rep., Center for Climate System Research, The University of Tokyo, 2004.

[17] E. Piñero, M. Marquardt, C. Hensen, M. Haeckel, K. Wallmann, et al., Estimation of the global inventory of mehtane hydrates in marine sediments using transfer functions, Biogeosciences, vol. 10, pp. 959-975, 2013; doi:10.5194/bg-10-959-2013.

[18] P. Yiou, J. Servonnat, M. Yoshimori, D. Swingedouw, M. Khodri, A. Abe-Ouchi, Stability of weather regimes during the last millennium from climate simulations. Geophys. Res. Lett., vol. 39, L08703, 2012; doi:10.1029/2012GL051310.

[19] C. Gao, A. Robock, and C. Ammann, Volcanic forcing of climate over the past 1500 years: An improved ice core-based index for climate models, J. Geophys. Res.-Atmos., vol. 113, p. D23111, 2008.

古環境研究のための多階層数値実験

課題責任者
阿部　彩子　　東京大学　大気海洋研究所
著者
阿部　彩子 *1，吉森　正和 *1，Wing-Le Chan*1，山本　彬友 *1，尾崎　和海 *1，大石　龍太 *2，
市野　美夏 *2，小澤　祐介 *1，小長谷貴志 *1，シェリフ多田野サム *1，新田　友子 *1，Alexandre Laine*2
*1　東京大学　大気海洋研究所
*2　情報・システム研究機構　国立極地研究所

大気海洋結合モデル MIROC4m を用いて、温暖な約 3.0 ～ 3.3 百万年前の鮮新世中期（mPWP）、氷期における千年スケールの寒冷期（亜氷期）、過去千年（西暦 850 ～ 2000 年）などの古気候シミュレーションを行った。MIROC4m mPWP シミュレーションでは、低緯度の温暖化には温室効果気体が、高緯度では反射率の低下が重要であることが示された。

また、亜氷期の急激な気候変動と、植生分布への影響を調べるために、淡水流入実験によって得られた境界条件のもとで、大気 GCM と全球動的植生モデルを走らせた。その結果、代替指標によって示される夏の乾燥化をよく再現した。一方で、亜氷期における植生への影響は森林の減少パターンの大局的な変化は再現したが、定量的には過小評価している。

温暖化時におけるメタンハイドレート分解が気候に与える影響を見積もるため、MIROC3.2 を用いて行われた大気二酸化炭素 4 倍増実験結果を用いた初期的な推定を行った。その結果、数千年スケールの時間をかけて多量のメタンハイドレートが分解することが示され、これにより海中の酸素を多量に消費する可能性があることが分かった。

さらに、時間変化する境界条件のもとで、過去千年の気候再現・感度実験も行われた。その結果、極端に大きな火山噴火イベントに対しては太平洋十年規模変動の位相が固定されることが示唆された。この結果は異なる初期値から積分した別のアンサンブルメンバーでも共通して見られた。

キーワード:大気海洋大循環モデル MIROC, 古気候モデリング, 鮮新世中期, 更新世後期, メタンハイドレート, 過去千年

Development of a High-Resolution Climate Model for Model-Observation Integrating Studies from the Earth's Surface to the Lower Thermosphere

Project Representative
Shingo Watanabe Research Institute for Global Change, Japan Agency for Marine-Earth Science and Technology

Author
Shingo Watanabe Research Institute for Global Change, Japan Agency for Marine-Earth Science and Technology

We investigated a reason why our T639L216 simulation of global middle atmosphere conducted last year was not successful, in which too strong gravity wave forcing destroyed the meridional structure of polar night jet soon after the simulation started. After several sensitivity studies changing the model's vertical resolution and horizontal diffusion parameters, we found that gravity wave forcing simulated in the model strongly depends on the model's vertical resolution. An increase of the model's vertical resolution from 500 m (216 layers) to 300 m (340 layers) dramatically improved the model's reproductively of the jet structures in the middle atmosphere.

Keywords: High-resolution climate model, atmospheric internal gravity waves

1. Introduction

This project aims at further developing gravity wave resolving global climate model and initiating integration studies of high-resolution model simulations and high-resolution observations with various measurement techniques (see our report Watanabe [1] for more details).

The main goal of this year was to investigate a reason why our high-resolution global simulation of the middle atmosphere using T639L216 (corresponding to 20 km horizontal resolution and 500 m in vertical) model was not successful, in which too strong gravity wave forcing destroyed the meridional structure of polar night jet soon after the simulation started. We took two approaches: one was sensitivity test simulation using the model (described later), and the other attempted to obtain observational constraints using a lidar observation dataset, that is, continuous measurements of temperature profiles at the Antarctic Davis station. In short, the former approach leaded to an improvement of the model, and the latter seemed to require further studies. This report particularly describes the former approach.

2. Model and experiment

The high-resolution climate model we are developing in this project is based on JAGUAR (Japanese Atmospheric General circulation model for Upper Atmosphere Research; Watanabe and Miyahara, [2]), and further modifications are outlined in our report in 2012 (Watanabe [1]). The model extends from the surface to a 150 km height. The model's configuration in the previous year was a horizontal resolution of T639 (about 20 km) and a vertical resolution of 500 m (has 216 vertical layers). This year we performed several sensitivity test simulations changing the model's vertical resolution and horizontal diffusion parameters. These sensitivity test simulations were conducted using the both of T213 (about 60 km) and T639 (about 20 km) horizontal resolution. After a series of T213 simulations changing only the model's vertical resolution, we performed a T639 simulation changing its vertical resolution from 500 m (L216) to 300 m (L340). The remaining of this report compares results of those two (T639L216 and T639L340) simulations. An initial condition of the T639L340 simulation was made by a linear interpolation from the T639L216 data of June 21, and the simulation was conducted from June 21 to June 30.

3. Results

Figure 1 compares the zonal mean zonal wind in June among observed monthly climatology, T639L216 one-day average on June 12, and T639L340 five-day average over June 26-30. The T639L216 model fails to reproduce the observed meridional structures of the wintertime polar night jet and summertime easterly jet in the middle atmosphere. In particular, the wintertime westerly jet in the Southern Hemisphere breaks down due to too strong gravity wave forcing in a 40-55 km height region (see Fig. 2c and the previous annual report; Watanabe [3]). On the other hand, T639L340 model better simulates the jet structures. This is mainly due to the fact that gravity wave forcing in the 40-55 km height region simulated by those model versions decreases with increasing model's vertical resolution (Fig. 2). The causal mechanisms of such dependence of gravity wave forcing on the model's vertical resolution is interesting,

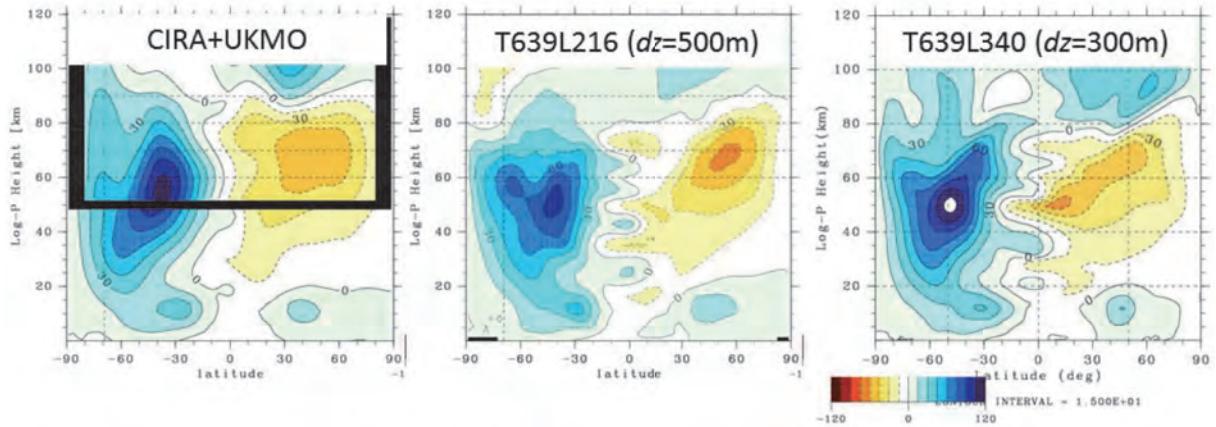

Fig. 1 The zonal mean zonal wind in June. Left: monthly climatology of the Met Office assimilation data (below 50 km) (Swinbank and O'Neill, [5]) and the 1986 Committee on Space Research (COSPAR) International Reference Atmosphere (CIRA) data (above 50 km) (Fleming et al. [6]). Center: T639L216 (*dz*=500m) Right: T639L340 (*dz*=300m). The model data corresponds to a one-day average of June 12 for T639L216, and a three-day average of June 28-30 for T639L340, respectively.

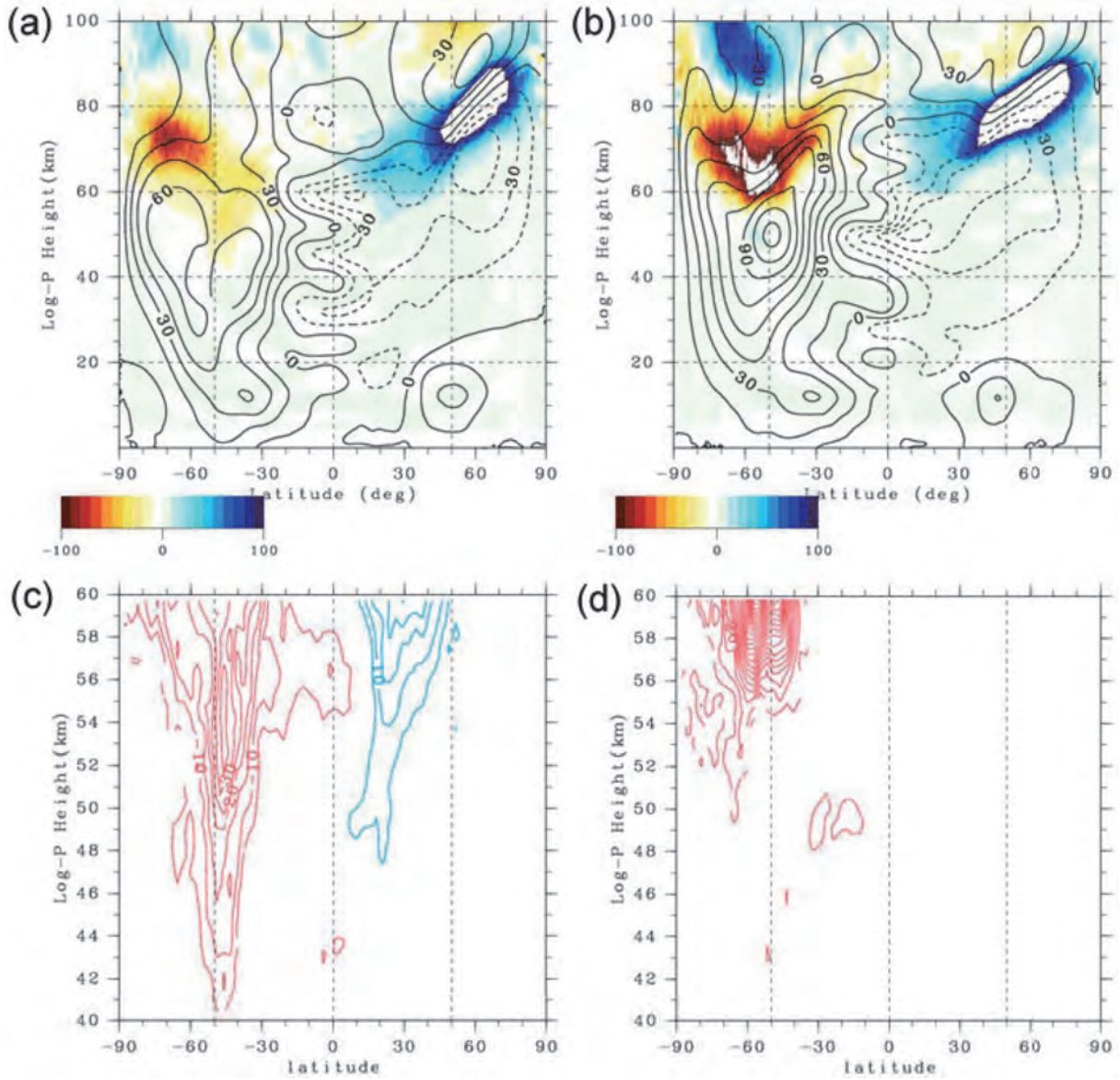

Fig. 2 The zonal mean zonal wind (contours with an interval of 15 ms^{-1}) and eastward gravity wave forcing (color shading with an interval of 10 $ms^{-1}day^{-1}$) in the T639L216 model during June 10-15 (a) and the T639L340 model during June 26-30 (b). Close up views of 40-60 km for the T639L216 (c) and T639L340 (d) models with the contour interval of 5 $ms^{-1}day^{-1}$.

and would be reported in the near future (Watanabe [4]).

Another interesting feature in Fig. 2 is that there exists a dipole structure of westward and eastward gravity wave forcing around 60-80 km and 80-100 km height of the SH mid-latitudes. The westward gravity wave forcing decelerates the upper part of wintertime westerly jet, while the eastward gravity wave forcing above that seems to maintain westerly winds along 50S of 80-100 km height. Since this westerly winds are absent in the observed climatology (Fig. 1), the eastward gravity wave forcing could be generated in unrealistic ways. Behaviors of gravity waves in this region must be investigated in the near future.

4. Closing remarks

This three-year project aimed at developing a state-of-the-art high-resolution global climate model which explicitly resolves a major part of vertically propagating atmospheric gravity waves, and initiating integration studies of high-resolution model simulations and high-resolution observations with various measurement techniques (Watanabe [1] and Watanabe [3]). We experienced that the increase of model's horizontal resolution from T213 (60 km) to T639 (20 km) was not successful, unless the vertical resolution was simultaneously increased. We have developed the T639L340 global climate model extending from the surface to about 150 km height with the 300 m vertical resolution, which qualitatively reproduces large-scale wind structures in the middle atmosphere. Our efforts to obtain statistical observational constraints on the model's gravity wave behaviors in the middle atmosphere has just started, and we need further time and new observations. Finally, we would like to thank this ES project, giving us a really good opportunity to start up several model-observation collaboration studies, whose outcomes would be reported in the future.

Acknowledgement

The author was partly supported by SOUSEI program, MEXT, Japan. The numerical simulations were performed using the Earth Simulator, and figures were drawn with the GFD-DENNOU library and GTOOL3.

References

[1] WATANABE, S., 2012: Development of a High-Resolution Climate Model for Model-Observation Integrating Studies from the Earth's Surface to the Lower Thermosphere. *Annual Report of the Earth Simulator Center April 2011 - March 2012*, http://www.jamstec.go.jp/esc/publication/annual/annual2011/pdf/2project/chapter1/119watanabe.pdf

[2] WATANABE, S. AND S. MIYAHARA, 2009: Quantification of the gravity wave forcing of the migrating diurnal tide in a gravity wave-resolving general circulation model. *J. Geophys. Res.*, **114**, D07110, doi:10.1029/2008JD011218.

[3] WATANABE, S., 2013: Development of a High-Resolution Climate Model for Model-Observation Integrating Studies from the Earth's Surface to the Lower Thermosphere. *Annual Report of the Earth Simulator Center April 2012 - March 2013*, http://www.jamstec.go.jp/esc/publication/annual/annual2012/pdf/2project/chapter1/117watanabe.pdf

[4] WATANABE, S., K. SATO, Y. KAWATANI, AND M. TAKAHASHI, Vertical resolution dependence of gravity wave momentum flux simulated by an atmospheric general circulation model, in preparation.

[5] SWINBANK, R. AND A. O'NEILL, 1994: A stratosphere-troposphere data assimilation system. *Mon. Weather Rev.*, **122**, 686–702, doi:10.1175/1520-0493(1994)122<0686:ASTDAS>2.0.CO;2.

[6] FLEMING, E. L., S. CHANDRA, J. J. BARNETT, AND M. CORNEY, 1990: Zonal mean temperature, pressure, zonal wind, and geopotential height as functions of latitude, COSPAR International Reference Atmosphere: 1986, Part II: Middle atmosphere models. *Adv. Space Res.*, **10**, 11 – 59, doi:10.1016/0273-1177(90)90386-E.

高解像度気候モデルの開発
－地表から下部熱圏大気のモデル・観測統合研究に向けて

課題責任者
渡邉　真吾　　海洋研究開発機構　地球環境変動領域
著者
渡邉　真吾　　海洋研究開発機構　地球環境変動領域

前年に行った T639L216 シミュレーションがうまく行かなかった（シミュレーション開始直後に、強すぎる重力波強制によって極夜ジェットの構造が壊れてしまった）理由について検討を行った。モデルの鉛直解像度や水平拡散パラメーターを変えながら行った一連の感度実験の結果から、モデルでシミュレートされる重力波強制の大きさが、モデルの鉛直解像度に強く依存することが判明した。モデルの鉛直解像度を 500m から 300m に増やすことにより、中層大気のジェットの構造が大きく改善された。

キーワード: 高解像度気候モデル , 大気内部重力波

Predictabilities of a Blocking Anticyclone and a Explosive Cyclone

Project Representative
Takeshi Enomoto Disaster Prevention Research Institute, Kyoto University

Authors
Takeshi Enomoto Disaster Prevention Research Institute, Kyoto University
Akira Yamazaki Earth Simulator Center, Japan Agency for Marine-Earth Science and Technology
Akira Kuwano-Yoshida Earth Simulator Center, Japan Agency for Marine-Earth Science and Technology
Mio Matsueda University of Oxford
Shunsuke Noguchi Disaster Prevention Research Institute, Kyoto University
Tetsuro Miyachi Disaster Prevention Research Institute, Kyoto University
Munehiko Yamaguchi Meteorological Research Institute, Japan Meteorological Agency
Shozo Yamane Doshisha University

In order to investigate the mechanisms of high-impact weather and seasonal variations of predictability, 10-day ensemble forecast experiments were conducted with the initial conditions on every day in a month in each season in 2010. This report describes the settings and preliminary results of the ensemble forecast experiments. Predictability studies are conducted on the Euro-Russian blocking anticyclone in the boreal summer and an explosive cyclone in the northwestern Pacific in the boreal winter among high-impact weather events occurred in 2010. Our preliminary investigation suggests that the Euro-Russian blocking anticyclone is maintained by the selective absorption of synoptic anticyclones and the predictability of the blocking anticyclone is strongly influenced by the storm-track activity in the north Atlantic. Our ensemble forecasts reproduced the rapid development of the explosive cyclone but with a 6–12 h delay in the forecast longer than 3 days. The forecast ensemble spread in our experiments share common features with those in operational ensemble forecasts from some centres, but not in those from other centres.

Keywords: Blocking Anticyclone, Explosive Cyclone, High-Impact Weather, Atmospheric General Circulation Model, Data Assimilation, Ensemble Forecast, Forecast Skill

1. Introduction

The aim of this project is to enhance knowledge on mechanisms of high-impact weather such as typhoons, explosive mid-latitude cyclones, blocking anticyclones and stratospheric sudden warmings and to clarify predictability variation associated with high-impact weather. Through the understandings on high-impact weather, we attempt to develop better data assimilation techniques and general circulation models to improve accuracy of numerical weather prediction.

In FY2013 10-day ensemble forecast experiments were conducted from every day in a month in each season at the Earth Simulator Center (ESC). Multi-model experiments were either postponed or conducted on other supercomputers. Instead ensemble forecast experiments for boreal spring and autumn planned for FY2014 were conducted in advance in FY2013 in addition to those for boreal winter and summer scheduled in FY2013. Almost all of the allocated computational resource was required to conduct these ensemble forecast experiments.

Case studies are conducted for the Euro-Russian blocking anticyclone in the boreal summer and an explosive cyclone in the northwestern Pacific in the boreal winter. The Euro-Russian blocking anticyclone lasted from July to August caused a number of disasters such as large-scale forest fires in Russia and floods in Pakistan and influenced remotely the heat wave in Japan. The explosive cyclone in the northwestern Pacific in early January caused severe meteorological and oceanic phenomena to highly impact Japan.

The present paper describes the experimental setting in section 2, the preliminary outcomes in section 3 along with the summary and some remarks in section 4.

2. Experimental Settings

In order to investigate the seasonal variations of predictability, ensemble forecast experiments were conducted using the Atmospheric General Circulation Model (AGCM) for the Earth Simulator (AFES) [1,2,3,4]. The spatial resolution

of AFES is T119L48 (1° horizontally and 48 levels vertically) and the ensemble size is 64 (including the forecast from the ensemble mean), matching that of ALERA2 (AFES–LETKF experimental ensemble reanalysis version 2, where LETKF stands for the local ensemble transform Kalman filter [5,6,7,8]) [9] used as the initial conditions. This ensemble forecast system, called ALEPS2 (AFES–LETKF ensemble prediction system version 2), was prepared in FY24 [10] and used in this study. The ensemble forecasts for 10 days were conducted from 1200 UTC every day in each month in January, April, July and October 2010, representing the boreal winter, spring, summer and autumn seasons, respectively. Produced ensemble forecast variables include the 6 hourly winds, temperature, specific humidity, surface and sea-level pressure, geopotential height, precipitation, snow, radiative and surface fluxes and soil moisture. Preliminary results on two case studies are described in the following section.

3. Results

3.1 Predictability Variation of the Euro-Russian Blocking Maintenance

A Euro-Russian blocking anticyclone (simply *blocking or block*, hereafter) occurred in early July and maintained until early August in 2010. This block stayed the same position over western Russia and caused an extreme heat wave in western Russia and flooding in Pakistan and northwestern India [11, 12]. Accurate medium-range forecasts of the Euro-Russian block would be useful to mitigate such disasters. Matsueda (2011) [13] showed that the predictability of the block maintenance varied through the blocking period. Fujii (2013) [14] pointed that the upstream trough influenced the predictability drop in late July and that the blocking was maintained by the generation of anticyclonic vorticity due to the low-frequency divergence. In the present study, daily predictability variation of the block was revisited with the ensemble forecast experiments.

The selective absorption mechanism (SAM) [15] has been proposed to explain the maintenance of the block by the interaction between synoptic eddies and blocking. In the SAM, a blocking anticyclone absorbs synoptic anticyclones in a Lagrangian sense to maintain its intensity. The SAM successfully explains a positive feedback between blocking and synoptic eddies. Our separate study shows that the SAM is effective for the maintenance of the Euro-Russian blocking (not discussed here). Provided that the SAM is the most effective mechanism of the maintenance of the Euro-Russian blocking, the following hypothesis may be suggested:

- Predictability variation of the Euro-Russian blocking is affected by the activity of synoptic eddies (storm tracks), and
- an inactive (active) storm track leads to low (high) blocking predictability.

The Atlantic storm track region, off the east coast of North America, is the major origin of synoptic eddies that interact with the block (Fig. 1). Despite over the ocean, observations are relatively dense and thus the initial errors are assumed to be small. Then if the storm track is active, we expect high predictability of the block because the major source of air parcels absorbed into the Euro-Russian blocking originates from the storm-track region with small initial errors. The hypothesis is verified with the ensemble forecast experiments.

The relationships between predictability variations of the Euro-Russian block and the activity of synoptic eddies in the

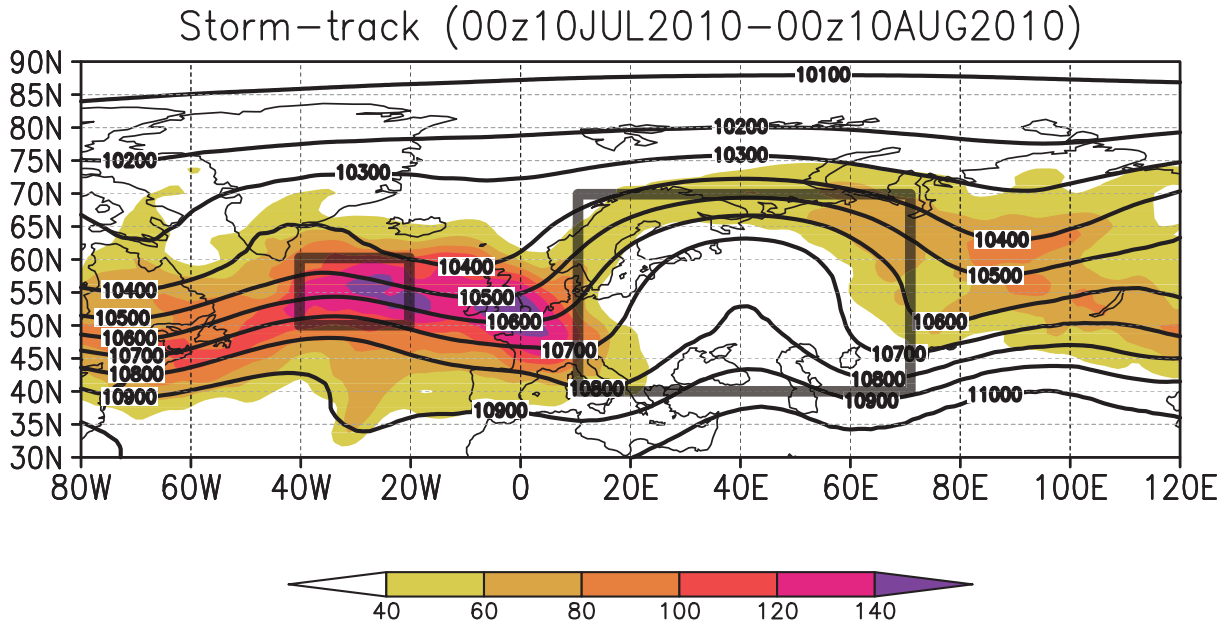

Fig. 1 The 2–8 days band-pass-filtered (eddy) kinetic energy (shade, m^2s^{-2}) and geopotential height (contour, m) at 250 hPa averaged over 0000 UTC 10 July–0000 UTC 10 August 2010. The former indicates the storm-track activity and the latter the Euro-Russian block. Small and large squares indicate frames of the storm-track and the blocking regions, respectively. Prepared from ALERA2.

storm-track region are investigated with the following two indices. To quantify the blocking predictability the forecast error index is defined by the root-mean-square difference (RMSD) of the 250-hPa geopotential height between the 5-day ensemble mean forecast and the ensemble mean analysis in ALERA2 at the valid time averaged over the blocking area defined in Fig. 1. The storm-track activity index is defined by the 2–8 days band-pass filtered eddy kinetic energy at 250 hPa obtained from the ALERA2 (Fig. 1), which has been conventionally used as an indicator of storm tracks in previous studies.

Figure 2 shows daily variation of the forecast error index (red line) and the storm-track activity index (black line). The forecast error index is negatively correlated with the storm-track activity index, during the period 19–31 July in particular. The largest forecast error on 20 July coincides with the inactive period of the storm-track activity. Conversely, the smallest forecast error on 29 July occurs simultaneously with the largest storm-track index. Note that the decrease of predictive skill for the blocking around 20 July occurred in other operational forecast models [13, 14]. This negative correlation, consistent with our hypothesis, suggests large influence of the storm-track activity on predictability variation of the blocking.

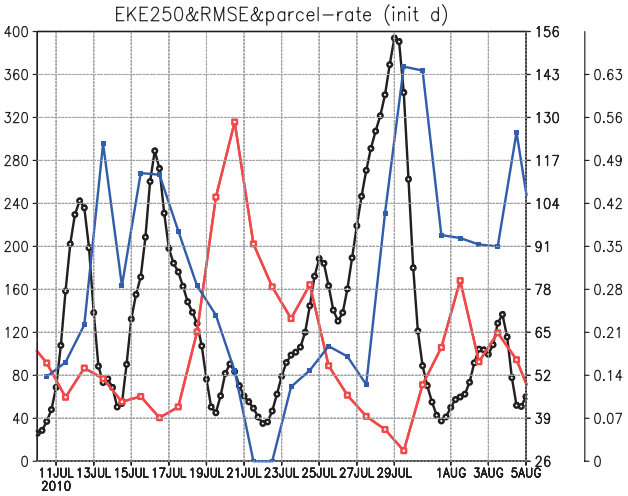

Fig. 2 The eddy kinetic energy (black, m^2s^{-2}) in the storm-track region and the 5-day forecast root-mean square difference (RMSD, red, m) in the blocking region and the absorption rate (blue). See text for the details. The three vertical axes are for black, red and blue lines from left to right, respectively. The horizontal axis indicates dates. Note that for the red line the dates correspond to the valid time of 5-day forecast.

Additional evidence for the hypothesis is obtained from the backward trajectory analysis. The strength of the positive feedback between the storm-track activity and the blocking is quantified by the rate of synoptic anticyclones originating from the storm-track region absorbed into the blocking anticyclone due to the SAM. The absorption rate is defined by the ratio of parcels that cross the storm-track region to those initially placed in the blocking in the backward trajectory for 5 days. The winds on the 330 K isentropic surface from the JRA25/JCDAS reanalysis dataset [16] are used to advect the parcels (see Yamazaki and Itoh (2013) [15] for the details). In Fig. 2 the absorption rate (blue line) takes the minimum and maximum on 22 July and 30 July, respectively. The both dates are about 1–2 days after the extrema of the forecast error. This can be interpreted as variation of the connection between the storm-track activity and the maintenance of the block due to the SAM. Daily backward trajectories indicate that the parcels cross the storm-track region with meandered westerlies when the absorption rate is high and the parcels pass the region to the south of the storm track when the absorption rate is low (Fig. 3).

3.2 Predictability of Explosive Cyclones in the Northwestern Pacific

A synoptic cyclone rapidly developed on 13 January to the east of Japan and the central pressure dropped to 978.3 hPa at (151.2E, 41.2N) on 14 January. With the enhanced westward pressure gradient, a typical pressure pattern near Japan in the winter, the explosive cyclone caused meteorological and oceanic

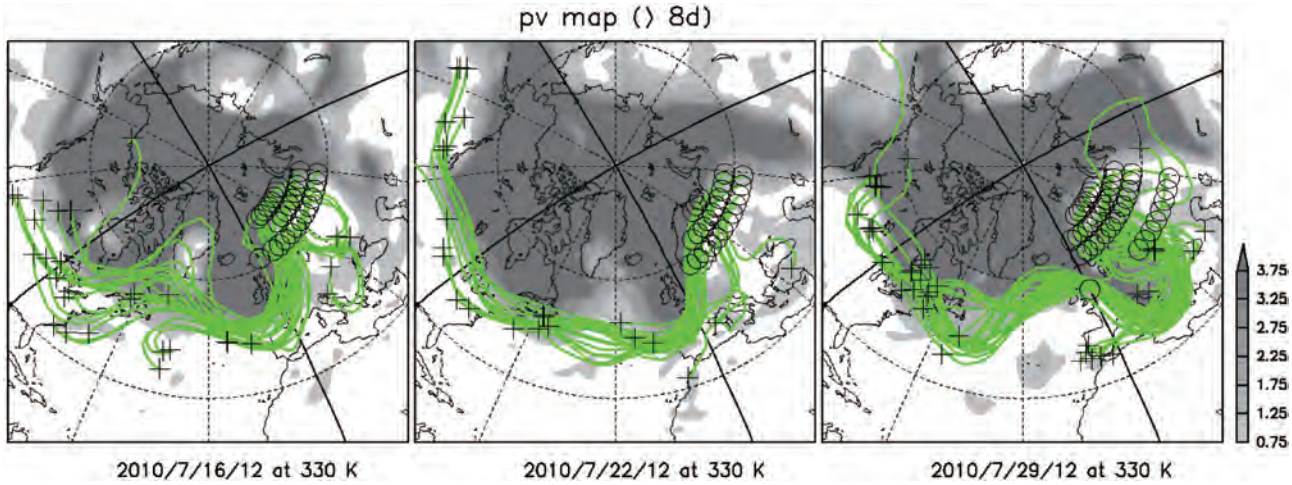

Fig. 3 The 6-day backward trajectories (green) from 1200 UTC 16, 1200 UTC 22 and 1200 UTC 29 July 2010, and the 8 days low-pass filtered Ertel's potential vorticity (PV PVU, shades) on the 330 K surface at these dates from left to right, respectively. The circles and + signs indicate the initial and end points of the backward trajectories, respectively. The PV is calculated from the JRA25/JCDAS on isentropic surfaces.

disasters such as wind burst, cold surge, heavy snow and rain and 5-m oceanic waves. The predictability of this explosive cyclone over the northwestern Pacific region was investigated using the 10-day ensemble forecasts at the ESC and operational forecasts from ECMWF, NCEP, JMA and UKMO in TIGGE database.

In the ESC forecasts using ALEPS2 longer than 3-day the development of the cyclone lags by 6–12 h, but the deepening of the cyclone is predicted well (Fig. 4). The operational forecasts can predict the rapid deepening timing even in the forecasts longer than 3 days. This is probably due to low quality of the ALERA2 over the ocean caused by the lack of satellite data assimilation.

The ensemble spreads for 3.5-day forecast are very different one another. In the ECMWF and JMA forecasts the ensemble spreads is large over the north of the cyclone, while in the NCEP, UKMO and ESC forecasts the ensemble spreads is large along frontal structures in the cyclone (Fig. 5). In addition the amplitudes are much larger in the ECMWF and JMA than those in the NCEP, UKMO and ESC forecasts. The difference could be attributed to the perturbation generation techniques: the singular vector (SV) method at ECMWF and at JMA and

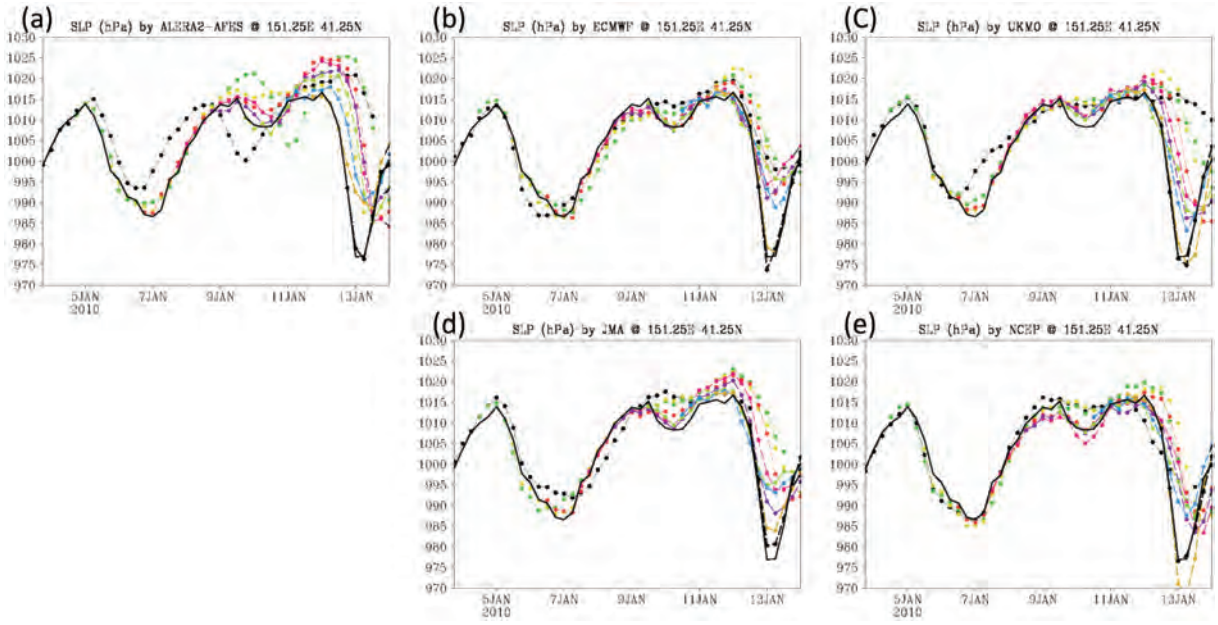

Fig. 4 The ensemble means of the SLP forecasts at 151.25E, 41.25N from every 1200 UTC 3–9 January (broken lines in black, green, yellow, red, magenta, purple, yellow-green, light blue, orange, black) of (a) ALEPS2, (b) ECMWF, (c) UKMO, (d) JMA and (e) NCEP. The solid black curve represents the SLP of ALERA2.

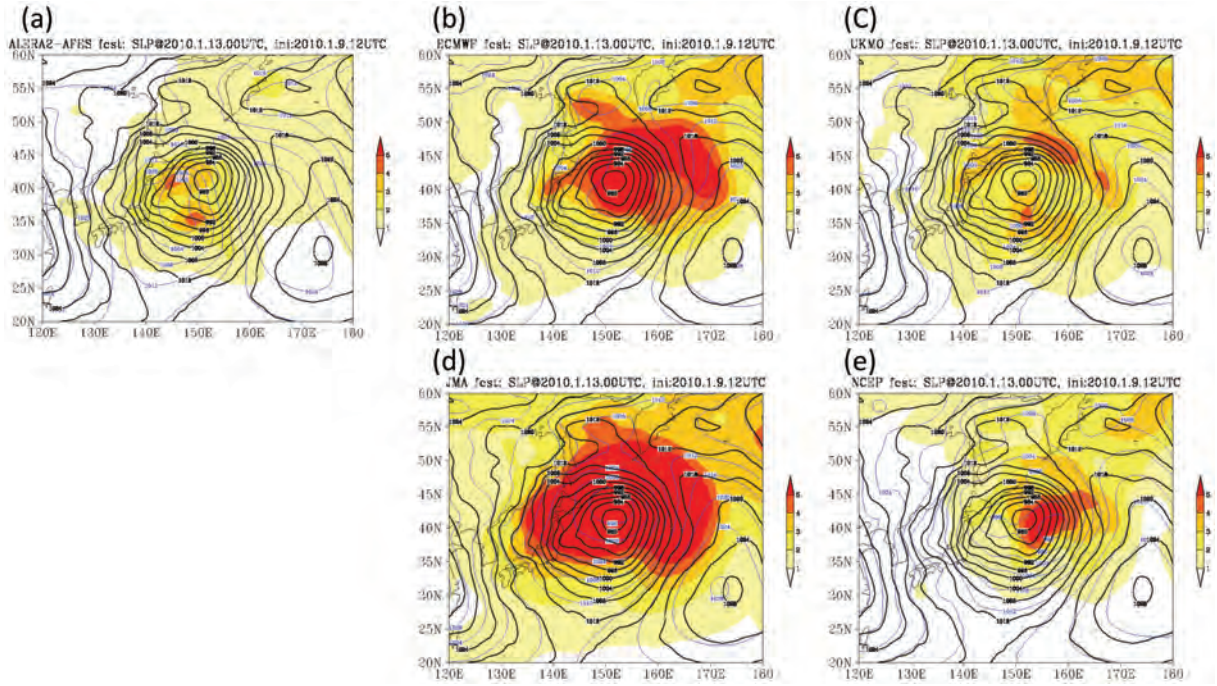

Fig. 5 The SLP forecasts at 0000 UTC 13 January from 1200 UTC 9 January. Ensemble mean (hPa, blue contour) and ensemble spread (colour shade). (a) ESC, (b) ECMWF, (c) UKMO, (d) JMA and (e) NCEP. The black contour represents the SLP of ALERA2.

the breeding vector (BV) method at NCEP and the ensemble Kalman filter (EnKF) method at UKMO and at ESC. Note that the both BV and EnKF perturbations are generated from the previous ensemble forecast and in this respect these methods are similar.

4. Summary and Final Remarks

Ensemble forecast experiments were conducted on the Earth Simulator and two case studies were conducted for the Euro-Russian blocking anticyclone in the boreal summer and an explosive cyclone in the northwestern Pacific in the boreal winter in 2010.

Our investigation indicates that the predictability variation of the Euro-Russian blocking is related to the activity of synoptic eddies in the western Atlantic storm track. This strong relationship between the blocking and the storm track offers evidence for the hypothesis that the Euro-Russian blocking was mainly maintained by the selective absorption of synoptic cyclones. In order to validate the SAM, we plan to conduct some sensitivity experiments to the storm track for the Euro-Russian blocking and investigation on other blocking events in the ensemble experiments.

The explosive cyclone in January 2010 is reproduced in our ensemble forecast experiments but with a delay of 6–12 h in forecasts longer than 3 days. The forecast ensemble spread in ALEPS2 is similar to those in the operational ensemble forecasts using the BV (NCEP) or EnKF (UKMO) as a perturbation generation method. We plan to conduct ensemble forecasts from the exchanged initial conditions to clarify the cause in the difference in the structure of the forecast ensemble spread.

In the future we wish to conduct observing system experiments for a future observation network design and sensitivity experiments with different parametrization schemes for model development in order to improve forecasts of high-impact weather.

List of Acronyms

AFES
AGCM for the Earth Simulator
AGCM
Atmospheric General Circulation Model
ALEPS2
AFES–LETKF ensemble prediction system version 2
ALERA2
AFES–LETKF experimental ensemble reanalysis version 2
BV
Breeding Vector
ECMWF
European Centre for Medium-range Weather Forecasts
ESC
The Earth Simulator Center
GrADS
Grid Analysis and Display System
JMA
The Japan Meteorological Agency
JRA25/JCDAS
The Japanese 25-year Reanalysis/JMA Climate Data Assimilation System
LETKF
Local Ensemble Transform Kalman Filter
NCEP
National Centers for Environmental Prediction, USA
PV
Potential Vorticity
RMSD
Root-mean square difference
SAM
Selective Absorption Mechanism
SLP
Sea-Level Pressure
SV
Singular Vector
UKMO
United Kingdom Met Office

Acknowledgement

The Earth Simulator was used under the support of JAMSTEC. Figures were drawn with GrADS [17] and the GFD-Dennou Ruby libraries.

References

[1] Numaguti, A., M. Takahashi, T. Nakajima, and A. Sumi, 1997: Description of CCSR/NIES atmospheric general circulation model. *In Study on the climate system and mass transport by a climate model, CGER's super computer monograph report*, **3**, National Institute for Environmental Studies, 1–48.

[2] Ohfuchi, W., H. Nakamura, M. K. Yoshioka,T. Enomoto, K. Takaya, X. Peng, S. Yamane, T. Nishimura, Y. Kurihara, and K. Ninomiya, 2004: 10-km mesh meso-scale resolving simulations of the global atmosphere on the Earth Simulator—Preliminary outcomes of AFES (AGCM for the Earth Simulator)—. *J. Earth Simulator*, **1**, 8–34.

[3] Enomoto, T., A. Kuwano-Yoshida, N. Komori, and W. Ohfuchi, 2008: Description of AFES 2: Improvements for high-resolution and coupled simulations. *In High Resolution Numerical Modelling of the Atmosphere and Ocean*, K. Hamilton and W. Ohfuchi (eds.), chapter 5, 77–97, Springer, New York.

[4] Kuwano-Yoshida, A., T. Enomoto, and W. Ohfuchi, 2010: An improved PDF cloud scheme for climate simulations. *Quart. J. Roy. Meteor. Soc.*, **136**, 1583–1597.

[5] Hunt, B., E. J. Kostelich, and I. Szunyough, 2007: Efficient data assimilation for spatiotemporal chaos: a local transform Kalman filter. *Physica D*, **230**, 1–2.

[6] Miyoshi, T. and S. Yamane, 2007: Local ensemble transform Kalman filtering with an AGCM at T159/L48. *Mon. Wea. Rev*., **135**, 3841–3861.

[7] Miyoshi T., S. Yamane, and T. Enomoto, 2007: The AFES-LETKF experimental ensemble reanalysis: ALERA. *SOLA*, **3**, 45–48. doi:10.2151/sola.2007-012.

[8] Miyoshi T., S. Yamane, and T. Enomoto, 2007: Localizing the error covariance by physical distances within a local ensemble transform Kalman filter (LETKF). *SOLA*, **3**, 89–92. doi:10.2151/ sola.2007-023.

[9] Enomoto, T., T. Miyoshi, Q. Moteki, J. Inoue, M. Hattori, A. Kuwano-Yoshida, N. Komori, and S. Yamane, 2013: Observing-system research and ensemble data assimilation at JAMSTEC. *In Data Assimilation for Atmospheric Oceanic and Hydrologic Applications II*, S. K. Park and L. Xu eds., 509–526, Springer-Verlag, Berlin Heidelberg.

[10] Enomoto, T., S. Yamane, A. Kuwano-Yoshida, M. Yamaguchi, M. Matsueda, T. Miyachi, A. Yamazaki, 2013: Predictability variation in numerical weather prediction: a multi-model muti-analysis approach. *Annual Report of the Earth Simulator Center*, April 2012–March 2013, 73–77.

[11] Hong, C.-C., H.-H. Hsu, N.-H. Lin, and H. Chiu, 2011: Roles of European blocking and tropical-extratropical interaction in the 2010 Pakistan flooding. *Geophys. Res. Lett*., **38**, L13806, doi:10.1029/2011GL047583.

[12] Watanabe, M., H. Shiogama, Y. Imada, M. Mori, M. Ishii, and M. Kimoto, 2013: Event attribution of the august 2010 Russian heat wave. *SOLA*, **9**, 65–68, doi:10.2151/ sola.2013-015.

[13] Matsueda, M., 2011: Predictability of Euro-Russian blocking in summer of 2010. *Geophys. Res. Lett*., **38**, doi:10.1029/2010GL046557.

[14] Fujii, A., 2013: Mechanism and Predictability of a Russian Blocking Event in Summer of 2010. *Master Thesis*, Department of Geophysics, Division of Earth and Planetary Sciences, School of Science, Kyoto University, 81 pp.

[15] Yamazaki, A. and H. Itoh, 2013: Vortex-vortex interactions for the maintenance of blocking. Part I: The selective absorption mechanism and a case study. *J. Atmos. Sci*., **70**, 725–742.

[16] Onogi, K., et al., 2007: The JRA-25 reanalysis. *J. Meteor. Soc. Japan*, **85**, 369–432.

[17] Grid Analysis and Display System Version 2.0.2 (Software), 2012: Calverton, Maryland, USA: GOLA/ IGES

ブロッキング高気圧と急速に発達する低気圧の予測可能性

課題責任者
榎本　剛　京都大学　防災研究所
著者
榎本　剛　京都大学　防災研究所
山崎　哲　海洋研究開発機構　地球シミュレータセンター
吉田　聡　海洋研究開発機構　地球シミュレータセンター
松枝　未遠　オクスフォード大学
野口　峻佑　京都大学　防災研究所
宮地　哲朗　京都大学　防災研究所
山口　宗彦　気象庁　気象研究所
山根　省三　同志社大学

影響の大きな気象のメカニズムを調べ、予測可能性の季節変動を調べるため、2010 年の各季節それぞれ 1 か月間の日々の初期値から 10 日間のアンサンブル予報実験を行った。本報告では、アンサンブル予報実験の設定と初期解析結果を示す。2010 年に発生した影響の大きな気象のうち、予測可能性研究を北半球夏季の欧露ブロッキング高気圧及び北半球冬季の北西太平洋における急速に発達する低気圧に対して行った。初期的な解析結果から、欧露ブロッキング高気圧は選択的に移動性高気圧を吸収することにより維持されており、ブロッキング高気圧の予測可能性は北西大西洋のストームトラックの活動度に大きな影響を受けていることが示唆された。急速に発達する低気圧はアンサンブル予報実験で再現されたが、3 日間を超える予報では 6 〜 12 時間の遅れを伴っていた。予報アンサンブル・スプレッドは、いくつかの現業アンサンブル予報のものと共通の特徴を持つが、別の現業アンサンブル予報とは大きく異なっていた。

キーワード:ブロッキング高気圧, 急速に発達する低気圧, 顕著現象, 大気大循環モデル, データ同化, アンサンブル予報, 予報精度

Computational Science of Turbulence in Atmospheric Boundary Layers

Project Representative
Takashi Ishihara Graduate School of Engineering, Nagoya University

Authors
Takashi Ishihara Graduate School of Engineering, Nagoya University
Kaoru Iwamoto Mechanical Systems Engineering, Tokyo University of Agriculture and Technology
Hiroya Mamori Mechanical Systems Engineering, Tokyo University of Agriculture and Technology
Tetsuro Tamura Interdisciplinary Graduate School of Science and Engineering, Tokyo Institute of Technology
Yasuo Kawaguchi Department of Mechanical Engineering, Tokyo University of Science
Takahiro Tsukahara Department of Mechanical Engineering, Tokyo University of Science

To understand the fundamental nature of turbulence in atmospheric boundary layers, we performed two kinds of direct numerical simulations (DNS) of turbulent boundary layers (TBL); one is the TBL along a flat plate and the other is the TBL with sinusoidal wavy wall. The data analysis of the former showed that the turbulent/non-turbulent interface of the TBL has a double structure which consists of a turbulent sub-layer with thickness of the order of the Taylor micro scale and its outer boundary (super layer) with thickness of the order of the Kolmogorov length scale. In the latter DNS, we observed the streaky structure at the downslope of the wavy wall, where the wall shear stress is negative due to the flow separation while the Sherwood number is positive. For the purpose of the estimation and control of the wind-blown sand in the atmosphere, we developed a code to simulate three-dimensional two-phase flow in conjunction with the four-way coupling. Using the code we successfully obtained basic statistics (e.g., the drag coefficient of a spherical solid particle) and demonstrated particle-particle interactions in low-Reynolds-number turbulence. We also performed LES of turbulent flows for dealing with urban environmental and strong wind disaster problems.

Keywords: High-resolution DNS, turbulent boundary layer, rough wall, wind-blown sand, LES, urban turbulent boundary layer

1. Data analysis based on the DNS of turbulent boundary layers

There are many environmental problems in which turbulent flows have sharp interfaces between turbulent region and non-turbulent region. To predict high-Reynolds-number turbulence phenomena more accurately, we need to understand the properties of such sharp interfaces. Recently turbulent and non-turbulent (T/NT) interface has been studied actively both in experiments and computations. A recent review is given by da Silva et al.[1]. However there are still open questions about the interfaces.

This year we studied the properties of the T/NT interface of turbulent boundary layers (TBL) using a series of DNS data of TBL. The values of the momentum-thickness-based Reynolds numbers, Re_θ, used for this study, are 500−2200. Figure 1 is a contour plot of vorticity magnitude near the boundary on a plane parallel to both the streamwise and wall-normal directions. As the figure shows, there is a sharp change of vorticity and we can define the T/NT interface of the TBL using a threshold like $\omega=\omega_c=0.7(U_\infty/\delta)$, where U_∞ is the free stream velocity and δ is the boundary layer thickness.

Analysis of the conditional statistics near the T/NT interface of the TBL shows that there is a small peak in the span-wise vorticity, and an associated small jump in stream-wise velocity. The velocity jump near the T/NT interface of the TBL is of the order of the *rms* value of velocity fluctuations near the interface. The results of the conditional statistics and their Reynolds number dependence show that the interfacial layer has a double structure that consists of a turbulent sub-layer with thickness of the order of the Taylor micro scale and its outer boundary (super layer) with thickness of the order of the Kolmogorov

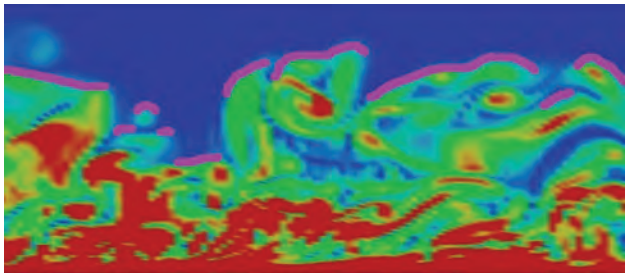

Fig. 1 A contour plot of the magnitude of vorticity near the wall of turbulent boundary layers. The contour curve (pink) defined by $\omega=\omega_c=0.7(U_\infty/\delta)$ captures well the T/NT interface of the TBL.

length scale. An approximate profile of the conditional average of span-wise vorticity near the interface fits well to the DNS data. Conditional cross correlation of the streamwise or the wall normal velocity fluctuations changes sharply across the interface. This result is consistent with the blocking mechanism (proposed by Hunt and Durbin [2]) of the vortical layers.

2. DNS of turbulent boundary layer on rough walls

Turbulent thermal boundary layer flow over a sinusoidal wavy wall surface is of importance in view point of the practical engineering application and the environmental problem. In order to investigate the effect of the sinusoidal wavy wall on the turbulent thermal boundary layer flow, we use the DNS code optimized for ES2. The sinusoidal wavy wall is a simple model of the roughness. The different wavelengths are investigated for λ / 2a =12.5, 15, 22.5 and 45. Here, the amplitude of the sinusoidal wavy wall, a, is kept constant.

Figure 2 shows the computational domain that consists of a main and a driver parts. Both domains are the boundary layer flows. The driver part generates the inflow condition of the main part by means of the recycle method [3]. The lower wall of the main part forms the sinusoidal wavy wall. The parallel and vectorization efficiencies of the present DNS code are 98.43% and 99.50%, respectively.

Figure 3 shows the visualization of the vortical structure over the wavy wall surface (λ/2a=15). The direction of the base flow is from left to right. The color contour on the wall indicates the wall shear stress (left) and the Sherwood number (right). The large wall shear stress and the Sherwood number are observed on the top of the wavy wall. At the downslope of the wavy wall, the wall shear stress is negative due to the flow separation while the Sherwood number is positive and the streaky structure is observed. This phenomenon implies the dissimilarity between the momentum and the mass transfers.

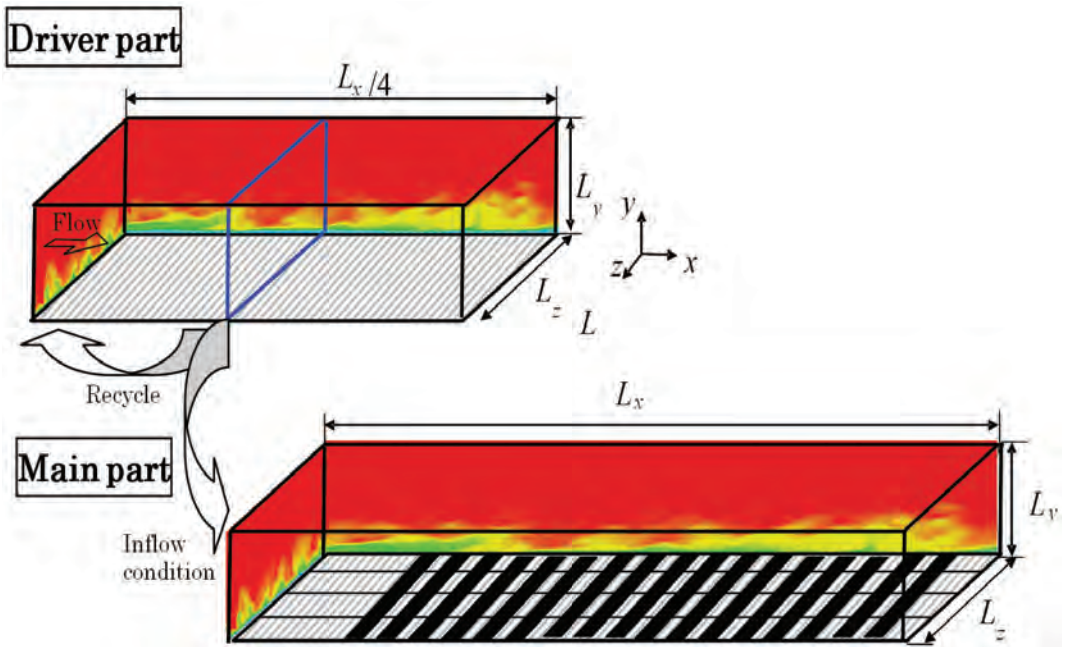

Fig. 2 Computational domains for turbulent boundary layer on several sinusoidal wavy walls.

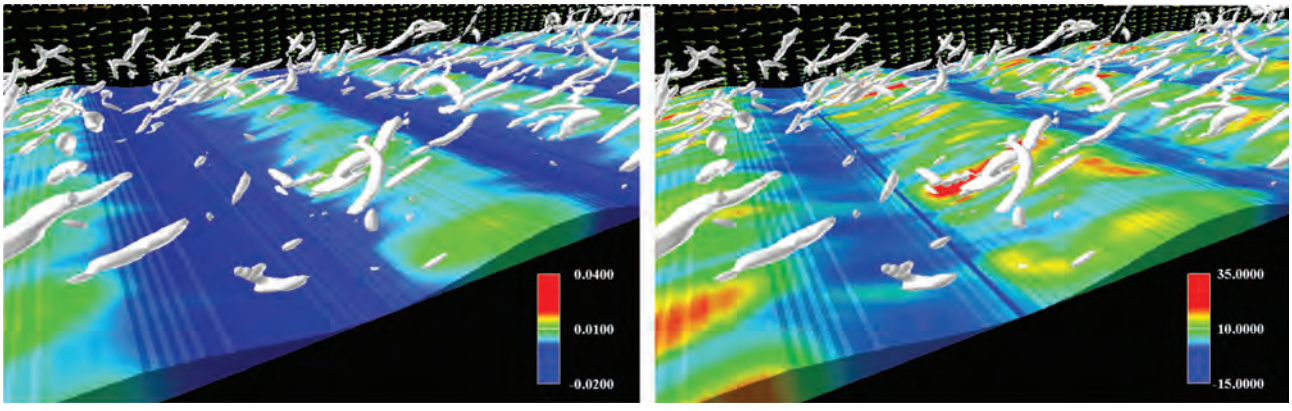

Fig. 3 Visualization of the vortical structure with the wall shear stress (left) and the Sherwood number (right) on the wavy wall surface (λ / 2a =15.0).

3. DNS of multiphase wall turbulence toward estimation and control of wind-blown sand in the atmosphere

The dynamics of wind-blow sand in ABL (atmospheric boundary layer) have been investigated by many researchers with the aim of combating desertification. The desertification is one of the serious global environmental issues, and its major cause is the sand movement triggered by wind on desert. This phenomenon is the most significant cause of sand storms and yellow dust, and it eventually induces further desertification, health damage, and atmospheric pollution such as PM 2.5 and 10. The wind-blown sand movement itself occurs as a result of complicated combinations of several factors of the sand-bed surface, dune and ripple topologies, ambient airflow, sand particles, and so on. In the context of these issues, it is important to clarify the mechanism of the wind-blown sand movement with the background of turbulent flow.

Preliminary works we have carried out so far are four-way coupling simulations of various two-phase laminar flows. The present numerical simulations considering particle-particle and particle-wall interactions have been done using the immersed boundary method to simulate three-dimensional viscous incompressible flows interacting with a moving, solid boundary, as shown in Fig. 4. These computed results were in good agreement with experimental measurements. Moreover, the effect of rotational motions of spherical particles was found to be significant when we analyzed the particle-particle interactions by the intermediary of ambient fluid without any collision of particles. This emphasizes the importance of rotational motions in four-way coupling simulations.

4. Application of LES of turbulent flows to urban environmental and strong wind disaster problems

The objective of this chapter is to elucidate turbulence characteristics of the wind flows around the structure or over the undulating ground surface with various types of roughness. Actual terrain has been selected for the LES of wind over the hills covered densely by trees. Using the canopy model or the logarithmic law based on the roughness length, the bottom boundary condition is imposed. The effect of the boundary treatment for the roughened undulating surface on the turbulence structures in the near-wall region has been discussed.

Next, based on the computed results, the turbulent flow characteristics around the curved surfaces such as a windmill and a complex terrain are investigated. Here, as a typical and a fundamental case in such a curved surface, a circular cylinder is focused on.

Ono and Tamura [5] performed LES analysis and investigate the asymmetric flow coupled with steady lift force around a circular cylinder in the critical Reynolds number (Re) region. Figure 5 shows the time histories of the drag coefficient (C_D) and the lift coefficient (C_L). Mean drag indicates to be equal to about 0.8 that is consistent with the previous experimental data [6]. Lift is largely fluctuating and its mean value is larger than mean drag. Figure 6 illustrates the time-averaged velocity field around a circular cylinder in the critical Reynolds number region. It can be recognized that the higher velocity occurs only on the upper side of the cylinder and the wake is located on down side. It means that the mass flow rate becomes larger on

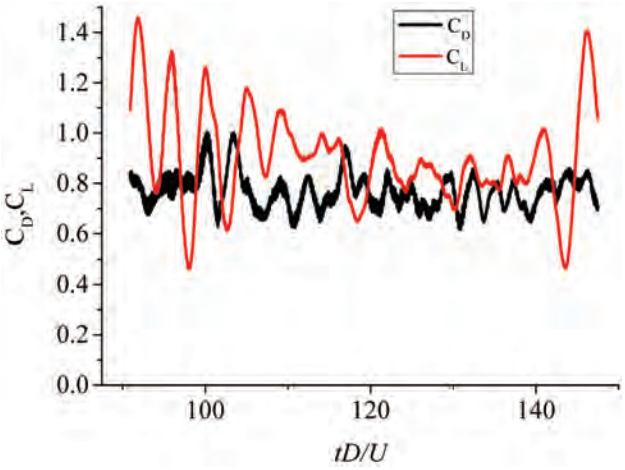

Fig. 5 The time histories of drag and lift coefficients.

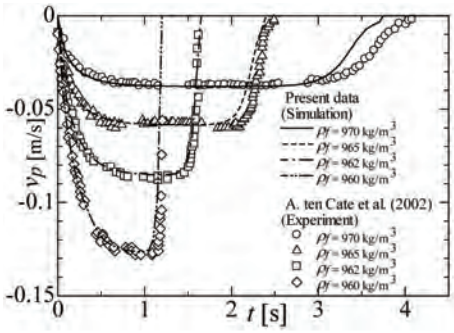

(a) Settling velocity of a solid particle.

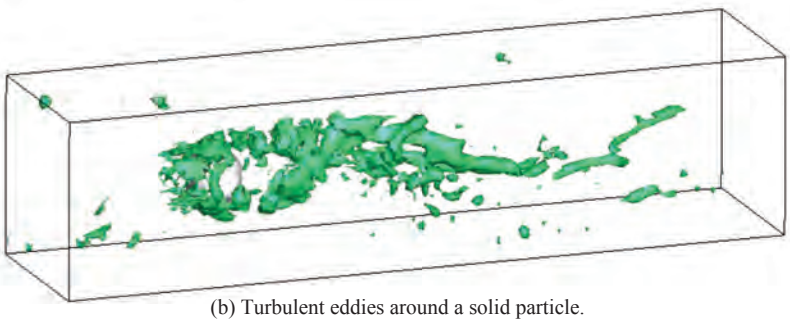

(b) Turbulent eddies around a solid particle.

Fig. 4 Results of preliminary simulations of solid-air two-phase flows using the immersed boundary method: (a) Temporal variation of the vertical velocity of a solid sphere settling in an initially static viscous fluid. Compared with experimental data [4]. (b) Visualization of eddies around a solid sphere suspended in a channel flow. The mean flow moves left to right.

the upper side. These physically important phenomena in the critical region such as the asymmetric flow and large value of the steady lift beyond to the drag coefficients could be simulated only in the case of using very fine grid resolution in the circumferential direction in addition to the span-wise direction.

Also, based on the computed flow, the time-averaged flow and pressure distributions in the critical Re region are investigated. As a result, the shifts of the stagnation points are recognized associated with imbalance of the flow on the both sides of the cylinder [5].

Ono and Tamura [5] clarified that the asymmetric flow in the critical Re region is not induced only the difference of the flow characteristics on the both sides of the cylinder. It is clarified that the asymmetric flow was brought about by the 3D interaction of the flow on the both sides. This 3D flow characteristic results in stable formation of the asymmetric flow state in the critical Re region.

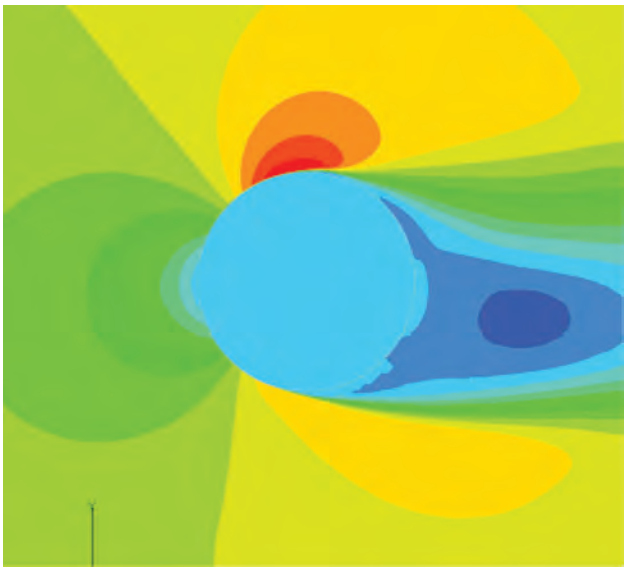

Fig. 6 The contours of time-averaged velocities.

References

[1] C. B. da Silva, J. C. R. Hunt, I. Eames, and J. Westerweel, "Interfacial Layers Between Regions of Different Turbulence Intensity," Annu. Rev. Fluid Mech., 46, 567–590, 2014.

[2] J. C. R. Hunt and P. A. Durbin, "Perturbed vortical layers and shear sheltering." Fluid Dyn. Res., 24, 375–404, 1999.

[3] T.S. Lund, X. Wu, and K.D. Squires, "Generation of turbulent inflow data for spatially-developing boundary layer simulations," J. Comput. Phys., 140, 233–258, 1998.

[4] A. ten Cate, C. H. Nieuwstad, J. J. Derksen, and H. E. A. van den Akker, "Particle imaging velocimetry experiments and lattice-Boltzmann simulations on a single sphere settling under gravity," Phys. Fluids, vol. 14, 4012–4025, 2002.

[5] Y. Ono and T. Tamura, "LES of the flow around a circular cylinder in the critical Reynolds number region -Study on asymmetric characteristics of flow and lift," Proc. of 10th International ERCOFTAC Symposium on Engineering Turbulence Modelling and Measurements (ETMM10), (To be published), 2014.

[6] M. M. Zdravkovich, *Flow around Circular Cylinders*, Oxford University Press, 1997.

大気境界層乱流現象解明のための計算科学

課題責任者
石原　　卓　　名古屋大学　大学院工学研究科
著者
石原　　卓　　名古屋大学 大学院工学研究科
岩本　　薫　　東京農工大学　工学府
守　　裕也　　東京農工大学　工学府
田村　哲郎　　東京工業大学　大学院総合理工学研究科
川口　靖夫　　東京理科大学　理工学部
塚原　隆裕　　東京理科大学　理工学部

大気境界層における乱流の性質を理解するため、我々は乱流境界層の 2 種類の直接数値計算（DNS）を実施した。そのうちの 1 つは平らな平面上の乱流境界層であり、もう一つは正弦波状の壁上の乱流境界層である。前者の DNS のデータ解析により、乱流境界層の乱流・非乱流界面が二重構造を持っており、それは幅がテイラー長でスケールする乱流・非乱流遷移層とコルモゴロフ長でスケールする表層部（スーパーレイヤー）から構成されていることが分かった。また、後者の DNS では、正弦波状の壁の下り坂部では、シャーウッド数が正であるのに対し、壁剪断応力は流れの剥離により負になることが分かった。大気による飛砂の評価と制御のため、我々は固 - 固、固 - 気の相互干渉を考慮した 3 次元二相流の DNS コードを開発した。開発したコードにより、球状粒子の抵抗係数などの基本的な統計量の妥当な結果が得られ、低レイノルズ数乱流中の複数粒子の追跡も可能であることが分かった。我々は、さらに、都市環境における環境問題や強風災害問題に対処する目的のための乱流のラージ・エディ・シミュレーション（LES）も実施した。

キーワード:大規模直接数値計算, 乱流境界層, 粗面, 飛砂, LES, 都市型乱流境界層

A Large-Scale Self-Organizing Map for Metagenome Studies for Surveillance of Microbial Community Structures

Project Representative
Toshimichi Ikemura Nagahama Institute of Bio-Science and Technology

Authors
Takashi Abe[*1], Yuki Iwasaki[*2], Kennosuke Wada[*2], Yoshiko Wada[*2] and Toshimichi Ikemura[*2]

*1 Department of Information Engineering, Faculty of Engineering, Niigata University

*2 Department of Bioscience, Nagahama Institute of Bio-Science and Technology

Metagenome analyses, which directly sequence mixed genomes of uncultured environmental microorganisms, have become widely used in earth sciences for clarifying a microbial community structure in an environmental ecosystem. We have previously developed an unsupervised clustering method “Batch-learning SOM: BLSOM” for oligonucleotide compositions in genomic fragments, which recognizes species-specific characteristics of oligonucleotide composition in individual genomes and can cluster tens millions of genomic sequences according to phylogenetic groups, solely depending on their oligonucleotide composition. For phylogenetic classification of metagenomic sequences obtained from environmental samples, we have annually updated a large-scale tetranucleotide BLSOM for all available sequences from species-known prokaryotes and eukaryotes, as well as from viruses and organelles. By mapping metagenomic sequences from an environmental sample on this large-scale BLSOM constructed by ES, we can clarify the microbial community structure in the ecosystem. This strategy, however, cannot be properly applied to short sequences (e.g. those shorter than 100 bp) and thus sequences obtained with new generation sequencers widely used currently. To solve this issue, we have developed an oligonucleotide BLSOM for tRNA genes (tDNAs) since their lengths are mostly shorter than 90 bp and their sequences have been stably conserved during evolution. When constructing BLSOM with species-unknown tDNAs obtained from metagenomic sequences plus species-known microbial tDNAs (ca. 0.6 million tDNAs in total), a large portion of metagenomic tDNAs has self-organized with species-known tDNAs, giving information on microbial communities in environmental samples. BLSOM also allows us to identify tDNAs suitable as phylogenetic markers for rare phylotypes.

Keywords: batch learning SOM, metagenome, microbial community, phylogenetic marker, tRNA, oligonucleotide composition, new-generation sequencer

1. Introduction

Metagenome analyses, which directly sequence mixed genomes of uncultured environmental microorganisms, have been widely used in earth and environment sciences. A massive amount of environmental metagenomic sequences has been registered in the International DNA Sequence Databanks (DDBJ/EMBL/GenBank) but poorly characterized, especially in cases of short sequences obtained from new generation sequencers, and therefore, a large portion of short metagenomic sequences has been stored in a less useful manner. In more detail, while homology search for nucleotide and amino-acid sequences such as BLAST has widely been used for a basic bioinformatics tool for phylogenetic characterization of gene/protein sequences, phylotypes of most metagenomic sequences, especially of short sequences obtained by new generation sequencers, cannot be properly assigned. This is because reliable phylogenetic trees required for their phylogenetic assignment cannot be constructed due to their sequence novelty and short length. To solve this issue, we have developed an unsupervised clustering method “Batch-learning SOM: BLSOM” for oligonucleotide composition [1-4]. This unsupervised clustering method recognizes species-specific characteristics of oligonucleotide composition in genomic fragments of individual genomes, permitting clustering (self-organization) of fragment sequences according to species without need for species information during BLSOM calculation. Furthermore, this BLSOM is suitable for actualizing high-performance parallel-computing with the high-performance supercomputer, ES [3-5].

Because BLSOM with oligonucleotide (e.g. tetranucleotide) composition can cluster genomic fragments relatively short in length (e.g. 500-bp sequences) according to phylotype, this method has been successfully applied to the phylogenetic

classification of a massive amount of metagenomic sequences [4-7]. When considering phylogenetic classification of species-unknown sequences obtained from environmental samples, it is important to construct and update, at least once a year, a large-scale BLSOM for all available sequences from species-known prokaryotes and eukaryotes, as well as from viruses and organelles. By mapping metagenomic sequences obtained from environmental samples on the newest BLSOM constructed with ES, we have clarified the microbial community structure in individual ecosystems analysed in Japan [7].

2. Materials and Methods

We have previously modified the conventional SOM for genome informatics on the basis of batch-learning SOM to make the learning process and resulting map independent of the order of data input [1,2]. The initial weight vectors were defined by PCA instead of random values, and genomic sequences were analysed as described previously [1-4].

We have constructed and updated a large-scale database for tRNA genes (tDNAs) obtained not only from the completely sequenced genomes but also from draft sequences of prokaryotic genomes in WGS (Whole Genome Shotgun) division in DDBJ/EMBL/GenBank. In accord with the remarkable progress of DNA sequencing technology, a vast quantity of metagenomic sequences obtained from a wide variety of environmental and clinical samples have been compiled in DDBJ/EMBL/GenBank, and short metagenomic sequences obtained even with new-generation sequencers contain a large number of full-length tRNAs because tRNA lengths are short. Therefore, tDNAs found from metagenomic sequences have also been included in the tRNA gene database [8-10]. To enhance the completeness and accuracy of tDNAs compiled in "tRNADB-CE" (http://trna.ie.niigata-u.ac.jp), three computer programs, tRNAscan-SE [11], ARAGORN [12], and tRNAfinder [13] were used in combination, since their algorithms partially differed and rendered somewhat different results. The tDNAs found concordantly by three programs were stored in tRNADB-CE after briefly checking anticodon sequences. Discordant cases among programs were manually checked by experts in tRNA experimental fields before inclusion into the database (8-10). In the newest version, approximately 0.4 million bacterial tDNAs obtained from more than 7000 complete or near complete genomes and approximately 0.2 million tDNAs obtained from more than 200 environmental samples have been compiled [10], and these tDNAs have been used in the present BLSOM analysis.

3. Results

3.1 Oligonucleotide BLSOMs for bacterial tDNAs

Because the annual updating of the large-scale tetranucleotide BLSOM with ES and its application to metagenome studies have been described in detail a few times in our previous annual reports, we will focus in this report on a newly developed BLSOM strategy suitable for phylogenetic analyses using short metagenomic sequences obtained from new generation sequencers, because of the following reason. Our previous oligonucleotide BLSOMs have shown that genomic sequences of 1 kb or longer can be clustered according to species with high accuracy and those of 300 bp with sufficient accuracy. However, this species-dependent clustering reduces evidently for sequences shorter than 100 bp, which are obtained mainly from new generation sequencers widely used. To solve this issue, we have focused on tRNA genes because their lengths are mostly less than 90 bp and their sequences have been stably conserved during evolution at least at a phylum level [9].

It should also be pointed out that oligonucleotides such as penta- and hexanucleotides often represent motif sequences responsible for sequence-specific protein binding (e.g. transcription factor binding). Occurrences of such motif oligonucleotides should differ from occurrences expected from the mononucleotide composition in the respective genome and may differ among genomic portions within a single genome. Actually, we have recently found that a pentanucleotide-BLSOM for the human genome can detect characteristic enrichment of many transcription-factor-binding motifs in pericentric heterochromatin regions [14]; i.e. BLSOM can effectively detect the characteristic and combinatorial occurrences of functional motif oligonucleotides in genomic sequences.

Each tRNA has characteristic and combinatorial occurrences of motif oligonucleotides, which are required for fulfilment of its function (e.g. binding to proper enzymes and other RNAs) and its structural formation (e.g. clover leaf), and these functionary important motif oligonucleotide are thought to be stably conserved during evolution. Taking these into account, we have constructed BLSOM for pentanucleotide compositions in prokaryotic tRNAs in tRNADB-CE (Fig. 1) as described previously [1,5]. Interestingly, the tRNAs are primarily separated according to amino acid, without giving information other than the oligonucleotide composition (manuscript in preparation); lattice points containing only tRNAs belonging to one amino acid are marked by the color representing the amino acid (Figs. 1A and 1B). This shows that the BLSOM can detect characteristic combinations of motif oligonucleotides required for proper recognition by various enzymes including aminoacyl-tRNA synthetases. The tDNAs for one amino acid form one or a few major territories and many tiny satellite-type spots (Fig. 1B). The number of tDNAs in each lattice point is important when considering biological significance of minor territories and tiny satellites, and thus the vertical bar in Fig. 1C presents the number of tDNAs for three examples of amino acids. Lattice points in major and minor territories of each amino acid apparently contain many tDNAs, and even some tiny satellites have multiple tDNAs (Fig. 1C). Satellites with multiple tDNAs may not represent improper cases, such

as those raised by DNA sequencing errors, but represent real tDNAs with certain nonstandard characteristics. The tDNAs belonging to a sharp peak in a satellite spot located away from the correspondent major territories have been found to primarily represent isoaccepting tDNAs (isoacceptors) of various species belonging to one phylogenetic family, which often differ in sequence for few bases. This finding indicates that the nonstandard-type tDNAs are candidates for molecular phylogenetic markers representing a specific phylotype; i.e. this BLSOM can provide a strategy to find phylogenetic marker tDNAs.

3.2 BLSOM for species-known plus species-unknown tDNAs

The tRNADB-CE has included tDNAs obtained from a massive amount of metagenomic sequences obtained from approximately 2000 environmental samples; tDNAs predicted concordantly by all three programs have been included and are abbreviated as metagenomic tDNAs. Since metagenomic sequences should be derived not only from bacteria, but also archaea and fungi, we have constructed BLSOM with species-unknown metagenomic tDNAs plus species-known bacterial, archaeal, and fungal tDNAs; 0.6 million tDNAs in total (Both in Fig. 2A). Species-unknown metagenomic and species-known microbial tDNAs are visualized separately in Metagenome and Known in Fig. 2A. Amino acid-dependent clustering is apparent, but their separation patterns are more complex than those for species-known bacterial tDNAs listed in Fig. 1A, and there are more black lattice points in Fig. 2A than in Fig. 1A. A major portion of black lattice points are observed for metagenomic tDNAs (Metagenome in Fig. 2A) while a minor portion is observed also for species-known tDNAs (Known in Fig. 2A). Detailed inspection of the species-known tDNAs belonging to black lattice points has revealed these to be primarily archaeal and fungal tDNAs, showing that BLSOM has separated archaeal and fungal tDNAs from bacterial tDNAs and that a significant level of metagenomic tDNAs should be derived from archaea and fungi.

The observation that a large portion of archaeal and fungal tDNAs are located in black lattice points in Fig. 2A indicates their self-organization to depend largely on their sequence characteristics distinct from bacterial tDNAs, rather than on distinctions between amino acids. To study amino acid-dependent clustering of archaeal and fungal tDNAs, BLSOMs

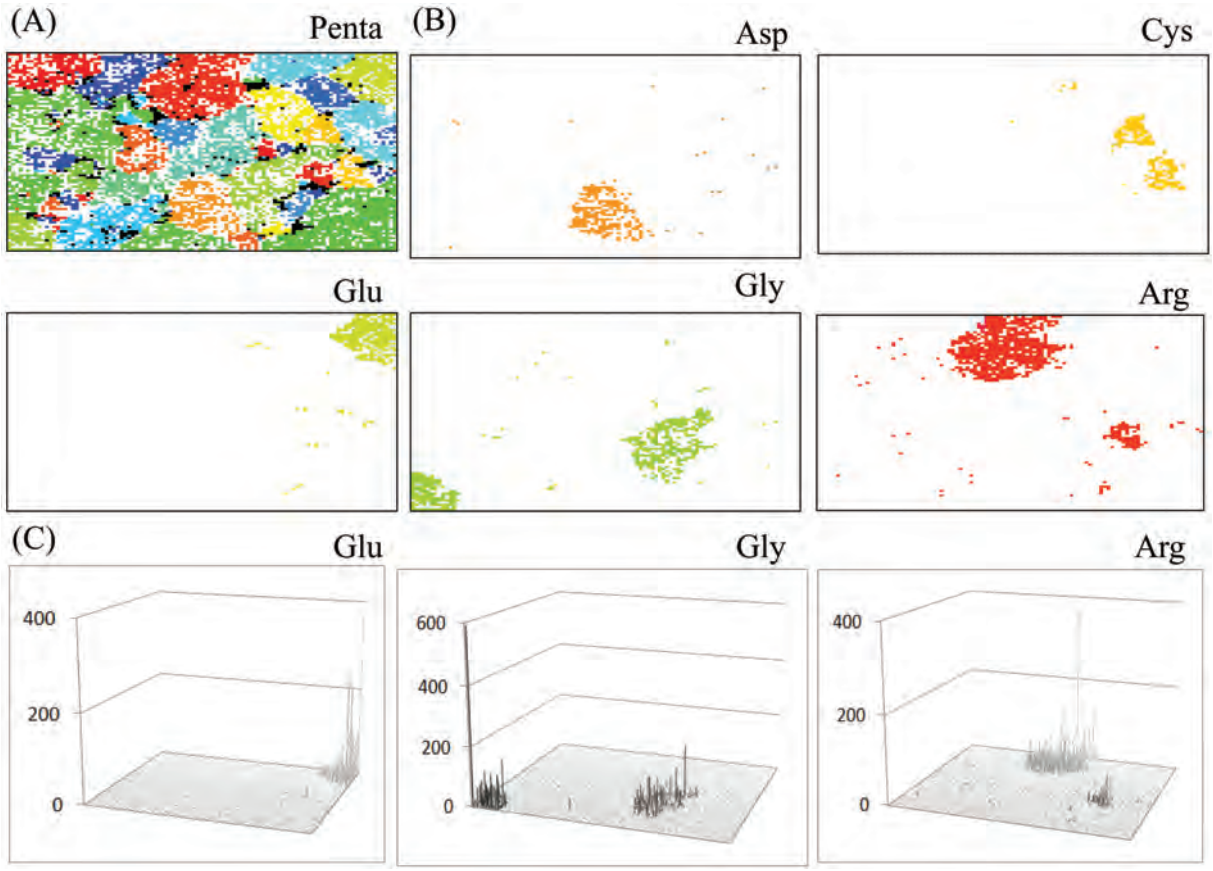

Fig. 1 Oligonucleotide-BLSOM for bacterial tDNAs. (A) BLSOM for tri-, tetra-, and pentanucleotide compositions (Tri-, Tetra-, and Penta). Lattice points containing tDNAs of multiple amino acids are indicated in black, and those containing tDNAs of a single amino acid are coloured as follows: Ala (■), Arg (■), Asn (■), Arp (■), Cys (■), Gln (■), Glu (■), Gly (■), His (■), Ile (■), Leu (■), Lys (■), Met (■), Phe (■), Pro (■), Ser (■), Thr (■), Trp (■), Tyr (■), and Val (■). (B) Lattice points containing tDNAs of four examples of amino acids on Penta in Fig. 1A are visualized separately with the colour used there. (C) Number of tDNAs in each lattice point on Penta is presented for individual amino acids by the height of the vertical bar. Lattice points containing multiple tDNAs, but not one or a few tDNAs, turn out to be detectable.

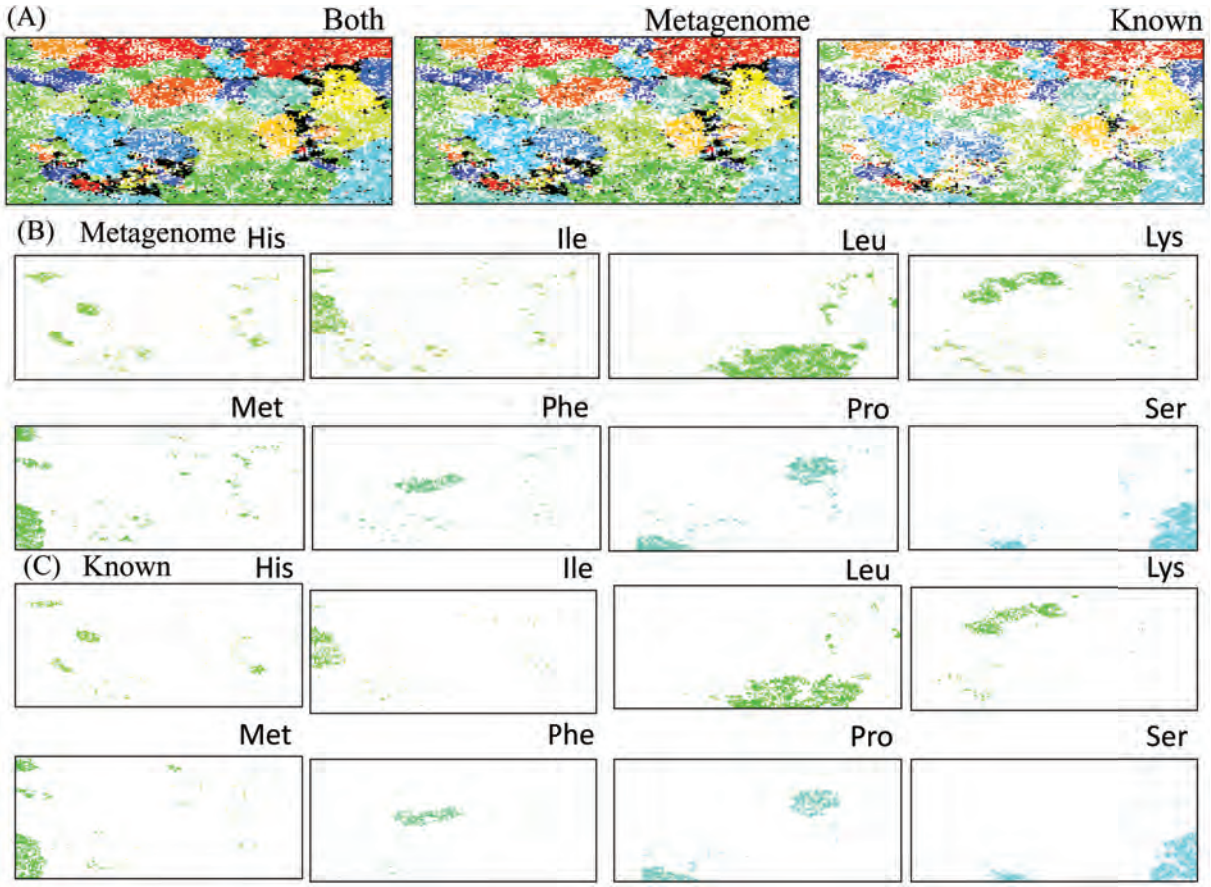

Fig. 2 BLSOM for metagenomic plus species-known microbial tDNAs. (A) Both; Lattice points are marked for both types of tDNAs as described in Fig. 1A. Metagenome or Known; lattice points containing only metagenomic or species-known microbial tDNAs are marked as described in Fig. 1A. (B,C) Lattice points containing metagenomic or species-known microbial tDNAs of individual amino acids are marked as described in Fig. 1B.

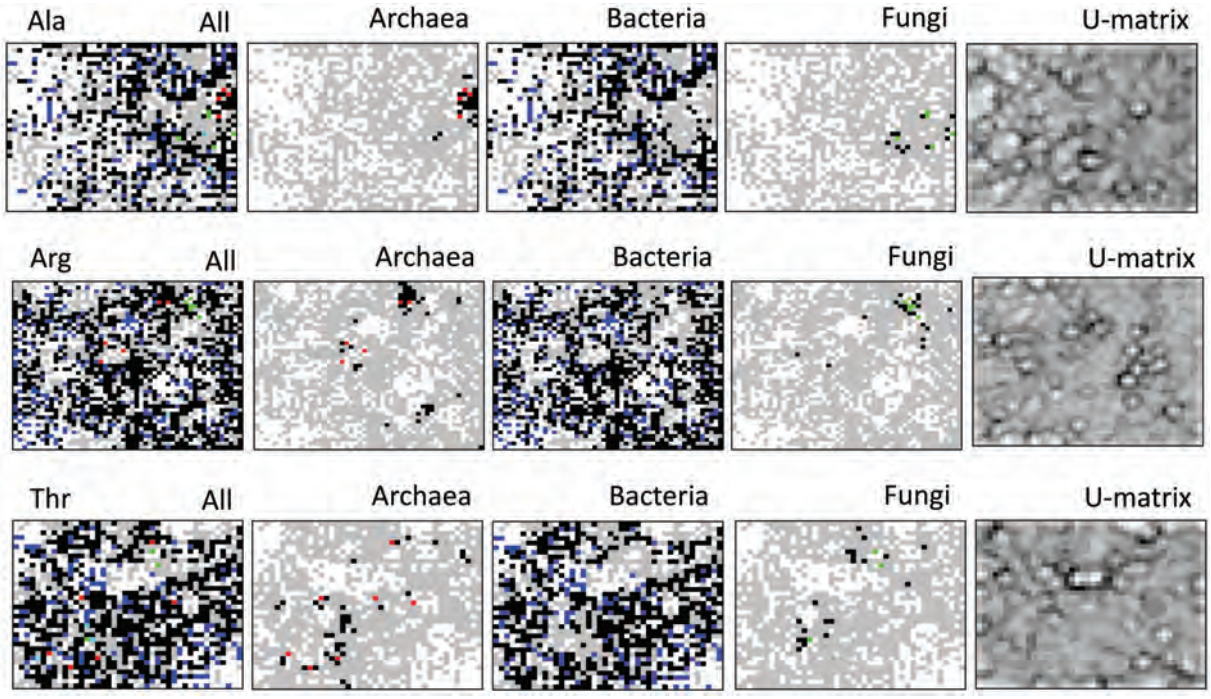

Fig. 3 BLSOM for metagenomic plus species-known microbial tDNAs of one amino acid. All; lattice points containing tDNAs derived from only bacterial, archaeal, fungal, or metagenomic sequences are coloured in blue, red, green, or gray, respectively, and those containing tDNAs from more than one category are marked in back. Bacteria, Archaea, or Fungi panel; lattice points containing metagenomic tDNAs plus bacterial, archaeal, or fungal tDNAs are separately coloured as described for the All panel.

have to be constructed only for archaeal and fungal tDNAs. The association of a large number of metagenomic tDNAs with archaeal and fungal tDNAs can be supported by the following analysis.

3.3 BLSOM for tDNAs of one amino acid

To investigate the phylotype-dependent separation of tDNAs more in detail, we have constructed a BLSOM for each amino acid for species-known plus species-unknown tDNAs, as shown by three examples of amino acids (Fig. 3). On the All panel, lattice points containing tDNAs from only bacterial, archaeal, fungal, and metagenomic sequences are coloured in blue, red, green, and gray, respectively; those containing tDNAs from more than one category are marked in black. On the Bacteria, Archaea, or Fungi panel, lattice points containing metagenomic tDNAs (gray) plus bacterial, archaeal, or fungal tDNAs are separately coloured as described for the All panel. A large portion of lattice points on the Bacteria panel are marked in black, showing that many metagenomic tDNAs are clustered (self-organized) along with known bacterial tDNAs, predicting their phylogenetic attribution. On the Bacteria panel, some clear gray contiguous areas contain metagenomic, but not bacterial, tDNAs, and a portion of the gray areas contain archaeal and fungal tDNAs (black on the Archaea or Fungi panel), providing phylogenetic attribution of these metagenomic tDNAs.

The U-matrix [15] listed in Fig. 3 visualizes the dissimilarity level of oligonucleotide composition between neighbouring lattice points as a blackness level. It should be mentioned that Dick et al. (2009) [16] has successfully applied the U-matrix method of an oligonucleotide-SOM to the phylogenetic clustering of environmental metagenomic sequences. On the U-matrix panel in Fig. 3, many white or pale black areas are surrounded by dark black circles. Because white and pale black on U-matrix means similar oligonucleotide compositions between neighbouring lattice points, and thus, between tDNAs located in neighbouring lattice points, phylogenetic predictions for metagenomic tDNAs within a white and pale black zone surrounded by a dark black circle can be obtained by referring to species-known tDNAs colocalizing in this zone, as described by Dick et al. (2009) [14].

4. Conclusion, discussion, and future prospects

Most environmental microorganisms cannot be cultured easily under laboratory conditions, and genomes of unculturable microorganisms have remained mostly uncharacterized but are thought to contain a wide range of novel genes of scientific and industrial usefulness. The most important contribution of the alignment-free clustering method BLSOM is to clarify microbial community structures in environmental ecosystems. When analysing a dataset composed mainly of metagenomic sequences shorter than 100 bp, an oligonucleotide BLSOM for tDNAs is useful. However, if the dataset is composed mainly of sequences longer than 500 bp, BLSOMs with tri- and tetranucleotide compositions in all genomic fragments should be more suitable than tRNA-BLSOM, because all genomic sequences are informative.

When searching for a certain genome of particular interest (e.g. from the view of earth sciences) by surveying a massive number of short metagenomic sequences, phylogenetic marker tDNAs should become very useful because a conventional sequence homology search can be used. Our group has started to search for tDNAs useful as phylogenetic markers, especially for rare genomes, and has planned to publish such markers in tRNADB-CE.

Unsupervised data mining (e.g. BLSOM) not requiring advanced knowledge, hypotheses, or particular models may provide the least expected knowledge and will become increasingly important in studies not only of metagenomic sequences, but also of genomic sequences from a wide variety of phylogenetic groups. Oligonucleotide BLSOM, which can analyse more than ten million sequences at once, is suitable for unveiling novel knowledge hidden within big sequence data, providing a timely tool for researches following remarkable progresses of high-throughput sequencing technology. Our recent oligonucleotide-BLSOM study of a wide range of fishes, including coelacanth, has revealed a characteristic oligonucleotide composition in the coelacanth genome evidently distinct from other fish genomes, and the characteristic composition found for coelacanth has been connected with the lowest dinucleotide CG occurrence (i.e. the highest CG suppression) among fishes, which is rather equivalent to that of tetrapods [17]. This evident CG suppression in coelacanth is thought to reflect molecular evolutionary processes of epigenetic systems including DNA methylation during vertebrate evolution. Actually, sequence of a *de novo* DNA methylase (Dntm3a) of coelacanth has been found more closely related to that of tetrapods than that of other fishes.

Oligonucleotide BLSOM, which can analyse more than ten million sequences at once by using high performance supercomputers as ES, is most suitable for unveiling novel knowledge hidden within big sequence data, providing a timely tool for researches following the remarkable progress of high-throughput sequencing technology.

Acknowledgements

This work was supported by a Grant-in-Aid for Publication of Scientific Research Results (no. 228056) for Scientific Research, from the Ministry of Education, Culture, Sports, Science and Technology, Japan, and by a NIG Collaborative Research Program (A). The computation for constructing a large-scale BLSOM was done with the Earth Simulator of Japan Agency for Marine-Earth Science and Technology.

References

[1] Abe T., Kanaya S., Kinouchi M., Ichiba M., Kozuki T., and Ikemura T. (2003) Informatics for unveiling hidden genome signatures. *Genome Res*, 13, 693-702.

[2] Kanaya S., Kinouchi M., Abe T., Kudo Y., Yamada Y., Nishi T., Mori H., and Ikemura T. (2001) Analysis of codon usage diversity of bacterial genes with a self-organizing map (SOM): characterization of horizontally transferred genes with emphasis on the E. coli O157 genome. *Gene*, 276, 89-99.

[3] Abe, T., Sugawara, H., Kanaya, S., and Ikemura, T. (2006) Sequences from almost all prokaryotic, eukaryotic, and viral genomes available could be classified according to genomes on a large-scale Self-Organizing Map constructed with the Earth Simulator. *Journal of the Earth Simulator*, 6, 17-23.

[4] Abe T., Sugawara H., Kinouchi M., Kanaya S., and Ikemura T. (2005) Novel phylogenetic studies of genomic sequence fragments derived from uncultured microbe mixtures in environmental and clinical samples. *DNA Res*, 12, 281-290.

[5] Abe, T., Sugawara, H., Kanaya, S., and Ikemura, T. (2006) A novel bioinformatics tool for phylogenetic classification of genomic sequence fragments derived from mixed genomes of environmental uncultured microbes. *Polar Bioscience*, 20, 103-112.

[6] Uchiyama T., Abe T., Ikemura T., and Watanabe T. (2005) Substrate-induced gene-expression screening of environmental metagenome libraries for isolation of catabolic genes. *Nature Biotech*, 23, 88-93.

[7] Nakao R., Abe T., Nijhof A. M., Yamamoto S., Jongejan F., Ikemura T., and Sugimoto C. (2013) A novel approach, based on BLSOMs (Batch Learning Self-Organizing Maps), to the microbiome analysis of ticks. *ISME J, 7*, 1003-1015.

[8] Abe, T., Ikemura, T., Ohara, Y., Uehara, H., Kinouchi, M., Kanaya, S., Yamada, Y., Muto, A., and Inokuchi, H. (2009) tRNADB-CE: tRNA gene database curated manually by experts. *Nucleic Acids Res.*, 37, D163-D168.

[9] Abe, T., Ikemura, T., Sugahara, J., Kanai, A., Ohara, Y., Uehara, H., Kinouchi, M., Kanaya, S., Yamada, Y., Muto, A., and Inokuchi, H. (2011) tRNADB-CE 2011: tRNA gene database curated manually by experts. *Nucleic Acids Res.*, 39, D210-D213.

[10] Abe, T., Inokuchi, H., Yamada, Y., Muto, A., Iwasaki, Y., and Ikemura, T. (2014) tRNADB-CE: tRNA gene database well-timed in the era of big sequence data and its use for metagenome studies. *Front. Genet.*, 01 May 2014 | doi: 10.3389/fgene.2014.00114.

[11] Lowe, T. M. and Eddy, S. R. (1997) tRNAscan-SE: a program for improved detection of transfer RNA genes in genomic sequence. *Nucleic Acids Res.*, 25, 955-964.

[12] Laslett, D. and Canback, B. (2004) ARAGORN, a program to detect tRNA genes and tmRNA genes in nucleotide sequences. *Nucleic Acids Res.*, 32, 11-16.

[13] Kinouchi, M. and Kurokawa. K. (2006) tRNAfinder: A software system to find all tRNA genes in the DNA sequence based on the cloverleaf secondary structure. *J. Comp. Aided Chem.*, 7, 116-126.

[14] Iwasaki, Y., Wada, K., Wada, Y., Abe, T., and Ikemura, T. (2013) Notable clustering of transcription-factor-binding motifs in human pericentric regions and its biological significance. *Chromosome Res.*, 5, 461-474.

[15] Ultsch, A. (1993) Self organized feature maps for monitoring and knowledge acquisition of a chemical process. In *Proc. ICANN'93*, Int. Conf. on Artificial Neural Networks, edited by S Gielen, B Kappen. London: Springer, pp. 864–867.

[16] Dick G. J., Andersson A. F., Baker B. J., Simmons S. L., Thomas B. C., Yelton A. P., Banfield J. F. (2009) Community-wide analysis of microbial genome sequence signatures. *Genome Biol*, 10, R85.

[17] Iwasaki, Y., Abe, T., Okada, N., Wada, K., Wada, Y., and Ikemura, T. (2014) Evolutionary Changes in Vertebrate Genome Signatures with Special Focus on Coelacanth. *DNA Res.*, doi: 10.1093/dnares/dsu012. First published online: May 6.

地球環境変動・保全に係わる全地球レベルでの微生物群集構造把握のためのゲノム情報基盤整備

課題責任者
池村　淑道　　長浜バイオ大学　バイオサイエンス学部
著者
阿部　貴志 *1，岩崎　裕貴 *2，和田健之介 *2，和田　佳子 *2，池村　淑道 *2
*1 新潟大学　工学部
*2 長浜バイオ大学　バイオサイエンス学部

地球環境の変動が生物生態系に多大な影響を与えると共に、生物生態系側も地球環境へ多大な影響を与えて来たが、そこに関与している微生物類の地球レベルでの生態については未知に残されている重要な課題が多い。地球環境への影響を知るには、個々の微生物種ではなく、微生物群集構造の包括的な把握が必須であるが、自然環境の微生物類の 99% 以上が実験室では培養が困難であり、関与する微生物類の特定を困難にして来た。最近の DNA 配列の解読技術の飛躍的な高速化は、「メタゲノム解析法」と呼ばれる革新的な手法を確立させ、全地球レベルでの大規模なメタゲノム解析が進行し、超大量なゲノム配列が集積している。我々が開発して来た、一括学習型自己組織化マップ法（BLSOM）は、オリゴヌクレオチド組成（連続塩基組成）だけで、断片ゲノム配列を生物系統ごとに高精度に分離（自己組織化）する能力を持つ。国際 DNA データバンクに収録された全ゲノム配列を対象に、ES で大規模 BLSOM を作成・更新し、メタゲノム解析で得られる大量配列をマップすることで、各環境中で生息する生物群集の全体像の把握が可能になり、加えて、環境保全・浄化に役立つ新規微生物類やそれらの保持する有用遺伝子類を発掘できる。本年度も、新たに国際 DNA 配列データベースに登録されたゲノム配列を追加して、4 連塩基組成の大規模 BLSOM を作成し、我が国の実験グループが解読をした大量メタゲノム配列の系統推定を行い、微生物集団構造を明らかにした。現時点で普及している新世代シーケンサーが解読する配列は 100bp 以下が大半であり、従来から我々が開発して来た連塩基組成の BLSOM 法に適しているとは言えない。この問題を解決する手段として、本年度は tRNA 遺伝子（tDNA）を対象にした BLSOM を開発して、新世代シーケンサーが解読するメタゲノム配列を用いて、環境中の微生物群集を推定する方法の開発も行った。tDNA の完全長が 100bp 以下であり、遺伝子配列が、特に機能モチーフ配列部位が進化的に保存性が高いことから、分子系統マーカーとしての有用性が高く、新世代シーケンサーを用いたメタゲノム研究における有用性が示された。

キーワード: 自己組織化マップ, BLSOM, 環境微生物 , メタゲノム解析 , 次世代シーケンサー , ビッグデータ

Surface Zonal Flows Induced by Thermal Convection in Rapidly Rotating Thin Spherical Shells : A Model for Banded Structures on Jupiter and Saturn

Project Representative
Shin-ichi Takehiro Research Institute for Mathematical Sciences, Kyoto University

Authors
Shin-ichi Takehiro Research Institute for Mathematical Sciences, Kyoto University
Youhei Sasaki Department of Mathematics, Graduate School of Science, Kyoto University
Keiichi Ishioka Department of Earth and Planetary Sciences, Graduate School of Science, Kyoto University

In order to investigate the origin of the banded structures observed at the surface of Jupiter and Saturn, we perform numerical simulations of Boussinesq thermal convection in whole thin spherical shells. The Prandtl number and Rayleigh number are fixed to 0.1 and 0.05, respectively. The Ekman number and radius ratio are 10^{-4} and 0.75, or, 3×10^{-6} and 0.85, respectively. The boundary conditions at the inner and outer boundaries are free-slip and horizontally uniform temperature. We do not assume any longitudinal symmetry adopted in the previous study.

Prominent banded structures in mid- and high-latitudes cannot be found, possibly because the integration periods may be insufficient. However, eastward spike features are observed near the tangent cylinder in the surface mean zonal profiles, which is considered to be caused by angular momentum transport of topographic Rossby waves excited by the small convective motions. This mechanism may explain the origin of the strong thin jet at about 25 degrees north observed at the surface of Jupiter.

Keywords: Jupiter, Saturn, banded structure, equatorial prograde jet, Rossby waves

1. Introduction

Surface flows of Jupiter and Saturn are characterized by the broad prograde zonal jets around the equator and the narrow alternating zonal jets in mid- and high-latitudes. It is not yet clear whether those surface jets are a result of fluid motions in the "shallow" weather layer, or they are produced by convective motions in the "deep" region.

"Shallow" models consider atmospheric motions driven by the solar differential heating and the intrinsic heat flow from the deeper region under the assumption of hydrostatic balance in the vertical direction as a result of the thin atmospheric layer compared with the radius of the planet. These models can produce narrow alternating jets in mid- and high-latitudes, while the equatorial jets are not necessarily prograde.

On the other hand, "deep" models, which describe thermal convection in rapidly rotating spherical shells whose thickness is comparable to the radius of the planet, can produce equatorial prograde flows easily, while it seems to be difficult to generate alternating jets in mid- and high-latitudes.

Heimpel and Aurnou (2007) [1] proposed thin spherical shell models and show that the equatorial prograde zonal jets and alternating zonal jets in mid- and high-latitudes can be produced simultaneously when the Rayleigh number is sufficiently large and convection becomes active even inside the tangent cylinder. However, they assumed eight-fold symmetry in the longitudinal direction and calculated fluid motion only in the one-eighth sector of the whole spherical shell. Such artificial limitation of the computational domain may influence on the structure of the global flow field. For example, zonal flows may not develop efficiently due to the insufficient upward cascade of two-dimensional turbulence, or stability of mean zonal flows may change with the domain size in the longitudinal direction.

Therefore, in the present study, we try to perform numerical simulations of thermal convection in the whole thin spherical shell domain.

2. Model

We consider Boussinesq fluid in a spherical shell rotating with a constant angular velocity Ω. The non-dimensionalized governing equations consist of equations of continuity, motion, and temperature [2]. The non-dimensional parameters appearing in the governing equations are the Prandtl number, $Pr = \nu/\kappa$, the Ekman number, $Ek = \nu/(\Omega D^2)$, and the modified Rayleigh number, $\mathrm{Ra} = \alpha\, g_o\, \Delta T/(\Omega^2 D)$, where ν, D, κ, α, r_o, g_o, and ΔT are the kinematic viscosity, the shell thickness, the thermal diffusivity, the thermal expansion coefficient, the outer radius of the shell, the acceleration of gravity at the outer boundary, and the temperature contrast between the boundaries, respectively.

The spherical shell geometry is defined by the radius ratio, $\chi = r_i/r_o$, where r_i is the inner radius of the shell. The boundary conditions at the inner and outer boundaries are free-slip and horizontally uniform temperature.

3. Numerical method

The numerical method used in the present study is a traditional spectral method [3]. The toroidal and poloidal potentials of velocity are introduced in order to satisfy the equation of continuity. The velocity potentials and the temperature field are expanded horizontally by the spherical harmonic functions and radially by the Chebychev polynomials. The non-linear terms of the governing equations are evaluated in the physical space and are converted back into the spectral space. The time integration is performed using the Crank-Nicholson scheme for the diffusion terms and the second-order Adams-Bashforth scheme for the other terms.

4. Experimental Setup

The combinations of the non-dimensional parameters and the resolutions of the model used in this study are summarized in Table 1. The initial condition of the velocity field is state of rest and that of the temperature field is the steady conduction solution with random temperature perturbations.

In order to save computational resources, we use hyperdiffusion with the same functional form as the previous studies [1,4]: $\nu = \nu_0$ for $l \leqq l_0$ while $\nu = \nu_0[1+\varepsilon(l-l_0)^2]$ for $l > l_0$, where l is total horizontal wave number.

Table 1 Summary of the nondimensional parameters and the resolutions used in this study.

Parameters	Experiment 1	Experiment 2	HA2007
Radius ratio χ	0.75	0.85	0.85
Prandtl number Pr	0.1	0.1	0.1
Rayleigh number Ra	0.05	0.05	0.05
Ekman number Ek	10^{-4}	3×10^{-6}	3×10^{-6}
Resolution (lon,lat,rad)	512×256×65	1024×512×65	128×512×65
Hyper viscosity	l_0=85, ε=0.01	l_0=42, ε=0.01	?

5. Results

Figure 1 shows snapshots of the surface zonal flow, axial vorticity and mean zonal flow at t=35000 for Ra=0.05, Pr=0.1, Ek=10^{-4}, and χ=0.75. (Experiment 1). Kinetic energy is almost saturated and the system seems to reach a statistically steady state. Obtained velocity field satisfies Taylor-Proudman theorem; it is almost uniform in the direction of the rotation axis. An equatorial prograde surface zonal jet emerges in the region outside the tangent cylinder. In the inside of the tangent cylinder, the surface zonal flows are retrograde.

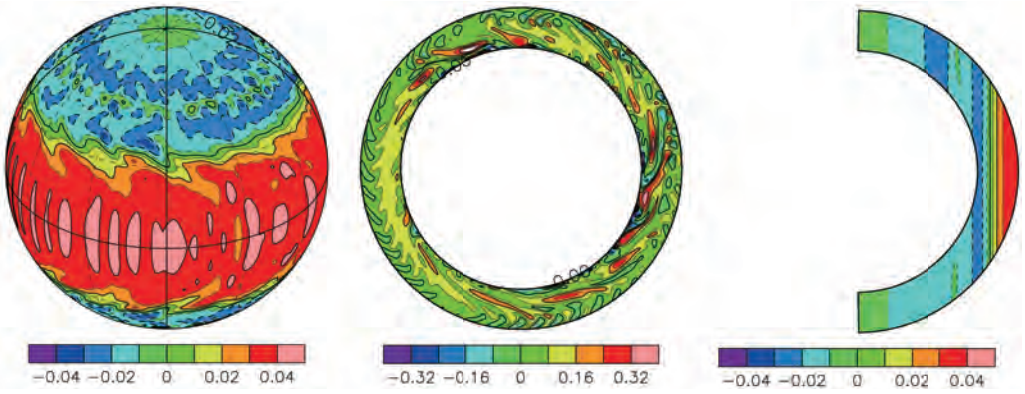

Fig. 1 Snapshots of surface zonal flow (left), axial vorticity at the equatorial cross section (center) and mean zonal flow (right) at t=35000 for Ra=0.05, Pr=0.1, Ek=10^{-4}, and χ=0.75.

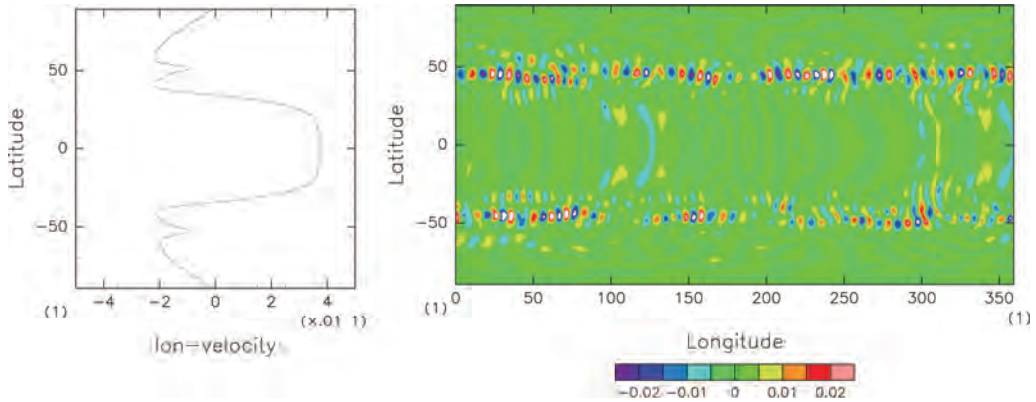

Fig. 2 Snapshots of surface mean zonal flow (left), and vertical velocity at the middle of the shell (right) at t=35000 for Ra=0.05, Pr=0.1, Ek=10^{-4}, and χ=0.75.

Figure 2 shows surface mean zonal flow profile and vertical velocity at the middle of the shell for Ra=0.05, Pr=0.1, Ek=10-4, and χ=0.75. Prominent multiple banded structure cannot be found, while eastward spike features appear near the tangent cylinder in low latitudes. Correspondingly, coherent small scale convective motions exist in these latitudinal zones. It is thought that these convective motions excite topographic Rossby waves which remove westward angular momentum from these zones, producing the eastward spike features.

Figure 3 shows snapshots of the surface zonal flow, axial vorticity and mean zonal flow at t=4700 for Ra=0.05, Pr=0.1, Ek=3x10^{-6}, and χ=0.85 (Experiment 2). In this case, toroidal kinetic energy is still growing and the system does not reach statistically steady state. However, some characteristics of obtained velocity field are similar to those of Experiment 1. A narrower equatorial prograde surface zonal jet emerges in the region outside the tangent cylinder, while sharp retrograde zonal flows appear just inside of the tangent cylinder.

Figure 4 shows surface mean zonal flow profile and vertical velocity at the middle of the shell for Ra=0.05, Pr=0.1, Ek=3x10^{-6}, and χ=0.85. Weak multiple banded structures can be found in high latitudes, while eastward spike features appear near the tangent cylinder in low latitudes. Again, coherent small scale convective motions exist in these latitudinal zones also in this case.

6. Concluding Remark

We have tried to perform numerical simulations of thermal convection in the whole thin spherical shell domain. It cannot be found prominent banded structures in mid- and high-latitudes, however, this may be due to insufficient integration time. The eastward spike features are observed near the tangent cylinder in the surface mean zonal profiles, which is considered to be caused by the angular momentum transport of topographic Rossby waves excited by the small convective motions. This mechanism may explain the origin of the strong thin jet at about 25 degrees north observed on the surface of Jupiter.

Acknowledgement

Numerical computations were carried out on the Earth Simulator (ES2) at the Japan Agency for Marine-Earth Science and Technology.

References

[1] M. Heimpel and J. Aurnou, “Turbulent convection in rapidly rotating spherical shells: A model for equatorial and high latitude jets on Jupiter and Saturn”, Icarus, 187, 540--557, April 2007.

[2] U. Christensen, J. Aubert, P. Cardin, E. Dormy, S. Gibbons, G. Glatzmaier, E. Grote, Y. Honkura, C. Jones, M. Kono, M. Matsushima, A. Sakuraba, F. Takahashi, A. Tilgner, J.

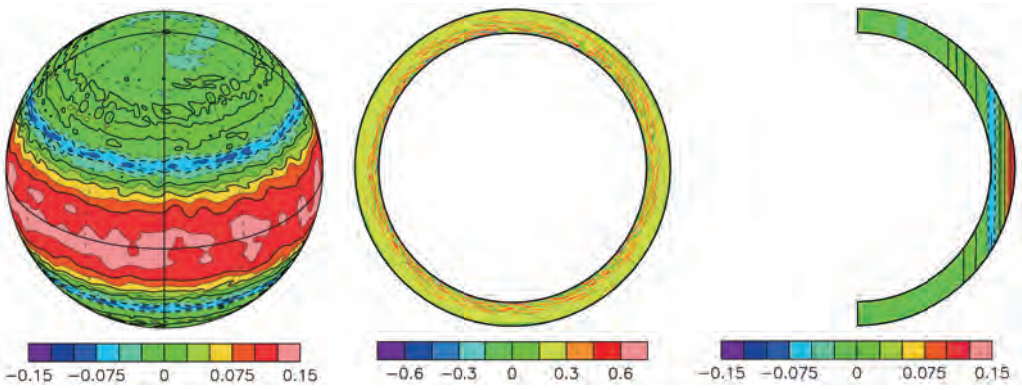

Fig. 3 Snapshots of surface zonal flow (left), axial vorticity at the equatorial cross section (center) and mean zonal flow (right) at t=4700 for Ra=0.05, Pr=0.1, Ek=3x10^{-6}, and χ=0.85.

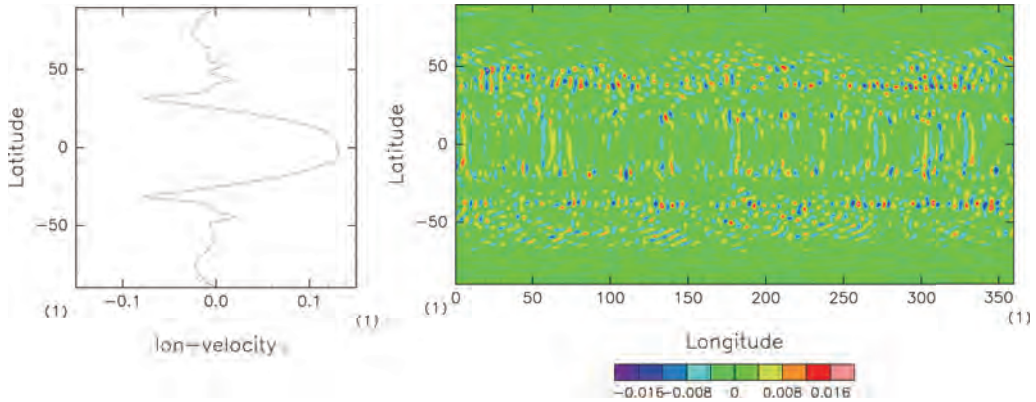

Fig. 4 Snapshots of surface mean zonal flow (left), and vertical velocity at the middle of the shell (right) at t=4700 for Ra=0.05, Pr=0.1, Ek=3x10^{-6}, and χ=0.85.

Wicht, and K. Zhang, “A numerical dynamo benchmark”. Physics of the Earth and Planetary Interiors 128, 25--34, December 2001

[3] G. A. Glatzmaier, “Numerical simulations of stellar convective dynamos. I - The model and method”, Journal of Computational Physics 55, 461--484, August 1984.

[4] W. Kuang and J. Bloxham, “Numerical Modeling of Magnetohydrodynamic Convection in a Rapidly Rotating Spherical Shell: Weak and Strong Field Dynamo Action”, Journal of Computational Physics, 153, 51--81, July 1999.

高速回転する薄い球殻内の熱対流により引き起こされる表層の帯状流：木星・土星の縞状構造のモデル

課題責任者
竹広　真一　　京都大学　数理解析研究所
著者
竹広　真一　　京都大学　数理解析研究所
佐々木洋平　　京都大学大学院　理学研究科数学教室
石岡　圭一　　京都大学大学院　理学研究科地球惑星科学専攻

木星･土星表面に観測される縞状構造の成因を探るために、薄い回転球殻ブシネスク熱対流の全球数値シミュレーションを行った。おそらく時間積分がまだ短いために、顕著な縞状構造は見出されていない。一方で、表面平均帯状流分布には東向きのスパイク構造が接円筒付近外側で生成されている。これは小スケール対流により生成された地形性ロスビー波の角運動量輸送により引き起こされていると考えられる。このメカニズムは木星の北緯 25 度付近に見られる強くて細いジェットの成因を説明するかもしれない。

キーワード:木星, 土星, 縞状構造, 赤道順行流, ロスビー波

1. はじめに

木星と土星の表層の流れは、赤道周辺の幅の広い順行ジェットと中高緯度で交互に現われる互いに逆向きの幅の狭いジェットが特徴的である。この表層のジェットが深部領域の対流によって生成されているのか、表層の流体運動の結果なのかは未だに明らかになっていない。流体層の厚さが惑星半径に比して十分小さい「浅い」モデル、すなわち、鉛直方向の静水圧近似の仮定の下で深部からの熱流と太陽加熱によって大気の運動が駆動されるモデルでは、中高緯度の交互に表われる幅の狭いジェットは再現されるものの、赤道域のジェットは必ずしも順行方向とはならない。一方で、流体層の厚さが惑星半径に匹敵する「深いモデル」、すなわち高速回転する球殻中の熱対流モデルでは、赤道域の順行するジェットは容易に生成されるものの、中高緯度の交互に表われるジェットの生成が困難である。

このような問題に対して Heimpel and Aurnou (2007) [1] は、これまでに考えられていた深いモデルよりも薄い球殻領域内の深部対流運動を考え、レイリー数が十分大きく内球接円筒での対流が活発な場合に、赤道域の順行流と中高緯度の交互に現われる狭いジェットが共存する状態を数値的に再現した。しかしながら、彼らの研究では経度方向に 8 回対称性を仮定しており、全球の 1/8 の領域の運動しか解いていない。このような領域の制限は流れ場全体の構造に影響を与えている可能性がある。例えば、2 次元乱流的なエネルギーの upward cascade が十分に作用せず、互い違いの縞状ジェットが生成されないかもしれない。また､生成される帯状流が不安定となって縞状ジェットが壊されてしまうかもしれない。そこで本研究では、薄い球殻対流の数値計算を全球で行うことで、赤道域および中高緯度領域の帯状流が形成されるか否かを吟味した。

2. モデルと結果

モデルは回転する球殻中のブシネスク流体の方程式系で構成されている。方程式系に現われる無次元数であるプランドル数 Pr を 0.1、エクマン数 Ek を 3x10-6、球殻の内径外径比 η を 0.85、修正レイリー数 Ra を 0.05 とした。境界条件は、温度固定、応力無し条件である。初期には回転系での静止状態にランダムな温度擾乱を加えた。4700 回転まで時間積分したところ、トロイダル成分の運動エネルギーがいまだに増え続け、統計的定常状態には達していない。しかしながら、得られた流れ場の構造はテイラープラウドマンの定理に従い回転軸方向にほぼ一様となっている（図 1 右）。表層の帯状流は、接円筒外側に相当する赤道域で一本の太い順行流が生成されている（図 1 左）。接円筒内側に相当する領域では弱い縞状構造が形成されつつあるように見える（図 2 左）。特に、接円筒に近い低緯度域で東向きのスパイク状の流れ分布が観察される。球殻中層での鉛直速度分布をみると、このスパイク状の分布の緯度帯に小スケールの対流運動が規則的に存在している（図 2 右）。これらの対流運動が地形性ロスビー波を励起し、西向き角運動量を抜き去ることによってスパイク状の流れが形成されているのかもしれない。このような力学的機構は木星表面の北緯 25 度付近に見られる強くて細い西風ジェットの生成機構を示唆している可能性がある。

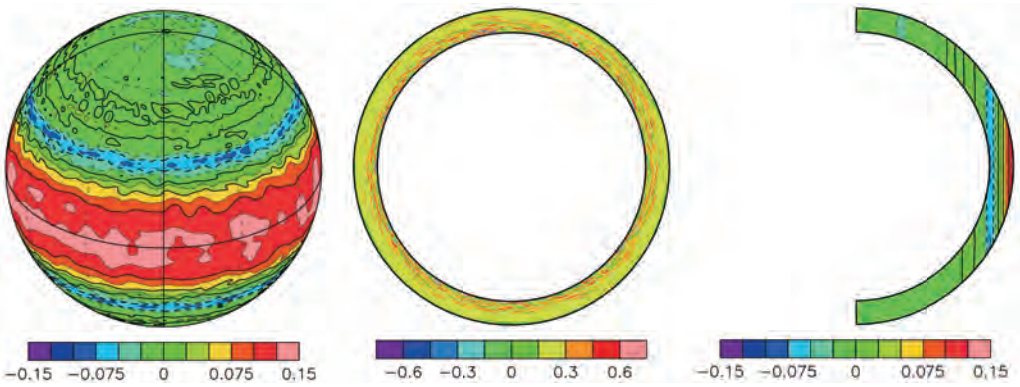

図 1 表面帯状流（左）、赤道面での回転軸方向渦度（中央）、平均帯状流（右）の t=4700 でのスナップショット。*Ra*=0.05, *Pr*=0.1, *Ek*=3x10^{-6}, η=0.85 の場合。

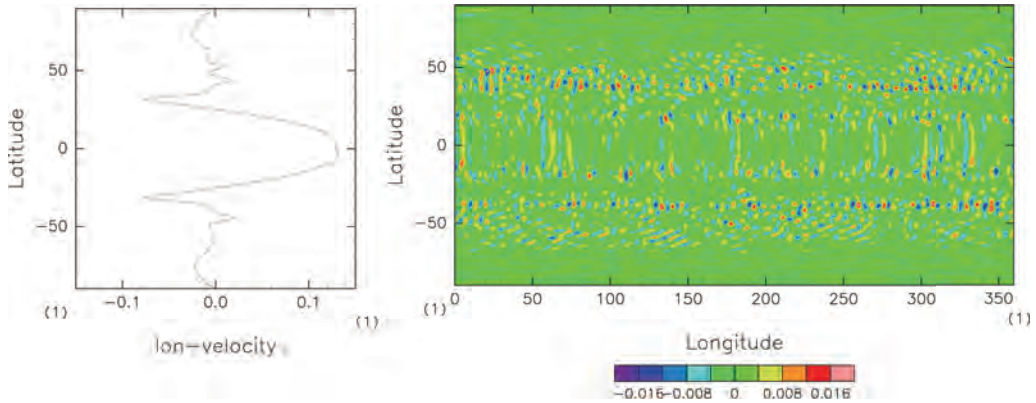

図 2 表面での平均帯状流（左）と球殻中層での鉛直速度の t=4700 でのスナップショット。*Ra*=0.05, *Pr*=0.1, *Ek*=3x10^{-6}, η=0.85 の場合。

謝辞

本研究の数値計算には海洋研究開発機構の地球シミュレータ（ES2）を用いた。

参考文献

[1] M. Heimpel and J. Aurnou, “Turbulent convection in rapidly rotating spherical shells: A model for equatorial and high latitude jets on Jupiter and Saturn”, Icarus, 187, pp.540-557 2007.

Study on the Real-time Ensemble Seasonal Prediction System and Its Application

Project Representative
Swadhin K. Behera Application Laboratory, Japan Agency for Marine-Earth Science and Technology

Authors
Takeshi Doi[*1, 2], Chaoxia Yuan[*2], Hirofumi Sakuma[*1, 2], Yushi Morioka[*1], Ratnam Venkata Jayanthi[*1, 2], Yukio Masumoto[*1], Toshio Yamagata[*2] and Swadhin Behera[*1, 2]

*1 Research Institute for Global Change, Japan Agency for Marine-Earth Science and Technology

*2 Application Laboratory, Japan Agency for Marine-Earth Science and Technology

The APL/JAMSTEC seasonal prediction system was built on the basis of the Scale Interaction Experiment-Frontier (SINTEX-F1) fully coupled global ocean–atmosphere GCM, which has been developed under the EU-Japan collaborative framework on the Earth Simulator. The SINTEX-F1 seasonal prediction system has so far demonstrated high performance of predicting the occurrences of El Niño-Southern Oscillation (ENSO), the Indian Ocean Dipole Mode (IOD) events in the tropics and subtropical dipole events in southern Indian and Atlantic Oceans.

Using the SINTEX-F1 prediction outputs, we found seasonal predictability of subtropical dipoles in southern Indian and Atlantic Oceans. Because of good performances of the SINTEX-F1 prediction on the subtropical dipoles, ENSO, and IOD, the prediction skill of the southern African summer precipitation is also high in the SINTEX-F1 system. In addition to those basin-scale climate variations, the predictability of the regional climate mode off the west coast of Australia, the Ningaloo Niño/Niña, is found two seasons ahead by the SINTEX-F1 seasonal prediction system.

We also explored possibility of a climate-based global yield prediction, and found that it is significantly skillful in predicting rich or poor harvest in the world.

Keywords: SINTEX-F1 seasonal prediction system, Subtropical Dipole Modes, the Ningaloo Niño/Niña, climate-based yield prediction

1. Introduction

The APL/JAMSTEC seasonal prediction system on the basis of the Scale Interaction Experiment-Frontier (SINTEX-F1) fully coupled global ocean–atmosphere GCM has been developed under the EU-Japan collaborative framework using the Earth Simulator. The SINTEX-F1 has emerged as the leading CGCM in the world to provide reliable real-time predictions of seasonal to interannual climate variations. The experimental seasonal predictions based on the CGCM are produced regularly, and the real-time outlook is published every month on our website since 2006 (http://www.jamstec.go.jp/frcgc/research/d1/iod/e/seasonal/outlook.html). In this fiscal year, the process studies and model development with the SINTEX-F2 GCM were initiated on another project (Project representative: Yukio Masumoto, RIGC/JAMSTEC). Therefore, we focused on investigating recent tropical climate variations and their prediction skills, and their experimental societal application in this project.

In the following sections, we introduce several important results obtained from our research activities in the fiscal year of 2013. In Section 2, we show recent important discoveries of seasonal predictability of subtropical dipoles and the new regional climate phenomenon off the west coast of Australia, the Ningaloo Niño/Niña. In Section 3, possibility of a climate-based prediction of global yield with the SINTEX-F1 seasonal prediction is discussed.

2. Discovery of seasonal predictability

2.1 Predictability of the Subtropical Dipole Modes

Seasonal predictability of the subtropical dipole modes is explored (Yuan et al. 2014a [1]) using the SINTEX-F1 coupled model (Fig. 1). Despite the known difficulty in predicting subtropical climate due to large internal variability of the atmosphere and weak ocean–atmosphere coupling, it is shown for the first time that the coupled model can successfully predict the South Atlantic Subtropical Dipole (SASD) 1 season ahead, and the prediction skill is better than the persistence in all the 1–12 month lead time in the hindcast experiments. The prediction skill is lower for the Indian Ocean Subtropical Dipole (IOSD), and only slightly better than the persistence till

6-month lead because of the low predictability of the sea surface temperature anomaly in its southwestern pole. However, for some strong IOSD events in the last three decades, the model can predict them 1 season ahead. The co-occurrence of the negative SASD and IOSD in 1997/98 austral summer can be predicted 5 months ahead. This is because the negative sea level pressure anomalies over the South Atlantic and the southern Indian Ocean in September–October (November– December) that trigger the occurrence of the negative SASD and IOSD are related to the well-predicted tropical IOD (ENSO).

Owing to the overall good performances of the SINTEX-F1 model in predicting the SASD, some strong IOSD, and ENSO, the prediction skill of the southern African summer precipitation is high in the SINTEX-F1 model (Yuan et al. 2014b [2]). The precipitation anomalies over southern Africa (16°– 33°E, 22°–35°S) in December-February are the most predictable from the October 1st initialization (Fig. 2). This study presents promising results for seasonal prediction of precipitation anomaly in the extra-tropics, where seasonal prediction has been considered a difficult task.

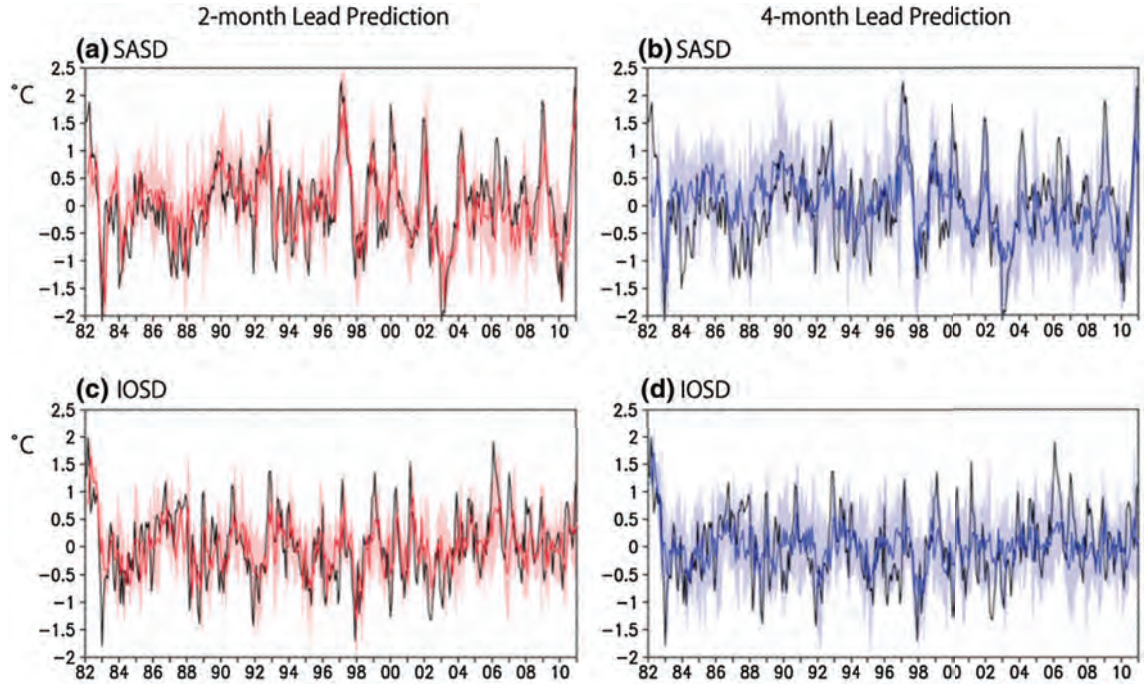

Fig. 1 Time series of (a,b) the SASD and (c,b) IOSD indices obtained from the observational data (black lines) and ensemble-mean predictions at (left panels, red lines) 2-month and (right panels, blue lines) 4-month leads. Red (blue) shading denotes the ensemble spread of 2 (4)-month lead predictions. No smoothing has been applied to all the monthly time series. (Fig. 15 in Yuan et al. 2014a)

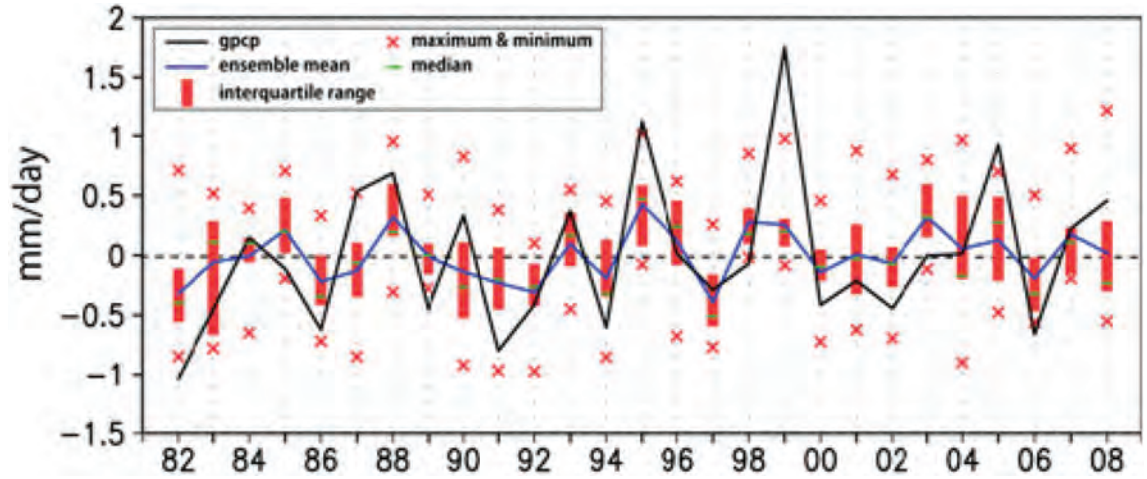

Fig. 2 Time series of the southern African precipitation indices in DJF. Years in the x-axis represent the 3-month-mean period from December of that year till the following February. Black (blue) solid line represents the index derived from GPCP (ensemble-mean predictions initialized on October 1st). Also shown are the box-and- whisker plots for the nine ensemble members at each year; the red boxes represent the interquartile ranges of the middle 56% ensemble members (five out of nine members). Green horizontal bars within the red boxes indicate precipitation anomalies of the median member, and red cross symbols show the maximum and minimum precipitation anomalies from the nine members (Fig. 2 in Yuan et al. 2014b)

2.2 Predictability of the Ningaloo Niño/Niña

The Ningaloo Niño is newly identified as a regional climate phenomenon, which is characterized as warmer-than-normal SST anomalies off the west coast of Australia. In particular, we experienced an unprecedented Ningaloo Niño in 2011. The SST anomalies in Feb.-Mar. 2011 reached about 3ºC off the west coast of Australia, which is above four times of the standard deviation of its interannual variation in recent 30 years. Using the SINTEX-F1 CGCM, we have examined its prediction skill of the Ningaloo Niño/Niña (Doi et al. 2013).

It has turned out that the model is skillful in predicting the Ningaloo Niño (anomaly correlation coefficient (ACC) > 0.6 and normalized root mean square error (RMSE) > 1) up to 5-month ahead when initialized on the first day of each month form May to November. In particular, the Ningaloo Niño is predicted very well when the model is initialized in austral winter-spring. Also, we have focused on the prediction of the unprecedented extreme warm event of the 2011 Ningaloo Niño. The SINTEX-F1 prediction initialized on June 1st, 2010 successfully predicted this extreme warm event in February 2011, i.e. 9 months in advance (Fig. 3). The potential source of this predictability is due to high prediction skill of La Niña. The model reasonably predicted the rapid development of the La Niña condition and the easterly wind anomalies over the equatorial western Pacific in December 2010. It also predicated successfully warm SST anomalies off the west coast of Australia with northerly wind anomalies, the intensification of the Leeuwin Current, and the coastal downwelling in February 2011.

3. Prediction of seasonal climate-induced variations in global food production

We present a global assessment of the reliability of crop failure hindcasts for major crops at two lead times derived by linking ensemble seasonal climatic prediction with statistical crop models (Iizumi et al. 2013 [4]). We found that moderate-to-marked yield loss over a substantial percentage (26–33%) of the harvested area of these crops is reliably predictable if climatic predictions are near perfect. However, only rice and wheat production are reliably predictable three months before the harvest using within-season hindcasts (Fig. 4). The reliabilities

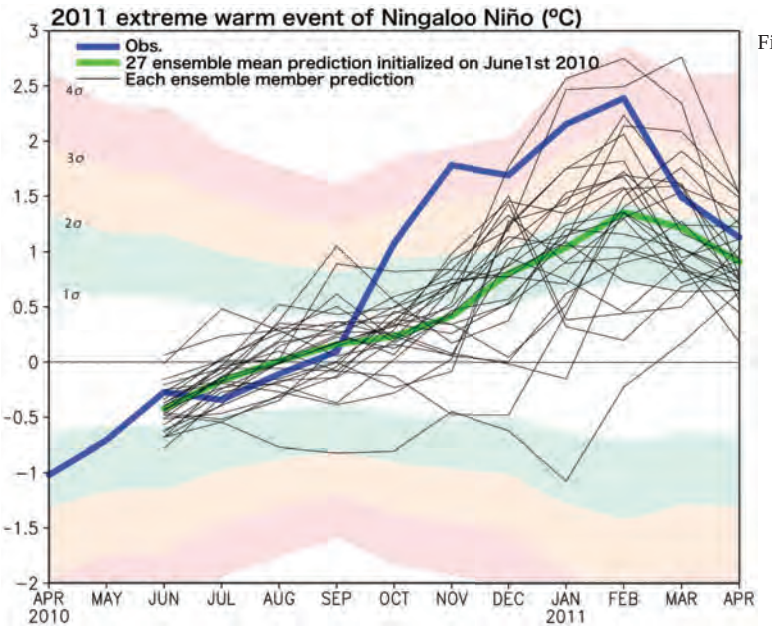

Fig. 3 Monthly time series of the Ningaloo Niño Index (NNI) for observational data of NOAA OISSTv2 (blue) and SINTEX-F1 27 ensemble member prediction initialized on June 1st, 2010 in ºC (ensemble member mean: green; each member: thin black). One, twice, three-, and four-times of the standard deviation of the observed NNI in 1983–2006 (σ) are also shown by shaded (Fig. 3 in Doi et al. 2013 [3]).

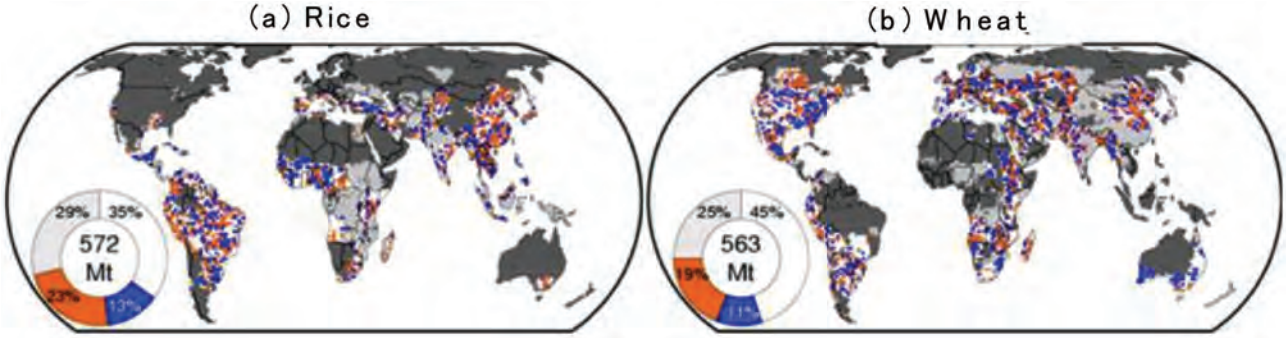

Fig. 4 3-month lead climate-based prediction of the year-to-year variations in the yields of rice (left) and wheat (right). A region where the model is skillful is shown by orange. Blue shows a region where the model fails to predict the yield variation owing to failure of seasonal climate prediction. White shows a region where the observed climate information (temperature and soil moisture) is not significantly correlated with the yield variation. Grey indicates a region where historical yield data is not available. The dark grey area indicates non-cropland.

of estimates varied substantially by crop: Rice and wheat yields were the most predictable, followed by soybean and maize. The reasons for variation in the reliability of the estimates included the differences in crop sensitivity to the climate and the technology used by the crop-producing regions. Our findings reveal that the use of our system to predict crop failures will be useful for monitoring global food production and will encourage the adaptation of food systems to climatic extremes.

Acknowledgement

We appreciate the support extended by the Earth Simulator in achieving our project goals. Also, we are grateful to Dr. Jing-Jia Luo. Dr. Sebastian Masson and our European colleagues of INGV/CMCC and L'OCEAN for their contribution to developing the prototype of the prediction model.

References

[1] Yuan, C., T. Tozuka, J. J. Luo, and T. Yamagata, 2014a: Predictability of the subtropical dipole modes in a coupled ocean–atmosphere model. *Clim Dyn*. DOI:10.1007/s00382-013-1704-1.

[2] Yuan, C., T. Tozuka, W. A. Landman, and T. Yamagata, 2014b: Dynamical seasonal prediction of Southern African summer precipitation. *Clim. Dyn*. DOI:10.1007/s00382-013-1923-5.

[3] Doi, T., S. K. Behera, and T. Yamagata, 2013: Predictability of the Ningaloo Nino/Nina. *Sci. Rep*., 3, 2892; DOI:10.1038/srep028.

[4] Iizumi, T., H. Sakuma, M. Yokozawa, J.-J. Luo, A. J. Challinor, M. E. Brown, G. Sakurai, and T. Yamagata, 2013: Prediction of seasonal climate-induced variations in global food production. *Nature Climate Change*, 3, DOI:10.1038/NCLIMATE1945.

リアルタイム－アンサンブル短期気候変動予測とその応用可能性について

課題責任者
スワディン ベヘラ　　海洋研究開発機構　アプリケーションラボ

著者
土井　威志 *1, 2，Chaoxia Yuan*2，佐久間弘文 *1, 2，森岡　優志 *1，Ratnam Venkata Jayanthi*1, 2，
升本　順夫 *1，山形　俊男 *2，スワディン ベヘラ *1, 2
*1 海洋研究開発機構　地球環境変動領域
*2 海洋研究開発機構　アプリケーションラボ

数ヶ月から数年スケールで発生する気候変動の理解ならびにその予測可能性研究のため、SINTEX-F1 大気海洋結合大循環モデルを日欧研究協力に基づき開発および改良してきた。その第一版である SINTEX-F1 は、リアルタイムの季節・経年変動予測実験に長く用いられており、近年発生したインド洋ダイポールモード（IOD）やエルニーニョ・南方振動（ENSO）現象のほとんどを現実的に予測している。本課題では、そのリアルタイムの季節・経年変動予測実験の計算と、その予測情報の社会応用可能性を研究する。SINTEX-F2 の開発やそれを使った気候変動プロセス研究を実施した課題（課題責任者：JAMSTEC/RIGC 升本　順夫）と本課題は相補的な関係にある。

SINTEX-F1 季節変動予測システムの結果を解析し、インド洋亜熱帯ダイポールモード現象と南大西洋亜熱帯ダイポールモード現象に予測可能性があることを世界で初めて示した。更に、SINTEX-F1 予測システムでは亜熱帯ダイポール、ENSO, IOD の予測精度が高いために、アフリカ南部の 12-2 月の降水量変動を 10 月初旬から予測できることも示した。これらの研究により、亜熱帯域の気候予測研究について新たな扉が開かれたと言える。また、オーストラリア西岸で発生する新しい地域気候変動現象「ニンガルー・ニーニョ」の発生についても、約半年前から予測可能であることを初めて示した。

気候変動予測情報の社会応用研究としては、本プログラムと農業環境技術研究所の共同研究チームによって、３か月先の短期気候予測による穀物の世界的豊凶予測の手法開発を行った。気温と土壌水分量の季節予測データを用いることで、コムギとコメの豊凶を世界の栽培面積の約２割について、収穫３か月前に予測できることを示した。

キーワード：SINTEX-F1 季節予測システム , 亜熱帯ダイポールモード , ニンガルーニーニョ / ニーニャ ,
気候ベースの豊凶予測システム

Published news articles：

< 成果 >（1）関係：
取材・制作協力
H25.5.21 取材 H25.5.28 掲載 H25.6. 9 掲載
日本経済新聞
（5/28 掲載）今年の梅雨や夏の予測について「米国の竜巻、背景に温暖化？　極端気象、日本でも」
（6/9 掲載）「ラニーニャ多発、なぜ」

取材・制作協力
H25.6.13
ET NOW（インドムンバイのテレビ局　※日本・トムソンロイターで収録）
インドの季節予測と農業への影響など

取材・制作協力
H25.7.18
夕刊フジ
今年の猛暑・異常気象の原因について（メールで回答）

取材・制作協力
H25.7.25
テレビ朝日
池上彰の学べるニュース　インド洋ダイポールモード現象について（メールで回答）

取材・制作協力
H25.7.29
報道ステーション
山口・島根豪雨の原因について（取材対応ができなかったため資料にまとめて回答）

取材・制作協力
H25.7.29 電話取材 H25.8.7 収録
テレビ朝日スーパー J チャンネル
今年の異常気象の原因について（7/29 電話で事前取材、8/7 収録）

取材・制作協力
H25.7.30
日刊ゲンダイ
今年の異常気象の原因について

取材・制作協力
H25.8.4
TBS サンデーモーニング
今年の異常気象の原因について（ニュース 23 クロスの映像を使用）

取材・制作協力
H25.8.6
テレビ朝日モーニングバード
異常気象のメカニズムについて

取材・制作協力
H25.8.14
読売新聞
猛暑の原因

取材・制作協力
H25.9.10
週刊プレイボーイ
今年の猛暑について

取材・制作協力
H25.10.22
NHK
10 月に台風が多いことについて（電話取材）

取材・制作協力
H25.11.7 事前打合せ H25.11.23 収録
BS ジャパン「咲くシーズ」出演（生島ヒロシとの対談）
12/21 放映予定

ラジオ NIKKEI 第 2 番組「Groovin’ × Groovin’」
「海洋システムから読み解く気候変動」についてトーク
12/19 収録予定

< 成果 >（3）関係：
•JAMSTEC プレスリリース“ニンガルー・ニーニョ現象の予測可能性を世界で初めて発見”
文部科学省記者クラブ
http://www.jamstec.go.jp/j/about/press_release/20131008_3/

•JAMSTEC 海と地球のフォトグラフィー　今週の一枚
http://www.jamstec.go.jp/j/hot_pictures/?334

• マイナビニュース“ニンガルー・ニーニョ現象の予測可能性を発見”
http://news.mynavi.jp/news/2013/10/10/199/

• 日刊工業新聞“海洋機構、ニンガルー・ニーニュ現象の予測可能性を発見”
http://www.nikkan.co.jp/news/nkx0720131009eaai.html

• 官庁通信　“ニンガルー・ニーニョ予測可能性　JAMSTEC 研究員が世界で初発見”
http://kancho5751.blog.fc2.com/blog-entry-511.html

• 科学新聞（2013, 10/18 号）“ニンガルーニーニョ現象　高精度予測手法を発見”

• 共同通信“ニンガルー・ニーニョ現象の予測可能性を発見”

• 時事通信“ニンガルー・ニーニョ現象の予測可能性を発見”

< 成果 >（4）関係：
• 農業環境技術研究所 プレスリリース
“世界のコムギとコメの不作を収穫 3 か月前に予測する手法の開発―季節予測による穀物の世界的豊凶予測―”
http://www.niaes.affrc.go.jp/techdoc/press/130719/press130719.html

• マイナビニュース
NIAES など、穀物の世界的「豊凶予測」を 3 カ月前に行う手法を開発
http://news.mynavi.jp/news/2013/07/23/105/

• 毎日新聞（2013,7.22 号）
“＜農業環境技術研＞ 3 カ月前にコメの豊凶を予測　手法を開発”

新聞記事など
NASA. Climate forecasts shown to warn of crop failures.
http://climate.nasa.gov/news/954, July 22, 2013.

University of Leeds. Climate forecasts shown to warn of crop failures.
http://www.leeds.ac.uk/news/article/3422/, July 23, 2013

SciDev. Computer model gives early warning of crop failure.
http://www.scidev.net/global/data/news/computer-model-gives-early-warning-of-crop-failure.html,
July 24, 2013.

Nature Climate Change. Highlights: Forecasting failure.
http://www.natureasia.com/en/research/highlight/8567, July 22, 2013.

Nature Japan. 日本の研究論文：季節的な気候による食糧生産の変動を、世界規模で予測する手法を開発 .
http://www.natureasia.com/ja-jp/nclimate/papers-from-japan/article/48675.

* この他に、毎日新聞、食品産業新聞、農業協同組合新聞、日本農業新聞で報道された。また、時事通信より取材があった。

Analysis of Global Ecosystem Ecology by Fragment Molecular Orbital (FMO) Method – Analyses of the interactions between virus hemagglutinins and their receptors –

Project Representative
Tadashi Maruyama Institute of Biogeosciences, Japan Agency for Marine-Earth Science and Technology

Authors
Yasuhiro Shimane[*1], Kazue Ohishi[*1], Misako Iwasawa[*2], Yuji Hatada*[1], Keiko Usui[*1], Yoshihiro Takaki[*1], Takao Yoshida[*1], Shigenori Tanaka[*3], Satoshi Anzaki[*3], Yuto Komeiji[*4], Chiduru Watanabe[*5], Yoshio Okiyama[*5], Yuji Mochizuki[*6] and Kaori Fukuzawa[*7]

∗1 Institute of Biogeosciences, Japan Agency for Marine-Earth Science and Technology
∗2 Earth Simulator Center, Japan Agency for Marine-Earth Science and Technology
∗3 Graduate School of System Informatics, Kobe University
∗4 Biomedical Research Institute, National Institute of Advanced Industrial Science and Technology
∗5 Institute of Industrial Science, The University of Tokyo
∗6 Department of Chemistry, Rikkyo University
∗7 Science Solutions Division, Mizuho Information and Research Institute

To understand the basis of global expansion of virus diseases, we analyzed the interaction between viral envelope protein and host receptor by using the Earth Simulator of JAMSTEC and fragment molecular orbital (FMO) method. We focused our attention to two virus groups, influenza viruses and morbilliviruses. Avian influenza viruses use sialic acid linked to galactose by an α2, 3 linkage (2-3 type), whilst human viruses use that by α2, 6 linkage (2-6 type), as the receptor. We examined the affinity of hemagglutinin (HA) of avian-origin H7N9 viruses, which have recently been reported to transmit to humans, to the receptors of humans and of birds. The FMO analysis showed that the HA protein of H7N9 has higher affinity to the human type of receptor, compared to low affinity of conventional avian H7N3 virus. These results agreed with the experimental data, and we have also elucidated the molecular mechanism underlying the binding affinities through comparative FMO analyses at residue level for the complexes between avian or human influenza virus HA and avian or human receptor.

Signaling lymphocyte activating molecule (SLAM) is a host receptor to which the morbillivirus HA protein binds. Using the crystal structure of the complex between measles virus (MV) HA and monkey SLAM, three dimensional (3D) structures of the complex of HA and the SLAMs of the other morbilliviruses and mammals were estimated by molecular dynamics calculations, respectively. FMO analysis showed that the binding affinities of MV-HA to the SLAMs of several mammals, such as human, monkey and seals, were estimated. They agreed with the infectivities of the viruses to these animals. However, those of the CDV-HA to SLAMs of several mammals were not well agreed. This was probably caused by low resolution of the 3D structure estimation of the HA and SLAM proteins.

The present study showed that FMO method is useful to estimate the interaction of the virus and its receptor, if their 3 D structures are available. To obtain better results, we need better 3D structure estimation method for the complexes of the virus HA and the receptor.

Keywords: Influenza virus, morbillivirus, receptor, fragment molecular orbital method, hemagglutinin, signaling lymphocyte activating molecule

1. Introduction

Recently pathogenic viruses are attracting much attention for human diseases and also for wild life diseases. Zoonotic viruses e.g. influenza virus, which infect not only humans but also wild animals, such as birds, are becoming more and more important for human health. In addition, the expansion of host range of viruses may cause a serious damage to the new host animals and to the ecosystems. Highly virulent avian influenza virus is now thought to be a potential threat to humans and poultry [1, 2]. In marine mammals, morbilliviruses cause mass mortalities in seals

and whales [3, 4]. One of the morbilliviruses, canine distemper virus (CDV), which has been thought to cause a severe disease, canine distemper, mostly in dogs, is now known to cause the disease also in seals and large cats [5].

The receptor molecules on the host cells play an essential role in viral attachment for invasion and determination of host tropism. The purpose of the present study is to simulate the interactions between the viruses and their receptors on the host animal cells by using fragment molecular orbiter (FMO) method and the Earth Simulator.

We focused our attention to two virus groups; influenza viruses and morbilliviruses. Humans and birds are major and natural hosts for influenza viruses, and the viruses use sialic acid as receptors to invade. Humans possess sialic acids linked to galactose by an α2, 6 linkage (2-6 type) on the epithelial cells of trachea, whilst birds possess those by an α2, 3 linkage (2-3 type) on the cells of intestine [6]. Human and avian viruses usually independently circulate in their natural hosts by using their specific receptors. However, unexpected transmissions of highly virulent avian influenza to humans have been reported [7]. Avian-origin influenza virus, the type H7N9 showed a high pathogenicity to humans [2]. In the present study, we simulated the interaction between the virus hemagglutinin (HA) of the avian-to-human H7N9 type and sialic acid receptors, in comparison with that of the avian H7N3 influenza viruses based on recently reported three-dimensional (3D) structures of the receptor-HA complexes [8, 9].

Signaling lymphocyte activating molecule (SLAM; CD150) is a host receptor for morbilliviruses [10]. SLAM is a member of SLAM family proteins (immunoglobulin superfamily), and its variable region (V) like domain provides an interface with morbilliviruses. To understand the high virus-host specificity of morbilliviruses, the interfaces of various animal SLAM sequences has been analyzed by 3D homology modelings based on the crystal structure of the other SLAM family proteins or of the complex between measles HA and monkey SLAM V region [11, 12, 13, 14]. In the present study, the interaction between HA protein of three morbillivirus species, MVs (L482R mutant and wild type), and CDV, and their host animal SLAMs, were examined by FMO method.

2. Materials and computational methods

2.1 Analysis of influenza virus-host receptor interaction

We employed X-ray crystal structures of complexes of HA protein (H7N3 or H7N9 type) and human or avian receptor [8, 9]. Their PDB codes are 4BSH (H7N3 and human receptor 6'SLN), 4BSI (H7N3 and avian receptor 3'SLN), 4KON (H7N9 and human receptor 6'SLNLN) and 4KOM (H7N9 and avian receptor 3'SLNLN). These H7N3 and H7N9 type HAs may be regarded as hemagglutinin proteins of avian and human infection type, respectively. Figure 1 illustrates the molecular structure of

Fig. 1 X-ray crystal structure of the complex of A/Anhui/1/2013 (H7N9) HA and human receptor (PDB entry: 4KON). The receptor (sialosaccharide) part is denoted by yellow color.

4KON. Hydrogen atoms were added to these complexes by the MOE (Molecular Operating Environment) software (Chemical Computing Group Inc.), and their positions were optimized with the Amber99 force field.

The FMO calculations [15, 16, 17, 18, 19] with the software ABINIT-MP were performed for these complexes, where we employed the Hartree-Fock (HF) and the second-order Møller–Plesset (MP2) perturbation methods with the basis set of 6-31G. While the HF method is a mean-field type approximation, the MP2 perturbation method is employed for the description of electron correlations in the present study, where the latter is expected to take into account the dispersion (or van der Waals) interactions appropriately [19]. Thus, we can quantitatively evaluate the binding energy in terms of the present MP2 method.

2.2 Analysis of morbillivirus-host receptor (SLAM) interaction

Docking structures of morbillivirus hemagglutinin (MoV-HA) proteins and their receptors on animal cells (SLAMs) were constructed by homology modeling followed by molecular dynamics (MD) simulations. MoV-HA and SLAM-V (V region of SLAM) sequences retrieved from Protein Data Bank (PDB)

Fig. 2 The crystal structure of the measles virus hemagglutinin and its receptor protein the signaling lymphocyte activating molecule domain V from marmoset. The receptor is shown in yellow.

and GenBank were: measeles virus (MV-L482R, one point mutant Leu482Arg of MV) PDB: 3ALX, wild type measeles virus (MV-Wild) AB012948, canine distemper virus (CDV-HA) AF164967, human SLAM-V NM_003037, marmoset SLAM-V PDB: 3ALX, dog SLAM-V AF325357, seal SLAM-V AB428368 and mouse SLAM-V NM_013730. Some chimeric mouse SLAM-Vs, mouse/63h, mouse/60h/61h and mouse/60h/61h/63h, were developed by a point mutation tool in Discovery Studio (Accelrys), which had 1, 2 or 3 points of human type amino acid substitutions on the positions indicated in their names (delimited with slash symbol).

Crystal structure of the measles virus hemagglutinin (MV-L482R) - marmoset SLAM V domain (marSLAM-V) complex PDB: 3ALX reported by Hashiguchi et al. [14] was used for both homology modeling template and coarse docking template in the model building (Fig. 2). Homology modeling, docking and energy minimizations were done using Discovery Studio under the CHARM22 force field [20, 21]. Optimization of molecular interface between MoV and SLAMs were achieved by 3 steps of energy minimization. In the first step, amino acids on the interface within 5 Å from each other protein was fixed, and remaining part (outside of interface) was optimized until the RMS (RMS: root mean square) gradient value reached a value smaller than 0.001. Second step, the fixed part was inverted and minimization was done in the same condition. For the last step, whole system was optimized, and the resultant model was used for MD and FMO simulations.

MD simulations were conducted to obtain relaxed docking models in explicit water solvent, were performed using combination of VMD [22] and NAMD [23] software running on the JAMSTEC super computer system (SGI ICE X Linux cluster). The simulations were carried out for times of up to 900 ns at 300 K, with a minimum step time of 1 fs. The molecular complex model was solvated with explicit water in the minimum depth of 20 Å from protein surface. All calculations were carried out using an NVT ensemble (NVT: constant number of particles, constant volume and constant temperature). The periodic boundary condition and particle mesh Ewald method were enabled for the study. After the calculations, protein structures at 900 ns were sampled from trajectories.

To investigate the interactions between MoVs and SLAM-Vs in a quantitative way, FMO (FMO: fragment molecular orbital) calculations worked out by ABINIT-MP package were chosen because of its high accuracy and high computational efficiency. We performed the FMO calculations with second-order Møller-Plesset perturbation theory (MP2) and the 6-31G basis set. The input protein models were divided at individual amino acid residues as “fragment”. The IFIE (IFIE: inter-fragment interaction energy) between MoV-HA and SLAM-V calculated by FMO method was used for the comparison of infectious risk.

3. Results

3.1 Interaction between influenza virus and the receptor

Table 1 lists the interaction energies between H7N3 (A/Turkey/Italy/214845/2002) or H7N9 (A/Anhui/1/2013) type HA and parts (SIA1, GAL2, NAG3 and GAL4, where SIA, GAL and NAG refer to sialic acid, galactose and N-acetyl glucosamine, respectively) of avian or human receptor obtained by the FMO calculations. As observed in this table, the H7N9 influenza virus HA shows weaker attractive interactions with the avian receptor than the H7N3 influenza virus HA, but even the former still keeps a moderate binding to the avian receptor. The H7N9 influenza virus HA, (Anhui), which may be regarded as a mutant from H7N3 influenza virus HA, shows a much stronger binding to the human receptor than to the avian receptor. The former binding is stronger than that between the H7N3 influenza virus HA and the avian or human receptor.

We have then investigated the molecular mechanism for these binding properties at the residue level and revealed the importance of structural changes of the HA-receptor complexes caused by the mutations (indirect effect) as well as the importance of the modification of interactions between the mutated residues and the receptors (direct effect). We can thus perform structure-based theoretical analyses of the binding affinity of HA-receptor complex in terms of accurate quantum-chemical calculations, which would provide useful information for the prediction of possible interspecies transmission associated with influenza pandemic and the development of influenza vaccines against target HA proteins with forthcoming mutations. More details concerning the molecular level studies will be reported elsewhere.

3.2 Morbillivirus-SLAM interaction

To examine the suitability of the calculation method of the morbillivirus-SLAM interaction, the MV and marmoset SLAM-V complex that consist of 419 and 109 amino acids respectively, was calculated by the FMO2-MP2/6-31G on 128 processors of the Earth Simulator 2. The total number of amino acid, fragment, electron and basis set were 528, 522, 31364 and 45438, respectively. The difference between total amino acids number and fragment number was derived from 6 disulfide links (cysteine-cysteine) in the complex model. The job took about 70 minutes.

We examined 26 kinds of data set in combinations of 3 types of MoV-HA (MV-L482R, MV-Wild, CDV), 8 types of SLAMs (marmoset, human, dog, spotted seal, mouse, chimera mouse/60h/61h, chimera mouse/60h/61h/63h, chimera mouse/63h) and 2 optimizing conditions (energy minimized model and relaxed model in water) by the FMO calculations. The results are shown in Table 2. FMO analysis showed that the interaction energies between MV-L482R and SLAMs of marmoset, dog and spotted seal, were reasonable in the order of the sensitivities of the animals to the MV. The same results were observed in the case of MV-Wild. However, the interaction energies of the CDV-H to SLAMs were not well estimated. The problem was probably caused by the accuracy of complex models depending on the quality of homology modeling and molecular dynamics simulations. We cannot go into great depth in considering them this time, but expect that further refinement will take place in the future.

References

[1] Horimoto T. and Kawaoka Y. (2005) influenza: lessons from past pandemics, warings from current incidents. Nature Review, 3, 591–600.

[2] Abdelwhab E.M., Veits J., and Mettenleiter T.C. (2014) Prevalence and control of H7 avian influenza viruses in birds and humans. Epidemiology and infection, 142, 896–920.

[3] Barrett T. and Rima B.K. (2002) Molecular biology of morbillivirus diseases of marine mammals. In: Pfeiffer C.J., ed. Molecular and cell biology of marine mammals. Malabar, Florida: Krieger Publishing, 161–72.

[4] Guardo G.D., Marruchella G., Agrimi U., and Kennedy S. (2005) Morbillivirus infections in aquatic mammals: a brief overview. J. Vet. Med. Series A, 52, 88–93.

Table 1 Interaction energies (in units of kcal/mol) between HAs of H7N3 or H7N9 and each part of saccharide receptors. (a) Avian receptor. (b) Human receptor. Sums of each contribution are also shown.

(a)

	SIA1	GAL2	NAG3	GAL4	Total (SIA1+GAL2+NAG3)	Total+GAL4
H7N3 (avian)	-188.8	-3.8	2.0		-190.6	
H7N9 (human)	-186.3	0.6	6.4	-1.8	-179.3	-181.1
⊿IFIE	-2.5	-4.4	-4.4		-11.3	

(b)

	SIA1	GAL2	Total IFIE
H7N3 (avian)	-183.6	-3.0	-186.6
H7N9 (human)	-204.2	0.9	-203.3
⊿IFIE	20.6	-3.9	16.7

Table 2 Interaction energies between morbillivirus hemagglutinins and mammalian signaling lymphocyte activating molecules (SLAMs). GenBank and Protein Databank accession numbers for viruses and SLAMs are shown in parentheses. Symbols for the infectiveness column: +, infectable; -, not infectable.

Virus	SLAM	Infectiveness	IFIE (kcal/mol)	
			Optimized	Relaxed
MV-L482R (PDB: 3ALX)	Marmoset (PDB: 3ALX)	+	-861	-773
	Human (NM_003037)	+	-849	-606
	Dog (AF325357)	-	-840	-666
	Spotted seal (AB428368)	-	-779	-497
MV-Wild (AB012948)	Marmoset (PDB: 3ALX)	+	-932	-644
	Human (NM_003037)	+	-893	-826
	Mouse (NM_013730)	-	-887	-517
	Chimera mouse/60h/61h	+	-949	-744
	Chimera mouse/60h/61h/63h	+	-894	-879
CDV (AF305419)	Dog (AF325357)	+	-884	-780
	Mouse (NM_013730)	-	-1235	-1051
	Human (NM_003037)	-	-1073	-957
	Chimera mouse/63h	+	-1216	-877

[5] Appel M.J.G., Yate R.A., Foly G.L., Bernstein J.J., Santinelli S., Spelman L.H., Miller L.D., Arp L.H., Anderson M., Barr M., Pearce-Kelling S., and Summers B. (1994) Canine distemper epizootic in lions, tigers, and leopards in North America. J Vet Diag Invest, 6, 277–88.

[6] Ito T. and Kawaoka Y. (2000) Host-range barrier of influenza A viruses. Vet. Microbiol., 74, 71–75.

[7] Horimoto T. and Kawaoka Y. (2005) Influenza: lessons from past pandemics, warnings from current incidents. Nat. Rev. Microbiol., 3(8), 591–600.

[8] Shi Y., Zhang W., Wang F., Qi J., Wu Y., Song H., Gao F., Bi Y., Zhang Y., Fan Z., Qin C., Sun H., Liu J., Haywood J., Liu W., Gong W., Wang D., Shu Y., Wang Y., Yan J., and Gao G.F. (2013) Structures and Receptor Binding of Hemagglutinins from Human-Infecting H7N9 Influenza Viruses. Science, 342, 243–247.

[9] Xiong X., Martin S.R., Haire L.F., Wharton S.A., Daniels R.S., Bennett M.S., Mccauley J.W., Collins P.J., Walker P.A., Skehel J.J., and Gamblin S.J. (2013) Receptor binding by an H7N9 influenza virus from humans, Nature, 499, 496-499.

[10] Tatsuo H., Ono N., Tanaka K., and Yanagi Y. (2000) SLAM (CDw150) is a cellular receptor for measles virus. Nature, 406, 893–897.

[11] Ohishi K., Ando A., Suzuki R., Takishita K., Kawato M., Katsumata E., Ohtsu D., Okutsu K., Tokutake K., Miyahara H., Nakamura H., Murayama T., and Maruyama T. (2010) Host-virus specificity of morbilliviruses predicted by structural modeling of the marine mammal SLAM, a receptor. Comp. Immunol. Microbiol. Infect. Dis., 33, 227–241.

[12] Shimizu Y., Ohishi K., Suzuki R., Tajima Y., Yamada T., Kakizoe Y., Bando T., Fujise Y., Murayama T., and Maruyama T. (2013) Amino acid sequence variation of signaling lymphocyte activation molecule and mortality caused by morbillivirus infection in cetanceans. Micorbiology and Immunology, 57, 624–632.

[13] Ohishi K., Suzuki R., Maeda T., Tsuda M., Abe E., Yoshida T., Endo Y., Okamura M., Nagamine T., Yamamoto H., Ueda M., and Maruyama T. (2014) Recent host range expansion of canine distemper virus and variation in its receptor, signaling lymphocyte activation molecule, in carnivores. J. Wildlife Disease, doi: 10.7589/2013-09-228 (in press).

[14] Hashiguchi T, Ose T, Kubota M, Maita N, Kamishikiryo J, Maenaka K, and Yanagi Y. (2011) Structure of the measles virus hemagglutinin bound to its cellular receptor SLAM. Nat Struct Mol Biol 18:135–41.

[15] Iwata T., Fukuzawa K., Nakajima K., Aida-Hyugaji S., Mochizuki Y., Watanabe H., and Tanaka S. (2008) Theoretical analysis of binding specificity of influenza viral hemagglutinin to avian and human receptors based on the fragment molecular orbital method, Comput. Biol. Chem., 32, 198–211.

[16] Fukuzawa, K., Omagari, K., Nakajima, K., Nobusawa, E., and Tanaka, S. (2011) Sialic acid recognition of the pandemic influenza 2009 H1N1 virus: Binding mechanism between human receptor and influenza hemagglutinin, Protein Peptide Lett., 18, 530–539.

[17] Takematsu K., Fukuzawa K., Omagari K., Nakajima S., Nakajima K., Mochizuki Y., Nakano T., Watanabe H., and Tanaka S. (2009) Possibility of mutation prediction of influenza hemagglutinin by combination of hemadsorption experiment and quantum chemical calculation for antibody binding, J. Phys. Chem. B, 113, 4991–4994.

[18] Yoshioka A., Fukuzawa K., Mochizuki Y., Yamashita K., Nakano T., Okiyama Y., Nobusawa E., Nakajima K., and Tanaka S. (2011) Prediction of probable mutations in influenza virus hemagglutinin protein based on large-scale ab initio fragment molecular orbital calculations, J. Mol. Graph. Model., 30, 110–119.

[19] Tanaka S., Mochizuki Y., Komeiji Y., Okiyama Y., and Fukuzawa K. (2014) Electron-correlated fragment-molecular-orbital calculations for biomolecular and nano systems, Phys. Chem. Chem. Phys., 16, 10310–10344.

[20] MacKerell Jr. A.D. (2001) Atomistic Models and Force Fields, in Computational Biochemistry and Biophysics, Becker O.M., MacKerell Jr. A.D., Roux B., Watanabe M., Eds., Marcel Dekker, Inc. New York, 7–38.

[21] MacKerell, Jr. A.D., Bashford D., Dunbrack, Jr. R.L., Evanseck J.D., Field M.J., Fischer S., Gao J., Guo H., Ha S., Joseph-McCarthy D., Kuchnir L., Kuczera K., Lau F.T.K., Mattos C., Michnick S., Ngo T., and Nguyen D.T. (1998) All-Atom Empirical Potential for Molecular Modeling and Dynamics Studies of Proteins, J. Phys. Chem. B, 102 (18), 3586–3616.

[22] Humphrey W., Dalke A., and Schulten K. (1996) VMD - Visual Molecular Dynamics, J. Molec. Graphics, 14, 33–38.

[23] Phillips J.C., Braun R., Wang W., Gumbart J., Tajkhorshid E., Villa E., Chipot C., Skeel R.D., Kale L., and Schulten K. (2005) Scalable molecular dynamics with NAMD, J. Comp. Chem., 26, 1781–1802.

フラグメント分子軌道法の地球生態系解析への応用 －ウイルスヘマグルチニンとそれらの受容体の相互作用の解析－

課題責任者
丸山　正　海洋研究開発機構　海洋・極限環境生物圏領域

著者
嶋根　康弘 *1，大石　和恵 *1，岩沢美佐子 *2，秦田　勇二 *1，臼井けい子 *1，高木　善弘 *1，
吉田　尊雄 *1，田中　成典 *3，安崎　聡 *3，古明地勇人 *4，渡邊　千鶴 *5，沖山　佳生 *5，
望月　祐志 *6，福澤　薫 *7

*1 海洋研究開発機構　海洋・極限環境生物圏領域
*2 海洋研究開発機構　地球シミュレータセンター
*3 神戸大学　大学院システム情報学研究科
*4 産業技術総合研究所　バイオメディカル研究部門
*5 東京大学　生産技術研究所
*6 立教大学　理学部化学科
*7 みずほ情報総研株式会社　サイエンスソリューション部

地球規模で拡大するウイルス感染症の基礎を理解するために、ウイルスのエンベロープタンパクと宿主の受容体との相互作用をフラグメント分子軌道法（FMO）により、JAMSTEC の地球シミュレータを用いて解析した。この解析で、我々はインフルエンザウイルスおよびモルビリウイルスの二つのウイルスに注目した。トリインフルエンザウイルスはシアル酸とガラクトースがα2,3 結合した受容体（α2-3 型）と親和性を有しているが、ヒトインフルエンザウイルスはα2,6 結合した受容体（α2-6 型）に結合する。我々は最近、ヒトへ感染することが報告されたトリ由来の H7N9 型インフルエンザウイルスのヘマグルチニン（HA）のヒトおよびトリ受容体への結合を解析した。FMO 法による相互作用解析の結果 H7N9 ウイルスの HA は通常のトリインフルエンザウイルスである H7N3 型ウイルスに比較して、ヒト型受容体に高い親和性があることが示された。これらの結果は、実験で得られた病原性のデータと一致しており、我々はさらに、トリ型あるいはヒト型インフルエンザウイルス HA と、トリあるいはヒトの受容体との結合親和性について、FMO 分析の結果を比較することで、分子機構の説明も試みた。

モルビリウイルス類はその HA が宿主動物の Signaling lymphocyte activating molecule (SLAM) を受容体に結合することで感染する。その仲間で研究が進んでいる麻疹ウイルス（MV）の HA とサルの SLAM の複合体は結晶化され立体構造が報告されていることから、その構造をテンプレートにして、HA-SLAM の立体構造を分子動力学的な計算により推定した。FMO 解析の結果推定された MV-HA と数種の哺乳類（ヒト、サル、マウス、イヌ、アザラシなど）の SLAM との結合親和性とこれらの哺乳類の MV に対する感受性は一致していた。しかし、まだ複合体の構造が報告されていないイヌジステンパーウイルス HA と幾つかの哺乳類の SLAM の間では、その両者は一致していないように思われた。そのような相違は、一次構造の類似度に依存した構造モデリングに一因があると思われ、複合体の立体構造を高精度で予測する工夫が必要である。

今回の研究から、ウイルスエンベロープである HA と宿主の受容体の結合の推定には、もし HA と受容体の立体構造が判明している場合には、FMO 法による解析でその親和性を推定することは、有効な方法であることが判明した。しかし、解析対象と類似の立体構造が明らかでない場合には、そこが問題となるため、今後、高精度で複合体構造を予測して相互作用解析を行うことが重要であることも明らかとなった。

キーワード: インフルエンザウィルス, モルビリウイルス, 受容体, フラグメント分子軌道法, ヘマグルチニン, Signaling lymphocyte activating molecule (SLAM)

A Large Scale 3D Global Full Particle Simulation of the Solar Wind-Terrestrial Magnetosphere Interaction for Bepi Colombo Mercury Exploration

Project Representative
Dongsheng Cai Faculty of Engineering, Information and Systems, University of Tsukuba

Author
Dongsheng Cai Faculty of Engineering, Information and Systems, University of Tsukuba

In the present paper, to our knowledge, the first 3D global full electro-magnetic particle simulation in the global view of solar-wind-magnetosphere interaction are performed, and compared with the statistical surveys of the plasma flows measured by the Cluster spacecraft in the high-altitude cusp region of the Northern Hemisphere. The magnetospheric polar cusp regions are considered to be key regions to transfer mass, and energy from the solar-wind to the plasma sheet. Using the global PIC simulation, we try to understand these key regions and the dynamical interactions that occur there. The basic structures of the so-called stagnant cusp exterior (SEC) are observed in the simulation. The sub-Alfvenic layers which consider to be the plasma depletion layer (PDL) are observed. The 3D PIC simulation reveals the global views of the solar-wind magnetosphere interactions and the magnetic polar cusp structures.

Keywords: PIC, Magnetosphere, Mercury, CUSP, PDL

1. Introduction

Large-scale global three-dimensional PIC simulations have been performed in order to analyze the interaction between the solar-wind with the whole terrestrial magnetosphere as shown in Fig. 1. To our knowledge, this is the first simulation performed within the global 3D PIC view. Present analysis is first focused on the polar magnetic cusp region, more precisely on the dynamics of the cusp boundaries and particle entry area. The interplanetary magnetic field (IMF) is purely northward in order to identify more clearly the main cusp features to be compared with statistical 3-years Cluster observations. Present simulations are performed with a higher resolution, where one grid size equal to 0.2 Earth radii, as compared with our previous works [1-11]. Results show that different quantities need to be used in order to identify appropriately the cusp boundaries, for example, Bt (total magnetic field), Grad-Bt, ion density, ion flow, etc.. Main features of the cusp for northward IMF are characterized as follows: (i) a more draped B topology close to the outer boundary, (ii) a strong density peak within the cusp with multiple humps; this peak shifts poleward and disappears for high latitude, (iii) a strong peak in ion field aligned flow within the cusp, with a tailward (sunward) convection at low (high) latitude. A particular point is the evidence of a layer characterized by (a) a subAlfvenic/superAlfvenic ion flow transition, and (b) slow mode feature (increase of B, and decrease of Ni). Both features are in favor of the formation of PDL at the exterior cusp near a possible lobe reconnection site in good agreement with experimental observations. In the present case, the location of this layer and of the reconnection site is slightly below latitude that evidenced in the statistics of Cluster data.

Statistical experimental observations of the cusp boundaries from Cluster mission made by [12] have clearly evidenced the presence of a transition layer inside the magnetosheath near the outer boundary of the cusp, This layer charaterized by Log(M_A)~1 allows a transition from super-Alfvenic to sub-Alfvenic bulk flow from the exterior to the interior side of the outer cusp and has been mainly observed experimentally as the interplanetary magnetic field (IMF) is northward. The role of this

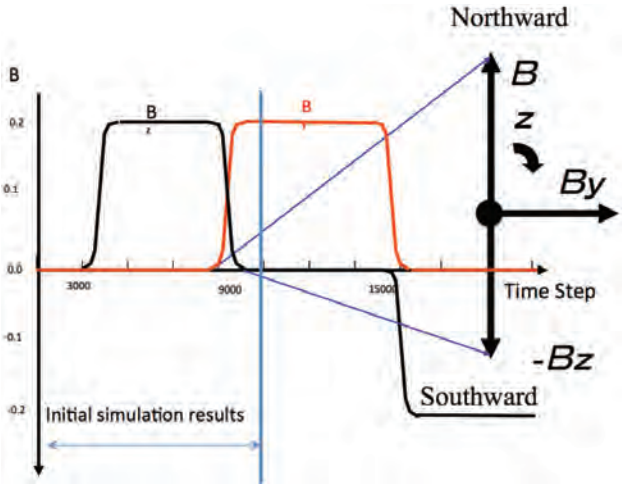

Fig. 1 Time sequence of IMF rotations from Bz to By.

layer is important in order to understand the flow variations and later the entry and precipitation of particles when penetrating the outer boundary of the cusp. Present results retrieve quite well the presence of this layer within the meridian plane for exactly northward IMF, but its location differs in the sense that it is located slightly below the X reconnection region associated to the nearby magnetopause (above the outer boundary of the cusp). In order to clarify this question, an extensive study has been performed by performing: a 3D mapping of this transition layer in order to analyze more precisely the possible spatial extension of this layer on the magnetosphere flanks.

2. 3D Global Simulation

In this section, we mainly discuss about main features of our simulations. The main advantages of present simulations are: (i) they are self-sonsistent simulations; (ii) the present simulation includes some kinetic effects although some attentions should be paid due to the limit size of grids; (iii) they are 3D simulations; and (iv) they are global. Therefore, some significant 3D fetures such as magnetic sashes, NENL (Near Earth Neutral Line) etc. can be included and we can self-consitently analyze how ions and electrons enter the magnetotail and where, when, and how they are energized. However, our global simulation also includes some limitations. For example, limited “space” resolution may exclude some effects such as: “thin” boundary layers, short wavelength instabilities etc.. These also may lead us to compromise on plasma parameters values. However, such limitations may be improved with the increase of computational ressources in the future.

The global MHD simulation can simulate properly the transport energy and momentum between different magnetospheric plasma regions despite their very large separation distances including the notion of magnetospheric convections, the general shape of magnetosphere, and their dependence on the incident solar wind conditions. Despite of these strong advantages, there still some questions remains because some evolutions of the global magnetospheric system may strongly depend on kinetic processes such as: (1) both precipitations and accelerations of both ions and electrons in the magnetic cusp region; and (2) transport of particles form the magnetic cusp to the plasma sheet. These strongly lead us to perform a 3D global electromagnetic full PIC simulation.

3. Simulation Results

In this section, we mainly discuss about main features of our simulations. As indicated in the time sequence of IMF rotation in Fig. 1, (a) the northward IMF has been applied after t=3000 and stay constant until t=9000; (b) the northward IMF gradually begin to rotate to dusk-dawn direction and stay constant until t=15000; and (c) finally rotate to southward and stay constant until 27000. The magnetic field configurations from IMF northward to southward are plotted in Fig. 2. Figure 2a is the northward IMF case and the magneto-tail magnetic field closed at x=-30Re and the magnetic field transit from the dipolar terrestrial to the tail magnetic field. As IMF rotates from north to dusk-dawn as shown in Fig. 2bc, the last closed dipolar field moves earthward from -30Re to -20Re. The magnetic sashes forms and rotates out to (Z, X) meridian plane. The stretching of the tail magnetic field occurs.

The southward IMF rotation can be decomposed into two sub-processes a and b as indicated in Fig. 2de. In sub-process a, the tail magnetic field stretches. The tail magnetic field progressively expands tailwards. In the sub-process b, tail magnetic field stops stretching. The abrupt transition between terrestrial and tail magnetic field occurs. The X-lines both at subsolar region and in the nearby tail at x=-12Re are formed. A neutral ring evidenced in the equatorial plane connects both X-regions. Magnetic field lines adjacent the equatorward cusp boundary connected to the open magnetopause at low latitude [13]. Magnetosheath plasma enters magnetopause and populates the fields lines, thus, strong parallel precipitations of particles can be expected. With southward IMF, the IMF and terrestrial magnetic fields are antiparallel, and these two magnetic field may reconnect at the dayside magnetopause, and one expect the consequent transport and magnetic flux to the tail lobes causes increased magnetic stress in that region. This build up of magnetic flux leads to reconnection in the magnetotail. Here we will not mention anything about the reconnection processes themselves due to the present constraints of the simulation. For example, reconnections on the tail will be developed, but they may not be the ones that are commonly discussed kinetic ones in magnetospheric physics community. Here, we try to identify whether the global features in terms of magnetic field gradient,

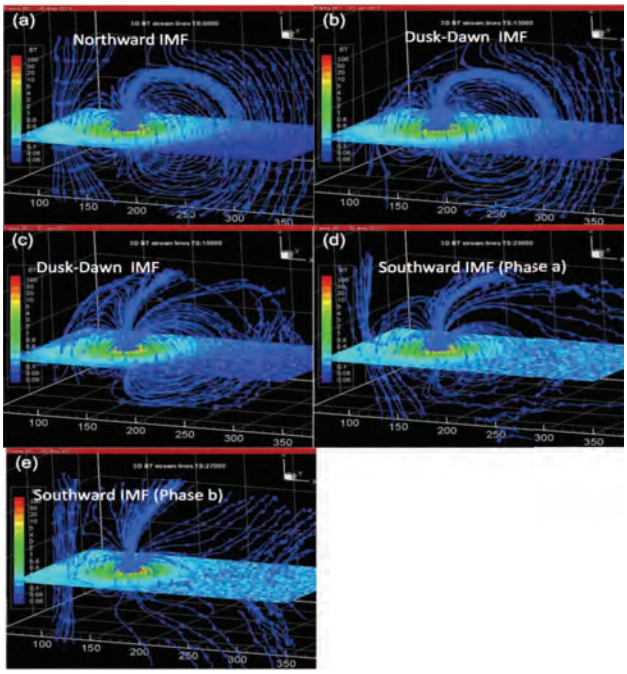

Fig. 2 Time sequence of magnetic field configurations in our simulation rotating IMF form north to south.

currents that are the ingredient necessary for magnetic substorm can be identified or not within this 3D PIC simulation approach.

We show the global view of magnetopshere of the northward IMF in 3D slicing in Fig. 3. A global view of the magnetosphere and the magnetic cusp structure can be observed. Asymetric reconnection X-lines in the polar region and piles up of magnetic field in the dayside magnetospheath and high latitude polar region close to magnetic reconnection X lines also can be observed. This asymetric structure can be better visualized showing 3D isofurface of Log(M_A)~1 in Fig. 4. Due to the complicate 3D reconneting flow, the part of Log(M_A)~1 over the exterior cups is strongly modified and move toward the earth. The complexisty of the cusp makes the 3D analysis exteremely difficult.

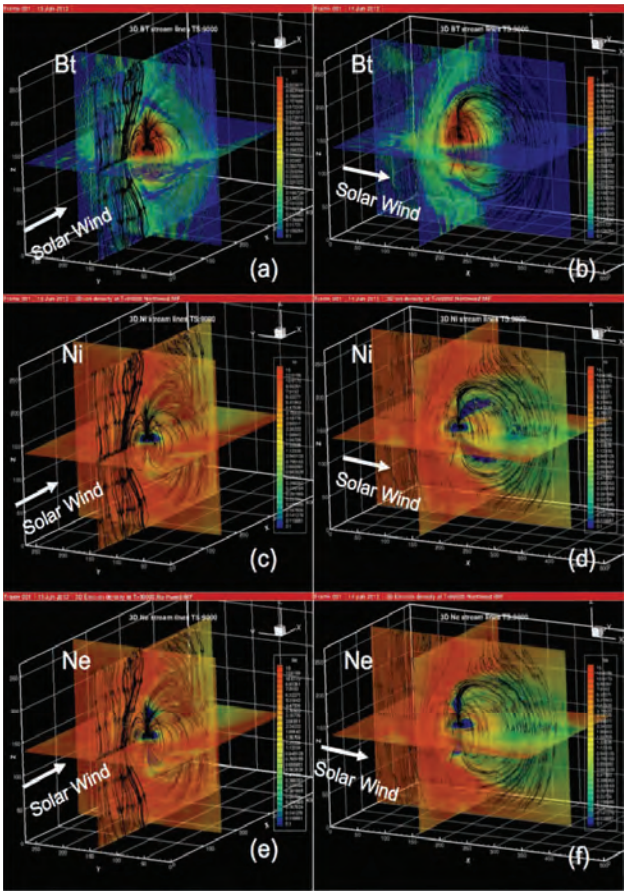

Fig. 3 3D global view of Bt, Ni, and Ne.

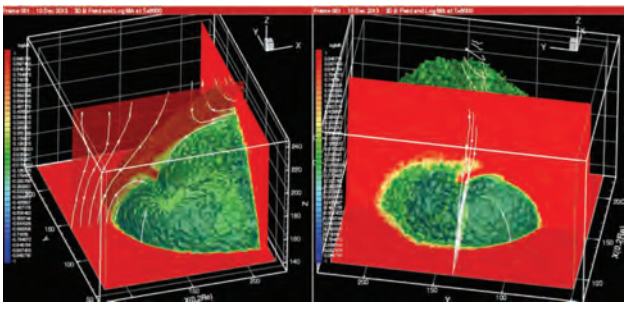

Fig. 4 Isosurface of Log(M_A)~1 layer near the magnetic cusp region.

4. Conclusions

Although the size of our global simulation is limited and still small, the post process procedure to compare with the observational results is not well established, and the extent of the physical validity of the global PIC is not so clear, the global PIC simulation is still the powerful tool to analyze the global interaction between solar-wind and magnetosphere as we evidenced in the present paper. The comparative study with MHD and statistical studies of CLUSTER satellite observations shows many significant features such as SEC, FAB, PDL layers can be simulated and analyzed using the global PIC simulations. The advancement of computer power can resolve many limitations of the global PIC simulation such as the limited size in the simulation. However, at the same time, the post process procedure and data analysis technique to map the simulation data to real physics is also significant.

Acknowledgements

We would like to thank Dr. Tatsuki Ogino for his valuable advice and Dr. Ogino for encouragements. We would also like to thank Dr. Lavraud valuable comments on our research.

References

[1] O. Buneman, *et al.*, "Solar wind-magnetosphere interaction as simulated by a 3-D EMparticle code," *Plasma Science, IEEE Transactions on*, vol. 20, pp. 810-816, 1992.

[2] D. Cai, *et al.*, "Magnetotail field topology in a three-dimensional global particle simulation," *PLASMA PHYSICS AND CONTROLLED FUSION*, vol. 48, p. 123, 2006.

[3] D. Cai, *et al.*, "Bifurcation and hysteresis of the magnetospheric structure with a varying southward IMF: Field topology and global three-dimensional full particle simulations," *Journal of Geophysical Research: Space Physics*, vol. 114, 2009.

[4] D. Cai, *et al.*, "Particle entry into the inner magnetosphere during duskward IMF By: Global three-dimensional electromagnetic full particle simulations," *Geophysical research letters*, vol. 33, 2006.

[5] D. S. Cai, *et al.*, "Visualization and criticality of three-dimensional magnetic field topology in the magnetotail," *Earth Planets Space*, vol. 53, p. 1011, 2001.

[6] B. Lembege, *et al.*, "Signatures of substorm triggering in the magnetotail during IMF," 2008.

[7] K.-I. Nishikawa and S.-i. Ohtani, "Global particle simulation for a space weather model: Present and future," *Plasma Science, IEEE Transactions on*, vol. 28, pp. 1991-2006, 2000.

[8] K. I. Nishikawa, "Particle entry into the magnetosphere with a southward interplanetary magnetic field studied by a three-dimensional electromagnetic particle code,"

Journal of Geophysical Research-Space Physics, vol. 102, pp. 17631-17641, 1997.

[9] K. I. Nishikawa and S. Ohtani, "Global particle simulation for a Space Weather Model: Present and future," *IEEE Transactions on Plasma Science*, vol. 28, pp. 1991-2006, 2000.

[10] K. I. Nishikawa and S. Ohtani, "Evolution of thin current sheet with a southward interplanetary magnetic field studied by a three-dimensional electromagnetic particle code," *Journal of Geophysical Research-Space Physics*, vol. 105, pp. 13017-13028, 2000.

[11] K. I. Nishikawa and S. Ohtani, "Particle simulation study of substorm triggering with a southward IMF," *Dynamic Processes in the Critical Magnetospheric Regions and Radiation Belt Models, Proceedings*, vol. 30, pp. 2675-2681, 2002.

[12] B. Lavraud, *et al*., "Cluster observations of the exterior cusp and its surrounding boundaries under northward IMF," *Geophysical research letters*, vol. 29, pp. 56-1-56-4, 2002.

[13] M. Lockwood and M. Smith, "Low and middle altitude cusp particle signatures for general magnetopause reconnection rate variations: 1. Theory," *Journal of Geophysical Research: Space Physics*, vol. 99, pp. 8531-8553, 1994.

水星探査計画「Bepi Colombo」のための大域的３次元電磁粒子シミュレーションを用いた水星磁気圏シミュレータの開発

課題責任者
蔡　　東生　　筑波大学　シスステム情報系
著者
蔡　　東生　　筑波大学　シスステム情報系

本研究では、2016 年打ち上げの予定の水星探査衛星「Bepi-Colombo」の観測結果をデータアシミレートするための大域的三次元電磁粒子シミュレーションを行う。シミュレーションの正当性、適用可能範囲を調べるため、最初に衛星 4 基で観測している Cluster 衛星の統計的観測結果との比較をカスプ領域を中心に行った。その結果、カスプ領域の境界である、磁気シースとの境界の Plasma Depletion Layer、磁尾部境界の磁気再結合ジェット、外部カスプの半磁性流を確認した。また、アルフベンマッハ速度が亜アルフベンマッハ速度に遷移する境界を詳しく調べることにより、３次元的なカスプ形状を詳しく調査した。これらにより、水星探査における、３次元粒子コードの有用性を確認した。

キーワード:粒子コード, 水星, ベッピコロンボ, カスプ, プラズマ排出領域

Chapter 2

Visualization

Studies of Large-Scale Data Visualization and Visual Data Mining

Project Representative
Fumiaki Araki Earth Simulator Center, Japan Agency for Marine-Earth Science and Technology

Authors
Fumiaki Araki[*1], Shintaro Kawahara[*1], Daisuke Matsuoka[*1] and Yumi Yamashita[*1]
*1 Earth Simulator Center, Japan Agency for Marine-Earth Science and Technology

This paper reports activities of Advanced Visualization and Perception Research Group (AVPRG), Earth Simulator Center (ESC) in the fiscal year 2013. Research themes in this fiscal year are as follows: improvement of a volume visualization software in the EXTRAWING project, development of a mobile user interface in the VFIVE project and visual analytics approaches for ocean currents and eddies.

In the EXTRAWING project, we have been continuously developing VDVGE, a content-making software tool for realizing volume rendering-like representation on Google Earth. New functions, which are display functions of topography and coastline and an iso-contour drawing function on each slice of an input volume data, were implemented in VDVGE.

In terms of VFIVE project, the function to extract visualization operations by using a mobile user interface was implemented to VFIVE. This function divides the history of user's visualization operations into groups when each time interval between the operations is over a certain threshold. The user can select the groups of the operations and reapply to VFIVE.

Progress of visual analytics techniques for oceanic field datasets is summarized as follows: multivariate visualization approaches and pixel-based approaches. In terms of multivariate visualization approaches, we carried out case studies to represent multiple physical features of oceanic structure at once. As a result, effective visual representation of the features for ocean currents was obtained. In terms of pixel-based approaches, we developed a couple of the methods for extraction of vortices and segmentation of streams.

Keywords: advanced visualization, VDVGE, mobile user interface, visual data mining, ocean simulation data

1. Introduction

Amidst significant social change derived from the “big data” technologies, computer visualization has brought to much stronger attention than ever before. The same can be said for natural scientific domains. Scientific visualization is nowadays becoming more important, with the appearance of new data sources and research environments like cloud services in addition to experiments, observations and numerical simulations. We are carrying out basic researches in the field of scientific visualization in order to contribute earth-scientific communities. Our research interests covers wide-ranging area, such as large-scale data visualization using high-performance computers, application of virtual reality technology, visual analytics and graphical representation methodology. Especially in the fiscal year 2013, we have proceeded the three projects, EXTRAWING (Section 2), VFIVE extension (Section 3) and the development of the visual data mining methods for oceanic phenomena (Sections 4 and 5). In the following sections, we introduce recent progress of these projects.

2. EXTRAWING

EXTRAWING is a research project to develop methods to share earth-scientific knowledge among researchers and conveyer it to the general public, through attractive visual representation of numerical simulation and observation data [1]. Our aim of visual representation is to show three-dimensional features in simulation results on Google Earth (GE). We have already been developed a method to visualize volumetric structural data on GE as shown in Fig. 1 [2] and also a software tool, which is called VDVGE (Fig. 2), to make GE contents based on the method [3].

In the fiscal year 2013, additional visualization functions, displaying topography and coastlines and drawing iso-contours, were implemented to VDVGE. For the topography representation, three digital terrain models of different resolutions, ETOPO1 [4], ETOPO2 [5] and ETOPO5 [6], are available. This function is designed to be able to set the respective altitude scales of upper and lower side of sea surface independently in order to facilitate to visualize oceanic simulation data. For the coastline representation,

GEODAS Coastline [7] is available. The optional function for command line execution was also added to VDVGE. VDVGE exports content files for GE without launching the GUI window. This function is effective to generate multiple GE contents automatically from a number of datasets by batch processing, whereas it is not possible to change the visualization configuration interactively during program execution.

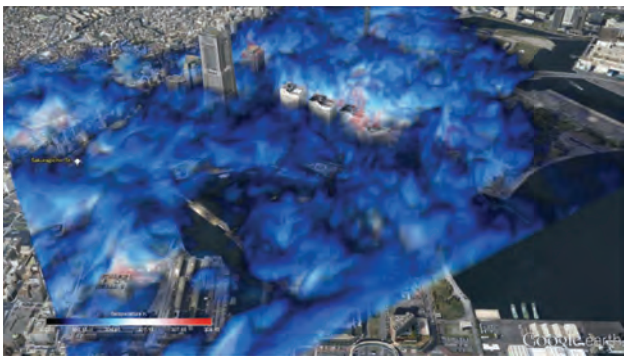

Fig. 1 Original volume representation method on Google Earth.

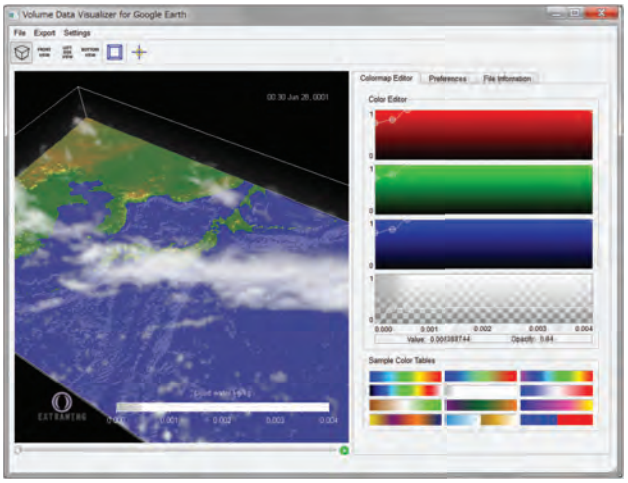

Fig. 2 Screen capture of Volume Data Visualizer for Google Earth (VDVGE).

3. Virtual reality visualization

Application of virtual reality (VR) technologies to data visualization is considered as an effective method to understand intuitively from given data. In particular, it is believed that immersive visualization environment as represented by a CAVE system [8] has a greater visual effect than the other VR devices such as a 3D-monitor and a head-mounted display because it covers the entire sight field of the user with multiple screens. We have installed the CAVE system called BRAVE [9] and continuously been developing VFIVE [10], a VR visualization software, shown in Fig. 3.

CAVE system, in general, strongly restricts user interface to portable devices like game controllers, because the system permits user's free movement and observation in the space different from desktop environment. Therefore, additional techniques are required for complicated manipulations such as character input, programming and optimal reconstruction of visualized objects. As for it, we are currently researching the methods to manipulate the system efficiently through utilizing mobile communication device like smart phone and analyzing human action. Shown in Fig. 4 is an example of the mobile user interface developed for VFIVE. In this picture, a list of the visualization operations that a user applied to VFIVE is displayed on the mobile user interface. The user can select some operations from this list and reapply to VFIVE.

In the fiscal year 2013, we implemented a function to extract visualization operations which satisfied with the specific conditions with a mobile user interface [11]. Here, we focused on time intervals between operations and assumed that time which a user observes scene became long when characteristic structures were visualized. We have carried out validation of the function, but it is not sufficient in number of the measurements. In the future research, it will be evaluated whether visualization operations extracted using this function lead to effective results.

Fig. 3 VFIVE, Interactive visualization software for CAVE-type virtual reality system.

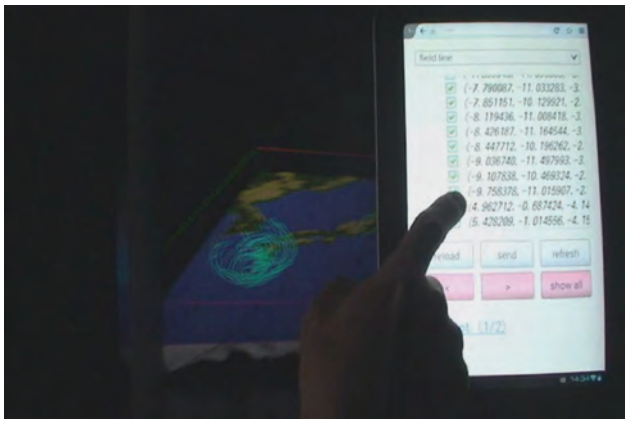

Fig. 4 Screenshot of the mobile user interface.

4. Multivariate visualization of ocean current

Global ocean simulation reproduces realistic ocean structures with a variety of physical characteristics. Ocean current, horizontal water streams in shallow ocean areas, has several physical properties such as current speed, velocity components, temperature and salinity. In order to investigate such properties of ocean currents, it is necessary to visualize multiple physical quantities simultaneously. This study attempts to visualize new aspects of ocean currents by means of multivariate visualization

methods.

Figure 5 shows a visualization result of the Pacific Equatorial Countercurrent and its three velocity components (zonal, meridional and vertical components) using multivariate layering. Each component is represented by mixed color. Figure 6 indicates a visualization result of the same current and its six velocity components (eastward, westward, northward, southward, upwelling and downwelling components) using multivariate color weaving. Fine-grained structures of velocity components with each direction can be found without color mixing. In both cases, novel representations in which scientists can effectively recognize ocean currents and their physical characteristics can be obtained [12].

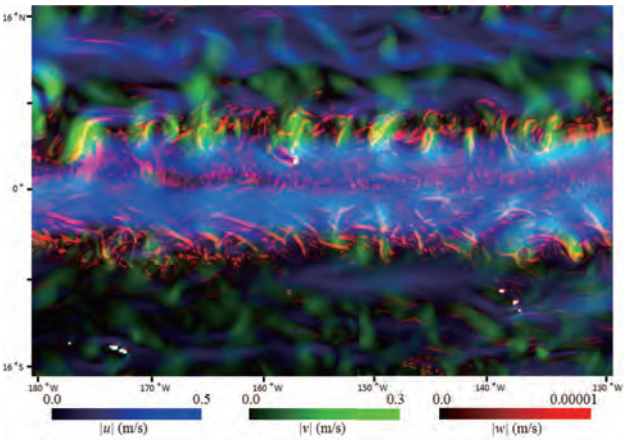

Fig. 5 Ocean current and velocity component: multivariate layering.

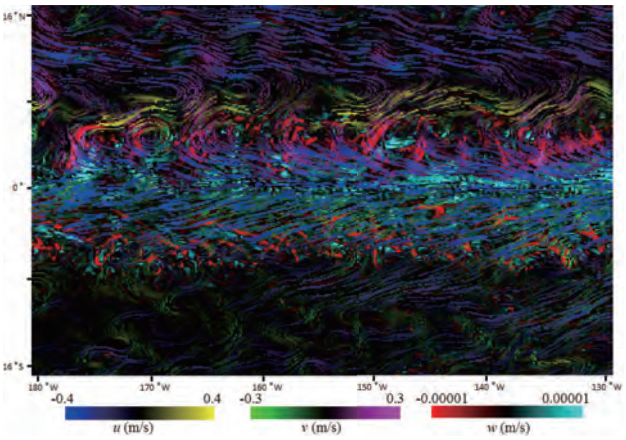

Fig. 6 Ocean current and velocity component: multivariate color weaving.

5. Extraction of vortices and segmentation of streams in the ocean flow field

The ocean flow field is mixture of innumerable multi-scale vortices and streams. They are highly intermingled intricately, and further, their boundary lines are ambiguous. Therefore, forms of these flows are indefinable. This makes us difficult to recognize the ocean flow structure. In this research, we extracted boundary lines of respective streams and vortices and visualized them to reveal the ocean flow structure. We propose independent extraction / segmentation methods for vortices and for streams.

The ocean flow field has vortex-core regions that mass do not mix with outer mass much. We define these regions are the regions to extract with our vortices extraction method. The saddle points, one of the singularities, can be appeared in outside of the vortices regions, and streamlines originated at the vicinity of the saddle points are expected not to enter the vortex-core regions because mass in the vortex-core regions do not mix with outer mass. Based on this consideration, we generated multiple widely spreading streamlines by seeding at the vicinity of the saddle points that have high Finite Size Lyapunov Exponent value, and extracted closed regions segmented with these streamlines if they include the center point (one of the singularities) inside. The extracted regions are regarded as the vortex-core regions. Figure 7 shows vortex regions obviously.

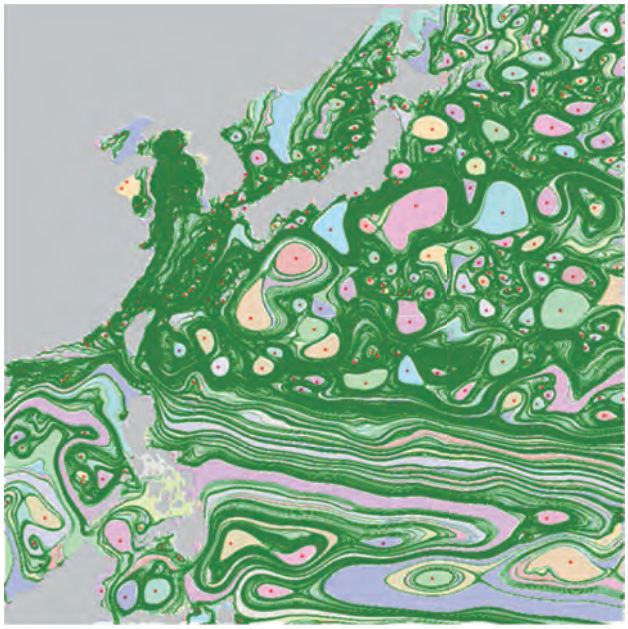

Fig. 7 Vortex regions with streamlines.

The individual streams are recognizable intuitively by regarding the stagnation points as terminations of each stream. In order to meet this recognition, our stream segmentation method firstly detect flow axis that is the series of the local maximum velocity points expanding to almost whole flow field without segmentation. The large detected axis can be segmented to axes of individual streams by removing points that has high velocity gradient between the adjacent local maximum points. This segmentation agrees to our intuitive recognition of termination of individual streams that is mentioned above. The residual points are associated to axes, and then all individual stream regions are determined. (Fig. 8)

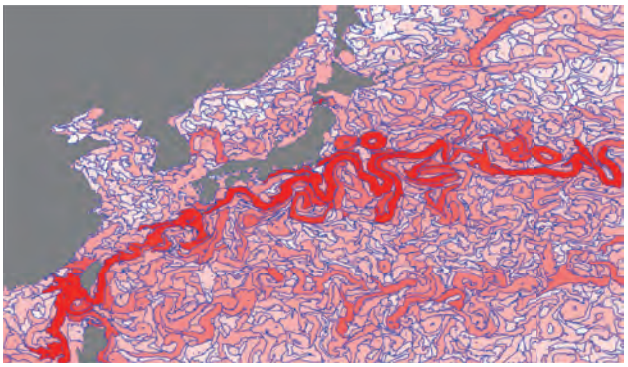

Fig. 8 Stream regions colored with internal velocity.

Acknowledgement

One of the authors (S. K.) was supported by JSPS KAKENHI Grant Number 25730080.

References

[1] Fumiaki Araki, Shintaro Kawahara, Daisuke Matsuoka, Takeshi Sugimura, Yuya Baba, and Keiko Takahashi, “Studies of Large-Scale Data Visualization: EXTRAWING and Visual Data Mining”, Annual Report of the Earth Simulator Center, April 2010-March 2011, pp.195-199, 2011.

[2] Fumiaki Araki, Tooru Sugiyama, Shintaro Kawahara, and Keiko Takahashi, “Visualization of Three-Dimensional Temperature Distribution in Google Earth”, Scientific Visualization Showcase, the international conference for High Performance Computing, Networking, Storage and Analysis (SC13), Denver, November 19th, 2013.

[3] VDVGE, http://www.jamstec.go.jp/esc/research/Perception/vdvge.ja.html.

[4] C. Amante and B. W. Eakins, “ETOPO1 1 Arc-Minute Global Relief Model”, Procedures, Data Sources and Analysis, NOAA Technical Memorandum NESDIS NGDC-24, p19, March 2009; http://www.ngdc.noaa.gov/mgg/global/global.html.

[5] 2-minute Gridded Global Relief Data (ETOPO2v2), National Geophysical Data Center, National Oceanic and Atmospheric Administration, 2006; http://www.ngdc.noaa.gov/mgg/global/etopo2.html.

[6] 5-Minute Gridded Global Relief Data Collection (ETOPO5), National Geophysical Data Center, National Oceanic and Atmospheric Administration; http://www.ngdc.noaa.gov/mgg/fliers/93mgg01.html.

[7] GEODAS Coastlines, GEODAS-NG web page, National Geophysical Data Center, National Oceanic and Atmospheric Administration; http://www.ngdc.noaa.gov/mgg/shorelines/shorelines.html.

[8] Carolina Cruz-Neira, Daniel J. Sandin, Thomas A. DeFanti, Robert V. Kenyon, and John C. Hart. 1992. The CAVE: audio visual experience automatic virtual environment. Commun. ACM 35, 6, pp. 64-72, 1992.

[9] Fumiaki Araki, Hitoshi Uehara, Nobuaki Ohno, Shintaro Kawahara, Mikito Furuichi, and Akira Kageyama, “Visualizations of Large-scale Data Generated by the Earth Simulator”, Journal of the Earth Simulator, vol.6, pp.25-34, 2006.

[10] Akira Kageyama, Yuichi Tamura, and Tetsuya Sato, “Visualization of Vector Field by Virtual Reality”, Progress of Theoretical Physics Supplement, No.138, pp.665-673, 2000.

[11] Shintaro Kawahara and Fumiaki Araki, “Effective VR Visualization Focused on Time Interval between Visualization Operations”, International Conference on Simulation Technology (JSST 2013), Tokyo, Japan, Sept. 2013.

[12] Daisuke Matsuoka, Fumiaki Araki, and Yumi Yamashita, “Applications of Multi-dimensional Transfer Function to Visualization of Geophysical Fluid Simulation: Case Studies”, International Conference on Simulation Technology (JSST 2013), Tokyo, Japan, Sept. 2013.

大規模データ可視化とビジュアルデータマイニングの研究

課題責任者
荒木　文明　　海洋研究開発機構　地球シミュレータセンター
著者
荒木　文明 *1，川原慎太郎 *1，松岡　大祐 *1，山下　由美 *1
*1　海洋研究開発機構　地球シミュレータセンター

地球シミュレータセンター高度計算表現法研究グループの 2013 年度の研究成果について報告する。2013 年度の研究テーマは、EXTRAWING プロジェクトにおけるボリューム可視化ソフトウェアの改良、VFIVE プロジェクトにおけるモバイルユーザインターフェースの開発、海洋諸現象に対するビジュアルデータマイニング手法の研究開発である。

EXTRAWING プロジェクトについて、我々は Google Earth 上でボリュームレンダリング的な表現の 3D コンテンツを作成するボリューム可視化ソフトウェア VDVGE の開発を進めている。地形と海岸線の表示機能、入力データの各層上での等値線描画機能があらたに VDVGE に実装された。

VFIVE プロジェクトについて、モバイルユーザインターフェースを使って可視化機能を抽出する機能を VFIVE に実装した。本機能はユーザの可視化操作の履歴を、その操作の時間間隔がある閾値を超えるときにグループに分割する。ユーザはその操作のグループを選んで VFIVE に再び適用することができる。本機能は現在開発中であり、評価方法を検討している。

海洋場のデータセットに対するデータマイニング手法については、多変量可視化手法およびピクセルベース手法の研究開発を実施した。多変量可視化手法については、海洋構造の複数の物理的特徴を同時に表現するためのケーススタディを行った。その結果、海流および関連する物理的特徴の効果的な可視化表現が得られた。ピクセルベース手法については、海洋流れ場からの渦抽出手法およびストリーム分割手法を開発した。

キーワード: 先進可視化技術, VDVGE, モバイルユーザインターフェース, ビジュアルデータマイニング, 海洋シミュレーションデータ

Annual Report of the Earth Simulator Center April 2013– March 2014

Center for Earth Information Science and Technology, Japan Agency for Marine-Earth Science and Technology

Published by

Center for Earth Information Science and Technology, Japan Agency for Marine-Earth Science and Technology

3173-25 Showa-machi, Kanazawa-ku, Yokohama, 236-0001 JAPAN

Tel: +81-45-778-5861 Fax: +81-45-778-5491

http://www.jamstec.go.jp/ceist/

First edition: October 23, 2014